Emission patterns of charged pions from Ag+Ag collisions at 1.58A GeV

Masterarbeit

am Institut für Kernphysik

vorgelegt beim Fachbereich Physik
der Johann Wolfgang Goethe-Universität
in Frankfurt am Main

von

Marvin Nabroth

März 2022

Erstgutachter: Prof. Dr. Joachim Stroth

Zweitgutachter: Dr. Manuel Lorenz

Zusammenfassung

Stark wechselwirkende QCD Materie unter extrem hohen Dichten wird in verschmelzenden Neutronensternen vermutet. Die dabei vorherrschenden Bedingungen lassen sich experimentell mittels relativistischer Schwerionenkollisionen generieren [6]. Die Untersuchung der kinematischen Eigenschaften der Reaktionsprodukte durch moderne Teilchendetektoren, ermöglicht Rückschlüsse auf diesen, wenige Femtosekunden andauernden, Materiezustand. Ein Experiment, das konzipiert wurde, um Hadronen und Dileptonen aus Schwerionenkollisionen mit Strahlenergien im 1 $AGeV$ Bereich zu untersuchen, ist der HADES-Detektor (High-Acceptance-Di-Electron-Spectrometer) an der GSI in Darmstadt [3]. In dieser Arbeit werden die am häufigsten produzierten Hadronen, elektrisch geladene Pionen, aus $6.9 \cdot 10^9$ selektierten Ereignissen von kollidierenden Silberkernen mit einer Schwerpunktenergie von $\sqrt{s_{NN}} = 2.55$ GeV analysiert. Die Messungen erfolgten durch HADES im März 2019. Ein Ziel der Arbeit ist, die auf Effizienz und Akzeptanz korrigierten Phasen-Raum-Spektren zu bestimmen. Diese bilden die Grundlage zur Untersuchung des Coulombeffektes. Dabei liegt der Fokus zunächst auf der Verbesserung der Datenqualität der Analyse aus [44]. Neue Eventselektions- und Teilchenidentifikationskriterien werden getestet, um die Symmetrie zwischen den Forward- und Backward-Spektren zu optimieren. Die rekonstruierten differentiellen Transversalspektren werden mit einer modifizierten Doppel-Boltzmann-Funktion modelliert, welche den Coulombeffekt berücksichtigt. Dabei wird angenommen, dass das Coulombfeld überwiegend durch die Ladungen der an der Interaktion partizipierenden Protonen erzeugt wird. Ausgehend von dem extrahierten Coulombpotential wird zudem ein Rückschluss auf die räumliche Ausdehnung des Feuerballs zum Zeitpunkt des kinematischen Freeze-Out gezogen. Für das Coulombpotential wird bei mittlerer Rapidität ein Wert von 8.1 ± 0.5 MeV für die 0-10 % Zentralsten Kollisionen ermittelt. Unter der Annahme einer sphärisch symmetrischen Ladungsverteilung folgt für die Baryonendichte ein Wert von 0.07 ± 0.02 $\rho_0 fm^{-3}$. Des Weiteren werden die elektrisch geladenen Pionen im Hinblick auf anisotrope Emissionsmuster relativ zur Ereignisebene untersucht. Die azimutale Winkelverteilung wird einer Fourieranalyse unterzogen, um die Fluss-Koeffizienten v_1, v_2 und v_3 zu bestimmen. Die Ereignisebene wird dabei aus der, mit einem Hodoskop gemessenen, Verteilung der Projektilspektatoren rekonstruiert. Die experimentell begrenzte Auflösung erfordert die Implementierung einer Ollitrault-Korrektur [49]. Die Spurrekonstruktionseffizienz des Detektors ist abhängig von der Teilchenspurdichte, was zur Folge hat, dass der gemessene gerichtete Fluss v_1 bei mittlerer Rapidität von Null abweicht. Um diese Verzerrung zu reduzieren, wird eine Occupancy-Korrektur durchgeführt. Die korrigierten Fluss-Koeffizienten werden sodann als Funktion der Rapidität und des Transversalimpulses für Kollisionszentralitäten im Bereich von 0-40 % untersucht und mit drei akutell gängingen Transportmodellen verglichen.

Abstract

Strongly interacting QCD matter under extreme densities is assumed to be found, e.g. in merging neutron stars. Such conditions can be produced experimentally by relativistic heavy-ion collisions [6]. The conditions of interest only persist for a few fractions of femtoseconds, impossible to be observed directly. However, the multiplicities and kinematic characteristics of the reaction products are accessible by modern particle detectors. An experiment especially designed to investigate hadrons and leptons originated in heavy-ion collisions with beam energies in the 1 AGeV regime is the HADES (High-Acceptance-Di-Electron-Spectrometer) detector [3], located at the GSI, Darmstadt.
In this thesis, charged pions, the most abundantly produced hadrons, emitted in $6.9 \cdot 10^9$ selected events of colliding sliver nuclei with a centre of mass energy of $\sqrt{s_{NN}} = 2.55$ GeV, measured in march 2019, are analysed. This thesis' first aim is to determine the acceptance and efficiency corrected phase space distributions, which are the starting point for investigating the Coulomb effect. At first, the focus is put on improving the data quality of the charged pion analysis conducted in [44]. New event selection and PID criteria are introduced to improve the spectra's forward and backward symmetry. The obtained transverse distributions are fitted with a modified Double-Boltzmann function that incorporates a description of the Coulomb effect, assumed to be mainly caused by the proton charges of the participant nucleons. Based on the extracted potential, an estimation of the spatial system size of the fireball at the point of the kinematic freeze-out is drawn. The obtained Coulomb potential at mid-rapidity is found to be at 8.1 ± 0.5 MeV for the 0-10 % most central collisions. The extracted baryon density, assuming a spherical uniform charge distribution, is derived to a value of 0.07 ± 0.02 $\rho_0 fm^{-3}$.
In the third part of the thesis, the charged pions are explored regarding emission anisotropies relative to the event plane. The azimuthal angular distribution is decomposed by a Fourier series in order to obtain the harmonics v_1, v_2 and v_3, quantifying the strength of the anisotropies. The event plane is extracted by considering the pattern of the spectator nucleons of the collision, measured with a Forward Wall hodoscope. Experimental limitations make it necessary to correct for fluctuations by implementing an Ollitrault correction [49]. The tracking efficiency of the detector is multiplicity-dependent, which causes a deviation of directed flow from the being zero at mid-rapidity. To reduce this issue, an occupancy correction is carried out. The corrected flow harmonics are inspected as a function of rapidity and transverse momentum for collision centralities in the range of 0-40 % and are compared to three state-of-the-art transport models.

Contents

1. Introduction and Motivation

1. Strong Interaction and QCD

Protons and Neutrons, the constituents of atomic nuclei, are effectively bound by residual forces, resulting from the interactions between quarks and gluons that build up the nucleon. In the last century, flourishing experimental and theoretical research led to a very successful fundamental theory of the strong interaction, called Quantum-Chromo-Dynamics (QCD). Its mathematical formulation is based on relativistic quantum field theory. Quarks are described by quantized, space and time-dependent spinor fields $q(x)$. The interaction is mediated by exchange particles corresponding to quantized fields as well. The quarks occur in 6 different flavours (Up, Down, Charme, Stange, Top and Bottom) and form bound states to hadrons. Their physical behaviour is, according to the principle of least action, derived via the Euler-Lagrange-Equation resulting from the Lagrangian $\mathcal{L}_{QCD}$ of the QCD. It condenses all aspects of the strong interaction in one single scalar equation, e.g. in [50]:

$$\mathcal{L}_{QCD} = \overline{q}(i\gamma^{\mu}D_{\mu} - m)q - \frac{1}{4}F^{a}_{\mu\nu}F^{\mu\nu}_{a} \tag{1.1}$$

(γ corresponds to Dirac-Matrices). The starting point in constructing $\mathcal{L}_{QCD}$ is the Dirac Lagrangian $\overline{q}(i\gamma^{\mu}\partial_{\mu} - m)q$ describing a free quark with mass m in accordance with quantum mechanics and special theory of relativity, enabling the transformation of energy into mass and vice versa. This results in the existence of quark-anti-quark pairs. In order to implement the strong interaction, the free Dirac equation is modified by demanding local SU(3) gauge invariance of the Lagrangian. This is motivated by the observation that colour, the field generating charge of the strong interaction, must exist in 3 different variants, named red, green and blue [1], which give rise to local SU(3) gauge symmetry instead of local U(1) gauge symmetry as for the QED (Quantum-Electro-Dynamics, Quantum field theory of the electromagnetic interaction). Local SU(3) gauge invariance is embedded into the Lagrangian by replacing the 4-derivative ∂_{μ} in the free Dirac equation by a new covariant derivative D_{μ} that fulfils the required symmetry condition [50]:

$$\partial_{\mu} \Rightarrow D_{\mu} = \partial_{\mu} - igA^{a}_{\mu}T^{a}. \tag{1.2}$$

T^{a} correspond to the Gell-Matrices. g is the coupling constant of the strong force. For all equations in this section, c is written in terms of natural units (c=1). This step couples the quarks to the strong interaction and introduce 8 additional fields A^{a}_{μ} that represent

[1] This was deduced by the experimental observation of the Δ^{++} baryon, where all of the tree quarks are equal as well as the spins is. Yet, a baryon is a fermion which has to obey the Pauli principles. This gives rise to a charge that comes in 3 different versions.

the exchange bosons of the QCD, called gluons. Due to this coupling, they are considered as objects which mediate the strong force. The dynamic behaviour of the gluon fields, the way how they intact, is described by $F^a_{\mu\nu}F^{\mu\nu}_a$, the colour field strength tensor. It is defined as [50]:

$$F^a_{\mu\nu} = \partial_\mu A^a_\nu - \partial_\nu A^a_\mu + g f_{abc} A^b_\mu A^c_\nu. \tag{1.3}$$

$F^a_{\mu\nu}$ consists of the introduced gluon field A^a_ν. The first dynamic part $\partial_\mu A^a_\nu - \partial_\nu A^a_\mu$ has the same structure as in the QED. In QCD, the additional term $g f_{abc} A^b_\mu A^c_\nu$ occurs, which expresses the fact that gluons can interact with themselves since they carry colour charge as this term couples them with g. Each of the 8 gluons carries one possible combination of colour and anti-color so that they are in accordance with the demanded SU(3) color symmetry. Another remarkable feature of the strong interaction is that the strength of the coupling g between color and gluons and quarks is not constant. Instead, it depends on the energy transfer Q in the considered interaction process. The coupling strength as a function of the energy scale Λ predicted by the QCD as well as the findings from experiments, extracted from, e.g. deep inelastic scattering, are displayed in figure (1.1). The coupling increases for small energy transfers or respectively for large distances [23]. For high energy transfers or small distances, the interaction strength becomes small. On a phenomenological level, this behaviour can be explained by vacuum polarisation: The fusion of the laws of special relativity and quantum mechanics enables the emergence of pairs of particle-antiparticles in the vacuum as long as they agree with the Heisenberg uncertainty principle. This causes polarisations of the vacuum pairs around an object that carries color charge, which leads to shielding effects. As opposed to QED, in QCD, this effect is anti-shielding because the gluons carry colour charge and therefore can self interact. Moreover, the coupling constant g in the QCD is much stronger than the coupling in QED. Therefore, vacuum polarisations effects are much more significant and complicated in the strong interaction. Considering a pair of a quark and anti-quark, the anti-shielding vacuum polarisations leads to a linear increase of the bounding potential if one tries to separate the quark pair. The stored energy rises till it is large enough to create a new quark-antiquark pair, again a colour-neutral object.

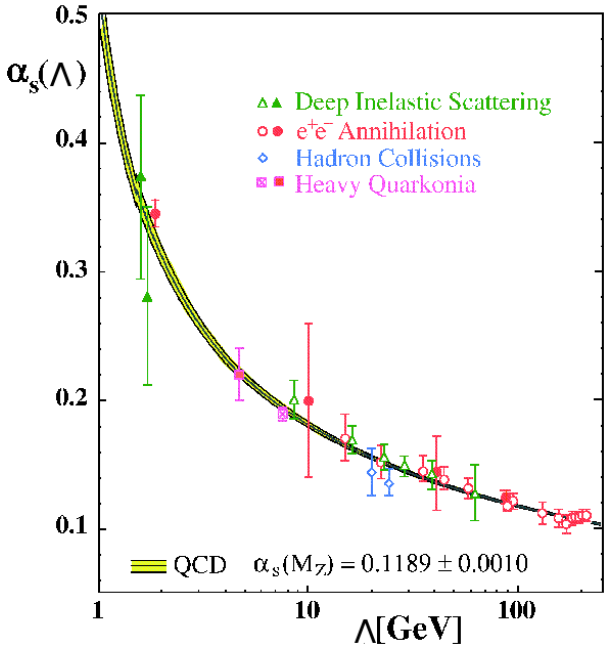

Figure 1.1: The functional dependence of the strong coupling constant from the energy scale of the QCD. The line corresponds to the behaviour predicated by the QCD. The displayed data points have been measured by the examination of e.g. deep inelastic scattering and e^-e^+ annihilations processes. The coupling increases for small energies and decreases towards high energies. Plot taken from [25].

This implies that quarks only exist in composed states under normal conditions, forming a color neutral object. This phenomenon is referred to as confinement [34]. Having three charges, color neutrality is realised in the form of a baryon, consisting of 3 quarks, or in the from of a meson composed of a quark and anti-quark.
Striking is the fact that the mass of the quarks alone can not explain the total mass of the baryon they build up. The quark masses correspond only to a tiny fraction of the total mass. The entire mass is generated by dynamic processes caused by the confinement [71]. This can be qualitatively explained by the Heisenberg uncertainty principle. The quarks are forced together within a tiny radius. This implies uncertainty in momentum, which is connected to a non-zero energy. The same holds for the gluon interaction. According to the relativistic relation of energy and momentum, the confined valance quarks, the emerging quark-anti-quark pairs and the gluons contribute to the observed mass.
More formally, the generation of mass can be explained by the spontaneous breaking of the chiral symmetry. Chirality is understood as the Lorentz invariant version of helicity. Helicity describes the projection of the spin vector onto the momentum vector. For massless objects, helicity is clearly defined. However, for massive particles, the projection is not uniquely anymore; instead, it depends on the relative velocity of the considered frame of reference. One distinguishes between right-handed (momentum- and spin-vector are orientated parallel) and left-handed (momentum- and spin-vector are orientated anti-parallel) particles. In the case of chiral symmetry, the right-handed and left-handed particles decouple. Chiral symmetry is broken twice in QCD. It is broken globally due to non-vanishing quark masses. However, this so-called explicit breaking is only weak for ordinary matter as the quarks of the flavour up and down posses small masses. In

addition, a spontaneous chiral symmetry breaking occurs, which is because the QCD vacuum is not empty but filled with chiral condensates, e.g. quark-antiquark-pairs [46]. The condensates can interact with the valence quarks inside the hadron, which leads to a mixing of the right and left-handed chiral components, causing the spontaneous breaking of the chiral symmetry. The interaction with the condensates is connected with energy, leading to mass generation. Therefore, the mass of hadrons delicately depends on the properties of the condensates of the QCD vacuum.

1.1. QCD Phase Space Diagram

As explained, the coupling constant of the strong force decreases with rising momenta or, as the uncertainty relation tells, with decreasing distances. This happens until the coupling between quarks and gluons is so weak that they behave like free particles. This breaking of the confinement is referred to as asymptotic freedom [34]. It gives rise to a new phase of nuclear matter, in which quarks are not bound in baryons or mesons [27]. This phase of matter is referred to as Quark-Gluon-Plasma (QGP). The phase transition from hadron matter to the QCD depends on the momentum transfer, which can be approximated for a system of multiple baryons by a temperature T. On the other hand, also the distances between the quarks influence the coupling. Thus, the net baryon density ρ_B and the temperature T are the two variables that determine the phase of strongly interacting matter. In figure (1.2), the phase space diagram as a function of the temperature T on the y-axis and as a function of the baryon-chemical potential μ_B on the x-axis is shown. μ_B is understood as an alternative observable for the baryon density. For low baryon-chemical potentials and low temperatures, nuclear matter is in the confinement state; quarks combine to colour neutral objects within baryons or mesons. This holds up to temperatures of $T \approx 150\ MeV$. For higher temperatures, a phase transition to the QGP is predicted. This transition is expected to be continuous up to a critical point (T_c, p) [11]. Towards higher densities, the phase transition is predicted to be discontinuous of first order. High temperatures $T > 150\ MeV$ were present in the the early universe [19]. High baryon destinies could be still found today in the universe: Astrophysical observations and calculations suggest that such conditions are fulfilled in neutron stars [51]. The phase diagram has been probed over the last decades by various heavy-ion collisions experiments, e.g. HADES [3], ALICE [66], and STAR [67], see section (2).

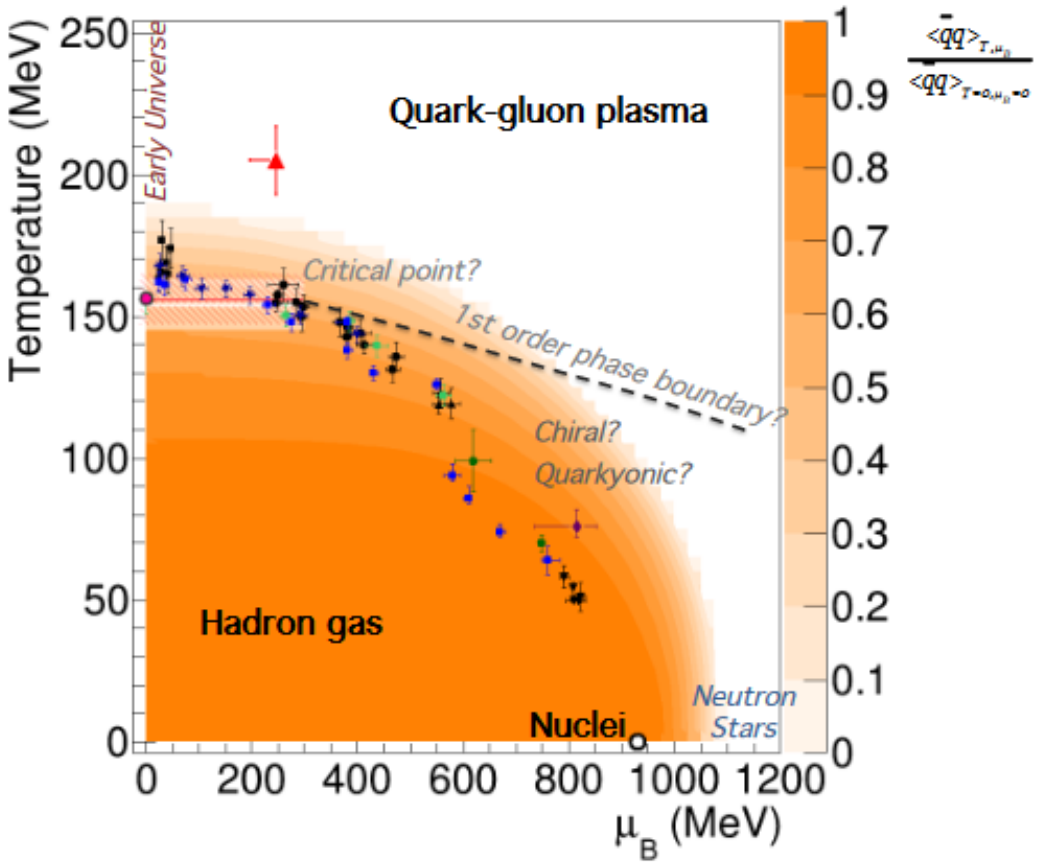

Figure 1.2: QCD phase space diagram as a function of baryon-chemical potential and temperature. In the region of low temperatures and low baryon-chemical potentials, quarks are confined within hadrons. Under these conditions the coupling constant of the strong interaction is large. With rising temperatures or for high baryon-chemical potentials, the coupling constant decrease until quarks and gluons are no longer subjected to the confinement. In this phase they act like gas of free particles. This state of strongly interacting matter is referred to as Quark-Gluon-Plasma [30].

2. Heavy-Ion Collisions

The different regions of the QCD phase space diagram can be probed by varying the two determinants, temperature and baryon density. This can be done experimentally by conducting collisions of heavy nuclei, which are accelerated to relativistic energies. After the collision, the nuclei are ripped apart in the reaction zone; the matter is strongly compressed and heated. Due to the high energies involved, also new particles are produced. The temperature reached in such a reaction depends on the incident beam energy, reaching from a few GeV at the SIS18 [56], and up to 1 TeV per nucleon at the LHC [40]. The baryon density can be changed by varying the collision energy as well as the chosen system size. One distinguishes between collider and fixed-target experiments. In collider experiments, both nuclei are accelerated in opposite directions relative to each other. In fixed-target experiments, nuclei are accelerated and headed onto a stationary

target. Heavy-ion collisions provide a suitable tool for probing the different regions of the QCD phase diagram.
Before the collision event, the accelerated nuclei are Lorentz-contracted due to their relativistic velocity, meaning their extent in the direction of motion is compressed, which causes the whole nucleus to assume a shape similar to a disk. The amount of nucleons that interact with nucleons of the nuclei they collide depends on the centrality of the collision. The centrality of a heavy-ion collision is characterized by the impact parameter b, corresponding to the distance between the centre of the two nuclei. The smaller b, the larger is the overlap zone between the nuclei. Subsequently, the higher the number of nucleons involved in the interaction process, forming the hot and dense matter state, which is of interest. The situation is illustrated in figure (1.3). The nucleons involved in the collision are named participants. Nucleons that are not located within the impact parameter range continue to move in their initial direction of motion at first order and are called spectators.

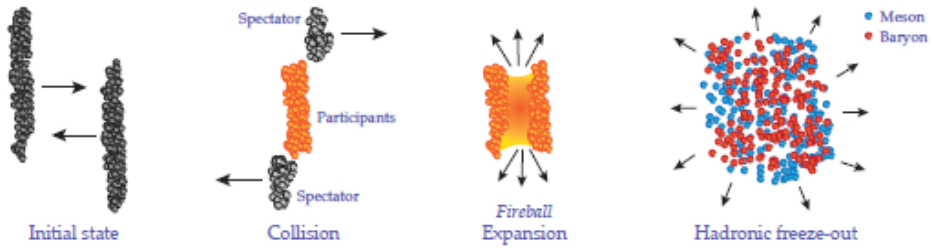

Figure 1.3: Illustration of the time evolution of a heavy-ion collision. The accelerated nuclei are Lorentz-contracted in the direction of motion due their relativistic energies. Nucleons which are within the overlap region are called participants. Their interaction leads to a dense and hot form of strongly-interacting matter (referred to as fireball). The high energies involved lead to the production of various mesons and baryons which can be measured by particle detectors, in order to draw conclusions on the nature of the fireball state. Nucleons which are not located within the overlap region continue less affected in their direction of initial acceleration and are called spectators [35].

The time evolution of a heavy-ion collision can be divided into different phases: A few fractions of femtoseconds after the first interactions, the entire system is in a pre-equilibrium state. It persists till the dense and hot matter is formed. High temperatures are reached due to multiple high energy scattering processes among the participants. The formed state of dense and hot, strongly interacting matter is referred to as fireball. The high temperature and the associated energies also allow the transformation of energy into masses, enabling the production of various exotic composed particles like pions or kaons. The high temperature causes a rapid expansion, leading to a cool-down of the system. When the involved energies are not large enough for the inelastic processes required to create hadrons, the particle composition is fixed. This point is called chemical freeze-out. However, still decays can occur. From now on, the particles interact elastically only. This happens till no scattering among the particles is possible, the point of kinematic freeze-out is reached, determining the particles' final momenta measured in the experiments.

Within the fireball phase, various regions of the QCD phase diagram might be reached [24]. However, these states last only for less than 10^{-22} seconds [24], which makes a direct observation not feasible. Only the final state after the kinematic freeze-out is measurable by most of the observables. Yet, the character of the fireball state might be still encoded in the measured particle composition, their kinematic distribution and emission pattern. Hence, conclusions about the fireball state can be drawn by analysing those observables and comparing them with model calculations.

2.1. Particle Flow and its Anisotropies

The collective emission behaviour of particles from a heavy-ion collision is referred to as collective flow. The emission pattern depends on the initial state of the system before the collisions as well as on the hydrodynamic properties of the fireball created after the equilibrium phase. One distinguishes between isotropic and anisotropic flow. Isotropic flow is also called radial flow as the emission is independent of direction. The collective emission is the same for all angles. Pure isotropic expansion occurs when the collision is completely central. In this case, no asymmetry is present in the initial state. Yet, asymmetry comes into the game for a non-zero impact parameter, and anisotropic patterns are observed in the momentum spectra. In semi-central collisions the overlap zone that defines the number of participants is now elliptic with respect to the azimuthal plane as illustrated in figure (1.4). The nuclei are moving among the beam axis z. The connection line between their centres defines the impact vector $\vec{b}$. The plane, spanned by $\vec{b}$ and the beams axis is called reaction plane. Because of the collision symmetry the particles are emitted symmetrically around the reactions plane.

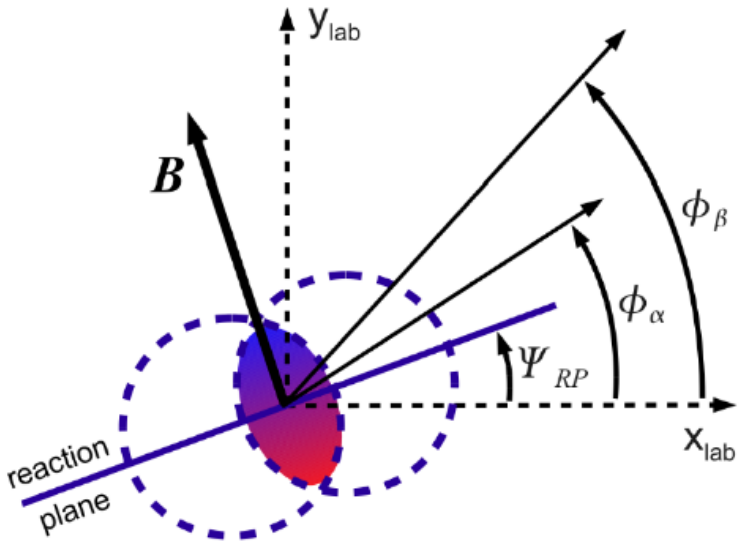

Figure 1.4: Schematic depiction of the geometrical situation of two colliding nuclei on the azimuthal plane (x-y-plane), which is orientated perpendicular with respect to the beam axis z. The connection line between the centres of the nuclei defines the impact vector $\vec{b}$. In combination with the vector pointing among the beam axis, the reaction plane is spanned [57].

The spatial anisotropy of the collision zone results in different, direction-dependent pressure gradients. The pressure gradient is translated into anisotropies in the momentum space [36]. As depicted in figure (1.5), the distribution of the spectators within the reaction plane is anisotropic. They are mainly present in the reaction plane. Whereas, towards a more perpendicular direction, much fewer spectators are found. By this geometrical situation, especially for low energy collisions, the number of particle interactions with the spectators is not the same for all emissions angles. This contributes to another source of azimuthal anisotropy.
In order to quantify the extent of azimuthal anisotropy, the distribution of the emission angle relative to the reaction plane needs to be considered. For quantification it can be disentangled by a Fourier series:

$$E\frac{d^3N}{d^3p} = \frac{1}{2\pi}\frac{d^3N}{p_t dp_t dy}(1 + 2\sum_{n=0}^{\infty} v_n cos(n(\phi - \Psi_{RP}))). \tag{1.4}$$

The sine terms are omitted due to the discussed symmetric geometry with respect to the reaction plane. The coefficients v_n define the extent to which the harmonic of order n contributes to the distribution. v_1 is referred to as directed flow. It describes to what degree the x component of the momentum is enhanced relative to the transverse momentum p_T

$$v_1 = \frac{p_X}{p_T}. \tag{1.5}$$

Hence, directed flow describes the emission in a specific direction towards the reaction plane. The source for directed flow can be illustrated by looking at figure (1.5). It results from bouncing effects of the colliding nuclei: During the overlap, pressure is generated between the nuclei. As a consequence, the particles expire a bounce off away from the beam axis into the reaction plane. Directed flow has the property of opposite sign in regard to the two hemispheres due to momentum conversation. v_1 flow and all other odd flow harmonics are sensitive to the early phase, the pre-equilibrium state, of the heavy-ion collision [24].
The second flow harmonic v_2 is called elliptic flow. It describes the ellipticity of the emission pattern. It corresponds to:

$$v_2 = \frac{p_X^2 - p_Y^2}{p_T^2}. \tag{1.6}$$

Elliptic flow depends delicately on how the pressure gradients are transformed into the momentum space. Thus, it is a sensitive observable when it comes to the determination of the nuclear equation state (EOS) [31]. The EOS determines the relation between macroscopic quantities like temperature, pressure or density. Next to the pressure gradient, the source for elliptic flow is, as mentioned, the angular dependent interaction with spectators. Therefore, in particular, in low energy collision, v_2 is a crucial observable for investigating the impact of, e.g. absorption processes within spectator matter. v_2 flow is negative if the emission predominately happens out off the reaction plane. On the contrary, a positive sign indicates that the emission is preferable within the reaction plane.

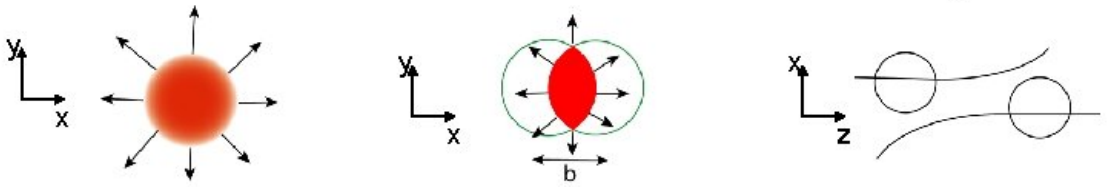

Figure 1.5: Schematic illustration of the different sources of flow. For completely central collisions there is no spatial anisotropy. Subsequently, the collective expansion is independent of direction (radial flow). For a non-vanishing impact parameter b, the spatial reaction zone is elliptic, leading to an anisotropic expansion. The spatial anisotropy is transformed by a direction-dependent pressure gradient into momentum anisotropies [13].

In general, the flow harmonics describe to what extent the emission pattern is covered by a particular geometry. As explained, v_1 describes whether the emission is in a specific direction, elliptic flow determines the eccentricity, and v_3 flow describes to what degree a triangular emission pattern is involved. This rationale can be extended to high order flow harmonics. Yet, with the rising order of n, the harmonics become smaller. For protons, the harmonics have been measured up to 6th order at HADES [22]. Whereas for pions, third-order flow currently determines the limit in experimental flow examinations [52].

2.2. Coulomb Effect in Heavy-Ion Collisions

The protons of the colliding nuclei introduce net electric charge into the generated fireball, which generates a Coulomb field that acts on all charged particles during the emission. This is connected with a modification of the emission spectra after the initial particle production. Positively charged particles feel a repulsion, whereas negatively charged ones are attracted by the positive charge. Hence, in addition to the particle's initial emission energy E_i, a contribution $\pm V_c$ corresponding to the potential of the Coulomb field comes into the game. The impact of the Coulomb effect is in particular expected to be significant in low energy collisions. For central collisions, the Coulomb field is mainly generated by the protons in the reaction zone. The contribution of the spectators is expected to be rather small as they move fast out of the collisions because they expire less stopping than the participants. However, out of mid-rapidity, the impact of the spectators can not be ignored anymore, as model calculations predict [59]. The Coulomb effect can be investigated by comparing particles that belong to the same species but occur with opposite polarities like charged pions or kaons. The charge-dependent energy shift leads to a difference in the maxima's position of the transverse momentum spectra. The difference are small; thus they are best observed for particles that are produced with high abundances, especially in the low transverse momentum phase space region. Moreover, the distortion of initial spectra is at largest for hadrons with low masses. Therefore, charged pions (2.3) with masses of only 139.57 MeV/c^2 are best suited for investigations regarding the Coulomb interaction. As the Coulomb potential is only in the order of a few MeV, pions with low initial emission energy are affected the most. The shifted emission maxima results in an increase of the π^-/π^+-ratio at low momenta. For higher momenta, the ratio decreases. This has been experimentally observed in Belvalc experiments [15] [45] [58]. Experiments at SIS [33], AGS [12] [20], SPS [24] followed and confirmed the presence of the Coulomb effect in heavy-ion collisions.
Within the scope of understanding the physics of the different regions of the QCD phase diagram, an exploration of the Coulomb effect is of special interest: If one can extract the potential from the measured spectra and relate it to appropriated models that describe the underlying charge distribution, one can draw connections to the system geometry in coordinate space of the fireball. This allows calculating the baryon density if the number of participant nucleons (e.g.via the Glauber-Monte-Carlo-Model) is known. Based on that also, a connection to the baryon-chemical potential is feasible if a suited functional-relation is assumed (e.g. an Ideal-Hadron-Gas). Therefore, Coulomb investigations could provide, next to Hadronic Statistical model fits [9], another method for determining the baryon-chemical potential.
There are currently two main procedures employed on various experimental pion data for different collision energies to investigate the Coulomb potential: Fitting the transverse spectra with a model that includes a description of the Coulomb interaction. Another approach is HBT interferometry. It involves the analysis of momentum correlated pion pairs.
In this thesis, an approach based on the first method will be tested in section (2). As a Coulomb inclusive model also provides a more realistic description of the spectra's shape in the low energy region where the Coulomb force leaves a large trace, a more precise extrapolation and yield measurement is possible.
In a recent paper from the HADES collaboration [21] such a Coulomb modified model

and its adjustment to the measured charged pion spectra from the KAOS [62], AGS [38], and HADES [2] experiment are investigated for Au+Au collisions. It reveals that the Coulomb potential is in the range of 5 to 20 MeV for centre of mass energies ranging from 2 to 6 GeV. A decrease of the potential with rising impact parameter is observed, as the number of charge decreases with less participants. The Coulomb potential as a function of $\sqrt{s_{NN}}$ is plotted in figure (1.6), a decrease with rising beam energy is found.

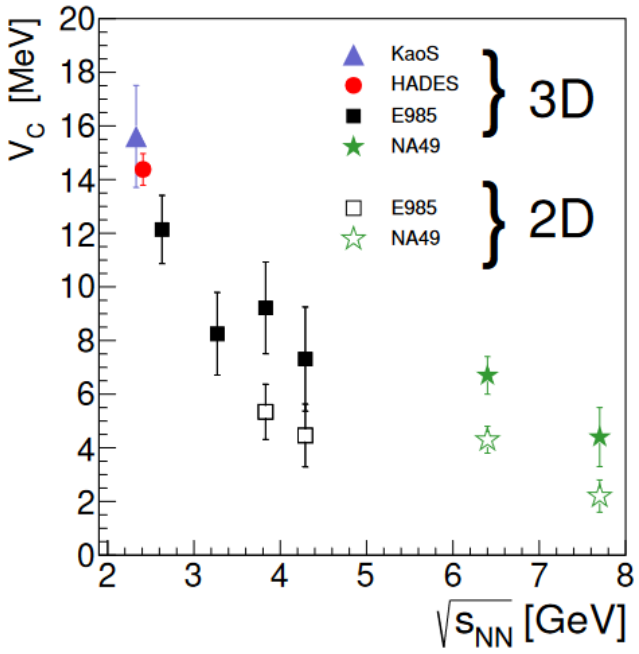

Figure 1.6: Contemporary results on the Coulomb potential as a function of the beam energy for Au+Au collisions. The potential has been extracted from charged pion spectra measured in low energy collisions experiments by HADES [2], KAOS [62], AGS [38]. Plot taken from [21].

2.3. Pions

As discussed in the section on QCD, chiral symmetry is spontaneously broken since the vacuum state is not symmetric under chiral transformation; only the general Lagrangian is. A spontaneously broken symmetry leads to so-called Goldstone Bosons, which are interpreted as effective exchange bosons that mediate the residual force between two neighbouring nucleons. The effective symmetry is referred to as SU(2). The existence of such an exchange particle was already predicted by Yukawa in 1920 within the Pion-Exchange model. Indeed, such a particle with as mass of 135 MeV has been experimentally confirmed by the examination of cosmic radiation by [18].
Pions exist in three different states: Two of them carry an electric charge. The third pion state is electrically neutral. Each pion is a bound object of a pair of a quark and anti-quark. Thus, they are forming a meson with a spin of zero. The masses of the charged pions are the same. The quark constitution, mass and charge are denoted in table (1.1).

charge	quark content	rest mass	mean life time	$Spin^{Paritaet}$
π^-	$\|\bar{u}d\rangle$	$139,57\ MeV/c^2$	$2,6033 \cdot 10^{-8}s$	0^-
π^0	$\frac{1}{\sqrt{2}}(\|u\bar{u}\rangle + \|d\bar{d}\rangle)$	$134,97\ MeV/c^2$	$8,52 \cdot 10^{-17}s$	0^-
π^+	$\|u\bar{d}\rangle$	$139,57\ MeV/c^2$	$2,6033 \cdot 10^{-8}s$	0^-

Table 1.1: Particle properties of π mesons [28].

From a quantum mechanical perspective, the neutral pion is described as a superposition state of quark and anti-quark-pairs consisting of $u\bar{u}$ and $d\bar{d}$. Pions are not stable in regard of the weak interaction. Charged pions decay in $99,9$ % of all cases into a muon and an anti-neutrino/neutrino [28]:

$$\pi^{\pm} \rightarrow \mu^{\pm} + \nu_{\mu}(\overline{\nu_{\mu}}) \tag{1.7}$$

The deacy of the neutral pion happens in most case into a photon under the emission of an election-positron pair:

$$\pi^0 \rightarrow e^+ + e^- + \gamma \tag{1.8}$$

Among all hadrons, pions have the lowest mass. Subsequently, their production threshold in heavy-ion reactions is reached already at low collision energies. This has the consequence that pions are produced most abundantly compared to all other heavier hadrons. Their relative long decay time, as well as statistical abundance, makes them an ideal detectable (via e.g. magnet-spectroscopy) probe of the fireball. Their kinematic distributions allow drawing conclusions about the condition at the kinematic freeze-out. Furthermore, the pion's multiplicities can also be considered as a measure for entropy created in the fireball [38]. The pion multiplicities, in particular, the ratio with respect to other particles, provide a sensitive measure for the comparison with models aiming to understand the underlying production mechanisms and physical processes. Due to the high statistics available in charged pion analysis, also a precise examination of the spectra's shape is feasible, e.g. enabling the investigation of the Coulomb interaction within the fireball, see section (2.2). Neutral pions can not be detected by magnet-spectroscopy. Instead, they are reconstructed on the basis of their decay products into electron-position pairs and photons.
Experimental investigations have revealed that the kinematic distribution of charged pions is describable by a superposition of distributions based on the relativistic Max-Well-Boltzmann statistic. In figure (1.7) the transverse mass distribution of negatively charged pions emitted in Au+Au collisions at 1.23A GeV measured by HADES [2] are depicted.

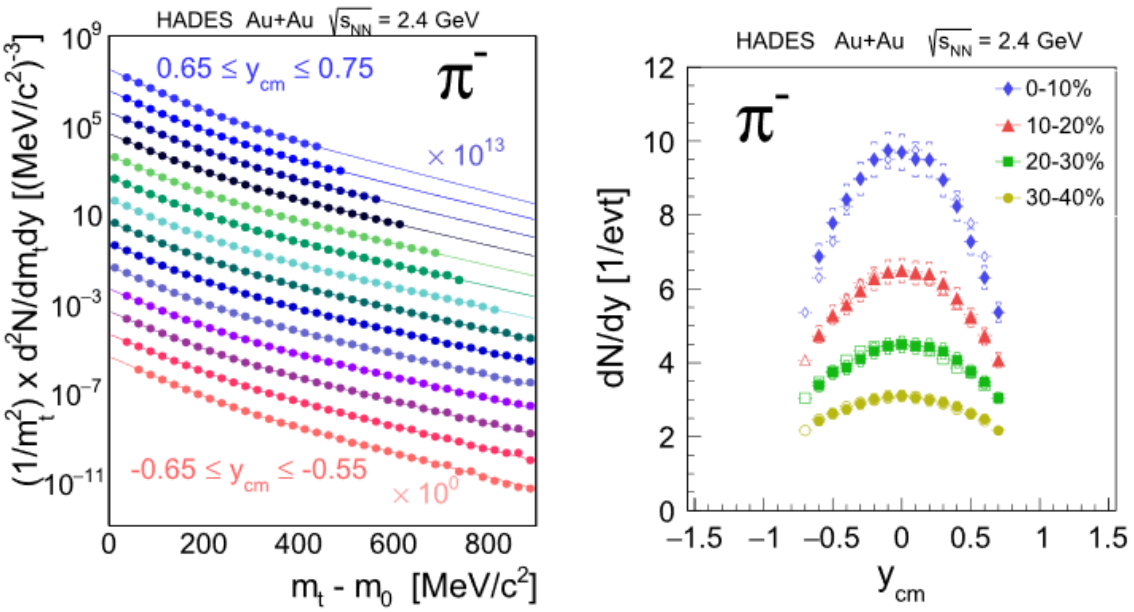

Figure 1.7: Recently published results on charged pion production in Au+Au at 1.23A GeV. Left: Reconstructed reduced transverse mass spectra. The different slopes reveal that charged pions are produced in processes with different energy transfers. Right: Distribution of pions in the scope of the longitudinal kinematic, represented by rapidity [2].

The reduced transverse mass $m_t - m_0$ distribution exhibits two different slopes, which indicate production origins with different energy transfers. The production channel of charged pions in the lower energy region is mainly attributed in literature to Δ-Resonance [2]. In these cases, the interaction of two nucleons leads to a spin-flip of one quark. This creates a resonate nucleon Δ. Delta resonances are not stable. They decay via the strong interaction to their ground state. The energy is released by the production of a pion:

$$NN \rightarrow N\Delta \rightarrow NN\pi. \tag{1.9}$$

For the pions in the higher energy region, the production might happen directly in a binary nucleon-nucleon collision, allowing for a higher energy transfer:

$$NN \rightarrow NN\pi. \tag{1.10}$$

The longitudinal kinematics is displayed on the right hand side of figure (1.7). A Gaussian-like shape has been found in the experimental data with a decreasing number of pions towards peripheral events. The world data of pion production in low energy collisions is summarized in figure (1.8). The data were collected by FOPI [1], E895 [38], TAPS [70] and HADES [4] [5]. The left hand side shows the number of totally emitted pions divided by the number of participants A_{part}. A rather constant A_{part}-scaling was found. On the right hand side the pion multiplicity normalized to A_{part} as a function of the the beam energy is plotted. A strong rise with increasing beam energy is observed. The excitation function can be described by a second order polynomial [2].

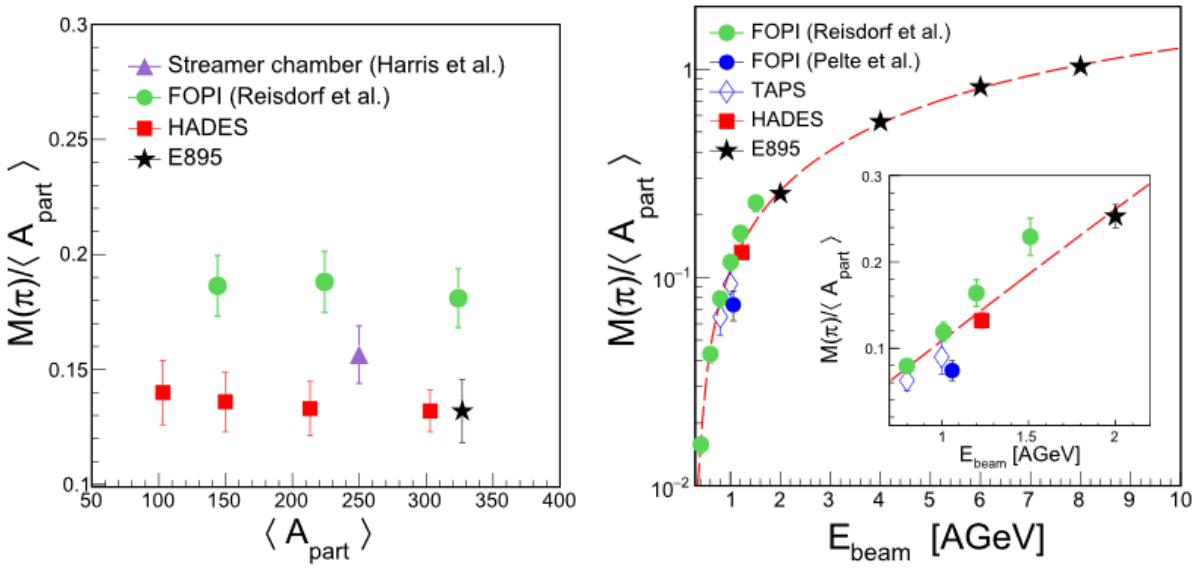

Figure 1.8: Left: Number of produced pions per number of participating nucleons as a function of $< A_{part} >$. A rather constant behaviour was found in experiments conducted by [2], [37], [70], [1]. Right: Excitation function of pion production for low beam energies [2].

2. Experimental Technique

1. HADES

At the GSI Helmholtzzentrum für Schwerionenforschung located in Darmstadt, Germany, heavy-ions are accelerated with the SIS18 synchrotron up to kinetic energies of $4A\ GeV$ [29]. Before the heavy-ions are injected into the synchrotron, they gain kinetic energy through the linear accelerator LINAC. The accelerated ions are headed on a fixed target, and particle detectors measure the created and scattered reaction products. An experiment especially designed to investigate Di-Leptons, and also various hadrons, is HADES [3] (High-Acceptance-Di-Electron-Spectrometry). It consists of 6 identical sectors built up behind the target among the beam axis. Each of sectors is divided into several detector modules. HADES provides a relative momentum resolution of 5 % at 500 MeV/c for electrons. The azimuthal plane is almost completely covered, except for the frame and magnetic coils between the different sectors. The polar angle of the particles is measured within the region of $15° < \theta < 85°$. The general reconstruction procedure is as follows: When a collision takes place, the START (1.1) detector records a time stamp. The particles from the reaction propagate through two Multi-Wire-Drift-Chambers (MDC, (1.3)), which ideally deliver two measurements of hit points of the trajectory. Behind these two inner MDC modules, the trajectories are bent due to the presence of a high magnetic field created by a superconducting toroidal magnet. The distracted particles are afterwards measured once again by two MDCs. Finally, via the META (Composed of RPC and TOF, (1.4)) detector system, another hit point is acquired, providing a final time stamp in order to obtain the time of flight. The track in between the MDCs is interpolated. Thereafter, based on the track deflection, the momentum can be reconstructed. Combining it with the measured time of flight enables to identify various charged particle species, see section (3). Furthermore, there are additional detectors, allowing to select events from the reaction zone (VETO) (1.1), distinguish leptons from hadrons (RICH) (1.2) and to estimate the centrality of the collisions and orientation of the event plane (Forward-Wall (1.5)). Behind the set-up, an electromagnetic calorimeter (ECAL) is placed, used for the reconstruction of dileptons. Figure (2.1) displays a cross-section of the HADES set-up, illustrating the arrangement of the detector elements. Each of the sub detector's working principles and interplay is explained in the following sections of this chapter.

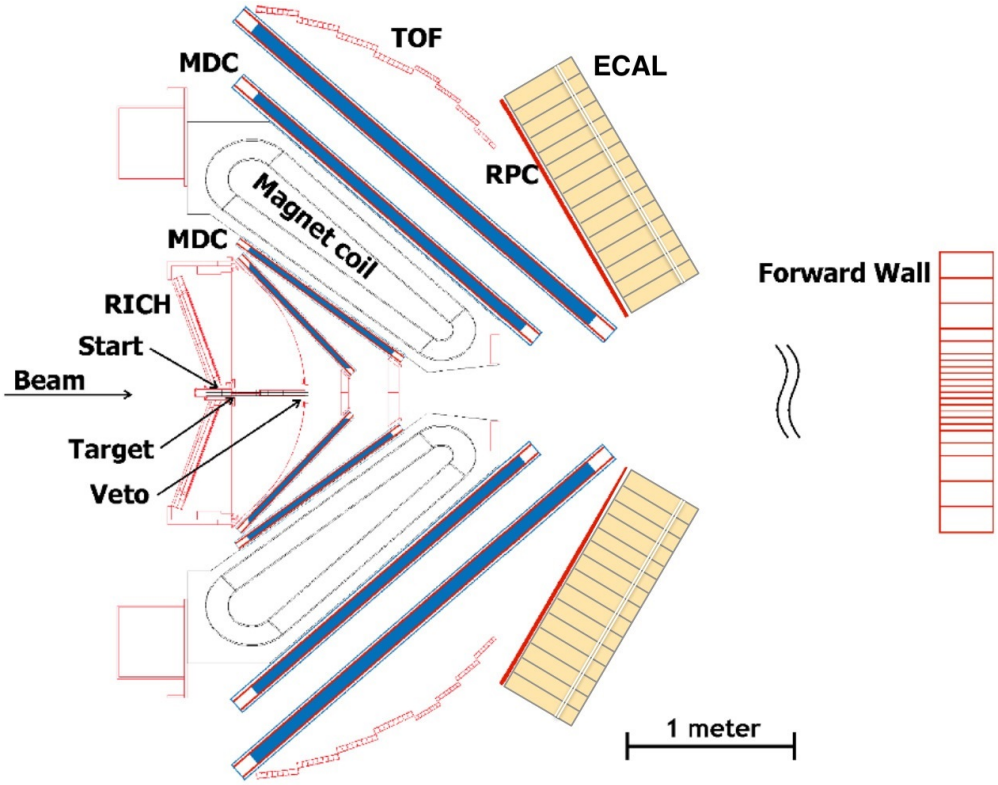

Figure 2.1: Schematic cross-section of the HADES detector. The beam is lead onto a fixed-target. Before a reaction takes place the START detector records a time point. Two position measurements of the particle's trajectory are conducted by MDCs in front of the magnetic field and another two are measured behind it in order to later derive the tack deflection. RPC and TOF deliver another hit and thus a time point, which, in combination with the start time, leads to the time of flight [64].

1.1. Start-Detector, Traget and VETO-Detector

The START detector detects passing ions and records a time-stamp, which is later used to obtain the time of flight with the help of the META detector. The START detector is located in front of the target and consists of a crystalline semi-conductor divided into several vertical and horizontal lines. Due to this structure, the START detector is also able to measure the beam position, which is a crucial parameter used to evaluate the beam quality and position relative to the target.
The target of the analysed beam time consisted of 15 silver foils, see figure (2.2). By using very thin foils, the probability of inner conversion of photons within matter into lepton pairs is reduced. Yet, by having multiple foils, the interaction cross-section of the nucleons is still large enough in order to have a sufficient amount of collision per second to saturate the data acquisition. The foils are fixed on an edge made of carbon which has the consequence that some events occur between the accelerated silver ions and carbon nuclei and subsequently are measured as well. Therefore, to discard those events in the analysis later on, an appropriate event selection has to be applied to filter only events between silver nuclei.
The purpose of the VETO detector is to veto falsely triggered events. The detection is

accomplished by a poly-crystal chemical vapour deposition sensor.

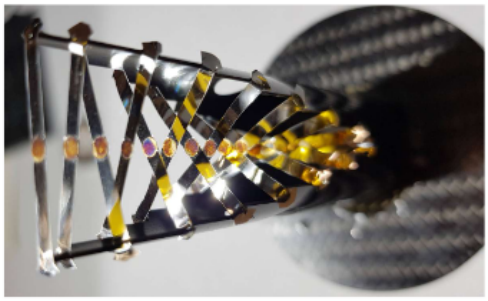

Figure 2.2: Target of the silver beam time. Made of 15 segmented silver foils [53].

1.2. RICH-Detector

The Ring Imaging Cherenkov Detector (RICH) aims to distinguish electrons and positrons from hadrons. The detection principle is based on Cherkenov radiation which is generated when a charged particle exhibits a velocity faster than the speed of light of the dielectric material through which the particle moves. The medium atoms are polarised by the impinging charged particle, resulting, according to the laws of electrodynamic, in the emission of radiation. Normally the emitted waves would cancel out, but because the particle is faster than the in-medium-speed of light, a cone-shaped wavefront with an opening angle θ:

$$cos(\theta) = \frac{c}{v} = \frac{1}{n\beta}. \tag{2.1}$$

around the particle's trajectory is emerging.
It depends on the velocity β and the refraction index n. In the RICH detector of HADES, the dielectric medium (Radiator) consist of C_4F_{10}, which has a refraction index of $n = 1.0015$. This implies that the threshold to produce Cherenkov radiation is $\beta > 0.999$. Such high velocities can mostly be reached by particles with a very low mass like leptons. The created Cherenkov photons are emitted towards a spherical mirror which reflects the photons onto photo-detectors, composed of 2872 pads, located in the opposite direction in front of the target, see illustration in figure (2.3).

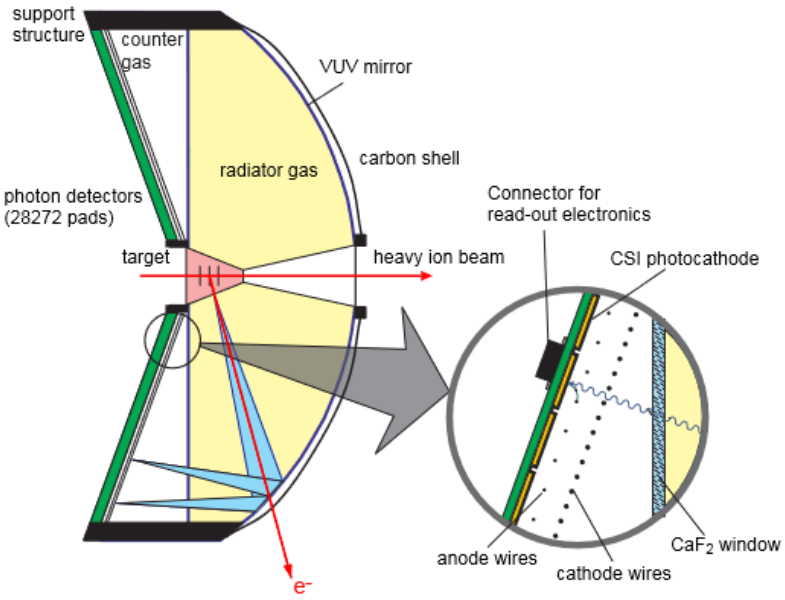

Figure 2.3: Set-up of the RICH-detector. Only leptons produce within a radiator gas Cherenkov-Photons. The photons are reflected onto pads of photo detectors by a spherical mirror [10].

1.3. MDCs and Magnet-Spectroscopy

The reconstruction of the particle's trajectory based on 4 Multi-Wire-Driftchambers (MDC) per sector and a superconducting magnet. Two of the MDCs (Inner-MDCs) measure the particle's position before it enters the magnetic field. The second pair (Outer-MDCs) is located behind the magnetic field, providing two other position measurements. The track course between the MDC hits is obtained by applying interpolation methods. Ultimately, based on the deflection of the reconstructed track in the magnetic field, the momentum is derived. The underlying method is described in more detail in section (2).

The magnetic field has to be in the order of a few Tesla to sufficiently bend the trajectory since the particles have relativistic energies. This is archived by 6 NbTi coils, which are cooled with liquid helium in order to reach a working temperature of only 4.7 K, which the super-conducting state demands. The coils are oriented symmetrically around the beam axis. By this configuration, an inhomogeneous, toroidal shaped magnetic field of up to 3.6 T is generated.

As mentioned, the MDCs have the task to capture the position of the particles as well as providing a measurement of the specific energy loss. The detection principle is based on gas ionization. Each chamber is filled with gas mixture composed of 70 % Argon and 30 % CO_2. The gas atoms of the first component are supposed to be ionized among the trajectory of the incoming charged particles. The later one takes the role of a quencher gas, aiming to reduce emerging photons, which would distort the measurement. Each MDC module consists of 6 layers of rows of sense and potential wires. The wires between different layers have a shifted orientation with respect to one-another, maximizing the probability for a measurement. With respect to the frame, the angles of the 6 layers

are 40°, ˇ20°, 0°, 0°, 20° and ˇ40°. There are also cathode wires between each layer to generate an electric field by applying a high voltage of 1750 V - 2150 V between the cathode and potential wires. When a charged particle with sufficiently high kinetic energy collides with a gas atom, a valence electron is dissolved and accelerated toward the closest potential wire, whereas the ion moves in the direction of a cathode wire. Due to the increasing gain of the electron's kinetic energy when it comes close to a wire, further gas atoms are ionized, which leads to the creation of multiple secondary free electrons and ions. In this way, a single ionizing event leads to an immense amount of free charge, large enough to generate a measurable electrical signal much higher than the magnitude of random noise, as it would be the case for only a few free electrons. The signal is measured by the charge influenced on the sense wires due to the field distortion of the slower propagating positively charged ions.
Moreover, the MDCs allow measuring the particle's specific energy loss since the number of generated secondary electrons and ions, and subsequently the corresponding width of the read-out signal, is proportional to the particle's kinetic energy, which triggered the charge avalanche.

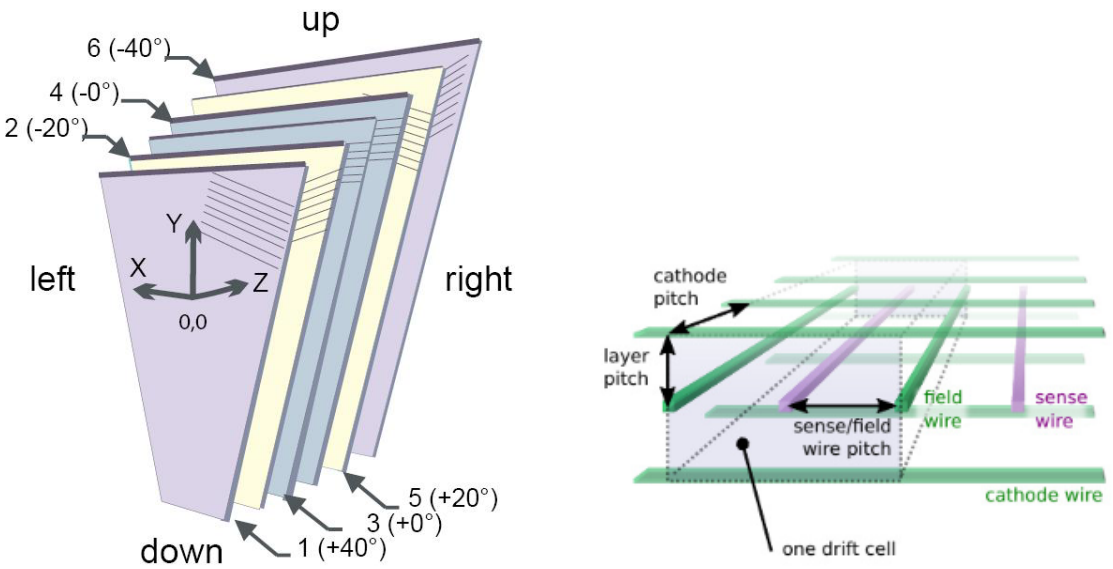

Figure 2.4: Left: 6 layers of a MDC chamber. The wires are orientated with different angle to another to maximize the detection probability [3]. Right: Depiction of the wire arrangement. There are sense- and potential wires, they are embedded by two planes of cathode wires. Via the process of gas ionization, charged particles are measured. The signal is read out at the sense wires [8].

1.4. META-Detector

The time of flight can be determined if a stop time is measured additionally to the time stamp recorded by the START detector. This is carried out by the META detector system (Multiplicity and Electronic Trigger Array), also called time-of-flight wall. It consists of the two detectors, RPC and TOF, which cover different polar angle regions. Both of them are divided in 6 sectors. In the following two subsections, their technical features and functionality are described.

1.4.1. RPC

The RPC detector (Resistive Plate Chamber) covers a polar angle of 18^o to 45^o. It provides a time resolution of 90 ps. Each sector module is composed of 187 modules, each of which consists of 3 parallel orientated aluminium electrodes with a high voltage applied on, generating an electric field. A module is operated with a gas mixture of 90 % SF_6 and 10 % $C_2H_2F_3$. The detection principle is, similar to the MDCs, based on gas ionizing, meaning that an entering particle generates free electrons and ions that gain energy due to the electric field, resulting in a measurable charge avalanche. As opposed to TOF, RPC is not suited for energy loss measurement.

1.4.2. TOF

The TOF (Time-of-Flight) detector covers the polar range of 44^o to 88^o. Each of the 6 sectors is divided into 8 modules that consist of 8 rods. The rods are long shaped plastic scintillators. If a particle is impinging, the electrons of the scintillator atoms are shifted to a higher energy state, which finally results in the emission of photons as it returns to the ground state. As the signal of one emitted photon is way too small to be directly detected, they are amplified by dynodes (PMT - Photomultipliers). Dynodes are composed of a photoelectrode. An electron is emitted due to the photo electric effect caused by the photon. The electrons are subsequently multiplied by a cascade of electrodes (dynodes) with a high voltage applied on. The signal on the electrodes is then converted into a signal whose amplitude scales linear with the energy of the generated scintillation photon, enabling the measurement of the specific energy loss. Based on the time difference of the signals between the two endpoints of a rod and the known group velocity of light in the scintillator material, the longitudinal position of the hit in the rod is determined. With this set-up a spatial resolution of up to 25 mm is feasible, the time point is measured with a precision of $\pm 150\ ps$.

1.5. Forward-Wall

The purpose of the Forward-Wall is to measure spectator nucleons of the collision. The spatial distribution of the projectile spectator hits is crucial for estimating the event plane, which is required in the analysis of azimuthal anisotropic flow. The Forward Wall is a hodoscope composed of 288 scintillator cells functioning according to the same working principle as described in the section about the TOF detector (1.4.1). It is located behind the META detector system. The size of the cells is getting smaller the more closer they are located to the beam axis to precisely determine the emission angle. The inner cells have a size of 4x4 cm. They are enclosed by cells with a size of 8x8 cm. The most outer cell have sizes of 16x16 cm.

1.6. ECAL

The recently installed (Firstly used in in the beam time of the analysed experiment of Ag+Ag collisions at 1.58A GeV in 2019) ECAL (Electromagnetic CAlorimeter) Detector is located behind the META detectors. Its purpose is the energy measurement, enabling detailed investigations of photons. The ECAl scopes a polar angle range from 12 to 45

degrees. The azimuthal range is almost completely covered. The ECAL is made of 978 glass modules distributed among 6 sectors.

1.7. Data Recording

A large amount of data arises in the scope of the measurement. In order to limit the data storage capacities, only events of physical interest are processed and stored for analysis. A multi-level trigger system conducts this pre-selection. For the signal of the START detector, a so-called minimum bias is demanded: It triggers only in the case a specific signal threshold is exhibited. Furthermore, the hits measured in the META detector, the sum of the RPC and TOF detector signal, are used as a trigger criterion. In the case of a PT2 trigger, at least 5 MEAT signals are required for data accusation. For the PT3 trigger, the threshold requires at least 20 measured signals. For a triggered event, the sub-detector's signals are sent by their read-out electronic to a hub and are later combined by an event-builder and stored in HLD files on server farms at the GSI for the analysis later applied on the data.

2. Charged Particle Track and Momentum Reconstruction

Based on the measured hit points in the MDCs, the particle's trajectory is reconstructed. In order to combine the hits to a track, at first a cluster finder algorithm is applied, projecting for each layer the wire signals of the MDCs in a plane. This helps identify clusters of fired sense wires which lie on top of each other, see figure (2.5) for illustration. The identified clusters are connected by a segment fitting algorithm delivering a straight-line connection. The vertex position can also be reconstructed by projecting into the target region based on the inner MDC segment. Both the inner and outer track segments are then extended to the region where the magnetic field is present, and the intersection point defines a so-called kick-plane allowing to estimate the deflection the track receives due to the acting Lorentz force.

Obviously, a straight track course within the magnetic field dose does not correspond

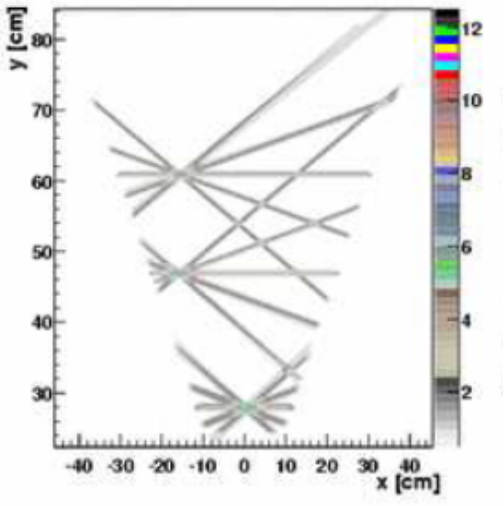

Figure 2.5: To identify hit points a projection of fired sense wires into a plane is applied [3].

to the correct physical behaviour. Hence, to reconstruct a realistic track, and in order to allow a more precise momentum determination, sophisticated interpolation methods need to be applied: Initially, a cubic spline in-between the inner and outer MDC-hit points is constructed to have a first guess of the trajectory described by $\vec{s}$. The change in momentum Δp after the deflection due to the Lorentz force acting on a particle of mass m and velocity v, is described by:

$$\Delta\vec{p} = \int d\vec{p} = \int \vec{F}dt = \int q\vec{v} \times \vec{B}dt. \tag{2.2}$$

The configuration of the magnetic field $B(\vec{r})$ as function of position $\vec{r}$ has to be precisely known. The velocity can be expressed in terms of the differential ds of the track path. Hence, the formula can be expressed as:

$$\Delta\vec{p} = -q \int \vec{B} \times d\vec{s}. \tag{2.3}$$

Figure illustrates (2.6) that the sine of the deflection angle is given by the ratio of the magnitude of momentum change Δp and the total momentum p:

$$sin(\frac{\Delta\theta}{2}) = \frac{\Delta p}{2p}. \tag{2.4}$$

Rearranging this equation and inserting the expression of equation (2.3) one yields for the particle's momentum:

$$p = \frac{-q \int \vec{B} \times d\vec{s}}{2sin(\frac{\Delta\theta}{2})}. \tag{2.5}$$

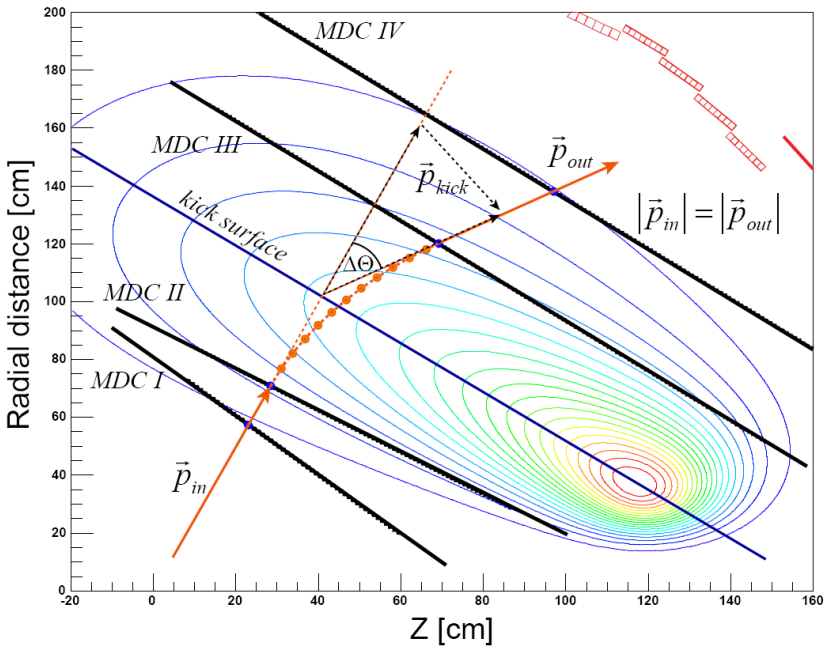

Figure 2.6: Depiction of the geometrical situation relevant for momentum reconstruction. The hit points are measured by the 4 MDC modules. The magnetic field is mainly present in-between the inner and outer MDCs. The track in between the measurements is interpolated based on the 4-order Runge-Kutta method. The starting points are obtained by Cubic-Spline interpolation [3].

The momentum estimation based on the cubic spline interpolation is subsequently taken as starting point for the 4th-order Runge-Kutta-Method [17]. The idea of this method is to solve the equation of motion, defined by the Lorentz force, numerically in an iterative procedure. The differential equation to solve is:

$$m\frac{d^2\vec{s}}{d^2t} = q(\frac{d\vec{s}}{dt} \times \vec{B}). \tag{2.6}$$

The reconstructed trajectory can be compared with the measured hit points y_i in the MDCs. In order quantify this comparison the mean squared difference between the measured points and the corresponding position of the reconstructed trajectory function $\vec{s}(x_i; p)$ is calculated:

$$\chi^2_{RK} = \sum_{i=1}^{N} (\frac{y_i - \vec{s}(x_i)}{\sigma_i}). \tag{2.7}$$

Furthermore, when extending the track based on interpolation to the META detector, another comparison to the measured points can be made, quantified by χ^2_{META}. Hence, the two introduced parameters provide a quality measure, later used in the analysis to select only particle candidates with certain matching quality. In order to find the optimal track interpolation, the Runge-Kutta procedure is iteratively repeated several times, and the one with the smallest χ^2 values is chosen finally.
Combining the reconstructed momentum with the two time points, measured in the STRAT- and META detector, one has all information required to identify the particle's species, see following section (3).

3. Particle Identification

3.1. Time of Flight

Based on the reconstructed track path $\vec{s}(t)$ and the two time points measured with the START- (time point: t_0) and META (time point: t_1) detector, now the particle's speed v can be derived. For this, one has to know the distance the particles travel in-between the time span t_0 to t_1 (time of flight). Consequently, the velocity is given by the arc length of track path $\vec{s}(t)$ divided by $t_1 - t_0$:

$$v = \frac{\int_{t_0}^{t_1} |\frac{d\vec{s}(t)}{dt}| dt}{t_1 - t_0}. \tag{2.8}$$

Combining the velocity with the reconstructed momentum p, one can use the relativistic relation between momentum and velocity which is according to special relativity given by:

$$p = m\beta\gamma c. \tag{2.9}$$

Where γ corresponds to the Lorentzfactor:

$$\gamma = \frac{1}{\sqrt{1-\beta^2}}. \tag{2.10}$$

It depends on β defined by $\beta = \frac{v}{c}$ (c corresponds to the speed of light in vacuum). Besides momentum and velocity this relation is determined by the particle's mass m, which is a unique property allowing to identify particles. Rearranging equation with respect to β, one yields the dependence to the momentum:

$$\beta = \sqrt{\frac{p^2}{(mc)^2 + p^2}}. \tag{2.11}$$

Hence, to find particles of mass m, it is convenient to consider the two-dimensional distribution of the variables β and p and inspect the resulting correlations. As the time of flight and momentum measurements are not infinitely accurate, the data points do not follow all exactly the parametrization (2.11) and are rather distributed around a mean according to this equation. Furthermore, because of the mentioned limited detector precision, one also observes tachyonic particles having velocities higher than the speed of light. In order to quantify the distribution of particles with mass m, one can divide the momentum axis into slices, resulting in 1D-β histograms, which can be fitted by a function that appropriately describes the observed shape. For particles like charged pions this method is acceptable, however especially for more rare hadrons, the distribution is superposed by a background caused by other particles with similar masses. In this case, one has to apply methods that distinguish the actual distribution of particles of interest from the background. Since the method of momentum reconstruction actually is only sensitive to the momentum to charge ratio, particles with the same ratio, e.g. deuterons and helium-4, can not be separated. Hence, additional information is required to separate those types of particles.

3.2. Specific Energy Loss

In order to also separate particles with the same mass to charge ratio the specific energy loss is an appropriate observable. The mean energy loss per distance $\langle \frac{dE}{dx} \rangle$ of a particle of mass m and velocity β is described based on a quantum mechanical approach by the Bethe-Bloch-Equation:

$$\langle \frac{dE}{dx} \rangle = 2\pi N_a r_a^2 m_e c^2 \rho \frac{Z}{A} \frac{z^2}{\beta^2} [ln(\frac{2m_e \gamma^2 v^2 W_{max}}{I_{pot}^2}) - \beta^2 - \frac{\delta(\beta\gamma)}{2}]. \tag{2.12}$$

It depends on the properties of the gas medium in which the particle deposits its energy. The medium-specific variables in this formula are the proton number of the gas atoms Z, the number of nucleons A, and the effective ionizing potential I. The constants are the electron mass m_e, elementary charge e and the Avogadro constant N_A. δ is a correction that accounts for the polarisation of neighbouring gas atoms. For low velocities, the energy loss is decreasing according to $\frac{1}{\beta}$ until a minimum is reached. Particles in the minimum are called to be minimum ionizing (MIP). For higher β, the energy loss is increasing again but logarithmically until reaching a saturation plateau.
W_{max} describes the maximal energy transfer as it occurs when the collision with the gas electron is completely central:

$$W_{max} = \frac{2m_e c^2 \beta^2 \gamma^2}{1 + 2\gamma m_e/M + (m_e/M)^2}. \tag{2.13}$$

The Bethe-Bloch-Equation is a function β, but it can be also expressed only in terms of the momentum. In HADES, a specific energy loss measurement is provided by the MDC and TOF detectors, see section (1.3) and (1.4.2). For particle identification the distribution of dE/dx vs. p is considered. One obverse that the particles are distributed according to the Beth-Bloch equation, whereby the curve is only determined by the particle's mass as the gas behaviour is considered to be constant. As mentioned, the Bethe-Bloch equation only describes the mean energy loss. The specific energy loss distribution can not be described by a simple Gaussian. Instead, there are energy loss counts toward higher values, spread among a tail shape. Thus, the energy loss, according to Bethe-Bloch, does not correspond to the most probable value; instead, it is always a bit higher. This implies that a quantification of the distribution requires a fit function that exhibits asymmetry like a Gaussian with two distinct sigmas.

4. Centrality Determination

In order to investigate the system size dependence of an observable, one needs to determine the number of participants A_{part} that make up the fireball state, see section (2). A_{part} is connected to the centrality of the heavy-ion collisions. Yet, the impact parameter is not directly accessible. However, the measured hit-multiplicities are correlated with the amount of participants A_{part}, since with increasing A_{part}, the production sources increases as well. Within the Glauber-Monte-Carlo (GM)model [35] it is assumed that the measured mean multiplicity of charged particles $< N_{ch} >$ is proportional to the mean number of participants $< N_{part} >$:

$$< N_{ch} >= \mu \cdot < N_{part} > . \tag{2.14}$$

Within the GM implementation, first, the distribution of charged particles is sampled using the Wounded-Nucleon model [35]. The parameter μ is determined by fitting the simulated distribution of N_{ch} to the experimentally measured one. This establishes an assignment between the average number of hit multiplicities to the number of participants. For details regarding the implementation of this approach, see [35] The multiplicities are usually divided into centrality classes. In table (2.1), the determined correlation between the impact parameter and the number of participants is denoted. Those values are used in this analysis for the centrality-dependent analysis.

C [%]	$0-10$	$10-20$	$20-30$	$30-40$	$40-50$
$\langle A_{part} \rangle$	$160,9 \pm 6,9$	$114,5 \pm 6,2$	$81,1 \pm 5,1$	$56,5 \pm 5,4$	$38,1 \pm 4,7$
$b[fm]$	$0-3,8$	$3,8-5,4$	$5,4-6,6$	$6,6-7,6$	$7,6-8,5$

Table 2.1

3. Analysis

The analysis chapter is split into three main parts: The first focuses on improving the quality of the phase space spectra of charged pions, which are the foundation for the determination of the 4π-production rates. Moreover, the obtained transverse spectra are the starting point for the second part of the chapter, covering the extraction of the Coulomb potential and the baryon density as a function of the number of participants. Finally, in the last part, azimuthal anisotropies in charged pion emission with respect to the reaction plane are explored. Hereby, the goal is the determination of the harmonics v_1, v_2 and v_3 as a function of transverse momentum and rapidity.

1. Finalizing the Momentum Spectra and Production Rates of Charged Pions

The aim of this section is to finalize the analysis of charged pion production. On the one hand, the goal is the reduction of Ag+C contamination, which occur for peripheral collisions and led in previous analyses to an asymmetry on the rapidity distribution in the centrality classes 30-40 % and 40-50 %. On the other hand, there is an issue attributed to protons, causing impurities in the positive pion spectra. Another task is to investigate systematic effects by analysing the different sectors separately as well as by varying the PID criteria in order to provide an estimation of the systematic error for the reconstructed production rates. The obtained transverse spectra are the foundation for the extraction of the Coulomb potential, discussed in (2).

1.1. General Analysis Procedure

The charged pion yield analysis process can be divided in 3 main segments: PID (Particle Identification), see section (3), acceptance and efficiency correction, see section (3.9) and extrapolation, see section (1.6.1). The goal is to determine the number of emitted charged pions per event with respect to the full solid angle and their distribution in the phase space. The analysis details regarding particle identification and the acceptance and efficiency correction were already described in more detail in [44]. Thus, the focus will be put more on new analysis steps introduced to improve the data quality. Figure (3.1) illustrates the analysing procedure with its main steps and the flow of data. After applying appropriate event selection as well as track quality criteria, the first step in the analysis is to identify charged pion candidates (PID). The phase space of charged pions is then considered differentially as a function of transverse mass (momentum) and rapidity. The detector's acceptance and reconstruction efficiency is limited and because

of the applied cuts, a certain amount of tracks are removed. This makes it necessary to employ a correction on the raw phase space distributions by using the simulations UrQMD [16] and GEANT [65]. In order to obtain the yield for the full emission angle, the corrected spectra are extrapolated into transverse phase regions where the coverage of the detector is zero .

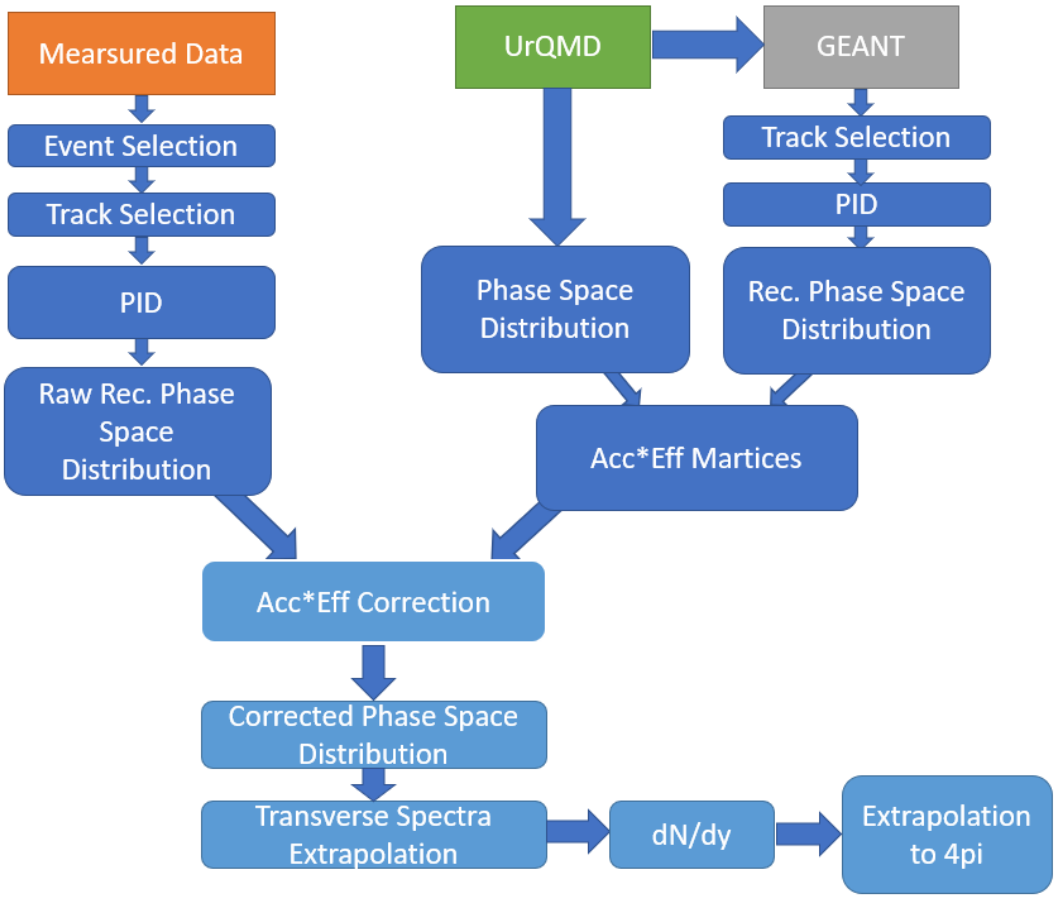

Figure 3.1: Depiction of the main analysis steps in the charged pion yield analysis.

1.2. Event Selection

The experimental data and simulation are based on calibration generation 5, analysed is the complete statistic with all days included.
As in previous analyses of HADES data from Ag+Ag and Au+Au collisions [54] the so-called standard event selection is applied, removing non-physical events caused by, e.g. Pile-Up effects etc. The included selection criteria are explained in more detail in [54], [44]. These standard event requirements result in $6.9201 \cdot 10^9$ selected events. Nevertheless, this basic selection is not sufficient to suppress the contamination with Ag+C events. Especially within the most peripheral collisions, Ag+C reactions are expected to contribute non-negligibly, causing an asymmetry of the reconstructed forward and backward bins on the rapidity distributions. Those distorted events can not be corrected with the help of the simulation. A consideration in the simulation would require modelling the detector's frame, including a description of the interaction process with the spectators,

which is not feasible as UrQMD only generates pure Ag+Ag events. Therefore, additional selection criteria that properly exclude most of the Ag+C contaminated events in the experimental data have to be found.

1.2.1. Selection on the Ratio of the Longitudinal and Transverse Energy

In [48], it has been shown that an observable which allows separating Ag+Ag from Ag+C events is the ratio between the sum of the transverse- E_t and longitudinal energy E_l over all particles in the analysed event:

$$ERAT = \frac{\sum_{i=1}^{N} E_i sin(\phi)}{\sum_{i=1}^{N} E_i cos(\phi)}. \tag{3.1}$$

Where ϕ represent the azimuthal angle, and E_i the total energy of the emitted particle. In order to locate a possible pattern related to the contaminated collisions, the distribution of standard selected events as a function of the EART value and the z-vertex (Figure (3.2), right) and the number of multiplicity hits, measured with the META detector (Figure (3.2), left), is considered. For low multiplicities, up to around 50 hits, it is observed that for ERAT < 0.6, there exists a region that is enhanced with hits towards smaller ERAT values. Because of the low multiplicity vicinity, an attribution to Ag+C events seems plausible since the number of emitted particles are expected to be much smaller due to the lower system size of Ag+C compared to Ag+Ag. On the right-hand side of figure (3.2) the 15-segmented structure of the target along the z-axis is visible. For higher ERAT values (ERAT > 0.6) the separation between each segment is observed. Though, for low ratios between the transverse and longitudinal energy, the event distribution is more smeared out. Those observations indicate that events from Ag+Ag reactions are preferably emitted in the transverse direction with respect to the beam axis. In contrast, Ag+C events tend to exhibit a lower ratio. Therefore, a cutting criterion of $ERAT > 0.6$ seems reasonable, as applied in the mentioned proton flow analysis [48]. Thereby, the ERAT selection is applied additionally to the standard event criteria.

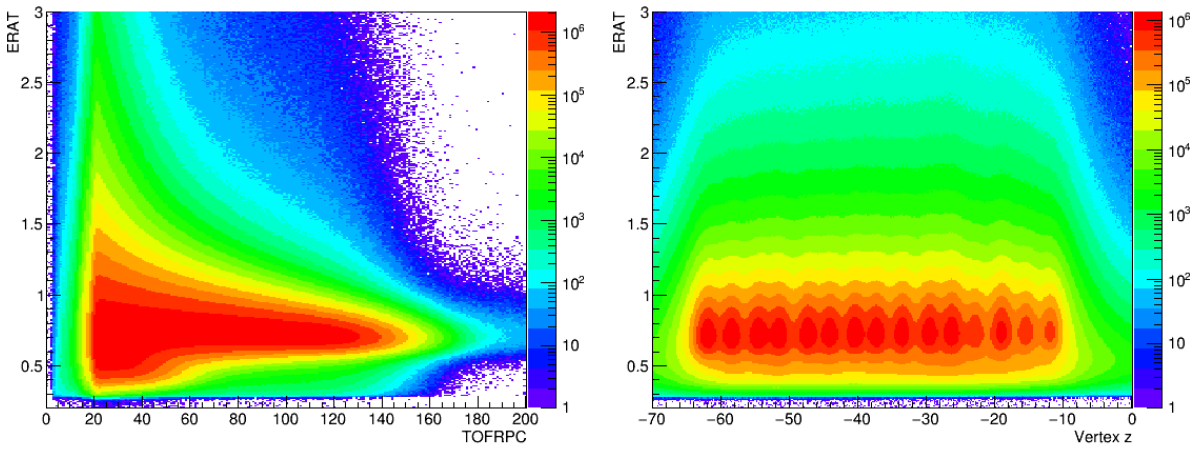

Figure 3.2: Left: Distribution of events as a function of the ERAT value and the multiplicity hits measured with TOF and RPC. Right: Dependence of the ERAT value from the vertex position among the beam axis. For low multiplicities and low ERAT values, a region is visible that might be related to Ag+C reactions.

In figure (3.3, left), the number of events remaining after applied EART-selection is compared to the number of standard selected events as a function of centrality. Overall, the EART selection discards 13 % of all standard selected events. Moreover, the day dependency has been investigated (figure (3.3, left)). The fraction of rejected events fluctuates between 9 % and 14 %. In the centrality range of 30-40 % and 40-50 % the cut rejects 16 % and 24 %. For more central collisions a smaller fraction is rejected: 3 % in the most 0-10 %, 4% for 10-20 % and 7 % for 20-30 % most central events. This observation supports the assumption that mainly Ag+C events are removed as they are dominant in centrality classes with more spectators. However, towards central events, particularly for 20-30 % centrality, with 7 % still a significant amount of data is discarded, although in this centrality region, Ag+C interactions are expected to be much less present due to a smaller number of spectators.

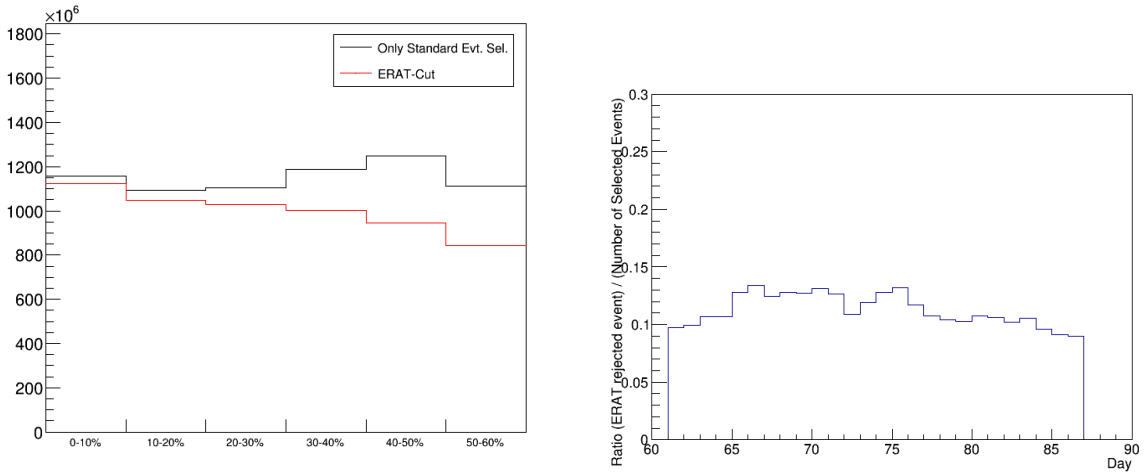

Figure 3.3: Left: Comparison of the number of selected events before and after applying the ERAT-cut. Right: Fractions of rejected events relative to the number of standard selected events for each day of the beam time.

For more detailed investigations, the distribution of events as a function of the hit multiplicity and z-vertex is plotted in figure (3.4). It is visible that mainly events with low hit numbers are discarded, but nevertheless, as already indicated, the EART selection also cuts into the vicinity of higher multiplicities.

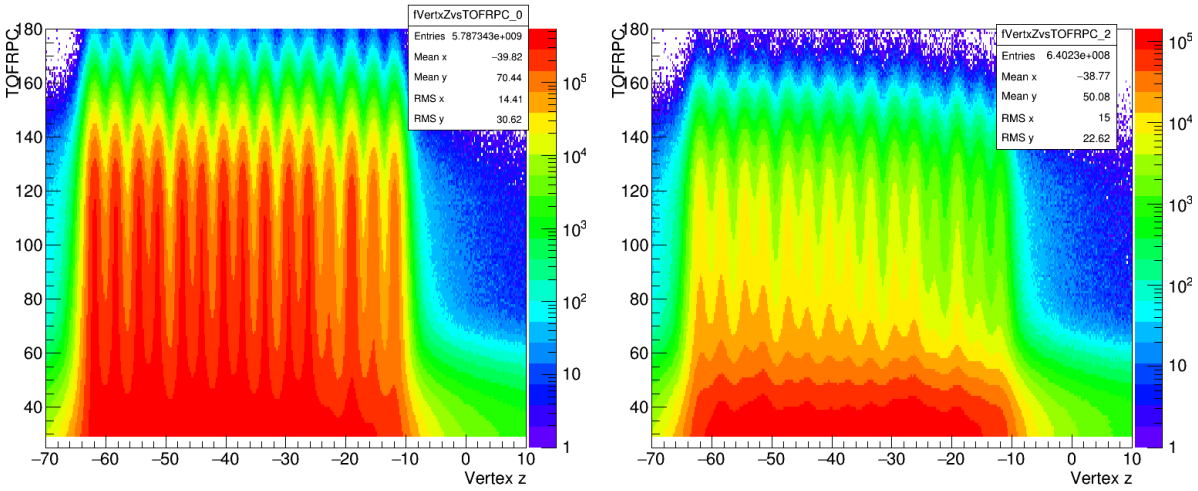

Figure 3.4: Distributions of the observables: number of multiplicity hits and z-vertex for the standard event selection (left). The same observables has been looked at for the events which are rejected by the ERAT-cut (right).

Furthermore, it is looked at the vertex x vs vertex z distribution in order to examine in which target regions the EART-selection specifically rejects events. Figure (3.5, right) shows the distribution of the fractions of discarded events. Comparing it with target segment's positions in z-direction (left hand side on figure 3.5), it is found that the fraction is at around 20 to 35 % in-between the segments. However, only less than 15 % of the events are rejected within the target segments themselves. Moreover, highest fractions (> 50 %) of discarded vertices are observed outside, behind or in front of the target set-up. This observation demonstrates that the ERAT selection mostly excludes non Ag+Ag events or those that exhibit a non-physical behaviour.

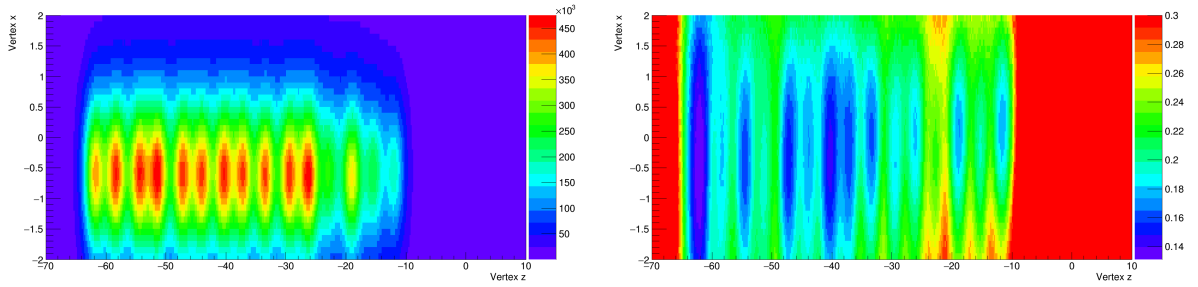

Figure 3.5: Left: Vertex x vs vertex z distribution for the standard event selection. Right: Distribution of the fractions of events removed by the ERAT selection relative to the number of standard selected events as a function of the vertex x and vertex z.

However, as mentioned, for the events with a vertex located in one of the 15 segments, still up to 15 % are removed. In order to make sure that events with good quality are not excluded, the charged pions from the ERAT-rejected events are differentially analysed according to the procedure depicted in (3.1). Within the scope of acceptance and efficiency correction, an ERAT selection is not applied as there it is obviously for sure that only Ag+Ag are generated. In figure (3.6), the resulting reconstructed rapidity

distributions as a function of centrality for the π^- mesons out of events rejected by the ERAT-selection are displayed.

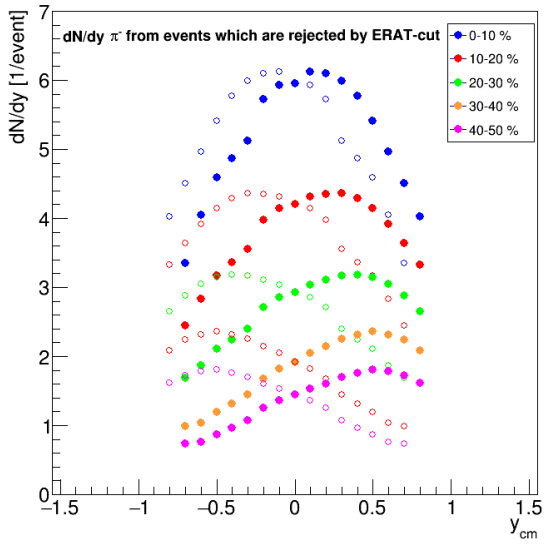

Figure 3.6: Acceptance and efficiency corrected dN/dy distribution of negatively charged pions from events which are rejected by the ERAT selection. A clear asymmetry between the forward and backward bins is observed over all centrality ranges.

As the comparison with the reflected points reveals, a strong asymmetry in the order of up to 50 % with respect to mid-rapidity is visible overall centrality classes. In conclusion, the ERAT selection mainly discards the highest fraction of events in the most peripheral events but also cuts significantly into regions of higher multiplicities. However, the observed asymmetry on the corrected dN/dy distribution of charged pions from the rejected events justifies using the introduced ERAT-event-selection in charged pion analysis. Eventually, after the applied ERAT selection, $6.0063 \cdot 10^9$ events are available in the following analysis.

1.2.2. Track Quality Selection

In order to access the quality of the tracks reconstructed by the interpolation method, as described in (2), the quality parameters χ^2_{RK} and χ^2_{META} are considered. In the charged pion analysis, rather open-cut conditions are applied as for tighter parameters a slight asymmetry on dN/dy had occurred for the π^+ after $Acc \cdot Eff$ correction. The selection condition's are the same as in [44] and reject around 2 % of all selected tracks: $\chi^2_{RK} < 400$ and $\chi^2_{META} < 3$. Compared to the previous analysis in [44], an additional track quality selection is used to discard tracks that are close to or go through the frame of a MDC module. This selection is motivated by the observation that the efficiency is decreased around the edges of a MDC module, which is probably due to distorted electric field lines at the boundaries. The detection efficiency has been estimated via simulations [43], see figure (3.7). It was observed that efficiency is much lower at the edges compared to the inner area of the MDC modules. The black lines represent the cut window around the frames with respect to Cartesian coordinates x, y. The cut removes around 5 % of all tracks [43].

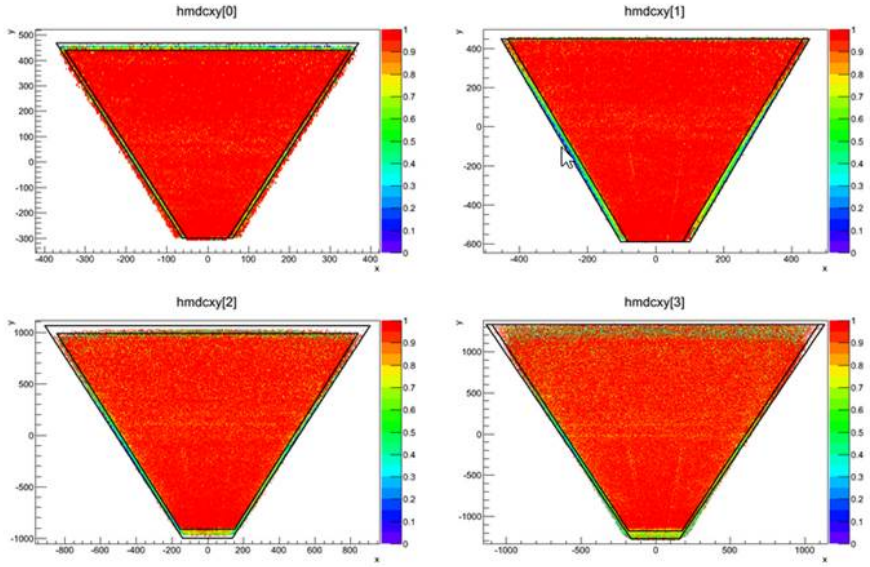

Figure 3.7: Estimated efficiencies for the MDC modules. Black lines illustrate the graphical cut used to exclude tracks around the MDC's frames. This plot has been provided by [43].

1.3. PID

1.3.1. Time of Flight PID

The foundation for charged pion identification is the time of flight measurement. Hence, the correlation between the velocity β and momentum p times the polarity is evaluated. The parametrization according to equation (2) can be used to find the spectra region that is enriched with charged pions. In order to quantify the distribution, the momentum axis is divided into intervals with a width of 20 MeV/c. For each interval slice, a 1D projection along the β-axis can be prepared and subsequently fitted with a Gaussian. Based on the adjusted parameters of each Gaussian, a graphical cut is generated with a width of 2 sigmas around the mean.
The problem of this method is that the charged pions populating the regions of lower momenta are not so well entangled from the muons as they exhibit similar masses. Moreover, for higher momenta, the distribution of protons start overlapping with the one of the pions. In order to eliminate this issue, a different procedure for generating the graphical cut has been developed by [55]. The idea is to transform into a new coordinate system where one axis corresponds to the squared mass of the particle. The coordinate transformation is defined as [55]:

$$m^2 := p^2(\frac{1}{\beta^2} - 1). \tag{3.2}$$

$$a^2 := 1 + p^2 s^2 - (1 - \beta^2)^2. \tag{3.3}$$

Where a is perpendicular to the squared mass axis, defining the second coordinate. S is a parameter adjusted to 0.072. The variables are squared to deal with particles measured with a velocity faster than the speed of light.
Figure (3.8) displays the distribution of β vs p including the new coordinate axes according to the transformation. On the right hand side, the distribution in terms of the new coordinates is displayed. It is visible that a better separation between the different particles is possible. The distribution of charged pions is quantified by creating projections along the a^2 axis and fitted with a Gaussian. Spectra, where the fit algorithm does

not converge, are fitted with the parameters of the previous fit slice [55]. The parameters of the Gaussian are transformed back to the old coordinate system of β and $p \cdot polarity$, and the PID cut is generated. The distribution of positively charged pions is better detached from the proton distributions in the new coordinate system, allowing to provide a more precise fit. Therefore, the graphical cut window on β vs $p \cdot q$, generated by this new procedure, is used in the following as a PID criterion for charged pions. In this way also, consistency with the time of flight PID of ongoing analyses of charged pions from lower beam energy experiments at HADES is guaranteed.

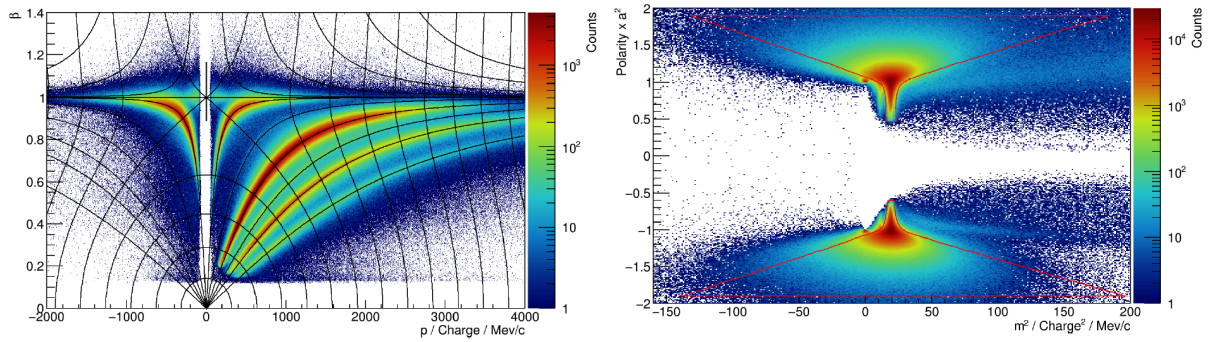

Figure 3.8: Left: Distributions of the observables β vs $p/Charge$. Drawn are also the coordinate lines defined by (3.2). Right: Distributions in the new coordinate system. The plots taken from [55].

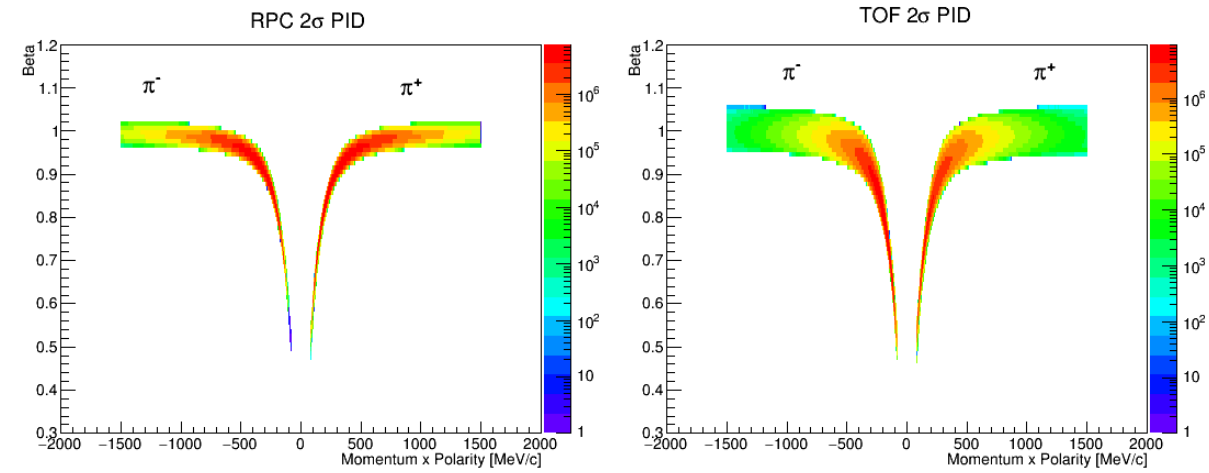

Figure 3.9: Selected distributions on the correlation between β and $p \cdot polarity$ for the RPC (left) and TOF (right) detector. The selected particles are in the following analysis considered as charged pions.

1.3.2. MDC dE/dx Selection

With the DST-analysis of generation 5 a better calibration of the specific energy loss measurement in the MDCs is provided. Hence, a new selection on the correlation between dE/dx vs p is introduced, aiming to suppress protons that contaminate the spectra of positive pions in regions of higher momenta. The dE/dx vs. p spectra are obtained after applying a mass selection of $m < 500\ MeV/c^2$. The momentum axis, ranging

from 0 to 2000 MeV/c, is divided into equally wide intervals with a size of 20 MeV/c. Subsequently, for each slice a projection among the dE/dx-axis is performed, resulting in 100 different dE/dx spectra. As figure (3.10) displays, the distribution of the specific energy loss does not exhibit a Gaussian shape, as it was observed for the β-spectra. Instead, a long tail towards higher momenta is visible. Therefore, in order to model the shape of the distributions appropriately, a Gaussian function with two different sigmas is chosen:

$$f(x) = \begin{cases} Ae^{\frac{-(x-\mu)^2}{2(\sigma_1)^2}} & \text{if x} < \mu \\ Ae^{\frac{-(x-\mu)^2}{2(\sigma_2)^2}} & \text{if x} > \mu. \end{cases} \tag{3.4}$$

Where x is the value of dE/dx. A corresponds to the amplitude, μ describes the peak position of the distribution. σ_1 characterizes the width of the Gaussian for $dE/dx < \mu$ and σ_2 for $dE/dx > \mu$. Adjusting the function is conducted using χ^2-minimization. The starting point of the parameter values are set to the mean given by the Bethe-Bloch-equation, see equation (3.10). Additionally, initial values for the errors are set to 5 % of the start value in order to have a smaller step size per iteration within the algorithm. Figure (3.10) (left) shows the obtained mean as a function of momentum. It is observed that the mean specific loss energy is highest for low momenta. dE/dx then drops to a minimum at $p \approx 450$ MeV/c. Finally, it slightly increases again, exhibiting a saturation plateau for $p > 1200$ MeV/c. Subsequently, based on the extracted information of the MDC dE/dx-spectra, a selection window on dE/dx vs p is generated. It curves alongside the extracted mean of the different momentum dependent dE/dx spectra. Towards the direction of lower energy losses, the width of the cutting windows is $1.5\sigma_1$, in the other direction $1.5\sigma_2$. The obtained dE/dx-selection is eventually applied as an additional identification criteria for the π^+ with momenta $p > 300$ MeV/c in order to suppress the background from protons. For $p < 300$ MeV/c, the selection is not applied as in this spectra vicinity, protons are not dominant.

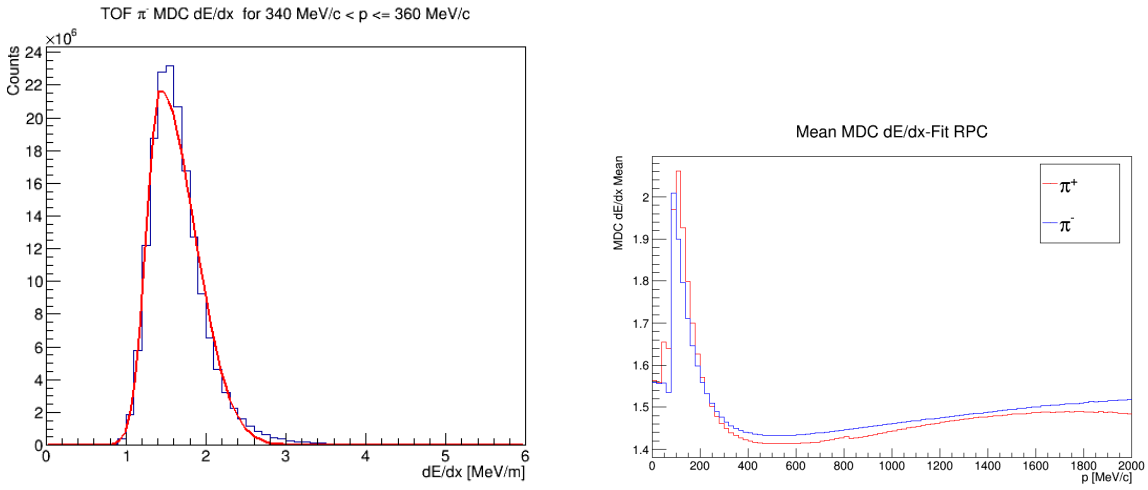

Figure 3.10: Left: Example of dE/dx spectra of the π^+ region, fitted with an asymmetric Gaussian. Right: Execrated mean of the asymmetric Gaussian as a function of momentum for π^- (blue) and π^+ (red).

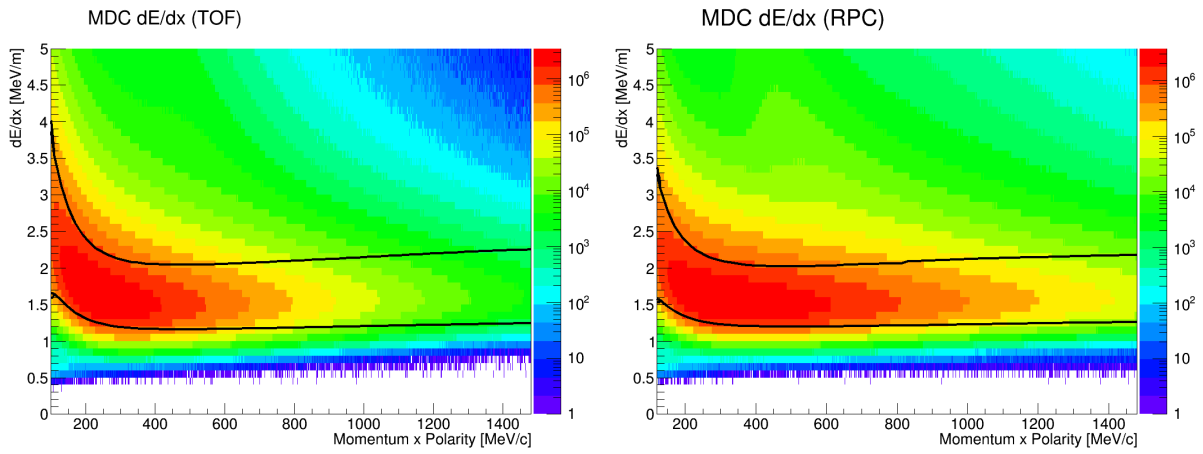

Figure 3.11: Generated 1.5σ graphical selection on the correlation between the specific energy loss dE/dx in the MDCs and the momentum p. Right: RPC. Left: TOF. The selection is employed for momenta higher than 300 MeV/c only.

In the scope of acceptance and efficiency correction, the applied selection in regard to the specific energy loss needs to be implemented in the simulation analysis in the same way as in the experimental data. This also allows estimating the purity of the identified pions selected by the applied criteria. Purity is defined as the fraction of true primarily emitted charged pions within the sample of all reconstructed (identified) pions for a given phase space cell, see also section (1.4):

$$P(p_t, y) = \frac{N_{primary,pions}(p_t, y)}{N_{rec}(p_t, y)} \tag{3.5}$$

Figure (3.12) display the obtained purity distribution on the correlation between transverse momentum p_t and rapidity y. A comparison with the situation without the additional dE/dx-selection indicates that the purities are increased by $2-4$ % in regions of intermediate momenta.

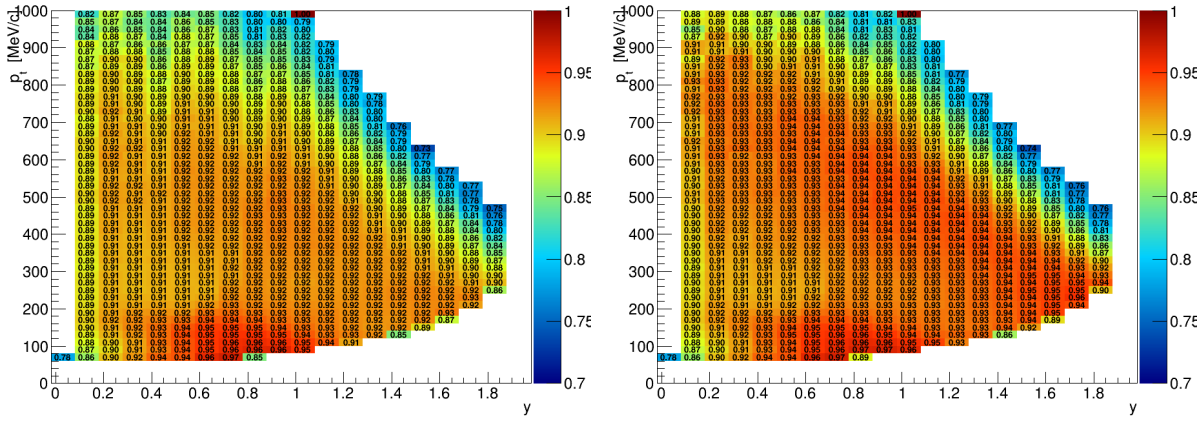

Figure 3.12: Obtained purities as a function of transverse momentum and rapidity. Left: without dE/dx-selection. Right: with MDC dE/dx-cut. The dE/dx-cut leads to an increase of the purities, in particular for the region of intermediate high momenta.

In order to check for potential systematic biases and decide whether this track selection helps improve the symmetry for the π^+ mesons on the corrected rapidity distribution; a comparison of the variants without and with included dE/dx selection is plotted in figure (3.13). It is visible that the additional selection leads to a more symmetric situation within the two most central event classes. However, a major impact on the spectra and improvement on the symmetry is not observed in the peripheral centrality classes.

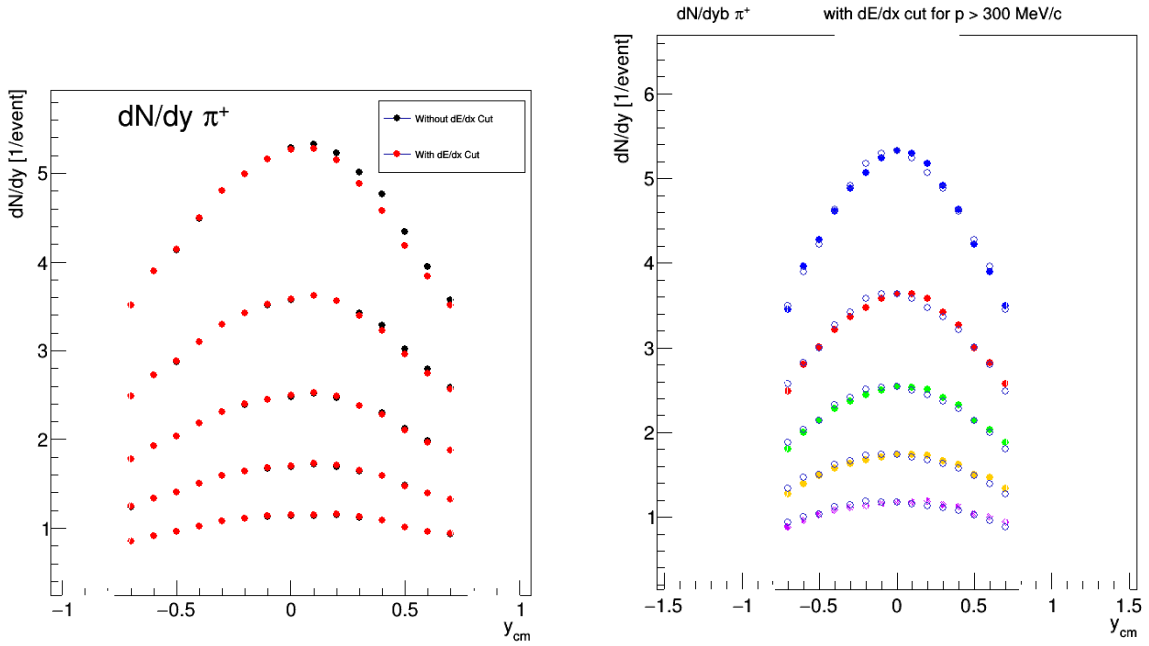

Figure 3.13: Left: Comparison of resulting dN/dy distribution between the analysis without and with the MDC dE/dx-selection. Right: Comparison with reflected data point (white). In particular for most central events a symmetry improvement is visible.

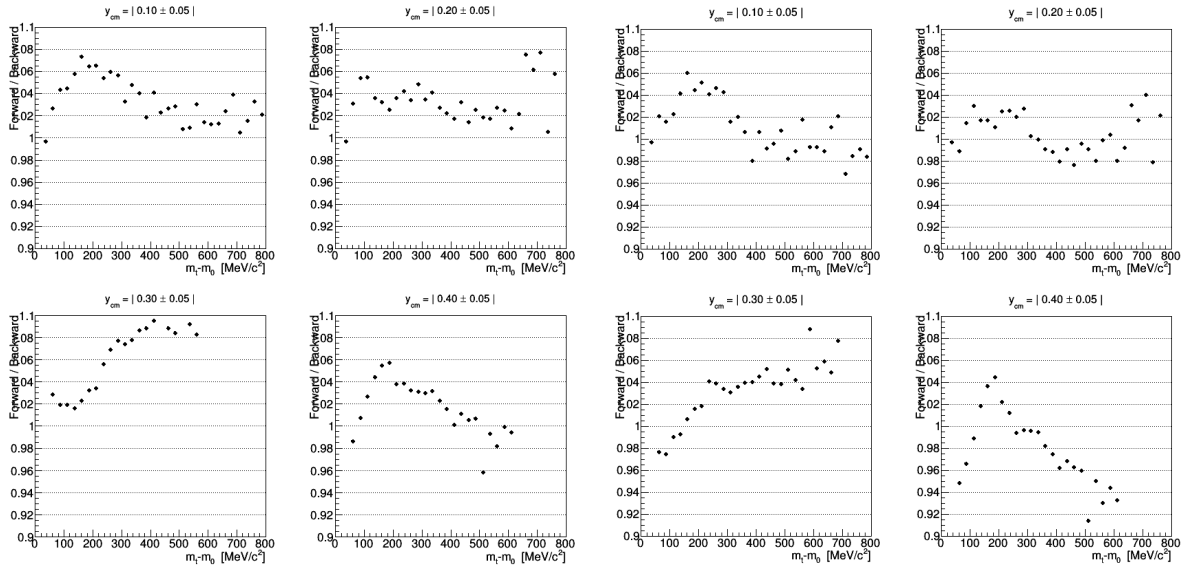

Figure 3.14: Ratios between forward and backward pt-bins (0-10 %) for the rapidity slices $y_{cm} = |0.1 \pm 0.05|$, $y_{cm} = |0.2 \pm 0.05|$, $y_{cm} = |0.3 \pm 0.05|$ and $y_{cm} = |0.4 \pm 0.05|$. Left: without MDC dE/dx-cut. Right: with MDC dE/dx-cut.

In order to investigate the differences between the PID with and without the MDC dE/dx-selection in more detail, the p_t spectra are compared for each $p_t - y$ bin. For the variant with the time of flight PID only, the ratio between forward and backward counts is generally higher than 1, leading to the asymmetry observed for the rapidity density distribution. With included specific MDC energy loss selection, the ratios are shifted downwards, see figure (3.14).
In summary, the employed MDC dE/dx-selection increases the purities for intermediate high momenta and suppresses protons. The corrected dN/dy spectra have shown that the cut helps improve the symmetry in the most central events. Hence, the generated MDC dE/dx-graphical cut is implemented as an additional PID selection criterion from now on to filter for π^+ candidates.

1.4. Phase Space and Acceptance/Efficiency Correction

Once the charged pions are identified, their kinematic distribution is inspected. They are crucial for drawing conclusions on the characteristics at the point of kinematic freeze-out and are the foundation for the extrapolation into uncovered regions. Assuming cylindrical collision symmetry, the kinematics can be described by two variables. In order to allow for a valid comparison between different beam energies, they should be Lorentz-invariant or at least exhibit a simple transformation behaviour. Usually, in the field of high energy physics, the longitudinal phase space among the beam axis is described by the quantity rapidity y:

$$y = \frac{1}{2} \ln \left(\frac{E + p_z}{E - p_z} \right). \tag{3.6}$$

Where E corresponds to the total energy and p_z to the momentum component in the direction of the beam axis. The transformation behaviour of the rapidity is additive. Thus, for conversion into the centre of mass system, the lab rapidity is subtracted by the

rapidity of the beam $y_{beam} = 0.82$.
The transverse energy component of the particles is covered by a Lorentz-invariant variable like the transverse mass or transverse momentum. In this analysis, both the transverse mass m_t and momentum, p_t are considered for evaluating eventual systematic difference when it comes to extrapolating into uncovered phase space regions (1.6.1). The transverse momentum p_t is defined by the transversal components p_x and p_y of the momentum p:

$$p_t = \sqrt{p_x^2 + p_y^2} = \sqrt{p^2 - p_z^2} = p \cdot sin(\phi). \tag{3.7}$$

The transverse mass follows by using the energy-momentum relation:

$$m_t = \sqrt{p_t^2 + {m_0}^2}. \tag{3.8}$$

The distributions for the count rates in terms of the transverse momentum (mass) and rapidity are considered differentially: Meaning, the spectrum is divided into sufficiently small cells with a size of $0.1 \cdot 25\ MeV/c$ in the range of $-0.03 < y < 1.97$, $0 < p_t < 1500$ MeV/c. In this way, the statistics per bin is sufficiently large enough. Moreover, the chosen bin size is consistent with previous HADES analyses on charged pion production [2].
The detector's acceptance and reconstruction efficiency is limited, and because of the track selections applied, a certain amount of charged pions are discarded. This has the consequence that the raw counts in a given phase space cell are expected to be smaller than the actual count rate, making it necessary to employ a correction. The combined acceptance and efficiency $Acc \cdot Eff$ is defined as the ratio between reconstructed N_{rec} and emitted particles N_{em}:

$$Acc \cdot Eff(p_t, y) = \frac{N_{rec}(p_t, y)}{N_{em}(p_t, y)}. \tag{3.9}$$

In order to determine $Acc \cdot Eff(p_t, y)$, simulation are utilized. The rationale is the following: Events of Ag+Ag collisions are simulated by the transport based model UrQMD (Ultras Relativistic Quantum Molecular Dynamic) [16], which solves the relativistic Boltzmann equation numerically and incorporates the experimentally known production channels. The generated particles of the reaction are afterwards propagated to GEANT (GEometry ANd Tracking)[65], simulating the detector's track reconstruction. The output is subsequently analysed in exactly the same as the experimental data in order to obtain simulation-based phase space spectra. Now, there are two phase space matrices available: The one from the initial UrQMD simulation and the reconstructed one of the GEANT emulated detector's response. By computing the ratio between the reconstructed $N_{rec,GEANT}$ counts and the counts $N_{UrQMD,primary}$ of primarily emitted charged pions for each phase space cell (p_t, y), one yields an estimation of the efficiency.

$$Acc \cdot Eff(p_t, y) = \frac{N_{rec,GEANT}(p_t, y)}{N_{UrQMD}(p_t, y)}. \tag{3.10}$$

The $Acc \cdot Eff$ matrices (3.15) are subsequently used to correct the experimental count rates by dividing the experientially measured count rates by the obtained $Acc \cdot Eff$ factor, resulting in the corrected count rate N_{corr}:

$$N_{corr} = \frac{N_{rec,exp}(p_t, y)}{Acc \cdot Eff(p_t, y)}. \tag{3.11}$$

Phase space bins with an acceptance below 15 % are neglected to allow for a more smooth shape of the spectra at the lower edge of the geometrical acceptance and to reduce uncertainties. By making use of the simulation, the purity of the pion sample selected by the applied criteria can be estimated, as already conducted when evaluating the dE/dx selection, see section (3.10). Purity is defined as the fraction of truly and primarily produced charged pions within the set of all reconstructed ones:

$$P(p_t, y) = \frac{N_{primary,pions}(p_t, y)}{N_{rec}(p_t, y)}. \tag{3.12}$$

In this way, the contamination of other particles like protons is estimated. The chosen purity cut condition is 85 %. This mainly rejects bins at the edges towards high transverse momenta and high rapidities where protons occur.

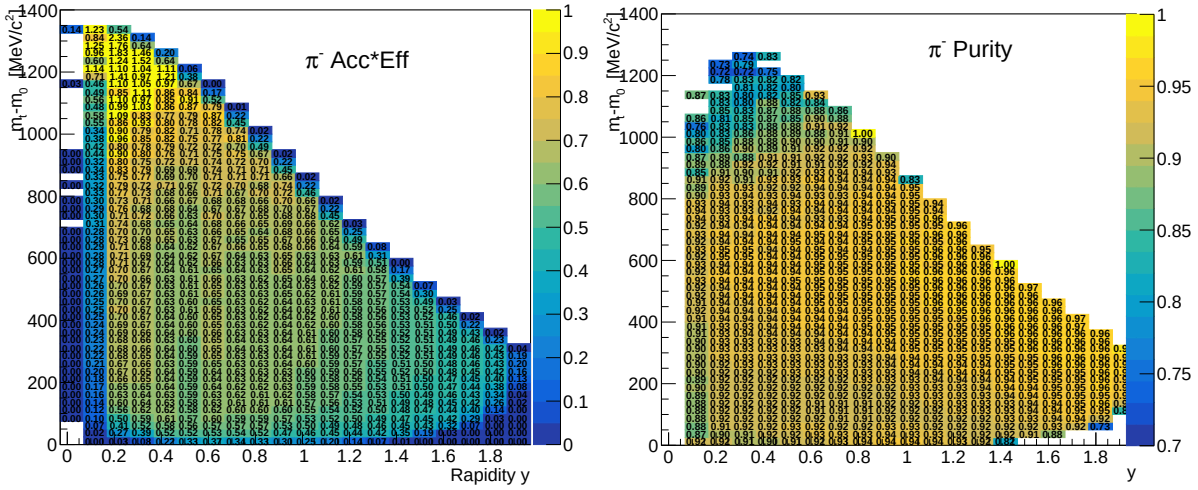

Figure 3.15: Left: Used efficiency distribution for the 0-10 % most central events for the π^- mesons. Right: Purity matrices.

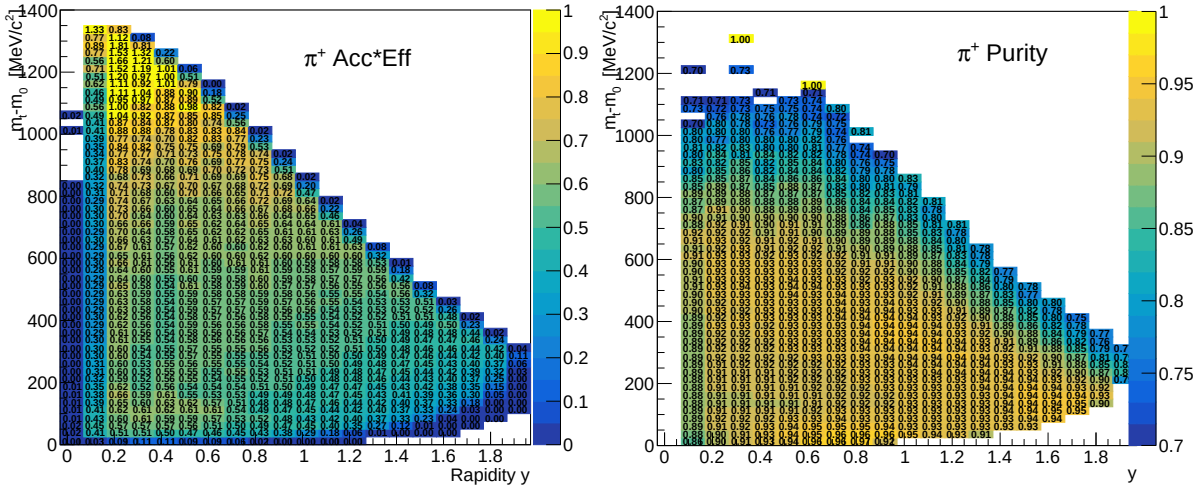

Figure 3.16: Left: Used efficiency distribution for the 0-10 % most central events for the π^+ mesons. Right: Purity matrices.

1.5. Phase Space Extrapolation

The corrected spectra need to be extrapolated into transverse phase regions where the coverage of the detector is zero, namely for low and high transverse momenta. In the standard approach this accomplished by fitting a Double Boltzmann function to the transverse spectra $\frac{dN}{dydm_t}$ and $\frac{dN}{dydp_t}$.

$$\frac{1}{m_t^2}\frac{d^2N}{dm_t dy} = Ae^{-m_t/T_1} + Be^{-m_t/T_2}. \tag{3.13}$$

The assumption behind this formula is that the charged pion's spectra behave according to a Max-Well distribution, as it would be the case if the production is of thermal origin. However, this is not exactly the case, though, in previously charged pion analyses, the Boltzmann functions have been proven as a good model to describe the measured data appropriately [2], [44]. However, in particular, for lower transverse momenta, the description with this simplified model reaches its limits. This e.g. can be attributed to the acting Coulomb force. Therefore, in section (2) a modified function that implements a Coulomb potential is tested for extrapolation. Equation (3.13) consists of a superposition of two Boltzmann distributions with different slope parameters T_1, T_2 in order to account for the fact that charged pions in the low transverse energy region are mainly produced by Δ-resonances which limits the available phase space and thus lead to a smaller inverse slope parameter.
Finally, the rapidity density distribution dN/dy is obtained by integrating the transverse spectra: For intervals exhibiting zero acceptance, the adjusted double Boltzmann function is used, whereas, in the covered areas, the data bins available are integrated.
Extrapolation in the longitudinal scope is conducted by scaling the rapidity distribution from UrQMD [16] so that the integral is consistent with the integral of the data points. The reason why UrQMD is preferred over a simple Gaussian extrapolation is that the underlying transport model provides a more realistic modelling of the situation in nature as it describes the heavy-ion collision on a microscopic level and includes several experimentally tested production channels, making it superior compared to a purely statistical model as it would be the case for a Gaussian function. Integrating over the variable rapidity finally results in the production rates with respect to the full solid angle of 4π.

1.6. Systematics

In the following three subsections, the impact of potential system effects is discussed. The aim is to provide an estimate of the systematic error. On the one hand, the extrapolation error resulting from the different representations of the differential spectra as well as the PID systematics by varying the bandwidth of the graphical cut window, is inspected. On the other hand, the systematics is investigated by analysing the charged pion spectra separately for each of the detector's 6 sectors.

1.6.1. Systematics from Transverse Extrapolation

Both the differential transverse reduced mass spectra $dN/(dyd(m_t - m_0))$ and transverse momentum spectra $dN/(dydp_t)$ are fitted by a function based on the Maxwell Boltzmann statistic. The underlying assumptions are the same. However, the transverse mass

spectra are scaled in a different way compared to the momentum representation. This might lead to deviations in the extrapolation, in particular for low transverse regions. In figure (3.17) the dN/dy spectra resulting from m_t and p_t based analysis are compared: In general, a good agreement is found for the π^-. For π^+ mesons, the deviations are sightly higher.

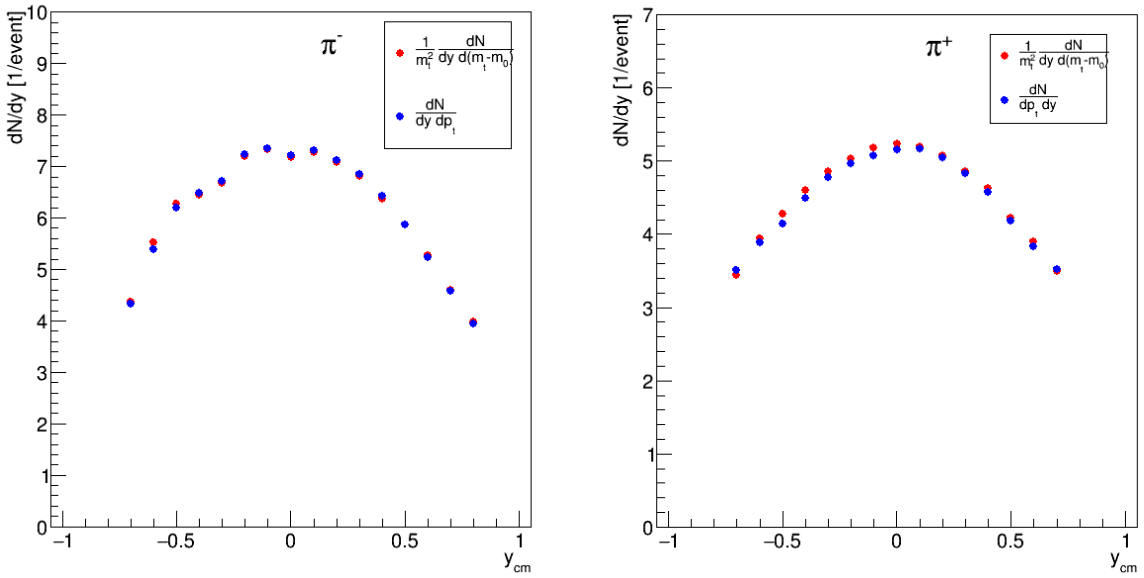

Figure 3.17: Comparison of the dN/dy distributions from m_t (Red) and p_t (Blue) based transverse extrapolation.

For the quantification of the systematic error, the relative deviation between the different dN/dy counts, reconstructed from m_t and p_t analysis, are calculated, see figure (3.18). The distributions are fitted with a constant, leading to an average extrapolation error of less than 1 % for the π^- and of 2 % for the π^+. The highest relative differences are observed for the outer backward rapidity bins. For the π^- mesons, the highest difference is found at $y_{cm} = -0.6$ with a value of 2.5 %. In the case of the π^+ mesons, the highest rel. difference is found at $y_{cm} = -0.5$ exhibiting a value of 3 %.

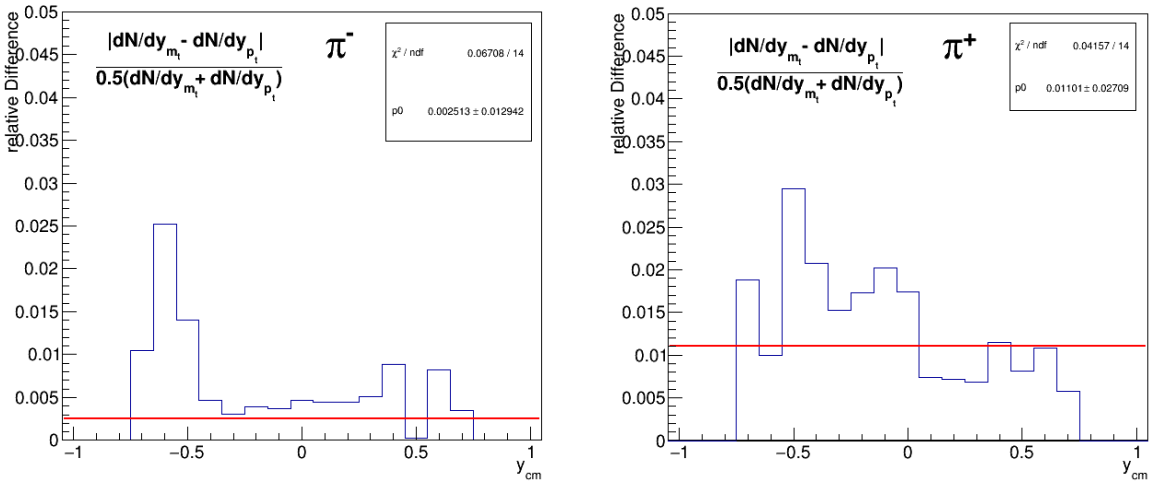

Figure 3.18: Relative differences between m_t and p_t based transverse extrapolation.

1.6.2. Variation of the PID Criteria

In this subsection, the PID selection criteria on the correlation between the velocity β and the momentum p are varied. For the standard analysis, a 2σ wide-cut window is applied (3). The width is now reduced to 1σ, and the analysis is repeated as before. Figure (3.19) displays the resulting corrected dN/dy distributions for both the 1σ (Red) and 2σ (Blue) versions. For quantification purposes, the relative differences are inspected in figure (3.20). It is revealed that for both polarities, the rel. differences of the PID criteria exhibit a rapidity dependent functionality: For bins close to mid-rapidity, the difference is rather small, less than 2 %. However, for increasing forward/backward rapidity, the rel. errors increase as well, reaching highest differences at the most outer bins with values of up to 6 % for the π^- mesons and up to 7 % in the case of the π^+ mesons. The average rel. error of the PID bandwidth variation is 1.6 % for the π^- and 1.9 % for the π^+ mesons.

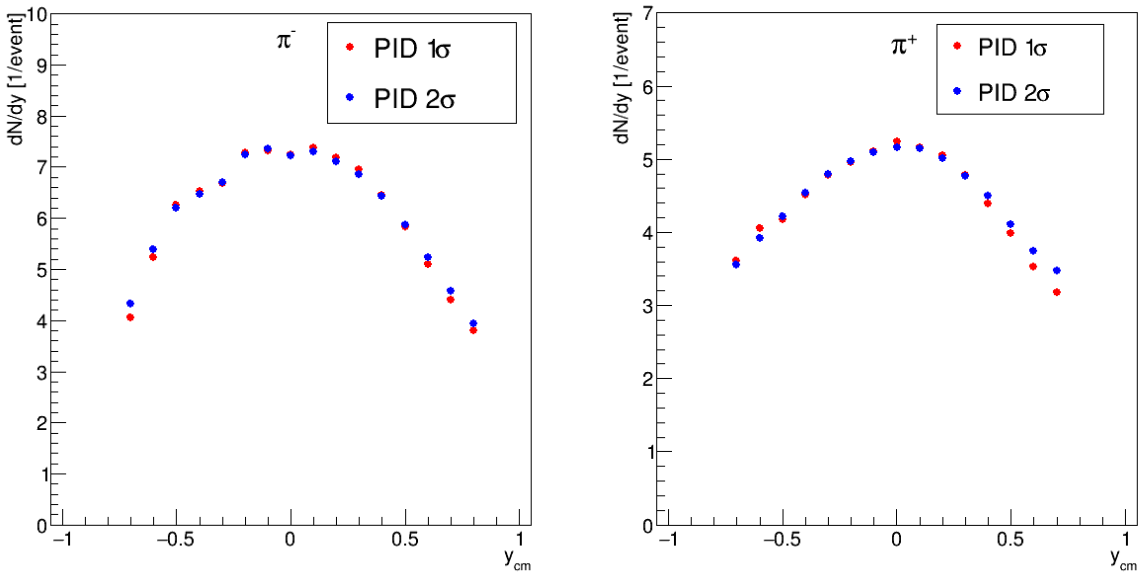

Figure 3.19: Comparison of the dN/dy (0-10 %) distributions with different PID-cut-widths - 1σ (Red) vs. 2σ (Blue).

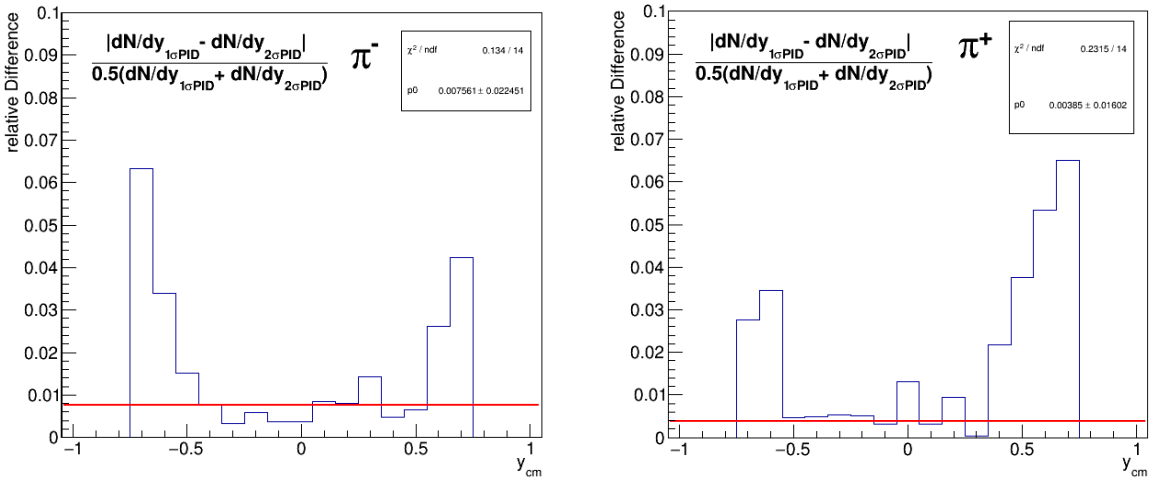

Figure 3.20: Relative differences of dN/dy (0-10 %) counts between the analysis of different PID-cut-widths - 1σ vs 2σ.

1.6.3. Variation between Different Sectors

Another way to investigate systematic uncertainties is by making use of the symmetry of HADEs. The six different sectors can be analysed individually and should yield differences as the efficiency differs due to deviation of the detector operands, e.g. high voltage. Moreover, the differences in the sector behaviour could be an explanation for the irregularities observed on the dN/dy spectra for the π^- mesons. Therefore, the charged pion analysis is performed separately for each sector. All charged pions are identified as described in (3), but the phase space distributions are established separately for each of the

6 sectors. Each raw spectrum is corrected into the full set-up. In order to account for the reduced acceptance and efficiency, the used cut value (1.4) is multiplied by 1/6. The resulting $Acc \cdot Eff$-corrected sector-wise rapidity distributions are displayed in figure (3.21), for the centrality class 0-10 %. The sector numbering starts from 0. For the π^- mesons, it is observed that the value of dN/dy at $y_{cm} = -0.3$ is significantly lower for sectors 4 and 5 than for the other sectors, resulting in a step in the rapidity distribution. The same holds for $0.15 < y_{cm} < 0.35$, for sector 4. On the contrary, for the π^+ mesons, such an irregular structure is not visible, the sector differences are more smoothly distributed. The deviation between the two polarities might be explained by the different bending directions of the magnetic field [60].
Since sectors 4 and 5 exhibit irregularities, they are removed from the analysis of the π^- mesons in the following.
In order to quantify the sector-wise deviations for each rapidity bin the relative difference between the dN/dy count rate of the sector with the highest $dN/dy_{max,sec}$ and the lowest value $dN/dy_{min,sec}$ are computed, see figure (3.22). For the π^- mesons, a large relative sector deviation of around 23% is observed for the most outer backward rapidity bin (y_{cm} =-0.7), corresponding to the bin where the acceptance and efficiency are lowest, making it an explanation for such fluctuations. The relative differences are fitted by a constant to quantify the average relative sector error. This leads to an error of 7.6 % for the π^- and of 5.7 % for the π^+ mesons.

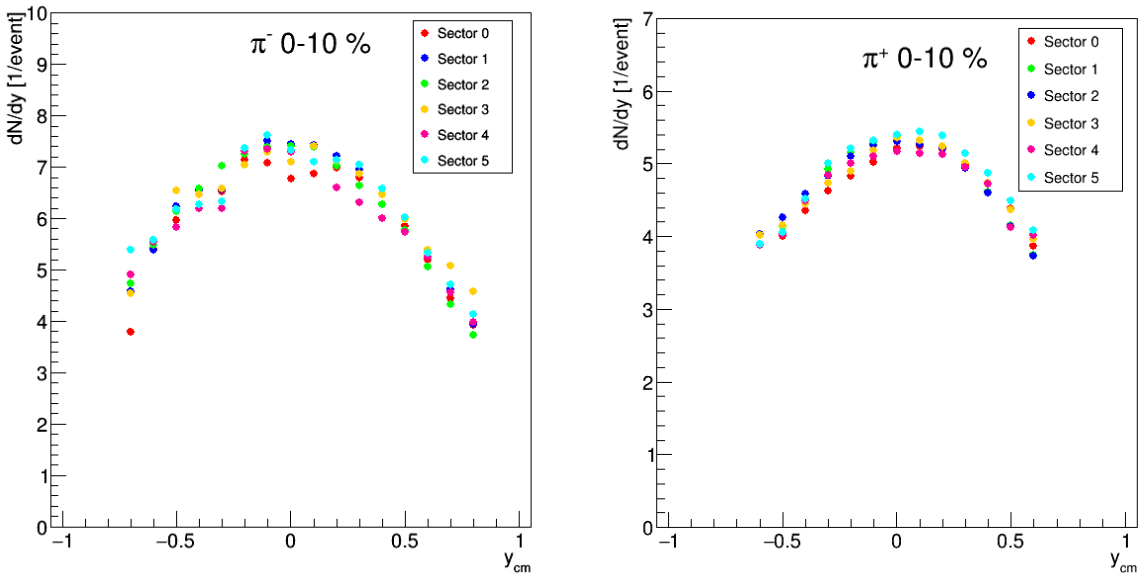

Figure 3.21: Sector-wise dN/dy distributions after the efficiency correction and extrapolation, for the 0-10 % most central events.

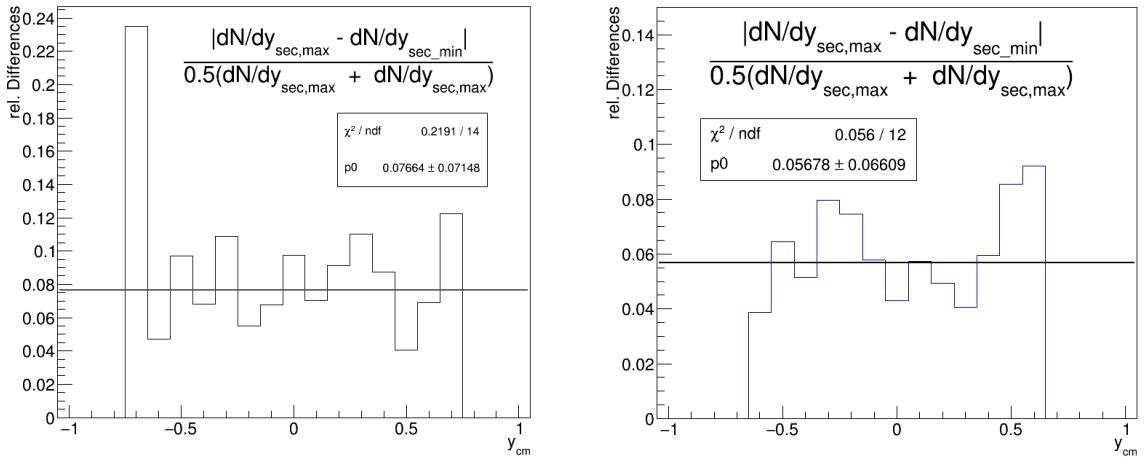

Figure 3.22: Relative differences between the dN/dy counts of the sector with highest value and lowest value as a function of y_{cm}. Left: π^-, Right: π^+.

1.6.4. Combined Systematic Error for the dN/dy Distribution

The quantified average systematic errors are combined by adding the relative errors from the different sources quadratically. The combined systematic error is then given by the square-root of the squared sum:

$$\Delta dN/dy = \sqrt{\Delta^2_{PID} + \Delta^2_{Extra} + \Delta^2_{Sec}} \tag{3.14}$$

As described, $\Delta dN/dy$ is composed of the extrapolation error Δ_{Extra} and the error Δ_{PID} resulting from the variation of the bandwidth of the PID cuts on β vs p. Additionally, the obtained average error Δ_{Sec} from the differing sector behaviour are considered. By that, one yields a relative total systematic error of 8 % for the π^- and of 7 % for the π^+ mesons.

1.6.5. Systematic Error on the Spectra

Lastly, in order to check whether the in previous sections (3.23) considered systematic sources are in reasonable order as well as to estimate a systematic error for the bins on the transverse momentum (mass) spectra, the counts on the forward and backward hemisphere are compared. This makes use of the expected collision symmetry. Figure (3.23) displays the rel. deviation between corrected forward and backward counts on the correlation of the transverse mass and rapidity (0-10 % centrality). We obverse that within $0.45 < |y_{cm}| < 0$ the rel. deviations are between 1 and 5 % for most of the bins. Though, for $|y_{cm}| > 0.45$ higher relative differences occur, up to 10 %. The highest differences of up to 15% are exhibited by a few bins at the edges for high transverse momenta. The rapidity dependence is in agreement with the findings of the PID systematics.

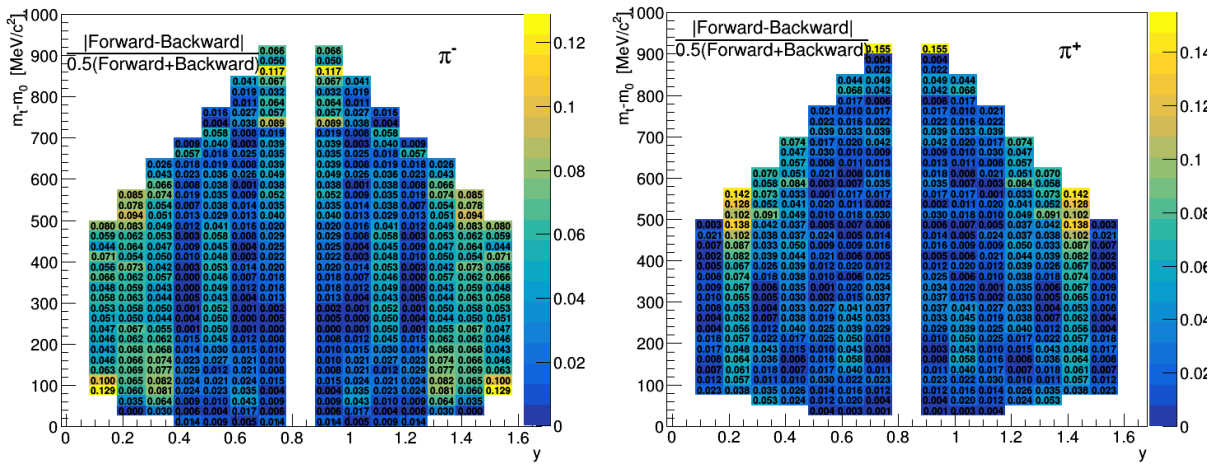

Figure 3.23: Relative differences of the forward and backward counts on the phase space grid for the correlation between the transverse mass and rapidity.

Finally, a rapidity dependent, averaged systematic error for the transverse spectra bins is determined for the slices $0.45 < |y_{cm}| < 0$ and $|y_{cm}| > 0.45$ separately. The systematic errors in dependence of the centrality classes and the rapidity interval are denoted in the tables (3.1) (π^-) and (3.2) (π^+).

Centr	sys. error ($\|y_{cm}\| > 0.45$) π^-	sys. error ($0.45 < \|y_{cm}\| < 0$) π^-
0-10 %	4.4 %	2.9 %
10-20 %	4.7 %	2.7 %
20-30 %	5.5 %	3.1 %
30-40 %	6.2 %	4.2 %
40-50 %	8.0 %	6.4 %

Table 3.1: Relative averaged transverse spectra error as a function of centrality for the π^- mesons.

Centr	sys. error ($0.45 < \|y_{cm}\| < 0$) π^+	sys. error ($0.45 < \|y_{cm}\| < 0$) π^+
0-10 %	3.7 %	2.0 %
10-20 %	3.6 %	2.3 %
20-30 %	3.6 %	2.5 %
30-40 %	3.7 %	3.4 %
40-50 %	4.0 %	4.3 %

Table 3.2: Relative averaged transverse spectra error as a function of centrality for the π^+ mesons.

1.7. Analysis Summary

In summary, the quality of charged pion data from peripheral collisions is improved on the event level by applying a selection on the ratio between the transverse and longitudinal energy additionally to the standard event selection. The track quality cuts used are the same as in the previous analysis, except for the additional MDC edge cut (1.2.2). Improved graphical cuts on β vs p spectra are applied concerning pion identification. In the case of the positively charged pions, a selection with respect to the measured specific energy loss in the MDCs is implemented, improving the symmetry on dN/dy for the most central collisions. The sector-wise analysis revealed the origin of irregular structures observed on the dN/dy distribution, which led to the decision of excluding the sectors 4 and 5 in the case of the π^- mesons.
The table below (3.3) summarizes all of the finally chosen event-, track- and PID criteria in the charged pion yield analysis.

	π^-	π^+
Standard Event Selection	True	True
ERAT cut	$ERAT > 0.6$	$ERAT > 0.6$
χ^2_{RK}	$\chi^2_{RK} < 400$	$\chi^2_{RK} < 400$
χ^2_{MetaQa}	$\chi^2_{MetaQa} < 3$	$\chi^2_{MetaQa} < 3$
MDC Edge cut	True	True
PID on β vs p	2σ	2σ
MDC dE/dx cut	False	1.5σ $(p > 300\ MeV/c)$
Momentum cut	$50 < p < 1500\ MeV/c$	$50 < p < 1500\ MeV/c$
Sectors included	0,1,2,3	0,1,2,3,4,5

Table 3.3: Summary of the event, track and PID selection criteria, applied in the yield analysis of charged pions.

The acceptance and efficiency correction is conducted by making use of the UrQMD and GEANT simulation, see section (3.16). The track selection criteria for the GEANT simulation are the same as denoted in the table above (3.3). In table (3.4), the properties of the phase space grid and the bin selection requirements within the scope of acceptance and efficiency correction are denoted.

	π^-	π^+
Ag+Ag sim	UrQMD 3.4, (no enhancement)	UrQMD 3.4, (no enhancement)
Tracking sim	GEANT	GEANT
$Acc \cdot Eff - cut$	$Acc \cdot Eff > 0.05$	$Acc \cdot Eff > 0.15$
$Purity - cut$	$P > 0.85$	$P > 0.85$
$m_t - m_0$-range	$0 < m_t - m_0 < 1500\ MeV/c^2$	$0 < m_t - m_0 < 1500\ MeV/c^2$
$m_t - m_0$-bin size	$25\ MeV/c^2$	$25\ MeV/c^2$
p_t-range	$0 < p_t < 1500\ MeV/c$	$0 < p_t < 1500\ MeV/c$
p_t-bin size	$25\ MeV/c$	$25\ MeV/c$
y_{cm}-range	$-0.75 < y_{cm} < 0.85$	$-0.75 < y_{cm} < 0.75$
y_{cm}-bin size	0.1	0.1

Table 3.4: Summary of the specifics in the acceptance and efficiency correction, including the applied selection criteria as well as the phase space grid division.

1.8. Results

In the following, the obtained results of the finalized charged pion production analysis of Ag+Ag collisions at $1.58A\ GeV$ are presented. For the negatively charged pions 16 differential transverse spectra are analysed within the rapidity range $-0.75 < y_{cm} < 0.85$. The rapidity bin size is 0.1 units. In the transverse direction, the bin size is $25\ MeV/c^2$ for the reduced transverse mass and $25\ MeV/c$ for the transverse momentum representation. For the positively charged pions, 15 transverse spectra are analysed within the rapidity range $-0.75 < y_{cm} < 0.75$. The bin size is the same as for the π^- mesons. The differential analysis is performed for 5 centrality classes in the range of 0-50 %. The differential count rates are normalized to the corresponding centrality class's selected number of events. The transverse reduced mass spectra for the 0-10 % most central event are displayed in (3.24), fitted with Double-Boltzmann functions used to extrapolate into uncovered transverse phase space regions. The transverse spectra of the other centralities are found in the attachment, see section (6.2).

1.8.1. Transverse Spectra and dN/dy

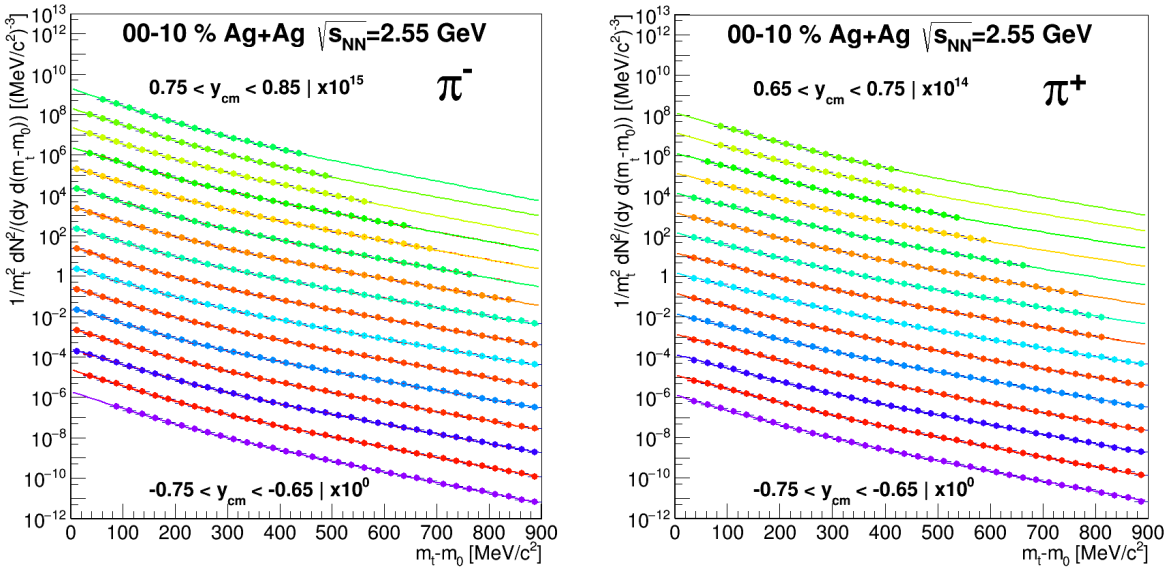

Figure 3.24: Transverse reduced mass spectra for the 0-10 % most central events, fitted with a Double-Boltzmann function used to extrapolate into uncovered transverse phase space regions. Left: π^- Right: π^+. The spectra have been scaled with powers of 10, with rising exponent per increasing rapidity bin. The counts are normalized to the number of selected events. For the π^- the spectra are in the rapidity range of $-0.75 < y_{cm} < 0.85$. For the π^+, the range is $-0.75 < y_{cm} < 0.75$. The phase space bin size is $0.1 \cdot 25\ MeV/c^2$.

In figure (3.25), the obtained rapidity density distribution dN/dy for each of the 5 analysed centrality classes are displayed. Full points correspond to the measured data. In order to evaluate the symmetry, the reflected data points are plotted as well (open circles). Furthermore, the scaled distributions of UrQMD are shown, used to extrapolate into the full longitudinal scope. Adjusted Gaussian are depicted as well. The error bars correspond to systematic uncertainties which are composed of the sector error, the PID and the extrapolation error (p_t vs. m_t), see section (1.6.3). The full production yield is determined by integrating the data points. In uncovered regions, the scaled UrQMD distribution is integrated and added to the measured yield, see section (1.6.4). The obtained 4π yields are listed in table (3.5). The first error corresponds to the described systematic uncertainties. The second error results from the differences between Gaussian and UrQMD based extrapolation and is used as an estimation for the systematic uncertainty of the extrapolation in the longitudinal direction.

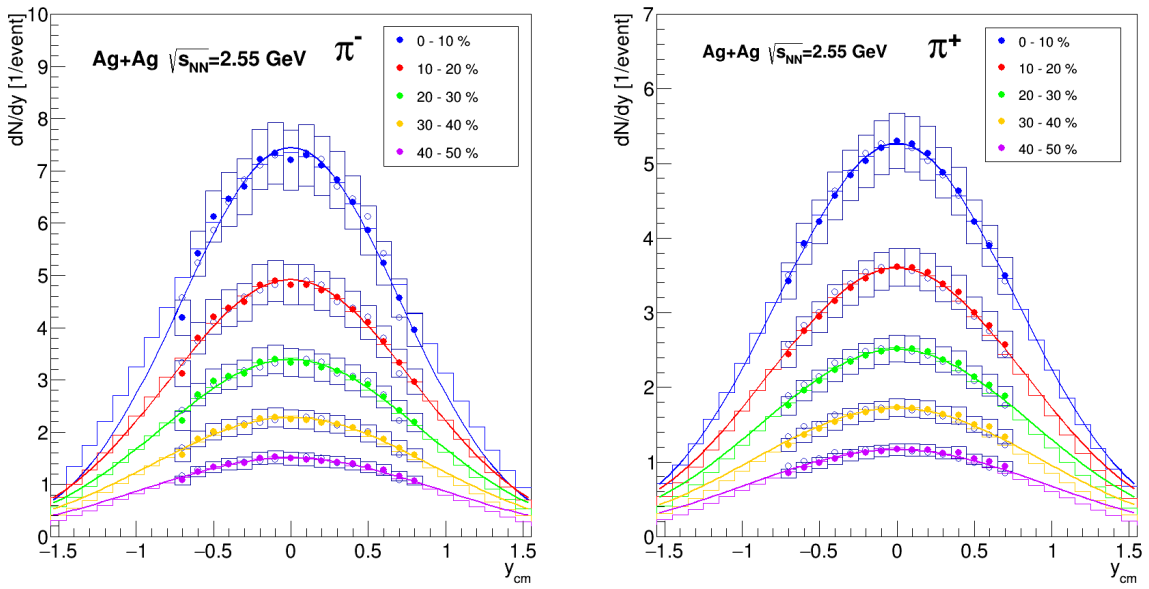

Figure 3.25: dN/dy distributions for each analysed centrality class. Obtained by integrating the transverse spectra using the Standard-Double-Boltzmann function for extrapolation. The plotted error bars correspond to systematic ones. The unfilled points represent the reflected data points. Plotted are also the scaled UrQMD distributions used for the 4π-yield determination.

C	$M(\pi^-)$	$M(\pi^+)$
$0-10\%$	$13.7 \pm 1.1 \pm 0.5$	$9.9 \pm 0.7 \pm 0.2$
$10-20\%$	$9.5 \pm 0.8 \pm 0.3$	$7.0 \pm 0.5 \pm 0.3$
$20-30\%$	$6.8 \pm 0.6 \pm 0.4$	$5.0 \pm 0.4 \pm 0.6$
$30-40\%$	$4.7 \pm 0.4 \pm 0.5$	$3.5 \pm 0.3 \pm 0.6$
$40-50\%$	$3.2 \pm 0.3 \pm 0.4$	$2.4 \pm 0.2 \pm 0.4$

Table 3.5: 4π production yields for the 5 centrality classes in the range of 0-50 %. The extrapolation for the transverse kinematics is based on the Double-Boltzmann functions. For extrapolation into the full rapidity scope the scaled UrQMD distributions are used. The first error corresponds to the systematic error. The second error indicates the difference between Gaussian and UrQMD based extrapolation in rapidity.

1.8.2. dN/dy_1 and dN/dy_2

In order to examine whether there are differences in the dN/dy pattern between the pions which populate the lower transverse energy region and those emitted with higher transverse energies, the two terms of the fitted double Boltzmann function are integrated separately. Where dN/dy_1 represents the pions in the low transverse energy region and dN/dy_2 the pions in higher transverse energy region. As opposed to the extrapolation of

the superposed yield, the adjusted analytic functions are integrated only:

$$dN/dy_1 = \int_0^\infty C_1 m_t^2 e^{-m_t/T_1}. \tag{3.15}$$

$$dN/dy_2 = \int_0^\infty C_2 m_t^2 e^{-m_t T_2}. \tag{3.16}$$

For the transverse mass spectra, the integral evaluates as:

$$\frac{dN(y)}{dy}_{1/2} = C_{1/2}((m_0c^2)^2 T_{1/2} + 2m_0c^2 T_{1/2}^2 + 2T_{1/2}^3). \tag{3.17}$$

In case of the transverse momentum representation the integral expression is given by:

$$\frac{dN(y)}{dy}_{1/2} = C_{1/2} T_{1/2} exp(\frac{-m_0}{T_{1/2}})(m_0^2 + 2m_0 T_{1/2} + 2T_{1/2}^2). \tag{3.18}$$

Where m_0 corresponds to the rest mass of charged pions. dN/dy_1 (Red) and dN/dy_2 (Blue) are displayed in figure (3.26) and (3.27) for each centrality class up to 50 % most central events. Additionally, the total dN/dy distributions are plotted in black. The fitted Gaussians provide a measure for the distribution width. In general, it is visible that pions from the low energy region are exhibiting a more flat-like distribution than dN/dy_2. In the case of the π^- for 0-10 % most central collisions, the σ of the Gaussian of dN/dy_1 is 0.91. The σ of the dN/dy_2 is 0.47. The width difference of the distributions is found to increases toward peripheral collisions. In the centrality class 40-50 %, the σ of dN/dy_1 is 4.65, whereas for dN/dy_2 it is found be at 0.49, similar to the most central events. Furthermore, towards more peripheral events a plateau is forming with a shape that has similarities to the dN/dy pattern of protons [55]. This observation will be discussed in detail in section (2.2).

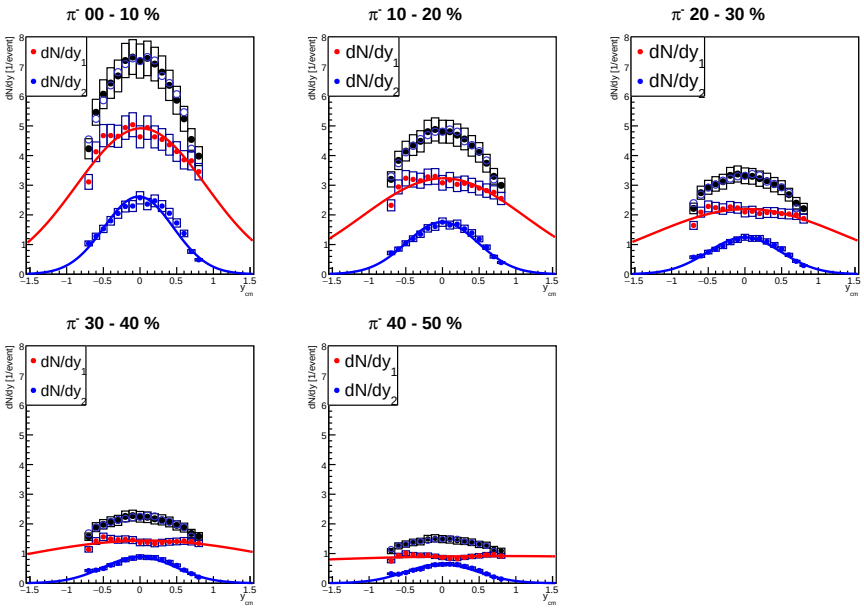

Figure 3.26: dN/dy distributions of the π^- mesons from different transverse phase space regions for each of the 5 centrality classes. dN/dy_1 (red) represents the low transverse mass region. dN/dy_2 (blue) represents the high transverse mass region. Additionally the total distribution is plotted in black.

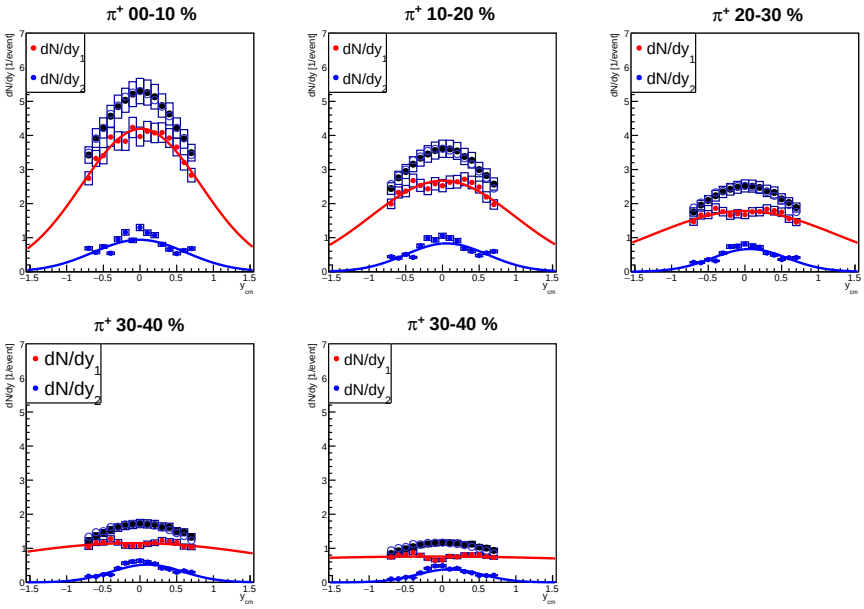

Figure 3.27: dN/dy distributions of the π^- mesons from different transverse phase space regions for each of the 5 centrality classes. dN/dy_1 (red) represents the low transverse mass region. dN/dy_2 (blue) represents the high transverse mass region. Additionally the total distribution is plotted in black.

2. Coulomb Effect on Charged Pions

2.1. Coulomb-Boltzmann-Model

The fact that a charged-dependent potential influences the emission of charged pions is observed best when comparing the differential transverse momentum spectra of both polarities: As displayed in figure (3.28), the maxima of the spectra are not at the same position on the transverse momentum axis. The maximum for π^- is located at 110 MeV/c. Whereas for the positively charged pions it is shifted towards higher p_t, at 150 MeV/c. This observation is attributed to the Coulomb force. As a result, the positively charged pions receive an acceleration in expansion since the fireball exhibits a positive charge due to the protons. Negative pions, on the other hand, expire a deacceleration.

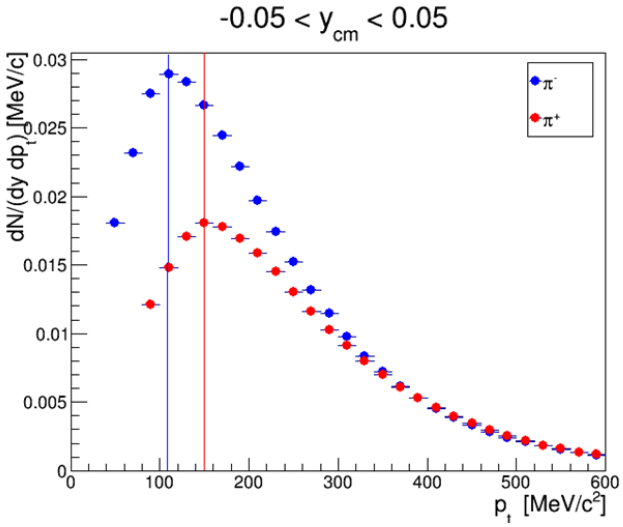

Figure 3.28: Comparison of the transverse momentum spectra of the π^- and π^+ mesons. A shift of the maxima is observed. Due to the Coulomb force, mainly generated by the proton charges, negatively charged pions are deaccelerated, whereas the positive ones are accelerated.

In order to derive the Coulomb potential from the measured charged pion spectra, one has to find a way to express the function of the Boltzmann-Statistic, used to fit the spectra in terms of that potential. Hence, an energy coordinate transformation needs to be implemented. As already explained, the transverse mass spectra of charged pions are usually fitted by a superposition of two Boltzmann functions, accounting for the different energy transfers occurring in the production processes. Assuming a $cosh(y_{cm})$ relation for the energy to transverse mass, the generalized form is:

$$\frac{1}{m_t^2}\frac{d^2N}{dm_t dy} = A(fe^{-E/T_1} + (f-1)e^{-E/T_2}). \tag{3.19}$$

Whereby E is a function of the transverse mass m_t and rapidity y:

$$E = m_t \cdot cosh(y_{cm}). \tag{3.20}$$

T_1 and T_2 correspond to the inverse slope parameters. f describes the composition between pions of the different energy transfers. A corresponds to the overall amplitude of the spectra. The aim is to express the observed energy E as a function of the Coulomb potential V_c. It is assumed that the charged pions are produced with the initial energy E_i. For the previous extrapolation method using the Standard-Double-Boltzmann model only, one presumes that this energy is equal to the measured final energy E_f. Yet, this is not true if an additional potential during the emission is at work. At the state when the charged pions are detected, their measured final energy also contains an additional energy component that corresponds to the Coloumb potential V_c. Meaning the pion's final energy E_f can be disentangled into the initial (production) energy E_i plus/minus the Coulomb potential V_c. For negativity charged pions, the sign of V_c is negative as they are attracted.

$$E_f(p_f) = E_i(p_i) \pm V_c. \tag{3.21}$$

Whereby, the energy is a functions of the initial and final momenta p_i (after production) and p_f (measured). According to the relativistic energy relation it holds:

$$p_f = \sqrt{E_f^2 + m^2}. \tag{3.22}$$

$$p_i = \sqrt{E_i^2 + m^2}. \tag{3.23}$$

The net charge of the fireball is mainly attributed to the protons. The spectator charges are neglected, as they are expected to move rapidly out of the collision zone. This should hold especially for central collisions and for charged pions exhibiting low longitudinal kinematics in the centre of mass system. However, with increasing rapidity and peripheral collisions, the spectators might very well influence the Coulomb interaction, as indicated in [59]. Moreover, V_c can not be considered as constant as a function of the pion energy since the charge distribution is not static. Instead, the dynamic expansion of the fireball makes it necessary to describe V_c by an effective energy-dependent potential V_{eff}. In general, slow pions that exhibit much smaller velocities than the expansion speed of the fireball proton's, enclose a smaller amount of charge. The protons that envelope these slower pions do not affect them according to Gauss's law of Electrodynamics. This causes slower pions to feel a less strong Coulomb force. In order to implement this attenuation effect, the distribution of the proton's expansion velocity has to be modelled appropriately. In [14] the assumption is made that the proton's velocities can be described by a non-Relativistic Boltzmann distribution, depending on the protons temperature T_p. According to [14], the reduction factor R of the Coulomb potential for a pion with velocity v_π is given by:

$$R = \frac{\int_0^{v_\pi} exp(-\frac{1}{2} m_p v^2/T_p) v^{(n-1)} dv}{\int_0^{\infty} exp(-\frac{1}{2} m_p v^2/T_p) v^{(n-1)} dv}. \tag{3.24}$$

This expression describes the fraction of protons that are slower than the considered pion. For high collisions energies, cylindrical expansion with n=1 is sufficient for a realistic description. However, this approach is not suited for low collision energy. Instead, a more accurate consideration with spherical 3D expansion is required, n=3. Performing the integrations in equation (3.24) results for the effective Coulomb potential in the

following expression [14]:

$$V_{eff} = \begin{cases} V_c(1 - e^{-x^2}) & \text{2D} \\ V_c(erf(x) - (2/\sqrt{\pi})xe^{-x^2}) & \text{3D.} \end{cases} \tag{3.25}$$

Hereby x is defined as:

$$x = \sqrt{(\frac{E_\pi}{m_\pi} - 1)\frac{m_p}{T_p}}. \tag{3.26}$$

This variable is connected to the energy of the pion E_π. $m_\pi = 139.57\ MeV/c^2$ corresponds to the nominal mass of a charged pion, $m_p = 938\ MeV/c^2$ to the proton mass and T_p to the freeze-out parameter, extracted from the transverse mass distribution of the protons in [55]. $Erf()$ represent the Gaussian error function, it originates when conducting the integration of equation (3.24)
The final goal is to parametrize the initial by the observed finial variables E_f and p_f. Using the equations (3.21) and (3.25), the initial momentum p_i can be expressed in the following way:

$$p_i(p_f) = \sqrt{E_i^2 + m^2} = \sqrt{(E_f \mp V_{eff})^2 + m^2}. \tag{3.27}$$

The equation above defines a coordinate transformation. It needs to be considered that the differentials of the momenta are affected. Therefore, the Jacobian $|det\frac{d^3p_i}{d^3p_f}|$ is computed. The 3-dimensional momentum derivative can be reduced to a 1-dimensional problem by transforming to spherical coordinates:

$$\frac{d^3p_i}{d^3p_f} = \frac{sin(\phi)p_i^2 d\phi d\theta dp_i}{sin(\phi)p_f^2 d\phi d\theta dp_i} = \frac{4\pi p_i^2 dp_i}{4\pi p_f^2 dp_f} = \frac{p_i^2 dp_i}{p_f^2 dp_f}. \tag{3.28}$$

The derivatives evaluates by applying the chain rule:

$$\frac{dp_i}{dp_f} = \frac{dp_i}{dE_i}(\frac{dE_i}{dE_f}\frac{dE_f}{dp_f} + \frac{dE_i}{dV_{eff}}\frac{dV_{eff}}{dp_f}). \tag{3.29}$$

For the static part, as it would be the case for a potential that is independent of time, one yield:

$$\frac{dp_i}{dE_f}\frac{dE_i}{dp_f} = \frac{E_i}{p_i}\frac{E_f}{p_f} = \frac{E_f \mp V_{eff}\sqrt{(E_f \mp V_{eff})^2 - m^2}}{E_f\sqrt{E_f^2 - m^2}}. \tag{3.30}$$

The dependence of V_{eff} from the pion energy leads to an additional dynamical part of the derivative:

$$\frac{dV_{eff}}{dp_f} = \mp\frac{2}{\sqrt{\pi}}\frac{V_c m_p}{m_\pi T_p}xe^{-x^2}. \tag{3.31}$$

Combining the obtained derivatives parts and inserting them into equation (3.28) results in the final effective Jacobian of the employed coordinate transformation:

$$J \cdot J_{eff} = \frac{E_f \mp V_{eff}\sqrt{(E_f \mp V_{eff})^2 - m^2}}{E_F\sqrt{E_f^2 - m^2}}(1 \mp \frac{2}{\sqrt{\pi}}\frac{V_c m_p}{m_\pi T_p}xe^{-x^2}). \tag{3.32}$$

Accordingly, the transformed coulomb modified Boltzmann function is given as:

$$\frac{1}{m_t^2}\frac{d^2N}{dm_t dy} = A(fe^{-(E_f \mp V_{eff})/T_1} + (f-1)e^{-(E_f \mp V_{eff})/T_2})J \cdot J_{eff}. \tag{3.33}$$

This formula is now adjusted to the measured transverse spectra with A, f, T_1 T_2 and V_c as free parameters in order to extract the Coulomb potential. Since charged pions only differ in their charges, it is assumed that they both freeze-out at common temperature and feel the same magnitude of the Coulomb potential.

2.2. Coulomb Modified Fit Procedure on the Transverse Spectra

As mentioned, it is assumed in the following that for both charges, the Coulomb potential V_c has the same magnitude since charged pions only differ in their polarity. This implies that they both freeze out at common temperatures. Thus, the transverse spectra of both polarities are fitted simultaneously with common V_c and common inverse slope parameters. For this purpose, the differential transverse mass spectra of π^- and π^+ mesons are combined into a 2D histogram where the x-axis corresponds to the reduced transverse mass $m_t - m_0$ and the second axis to the polarity. As there are only two possible polarities, the later axis is only divided into two bins. The 2-dimensional-function that is adjusted depends on the transverse mass and the polarity z:

$$\frac{d^2N}{dm_t dy}(m_t, z) = \begin{cases} A_- \cdot m_t^2 (f_- e^{-(E_f+V_{eff})/T_1} + (f_- - 1)e^{-(E_f+V_{eff})/T_2}) J J_{eff} & \text{for z=-1} \\ A_+ \cdot m_t^2 (f_- e^{-(E_f-V_{eff})/T_1} + (f_+ - 1)e^{-(E_f-V_{eff})/T_2}) J J_{eff} & \text{for z=+1} \end{cases} \tag{3.34}$$

A_+, A_- are the normalizing factors of the π^- (π^+). V_{eff} represents the effective Coulomb potential according to equation (3.25). It is a function of the final pion energy E_f. The factor $J \cdot J_{eff}$ corresponds to the Jacobian, see equation (3.25). T_1 and T_2 are the inverse slope parameters. f_-, f_+ account for the fraction between the different slopes. Whereby E_f depends on the transverse mass and the rapidity in the centre of mass system:

$$E_f = m_t \cdot cosh(y_{cm}). \tag{3.35}$$

The fitting is performed using the χ^2-minimizing algorithm, implemented in ROOT. Without appropriate starting values for the parameters, one usually does not yield a converging fit. For this purpose, starting points are set. First, the standard Double-Boltzmann fit is performed separately for the π^- and π^+ spectra. Fitting is carried out in two steps. Initially, two single Boltzmann functions are adjusted to data. One for the data range in the interval from 0 to 300 MeV/c^2 and second in the range from 300 to 800 MeV/c^2. The resulting parameters are set as initial values for the Double-Boltzmann fit. The obtained parameters are subsequently taken as starting points for the parameters $A-$, $A+$, $f+$, $f-$, T_1 and T_2 of the 2D-fit function. Furthermore, to decrease the step size per iteration, the parameter error is initially set to 5 %. For the inverse slope parameters, limits in the range from ± 20 MeV are applied. Also, the allowed range of the Coulomb potential is at first limited to $0 - 20$ MeV. The fit is then carried out within the region of 25 to 650 MeV/c^2 on the reduced transverse mass spectra $m_t - m_0$. After that, the χ^2 adjusting-algorithm is performed once again, but now with an open range for V_c, T_1 and T_2. For the inverse slope parameters T_p of the protons at mid-rapidity, the numbers shown in table (3.6), are used. They are taken from the proton analysis of the same experiment [55].

Centrality	0-10 %	10-20 %	20-30 %	30-40 %	40-50 %
T_p [MeV]	144	132	124	117	113

Table 3.6: Used centrality-dependent inverse slope parameters of protons at mid-rapidity. Values are taken from [55].

For all analysed mid-rapidity spectra, as well as for the majority of the forward and backward spectra, this approach leads to a converged fit. However, for a few for/backward bins still, convergence is not feasible. In such cases, the starting points are taken from the neighbouring rapidity bin, and tight parameter constraints of $\pm 7\%$ around them are applied.
To have an estimation of the systematics induced by the specific representation of the transverse kinematics, 2D Coulomb-fitting is also performed for the transverse momentum spectra representation. Using the relation between transverse mass and transverse momentum:

$$m_t = \sqrt{m^2 + p_t^2}. \tag{3.36}$$

(Where is $m_0 = 139.6\ MeV/c^2$ the rest mass of a charged pion), one finds for the 2D-Coulomb-fit on the $\frac{d^2N}{dp_t dy}$ spectra:

$$\frac{d^2N}{dp_t dy}(p_t, z) = \begin{cases} A_- p_t m_t (f_- e^{-(E_f + V_{eff})/T_1} + (f_- - 1) e^{-(E_f + V_{eff})/T_2}) JJ_{eff} & \text{for z=-1} \\ A_+ p_t m_t (f_- e^{-(E_f - V_{eff})/T_1} + (f_+ - 1) e^{-(E_f - V_{eff})/T_2}) JJ_{eff} & \text{for z=+1} \end{cases} \tag{3.37}$$

The fitting of the p_t-spectra is conducted in a similar way as for the $m_t - m_0$ spectra: At first, standard double Boltzmann functions are fitted. Then the adjusted parameters are taken as initial values for the 2D fit function. In this case, the fitting range is set to $87 - 777\ MeV/c$, which corresponds to the converted range used on the reduced transverse mass spectra.
The resulting fits, including their parameters, are shown in figure (3.29) (m_t) and (3.31) (p_t).

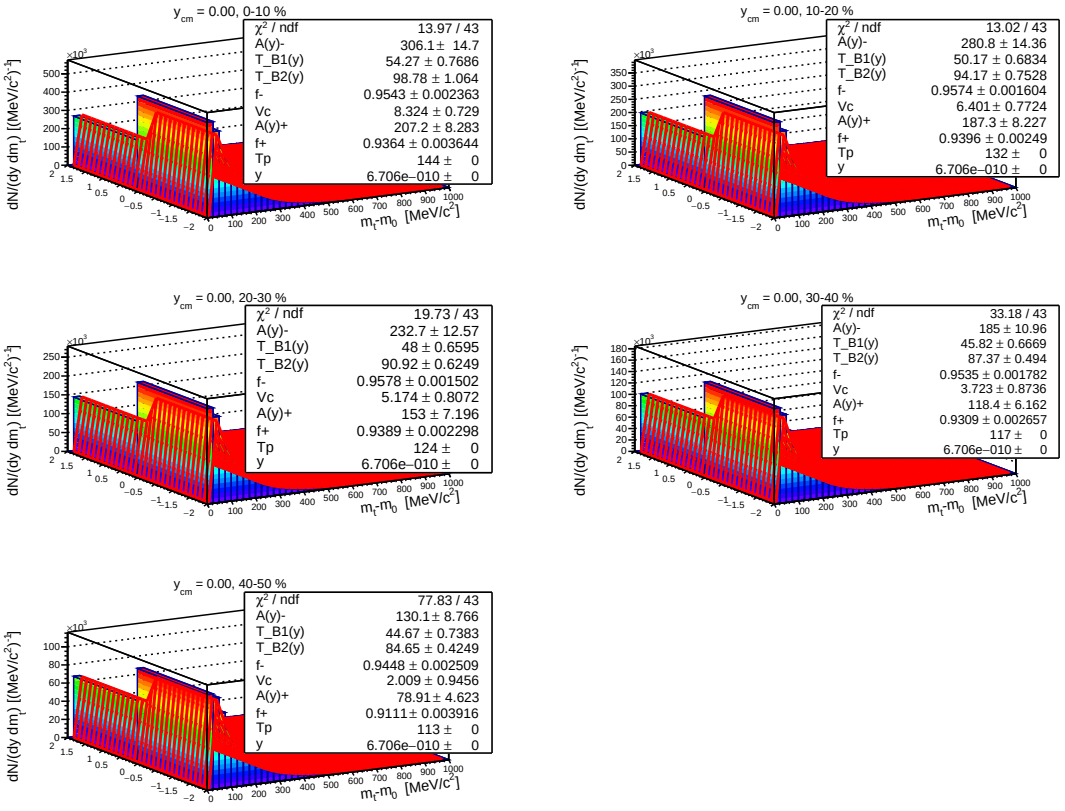

Figure 3.29: Transverse mass spectra $dN/(dyd(m_t - m_0))$ at mid-rapidity for both charges, combined in a histogram exhibiting a third axis that corresponds to the polarity: The bin with the centre of -1 contains the π^- spectrum. In the $+1$-bin, the π^+ spectrum is filled. Fitting has been conducted for all of the five analysed centrality classes. Denoted are the adjusted parameters, including the Coulomb potential, of the fitted Coulomb-Boltzmann functions.

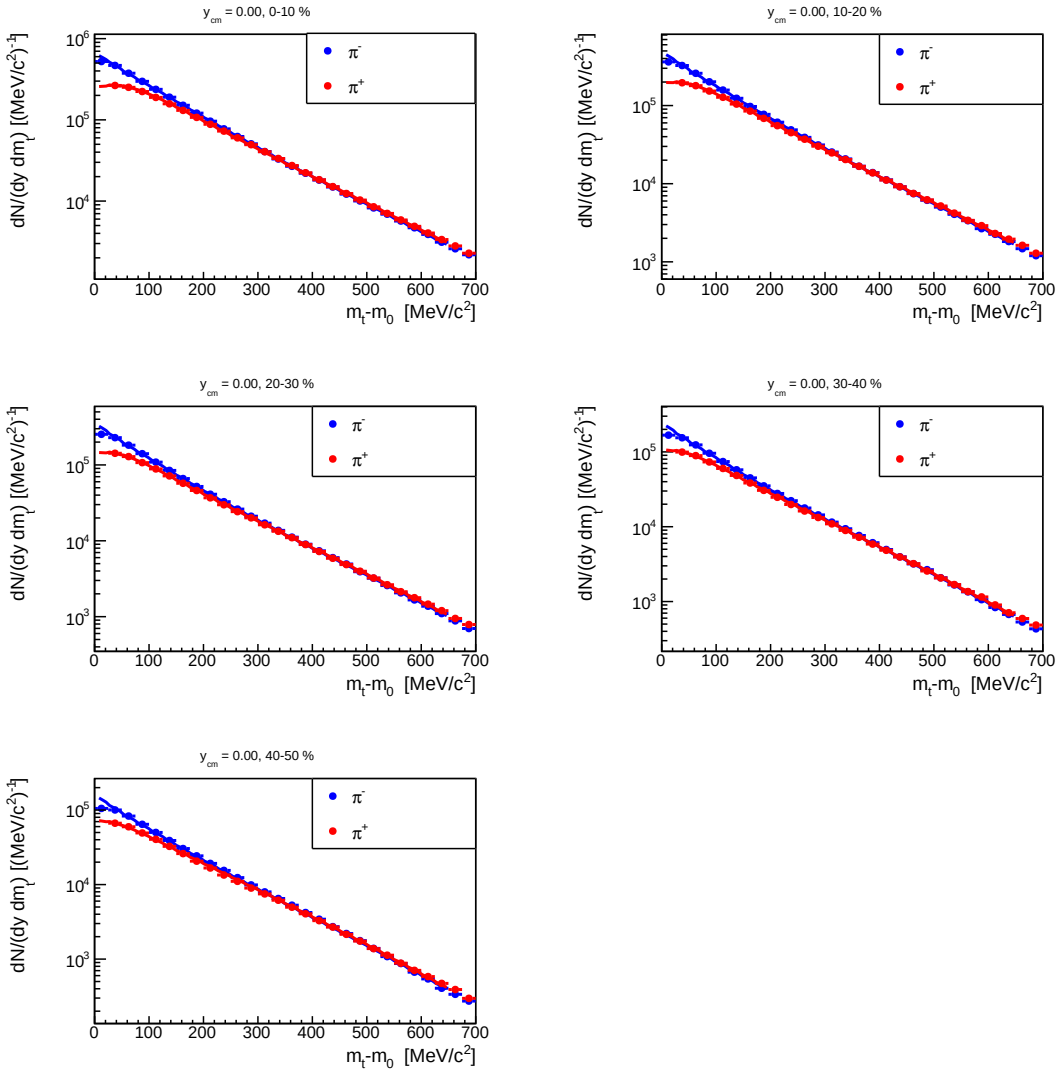

Figure 3.30: Transverse mass spectra $dN/(dyd(m_t - m_0))$ for both charges with fitted Coulomb-Boltzmann functions (3.37) in 1-dimensional display.

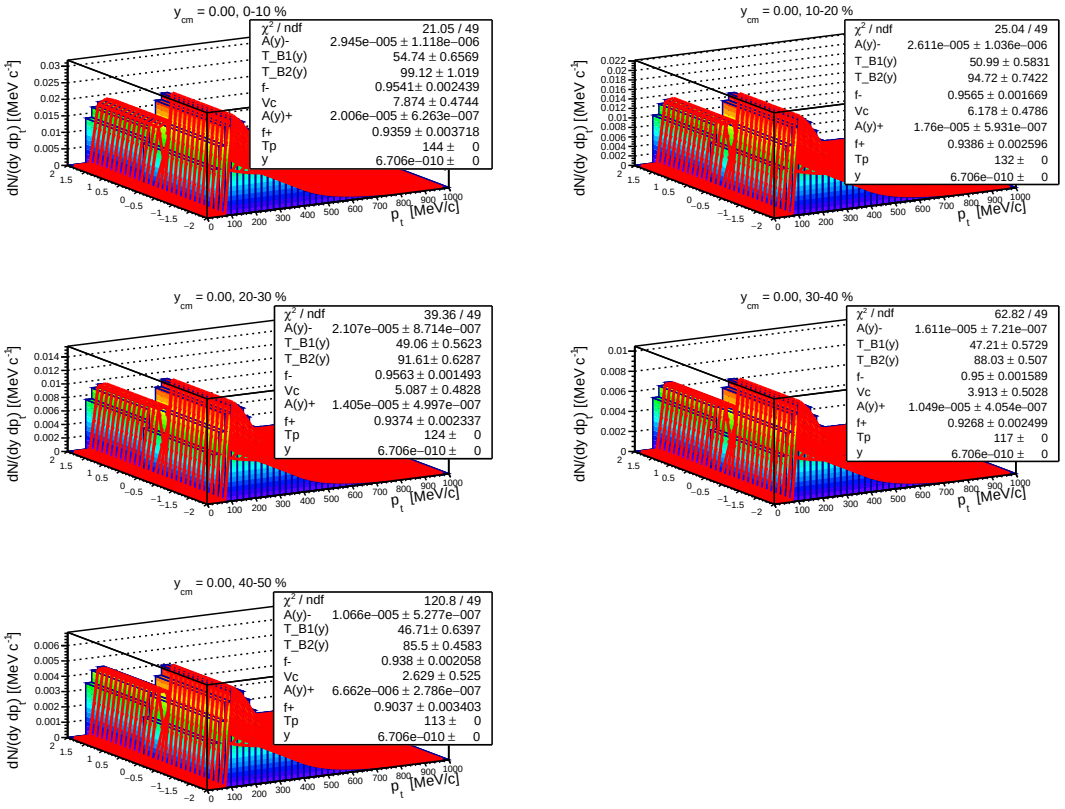

Figure 3.31: Transverse momentum spectra $dN/(dydp_t)$ at mid-rapidity for both charges, combined in a histogram exhibiting a third axis that corresponds to the polarity: The bin with the centre of -1 contains the π^- spectrum. In the $+1$-bin, the π^+ spectrum is filled. Fitting has been conducted for all of the five analysed centrality classes. Denoted are the adjusted parameters, including the Coulomb potential, of the fitted Coulomb-Boltzmann functions.

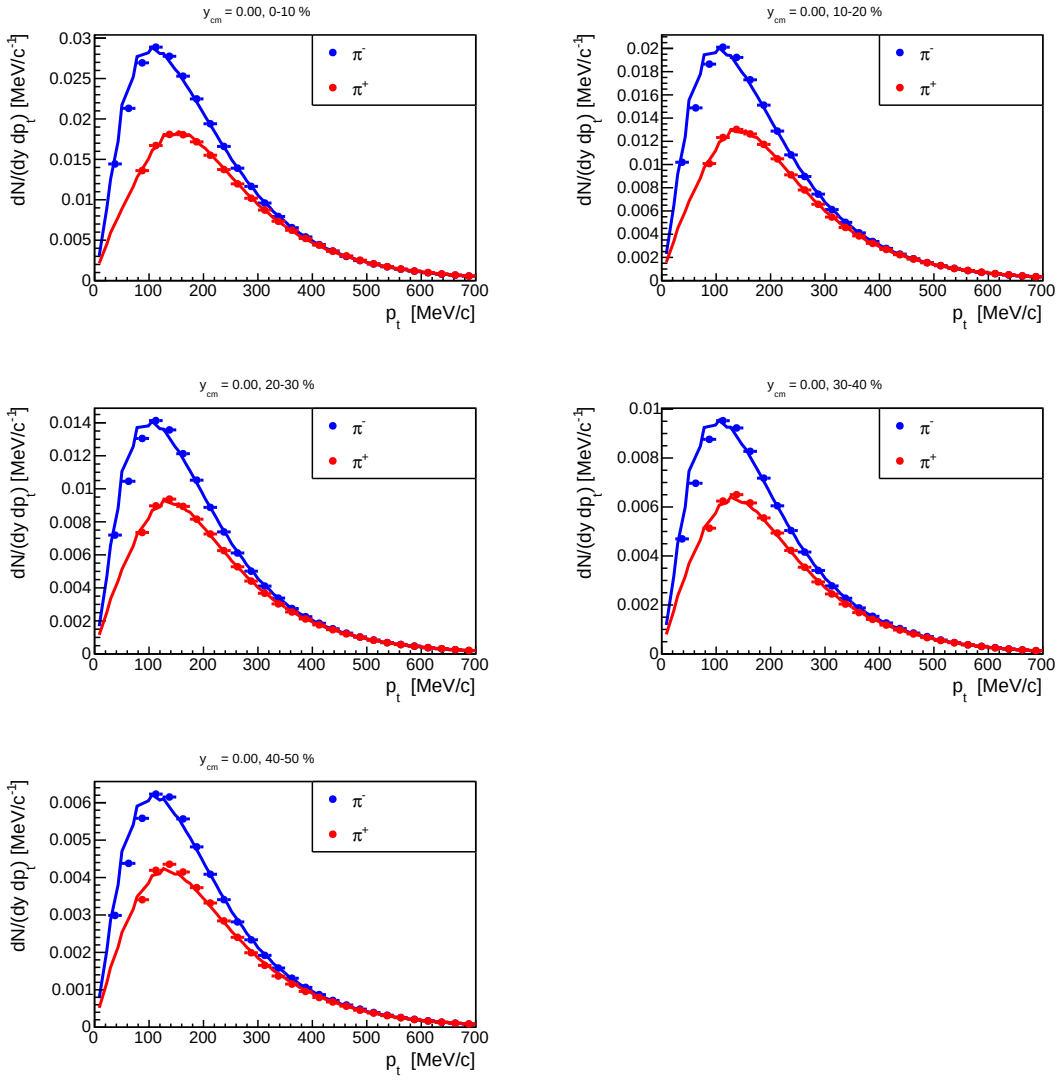

Figure 3.32: Transverse momentum spectra $dN/(dydp_t)$ for both charges with fitted Coulomb-Boltzmann functions (3.37) in 1-dimensional display.

2.3. Results

2.3.1. Coulomb Potential at Mid-Rapidity

The subsequent figure (3.33) displays the extracted Coulomb potential V_c at mid-rapidity as a function of the average number of participating nucleons $< A_{part} >$. Plotted are both the results of transverse momentum and transverse mass spectra analysis. The errors shown correspond to the statistical ones.

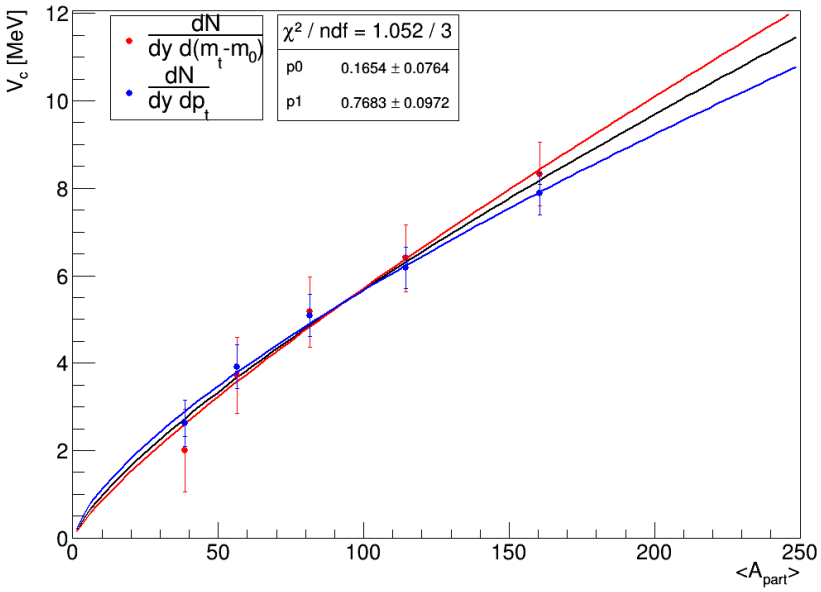

Figure 3.33: Extracted Coulomb potential from p_t and m_t based analysis at mid-rapidity as a function of the number of participating nucleons. The plotted functions correspond to fit of the scaling function, see equation (3.38).

The highest Coulomb potential $V_c = 8.1 \pm 0.5\ MeV$ ($V_c = 8.3 \pm 0.5\ MeV$ (m_t), $V_c = 7.8 \pm 0.5\ MeV$ (p_t)) is extracted for the most central collisions with an average number of participating nucleon of $< A_{part} >= 150 \pm 6.9$. The potential decrease towards peripheral collisions. The lowest potential is extracted for the centrality class 40-50 % $V_c = 2.3 \pm 0.5\ MeV$ ($V_c = 2.0 \pm 0.7\ MeV$ (mt), $V_c = 2.6 \pm 0.6\ MeV$ (pt)). The systematic differences are in the order of 4 % for the most central events and 26 % in the most considered peripheral events. To investigate the scaling in terms of A_{part} in detail, the data is fitted with the function:

$$V_c = C \cdot < A_{part} >^{\alpha} . \tag{3.38}$$

Whereby α is a parameter that characterizes the scaling. C represents a normalizing factor. For both transverse analysis variants the scaling is weaker than for a pure proportional α: $\alpha = 0.82 \pm 0.2$ (m_t) and $\alpha = 0.70 \pm 0.1$ (p_t). The scaling parameter resulting from the average fit is $\alpha = 0.77 \pm 0.1$. Potential physical interpretations for the findings are discussed in section (1.1).

2.3.2. Effective Radius and Baryon Density

The extracted Coulomb potential allows for an estimation of the system size in the coordinate space of the reaction. V_c can be linked to an effective radius if one assumes that the origin of the potential can be described by a homogeneously charged sphere. For such a simple model, the Coulomb potential can be easily derived due to the spherical

symmetry. One finds [26]:

$$V_c(r) = \begin{cases} \frac{3}{2}\frac{Ze^2}{r_{eff}}(1 - \frac{1}{3}(\frac{r}{r_{eff}})^2) & \text{for} r < r_{eff} \\ \frac{Ze^2}{r} & \text{for} r > r_{eff} \end{cases} \tag{3.39}$$

r is the distance from the centre of the assumed sphere. r_{eff} corresponds to sphere's radius, Z to the number of protons. As the fireball expansion is a dynamic scenario it is assumed that the extracted Coulomb potential corresponds to a mean potential $< V_c >$. Using equation (3.39) one finds:

$$< V_c >= \frac{\int d^3r\Theta(r - r_{eff})V_c(r)}{\int d^3r\Theta(r - r_{eff})} = \frac{6}{5}e^2\frac{Z_{part}}{r_{eff}} \tag{3.40}$$

The number of participating nucleons Z_{part} is needed in order to obtain the number of protons Z. It is obtained by multiplying the fractions of protons for silver $Z_{Ag}/A_{Ag} = 0.435$ with the reconstructed number of participating nucleons $< A_{part} >$:

$$Z_{part} = \frac{A_{part}Z_{Ag}}{A_{Ag}} \tag{3.41}$$

Deriving equation (3.40) with respect to the effective radius r_{eff}, results in:

$$r_{eff} = \frac{6}{5}e^2\frac{Z_{part}}{< V_c >} \tag{3.42}$$

The calculated effective radii as a function of $< A_{part} >$ are displayed in figure (3.34). The errors shown result from applying Gaussian error propagation of the statistical error for equation (3.42).

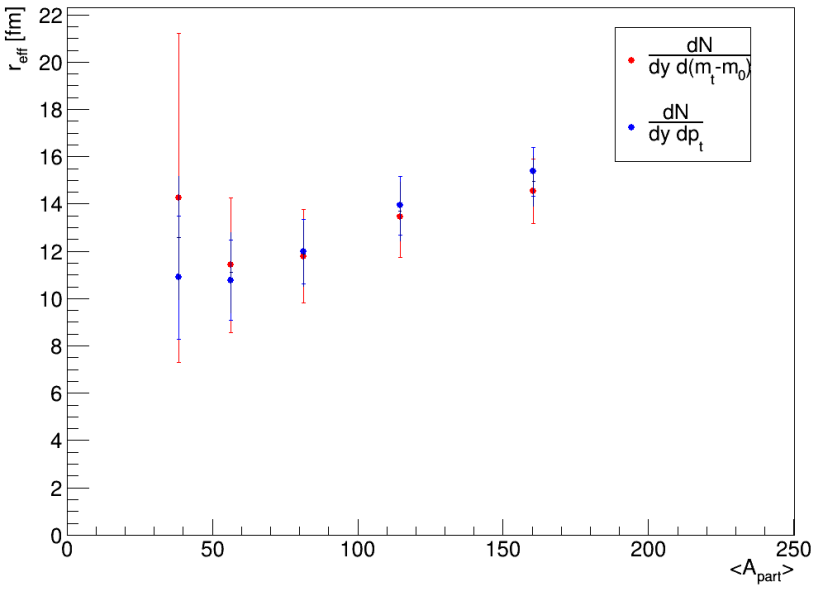

Figure 3.34: Calculated effective radius as a function of the number of participating nucleons, assuming a uniformly charged sphere. Red points correspond to the m_t based analysis and blue ones to the p_t analysis. The errors result from Gaussian propagation of the statistical errors within equation (3.42).

Once the effective radius is known, also an estimation of the baryon density is feasible. ρ_B is obtained by dividing the number participating nucleons $< A_{part} >$ by the volume V, which corresponds, as introduced, the one of a sphere:

$$\rho_B = \frac{< A_{part} >}{\frac{4}{3}\pi r_{eff}^3}. \tag{3.43}$$

The obtained densities are displayed in figure (3.35). The rather wide error bars result from Gaussian error propagation.

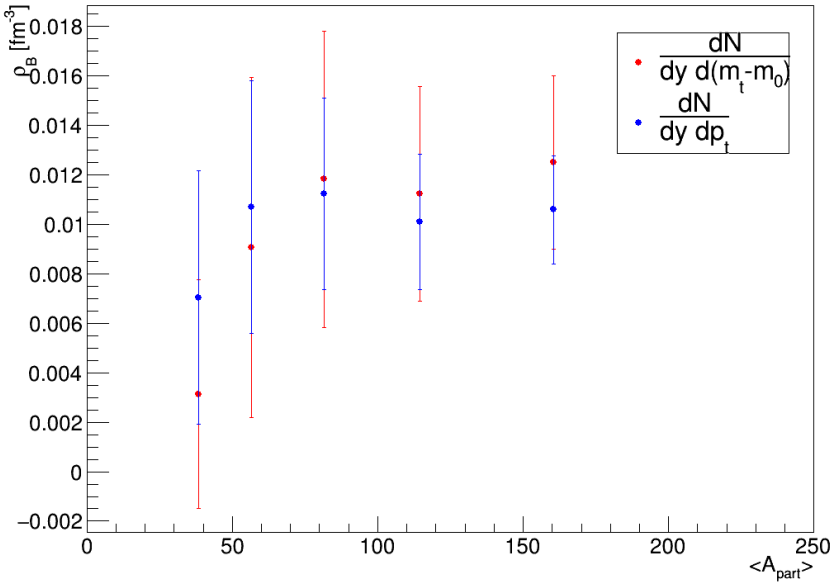

Figure 3.35: Calculated baryon density as a function of the number of participating nucleons. Red points correspond to the m_t based analysis and the blue ones to the p_t analysis. Errors result from Gaussian propagation of the statistical errors within equation 3.43.

For the most central collision a destiny of $\rho_B = (0.012 \pm 0.004)\ fm^{-3}$ (m_t) and $\rho_B = (0.010 \pm 0.003)\ fm^{-3}$ (p_t) is estimated. The error is followed by propagating the statistical errors of V_c in the cosponsoring equation. Due to the wide error range in the order of up to 30 %, a clear statement about the functional behaviour is not feasible.

2.3.3. Rapidity Dependence

The Coulomb-Modified-Boltzmann model is also tested for fitting the transverse spectra of the forward and backward rapidity bins. Tough, it is disputable to use this rather simple model since we need to make some assumptions. On the one hand, we assume that the scaling of the inverse slope parameters follows a $\frac{1}{cosh(y_{cm})}$ parametrization as predicted by the statistical model. The same holds for the inverse slope parameters of the protons. Also, the description of the effective potential is shakier for the spectra beyond mid-rapidity as an isotropic description is used, but as it will seen in flow analysis, the

emission of charged pions is not exactly isotropic. Fitting of the forward and backward spectra is performed as described in section (2.2). Though, adjusting the Coulomb-modified function here is more difficult to conduct. In particular, for the most outer forward and backward spectra, data points very close to zero p_t/m_t are not available due to limited acceptance and efficiency. However, in this region, the information of the spectra' shape is crucial for extracting the Coulomb potential. The more the transverse spectra are distant from mid-rapidity, the more it is necessary to demand an upper limit for the Coulomb potential. Otherwise, the fit function would overshoot the data resulting in a too high yield. Moreover, for high rapidity, the influence of the neglected spectators could play a major role as indicated in [59]. Figure (3.36) and (3.36) present the extracted parameters and adjusted functions of transverse momentum and transverse mass representation.

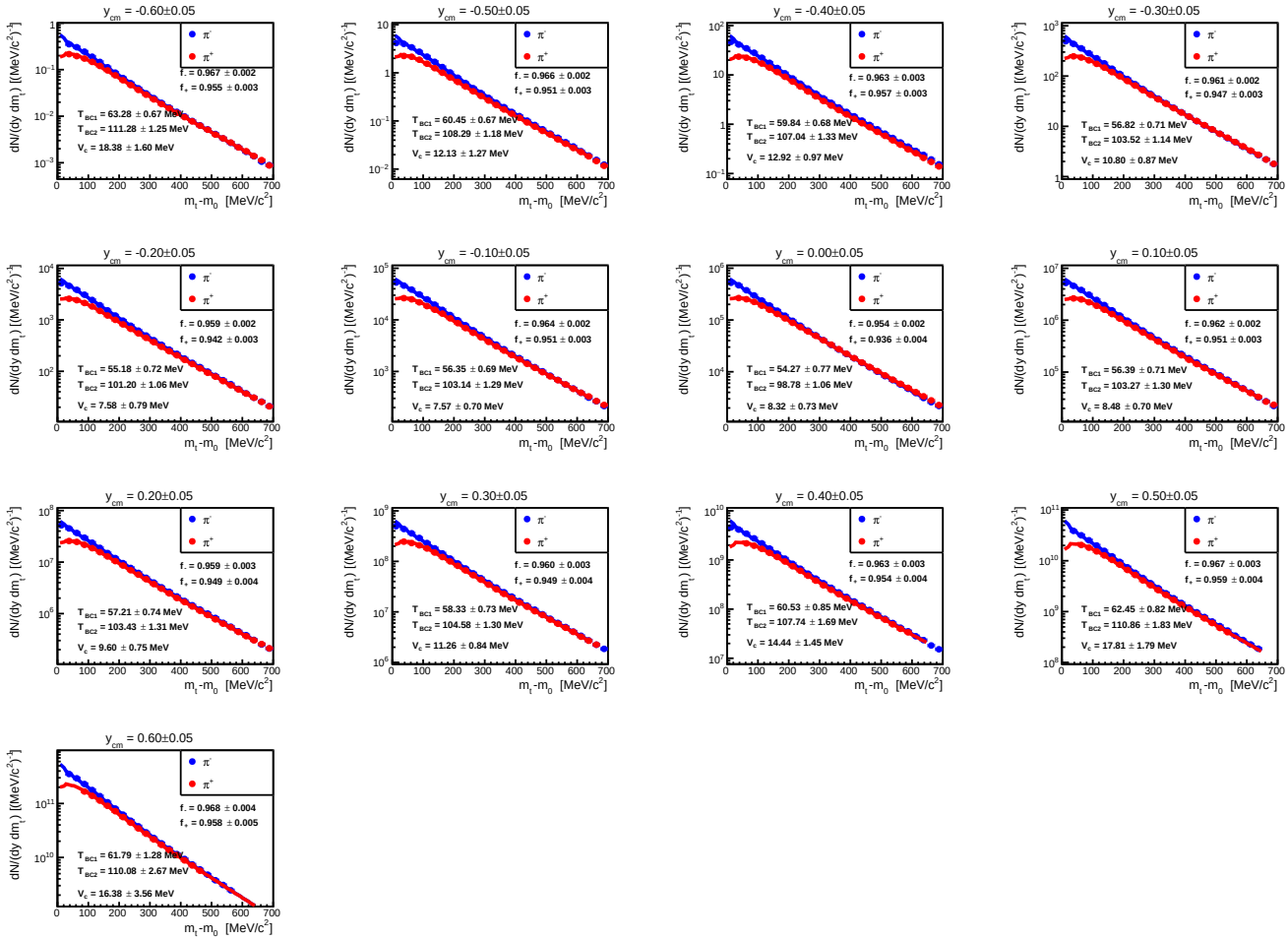

Figure 3.36: Transverse mass spectra $dN/(dydm_t)$ for the forward and backward rapidity bins (0-10 % centrality) for both charges. Denoted are the adjusted parameters of the fitted Coulomb-Boltzmann functions, including the Coulomb potential.

Figure (3.37) displays the ratio of the fit prediction to the data value as a function of $m_t - m_0$ for all analysed rapidity bins. The deviations are low for transverse masses between 100 and 600 MeV/c^2, below 2 to 3 %. For low m_t the differences are smaller

than 5 % for $-0.45 < y_{cm} < 0.45$. Opposed to the standard Boltzmann function, this holds for both polarities. With the standard approach, the π^+ were in general overshot by the function.

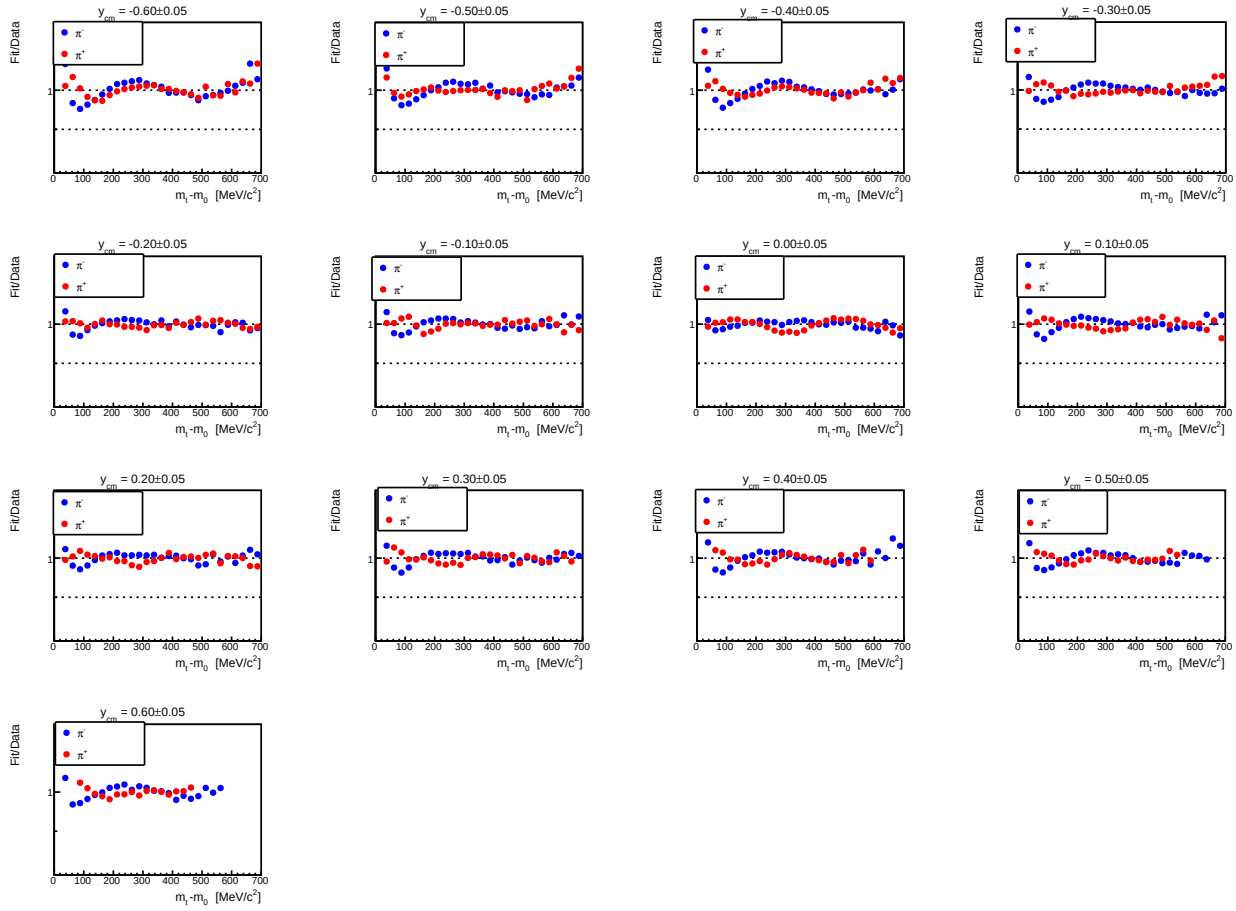

Figure 3.37: Ratio of the Coulomb fit prediction to the data value as a function of $m_t - m_0$ for the analysed rapidity bins, for 0-10 % centrality.

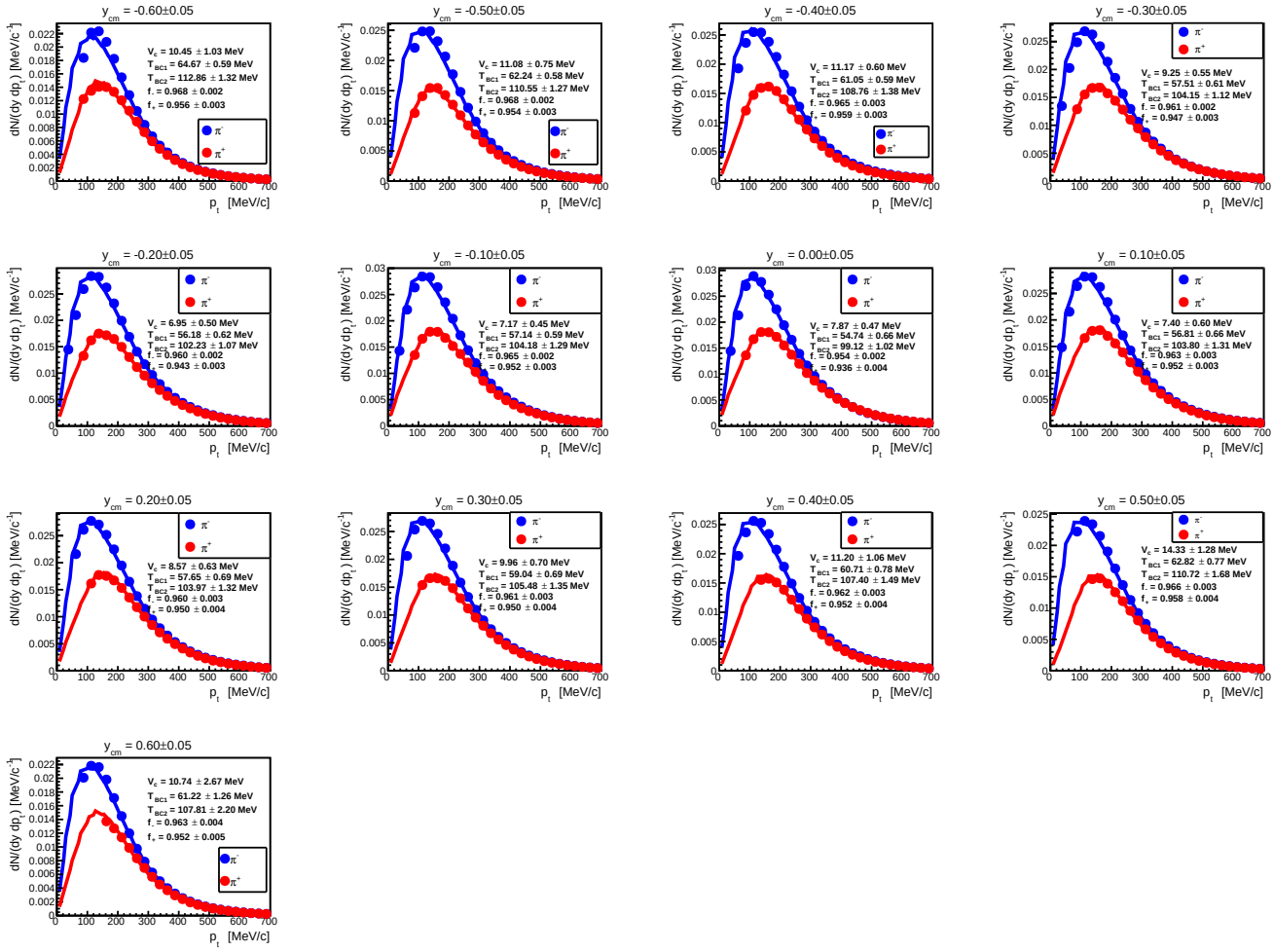

Figure 3.38: Transverse momentum spectra $dN/(dydp_t)$ for the forward and backward rapidity bins (0-10 % centrality) for both charges. Denoted are the adjusted parameters of the fitted Coulomb-Boltzmann functions, including the Coulomb potential.

The extracted rapidity-dependent Coulomb potentials from p_t (blue) and m_t (red) based spectra are displayed in figure (3.39). An increase of the potential with rising forward and backward rapidity is observed throughout all centrality classes. The shape reminds of a parabola, but it has to be considered that the error bars and the differences between p_t and m_t analysis are quite large to allow for a statement about the functional behaviour. As already seen at mid-rapidity, V_c decreases towards more peripheral events. For the highest rapidity bins ($y_{cm} > 0.4$) statistical errors over 50 % occur.

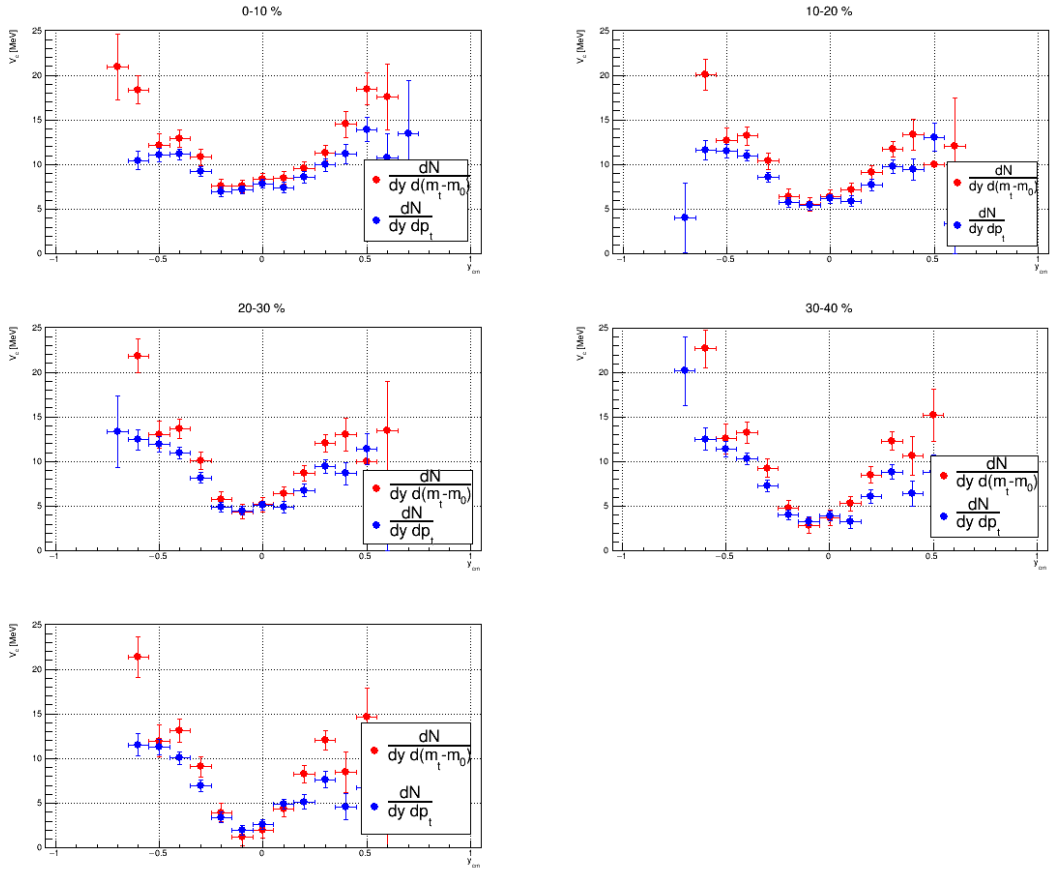

Figure 3.39: Extracted Coulomb potential as a function of rapidity in the centre of mass system for the 5 centrality classes in the range of 0-50 %. Blue points represent the potential from transverse momentum analysis. Red points are from the transverse reduced mass spectra analysis.

2.3.4. Extrapolation using the Coulomb-Boltzmann Function

The findings in the last subsection show that the extraction of the Coulomb potential is shaky for the spectra out of mid-rapidity. However, the Coulomb-Boltzmann function out of mid-rapidity could still be of interest when it comes to the extrapolation to zero p_t because they provide a more realistic description of the measured data. The resulting rapidity distribution can be seen in figure (3.40). The integration is performed as proceeded with the standard Boltzmann function: In the uncovered region, the fitted function is integrated. Otherwise, the measured data points are summed. Comparing with the rapidity distribution obtained by using the standard Boltzmann extrapolation, shown in figure (3.25), reveals no major difference for the π^- mesons around mid-rapidity, the differences are less than 1 %. The differences increase to 5 % towards outer rapidity bins. In the case of the positively charged pions, the differences are larger, also around mid-rapidity. The yield, in general, is by 3-5 % smaller than with the standard approach. Furthermore, with Coulomb inclusive extrapolation for the π^+ meson, more data points coincide slightly better with the reflected ones. However, one should keep in mind that the most forward rapidity bin had to be omitted due to difficulties conducting the Coulomb modified fitting. Here, for the π^+ mesons, irregularities for the centrality classes 30-40 %

and 40-50 % occur for $y_{cm} > 0.55$. The bins fell out of the line, delivering too high values.

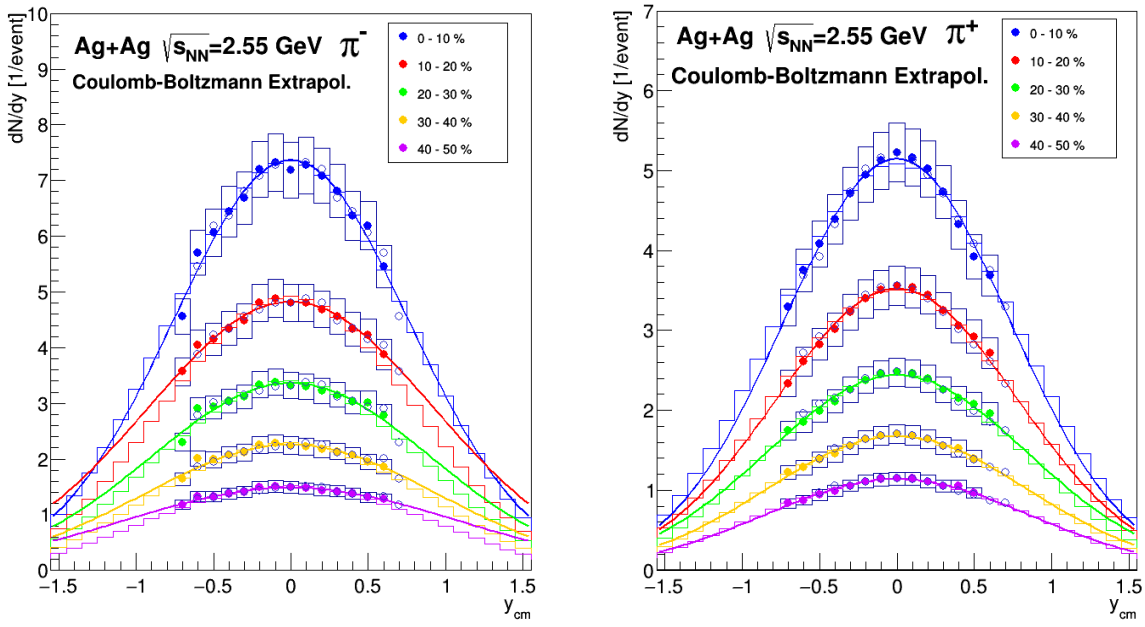

Figure 3.40: dN/dy distributions for each of the 5 analysed centrality classes up to 50 % centrality, obtained by integrating the transverse spectra, now using the Coulomb-Double-Boltzmann function for extrapolation. Plotted error bars correspond to the systematic errors. The unfilled points are the reflected data points. Drawn are also the scaled UrQMD distributions later used for the 4π yield determination.

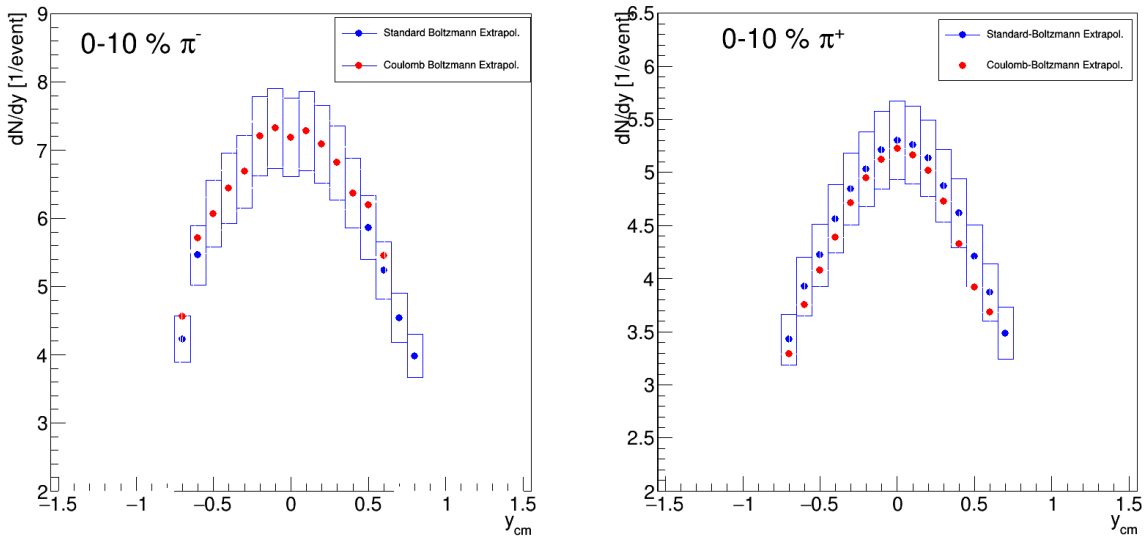

Figure 3.41: Comparison between the dN/dy spectra resulting from the standard Boltzmann (Blue points) and Coulomb-Boltzmann (Red points) transverse extrapolation. Especially for the π^+, differences are observed.

In order to see how those slightly different dN/dy distributions based on Coulomb extrapolation change the 4π yield, the procedure of longitudinal extrapolation is performed as usual by scaling the UrQMD distributions. The obtained yields are denoted in table (3.7) and are compared to yields from the standard Boltzmann extrapolation.

C	$M(\pi^-)$ (Coulomb)	$M(\pi^+)$ (Coulomb)	$M(\pi^-)$ (Boltzmann)	$M(\pi^+)$ (Boltzmann)
$0-10\%$	$13.9 \pm 1.1 \pm 0.2$	$9.6 \pm 0.7 \pm 0.2$	$13.7 \pm 1.1 \pm 0.5$	$9.9 \pm 0.7 \pm 0.2$
$10-20\%$	$9.6 \pm 0.8 \pm 0.9$	$6.8 \pm 0.5 \pm 0.1$	$9.5 \pm 0.8 \pm 0.3$	$7.0 \pm 0.5 \pm 0.4$
$20-30\%$	$6.8 \pm 0.6 \pm 0.8$	$4.8 \pm 0.4 \pm 0.3$	$6.8 \pm 0.6 \pm 0.4$	$5.0 \pm 0.4 \pm 0.6$
$30-40\%$	$4.7 \pm 0.4 \pm 0.7$	$3.4 \pm 0.3 \pm 0.2$	$4.7 \pm 0.4 \pm 0.4$	$3.5 \pm 0.3 \pm 0.6$
$40-50\%$	$3.2 \pm 0.3 \pm 0.6$	$2.3 \pm 0.2 \pm 0.1$	$3.2 \pm 0.3 \pm 0.4$	$2.4 \pm 0.2 \pm 0.4$

Table 3.7: Centrality-dependent 4π production yields. The extrapolation in the transverse direction is now based on the Coulomb-Boltzmann functions. For extrapolation into the full rapidity scope, the scaled UrQMD distributions have been used. The first error corresponds to the systematics error. The second error indicates the difference between Gaussian and UrQMD based extrapolation.

A more sensitive observable to see differences is to look at the ratio between the π^- and π^+ yield. The ratios are shown in table (3.8). Due to the slightly lower π^+ yield, the ratio increases. The ratio ranges from 1.38 to 1.45 with Coulomb based transverse extrapolation.

C	$M(\pi^-)/M(\pi^+)$ (Coulomb)	$M(\pi^-)/M(\pi^+)$ (Boltzmann)
$0-10\%$	1.45 ± 0.12	1.38 ± 0.12
$10-20\%$	1.41 ± 0.24	1.36 ± 0.12
$20-30\%$	1.42 ± 0.20	1.36 ± 0.14
$30-40\%$	1.38 ± 0.22	1.34 ± 0.17
$40-50\%$	1.39 ± 0.32	1.33 ± 0.20

Table 3.8: Ratio of π^-/π^+ for the 4π yields based on Standard-Boltzmann (right) and the Coulomb-Boltzmann (left) transverse extrapolation.

3. Anisotropic Flow Analysis of Charged Pions

This chapter investigates azimuthal flow anisotropies in the emission of charged pions. At first, the basic analysis principles based on Fourier decomposition and the applied method of reconstructing the event plane are established in section (3.3). For the reconstruction of flow, two corrections need to be implemented. The so-called Ollitrault correction accounts for limited resolution of the event plane angle, see section (3.4). The second corrects for the detector inefficiencies, which are dependent on the track multiplicity causing occupancy effects. This especially impacts the behaviour of directed flow. In section (3.7), two possible systematic variations are examined. Finally, in section (3.8.1), the obtained directed, elliptic and triangular flow harmonics are presented

multi-differentially as a function of transverse momentum p_t and centre of mass rapidity y_{cm} for various collision centralities.

3.1. Data Selection

The event and track selection criteria are the same as in the charged pion yield analysis, discussed in section (1.2.2) and (1.2.2): The charged pion candidates are identified by the 2σ-PID-graphical selection on the β vs. momentum spectra, discussed in section (3). For positively charged pions, additionally the 1.5σ-MDC-dE/dx-selections is applied as described in section (1.3.2) in order to suppress the contamination caused by protons. The only difference to the yield analysis is the inclusion of all sectors for the π^- mesons; otherwise, asymmetries occur in the angular distributions.

3.2. Analysis Procedure for Flow Anisotropies

The aim is to quantify the anisotropic emissions within the plane perpendicular to the beam axis. Hence, the observable to consider is the azimuthal emission angle ϕ of the pions relative to the event plane angle Ψ_{EP}:

$$\phi - \Psi_{EP}. \tag{3.44}$$

The event plane angle Ψ_{EP} is understood as an approximation of the reaction plane angle Ψ_{RP}. Due to fluctuations and finite resolutions within the experimental measurement, they are not necessarily equal. An useful tool to quantify angular dependencies is to perform a Fourier decomposition: The observed angular distribution of $N(\phi - \Psi_{EP})$ is disentangled in regard to a linear superposition of cos- and sin-terms. Since, the particles are emitted symmetrically with respect to the event plane due to the collision symmetry, we expect the Fourier series to be a symmetric function around zero degree. Thus, the sin terms are neglected as the sin is a point-symmetric function. The Fourier series for anisotropic flow analysis therefore just reads as:

$$\frac{dN}{d(\phi - \Psi_{RP})} = A \cdot (1 + 2\sum_{n=0}^{\infty} v_n cos(n(\phi - \Psi_{RP}))). \tag{3.45}$$

The goal in Fourier decomposition is to determine the flow harmonics v_n. This is done by two different methods in this analysis. The terms of the Fourier series can be fitted to the distribution of $\phi - \Psi_{EP}$, whereby the coefficients v_n are free parameters supposed to be adjusted.
Another approach avoids the fitting procedure. The idea is to calculate the harmonics v_n directly by making use of the following: The Fourier series is mathematically considered a complete set of orthogonal functions. Therefore, each function (distribution) can be expressed by a linear combination of a basis. The basis are the cos terms of order n: $cos(n\phi)$. The coefficients therefore can be obtained by integrating over $cos(n\phi)$ times the normalised distribution:

$$v_n = \frac{\int_{-\pi}^{+\pi} \frac{dN}{d(\phi - \Psi_{RP})} cos(n(\phi - \Psi_{EP}))d(\phi - \Psi_{RP})}{\int_{-\pi}^{+\pi} \frac{dN}{d(\phi - \Psi_{RP})}}. \tag{3.46}$$

Integrating over a normalised distribution times a quantity is nothing else than the mean of that quantity. Hence, in the analysis of the data v_n is obtained by looping over all charged pion candidates in the analysed events and computing the value of $cos(n\phi)$, adding it up and afterwards divide by the number of totally analysed charged pions $N_{particles}$ and the number of selected events N_{events}:

$$v_n = \langle cos(n(\phi - \Psi_{RP}))\rangle = \frac{1}{N_{events}} \sum_{i=1}^{N_{events}} [\frac{1}{N_{particles(i)}} \sum_{k=1}^{N_{particles}} cos(n(\phi_{i,k} - \Psi_{RP}))]. \quad (3.47)$$

The required azimuthal emission angle ϕ is reconstructed based on the measured hit points in the two inner MDCs, as one wants to know the emission angle before the track deflection. The determination of the azimuthal angle of the event plane is more complicated. It can be derived from the information of the spectator hit pattern measured with the Forward-Wall. The applied event plane reconstruction method is depicted in the following subsection (3.3).
Within flow analysis, the so-called Ollitrault [49] correction accounts for fluctuations that are expected in the reconstruction method of the event plane. The details are described in section (3.4). Another circumstance that distorts the measurements are occupancy effects resulting from the fact that the detector's efficiency is not equally distributed in one event and based on the local track multiplicity. The correction is carried out by a fully data-driven approach, where a simple, functional dependence between multiplicity density and efficiency is assumed [22]. The related correction procedure is treated in section (3.6). Figure (3.42) summarises the general analysis process and its flow of data.

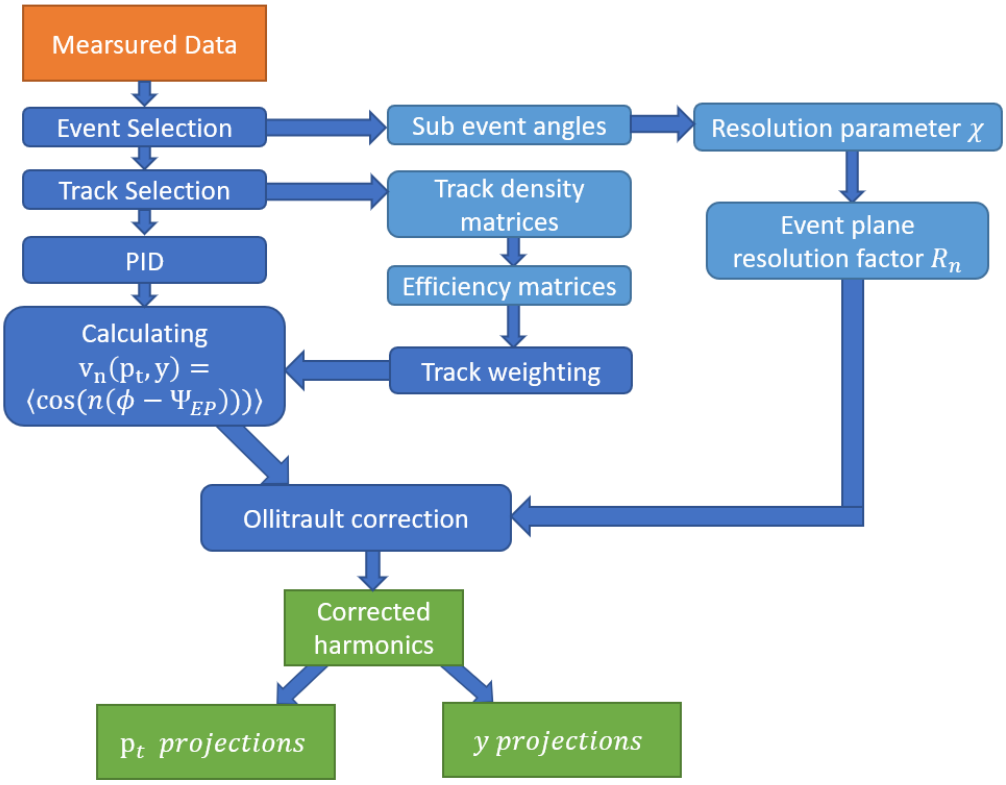

Figure 3.42: Schematic illustration of the flow analysis process. After the event (1.2.1) / track selection (1.2.2) and PID (1.3.1) the flow harmonics, corresponding to the coefficients of a Fourier series, are calculated. Two corrections are conducted: The Ollitrault correction [49] accounts for fluctuations which occur for the event plane. This correction is based on the sub-event method, see (3.4). Moreover, due to the detector's occupancy an angular and centrality-dependent efficiency is estimated based on the track density, see section (3.6). The determined efficiency matrices are used for weighting the tracks accordingly when calculating the flow coefficients.

3.3. Event Plane Reconstruction

As suggested, the orientation of the reaction plane, needed to calculate the azimuthal emission angle of the pions relative to this plane (3.44)), is not directly measurable. However, an approximated version of the reaction plane, called event plane, can be determined by making use of the following: The emission of the spectators of a collision is connected to the spatial anisotropy of the collision shape, determined by the reaction plane. Thus, the information of the reaction plane is expected to be encoded in the distribution pattern of the projectiles spectator hits measured by the Forward Wall hodoscope, see section (1.5).

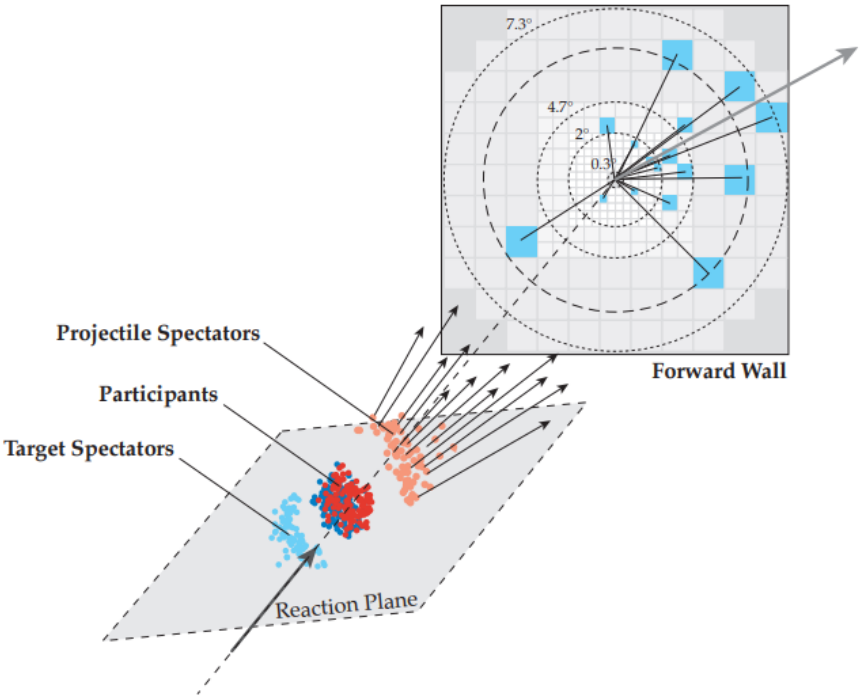

Figure 3.43: Depiction of the event plane reconstruction principle. The measured hit pattern of the projectile spectators on the Forward wall is related to a vector that lies approximately parallel to the reaction plane and is perpendicular to the beam axis. This so-called Q-vector is then used for the determination of the azimuthal angle of the event plane [22].

Figure (3.43) illustrates the principle: Due to the fixed-target set-up the projectile spectators are mainly emitted in the direction of the detectors. As a result, the spectator's azimuthal distribution pattern is projected onto the Forward Wall cells. The balance points Q_x and Q_y in the two directions define a so-called $\vec{Q}$-vector, which lies parallel to the azimuthal plane as well as approximately parallel to the reaction plane. Due to finite hit multiplicities, it does not correspond to the actual reaction plane. Instead, fluctuations of that vector around the reaction plane occur. The mean hit locations in the Forward Wall in the X- and Y- direction are $\langle X \rangle$ and $\langle Y \rangle$. The corresponding variances of the hit distributions are σ_X and σ_Y. In order to account for non-uniformities of the acceptance of the scintillators cells and variation of the beam spot, the hits are re-centred by shifting them to the mean and normalising to their variances [22]. The balance points in both directions are then obtained by summing over all cells, whereby each term is weighted by the factor w_i, which is proportional to the magnitude of deposited charge, linked to the measured signal in cell i.

$$Q_x = \frac{1}{N_{FW}} \sum_{i=0}^{N_{FW}} w_i \frac{X_{FW,i} - \langle X_{FW} \rangle}{\sigma_{X,FW}}. \tag{3.48}$$

$$Q_y = \frac{1}{N_{FW}} \sum_{i=0}^{N_{FW}} w_i \frac{Y_{FW,i} - \langle Y_{FW} \rangle}{\sigma_{Y,FW}}. \tag{3.49}$$

Additionally, a by day dependent flattening procedure is applied in order to remove residual differences. For details, see [22]. From trigonometry it follows that the angle of the event plane Ψ is given by

$$\Psi_{EP} = arctan(\frac{Q_x}{Q_y}). \tag{3.50}$$

The described method of the event plane reconstruction is implemented in the Hydra class HParticleEvetChahra (developed by [35]) and is used in this analysis to extract the azimuthal angle of the event plane. For some events, the reconstruction is not feasible, e.g. due to a limited number of measured spectator hits. In this case, the angle returned by the implemented function is -1. Such events are excluded from further analysis. Figure (3.44) shows the distribution of the reconstructed event plane angle Ψ for different centrality classes up to 50 % centrality.

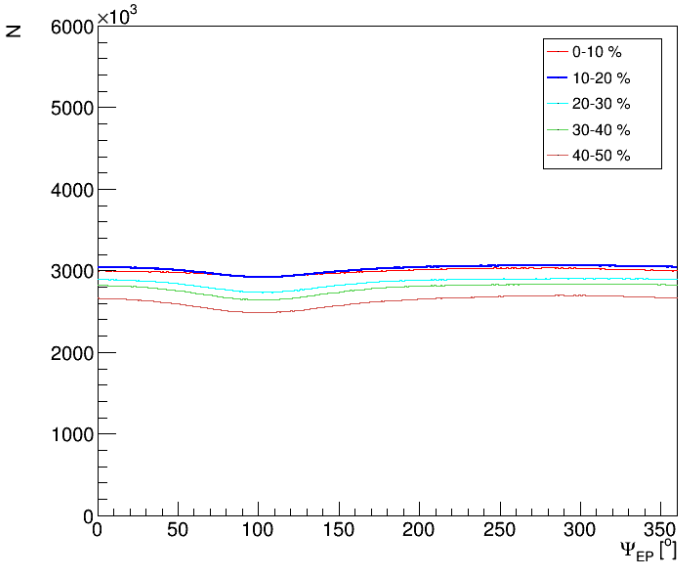

Figure 3.44: Distribution of the reconstructed event plane angle for the five considered centrality classes up to 50 %. The event plane angle is reconstructed by determining a $\vec{Q}$ vector which lies approximately parallel to the impact vector. For the extraction, the Hydra class HParticleEvetChahra [35] is used. It includes a re-centring procedure to account for non-uniformities as well as a by day dependent faltering procedure [35].

3.4. Ollitrault Correction

The reconstructed event plane only approximates the true reaction plane due to finite hit multiplicities in the forward wall horoscope. This cause the measured harmonic $v_{n,obs}$ in general to be smaller than real harmonic [49]. To correct for the fluctuations, at first, the resolution of the event plane angle needs to be estimated. This is done by following the approach in [22]. The event plane resolution factor R_n depends on the order n of the considered harmonic. The real corrected flow coefficients v_n are obtained by dividing the observed, uncorrected flow $v_{n,obs}$ coefficient by the resolution factor:

$$v_n = \frac{v_{n,obs}}{R_n} = \frac{\langle cos(n(\phi - \Psi_{RP})) \rangle}{R_n}. \tag{3.51}$$

Whereby R_n is given by the mean of the cos of n times the difference between the true reaction plane angle Ψ_{RP} and the reconstructed event plane angle Ψ_{EP} [49]:

$$R_n = \langle cos(n(\Psi_{EP} - \Psi_{RP}))\rangle. \tag{3.52}$$

Assuming that a Gaussian can describe distribution of the fluctuations of the Q vector around the reaction plane, one can show that R_n is expressible in terms of modified Bessel functions I_x of order n [49]:

$$R_n = \frac{\sqrt{2}}{2}\chi e^{\chi^2/2}[I_{\frac{n-1}{2}}(\frac{\chi^2}{2}) + I_{\frac{n+1}{2}}(\frac{\chi^2}{2})]. \tag{3.53}$$

The modified Bessel function of order n is given by:

$$I_x(\chi) = \sum_{m=0}^{\infty} \frac{1}{m!\Gamma(m+x+1)}(\frac{\chi}{2})^{2m+x}. \tag{3.54}$$

3.4.1. Sub-event method

In order to obtain the resolution parameter χ, the sub-event method is employed. Hereby, the measured spectator hits of each event are randomly divided into two subsets with an equal number of hit multiplicity to measure the fluctuations. These two sets of hits are subsequently treated as two separate events. For each of which the event plane angles Ψ_A, and Ψ_B are extracted by following the procedure described in section (3.3). According to equation (3.53) the sub-event angles is related to the reaction plane angle Ψ_{RP}.

$$R_{n,subevent} = \langle cos(n(\Psi_{A,B} - \Psi_{RP})\rangle = \sqrt{\langle cos(n(\Psi_A) - \Psi_B)\rangle}. \tag{3.55}$$

By inverting equation (3.55) with respect to $\chi_{A,B}$, χ is obtained by:

$$\chi = \sqrt{2}\chi_{subevent}. \tag{3.56}$$

Finally, after inserting the obtained value for χ in equation (3.53), the resolution R_n can be calculated. In order to avoid inverting the Besselfunction, an alternative approach is followed, as applied in previous flow analyses within the HADES collaboration [22]. The idea is to directly derive χ from the distribution of the difference between the two reconstructed sub-event angles Ψ_A, Ψ_B:

$$\Delta\Psi = \Psi_A - \Psi_B. \tag{3.57}$$

In [49] it is has been shown that this quantity can be related to χ. Accordingly the integral N_1 for the interval $180^o < |\Psi_A - \Psi_B| < -90^o$ as well as N_2, the integral for the interval $-180^o < |\Psi_A - \Psi_B| < +180^o$, are calculated:

$$N_1 = \int_{-180}^{-90} N(\Delta\Psi)d\Delta\Psi + \int_{90}^{180} N(\Delta\Psi)d\Delta\Psi. \tag{3.58}$$

$$N_2 = \int_{-180}^{180} N(\Delta\Psi)d\Delta\Psi. \tag{3.59}$$

Based on the ratio of N_1 and N_2 the value for χ is obtained using the relation [49]:

$$\frac{N_1}{N_2} = \frac{exp(-\chi^2/2)}{2}. \tag{3.60}$$

For χ follows:

$$\chi = 2\sqrt{-ln(2\frac{N_1}{N_2})}. \tag{3.61}$$

Ultimately, χ is inserted into equation (3.53), leading to the resolution factor R_n. The measured distribution of the observable $\Delta\Psi = \Psi_A - \Psi_B$ is shown in figure 3.45.

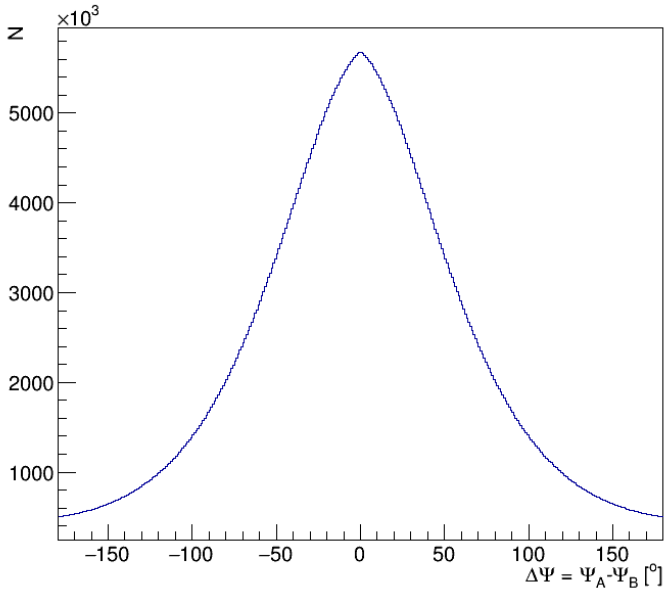

Figure 3.45: Distribution of $\Delta\Psi = \Psi_A - \Psi_B$ for the 0-10 % most central events. Based on equation (3.61), the resolution parameter χ is obtained by calculating the integral for $180^o < |\Psi_A - \Psi_B| < -90^o$ as well as for the entire definition range. The ratio of those two integrals is plugged in equation (3.61) in order to compute the resolution parameter χ, later used to obtain the event resolution factor.

As the fluctuation of the event plane is sensitive to the number of spectator hits, the resolution has to be determined as a function of centrality. Figure (3.46) displays the calculated R_n for the first three flow harmonics as a function of the five analysed centrality classes. It is observed that the resolution of the event plane decreases with decreasing order of n. Furthermore, the lowest resolution is obtained for the events from the most central collision class for each order. The resolution factor reaches a maximum for the $20 - 30\%$ centrality range. For more peripheral events, the resolution slowly decreases compared to the maximum value.

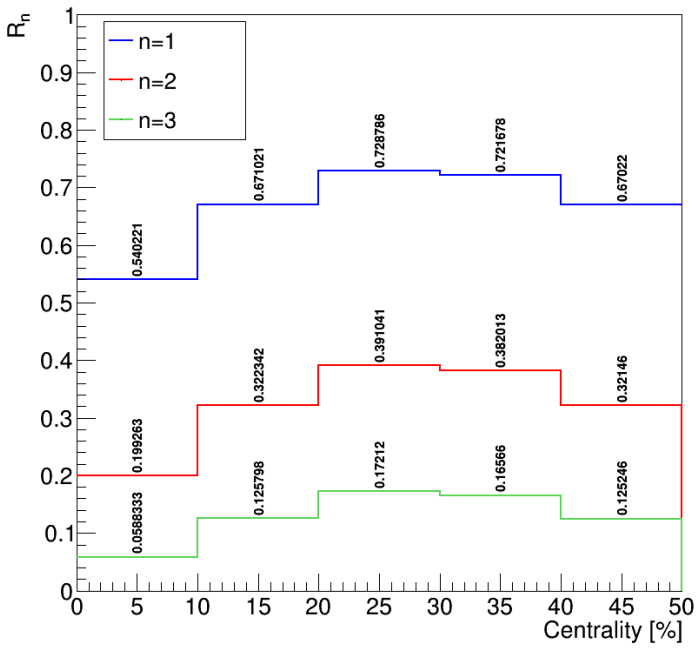

Figure 3.46: Obtained resolution factors, extracted via the sub-event method.

3.5. Flow - Phase Space Binning

For detailed insights into the flow pattern of charged pion, the harmonics are explored as a function of transverse momentum and rapidity in the centre of mass system.
In order to exclude phase space bins for which the detector's acceptance and efficiency are limited, we consider the $Acc \cdot Eff$ matrices, obtained within the correction of the differential spectra count rates, see section (1.1). By making use of the simulation additionally the estimated purity P is considered. The applied selection conditions in the flow analysis are:

$$Acc \cdot Eff > 0.15 \text{ and } P > 0.95. \tag{3.62}$$

This phase space bin selection is applied before filling the flow spectra by asking for the reconstructed rapidity and transverse momentum of the potential pion track, whether the required conditions are fulfilled.
Lastly, we discuss the size of the phase space grid. The bin sizes are chosen in such a way that the statistics are sufficiently large to allow for significant harmonics for most of the considered phase space regions. The transverse momentum axis ranges from 0 to 1000 MeV/c and is divided into 20 bins, resulting in an interval width of $\Delta p_t = 50\ MeV/c$. For the rapidity axis, a bin width of 0.1 units is chosen, ranging from -0.75 to 0.75. By that, the statistics is large enough to have moderate statistical errors for the directed and elliptic flow. However, for v_3 flow investigations, this axis division is too granular to allow for significant values. Thus, the bin-width for the p_t axis is chosen to be $\Delta p_t = 200$ MeV/c and for the rapidity axis: $\Delta y = 0.2$. In order to observe the functional properties of the flow harmonics in terms of the phase space in more detail, 1D projections among each axis are prepared.

Binning	v_1	v_2	v_3
$p_{t,min}[MeV/c]$	0	0	0
$p_{t,max}[MeV/c]$	1000	1000	1000
N_{bins,p_t}	20	20	5
y_{min}	-0.75	-0.75	-0.7
y_{max}	1.15	0.15	1.3
$N_{bins,y}$	19	19	10

Table 3.9: Transverse momentum p_t and rapidity y_{cm} axis grid size for the three analysed flow harmonics.

3.6. Occupancy Correction

It needs to be taken into account that due to the high multiplicity environment of the Ag+Ag collision system, occupancy effects can play a major role. Occupancy is understood as the number of hits in a certain active detector volume. The sub-detectors, in particular, their set-up with multiple drift cells of the MDCs, do not have equal reconstruction efficiency with respect to the track multiplicity. In addition, the magnetic field configuration contributes to detector regions that differ in their reconstruction efficiency. In general, it is expected that occupancy increases with increasing event multiplicities and decreases with the polar angle. As occupancy might significantly impact the directed flow harmonic due to modulation effects, a correction is required.
An indicator for the impact of occupancy in flow reconstruction is the transverse momentum dependence of directed flow v_1 at mid-rapidity. As described in chapter (2.1), from a physical perspective, due to the reaction symmetry and momentum conservation, the magnitude of v_1 should be close to zero at mid-rapidity as well as constant as a function of transverse momentum. Moreover, point-symmetry between the forward and backward rapidity bins is expected. Therefore, for evaluating the contribution of occupancy effects, v_1 for both the π^- and π^+ mesons is inspected in figure (3.47) and (3.48) as a function of transverse momentum for the rapidity bins $y_{cm} = 0$, $y_{cm} = |0.15| \pm 0.05$, $y_{cm} = |0.25| \pm 0.05$ and $y_{cm} = |0.35| \pm 0.05$. In order to review the extent of point-symmetry, the backward bins are multiplied by -1 and plotted as well.

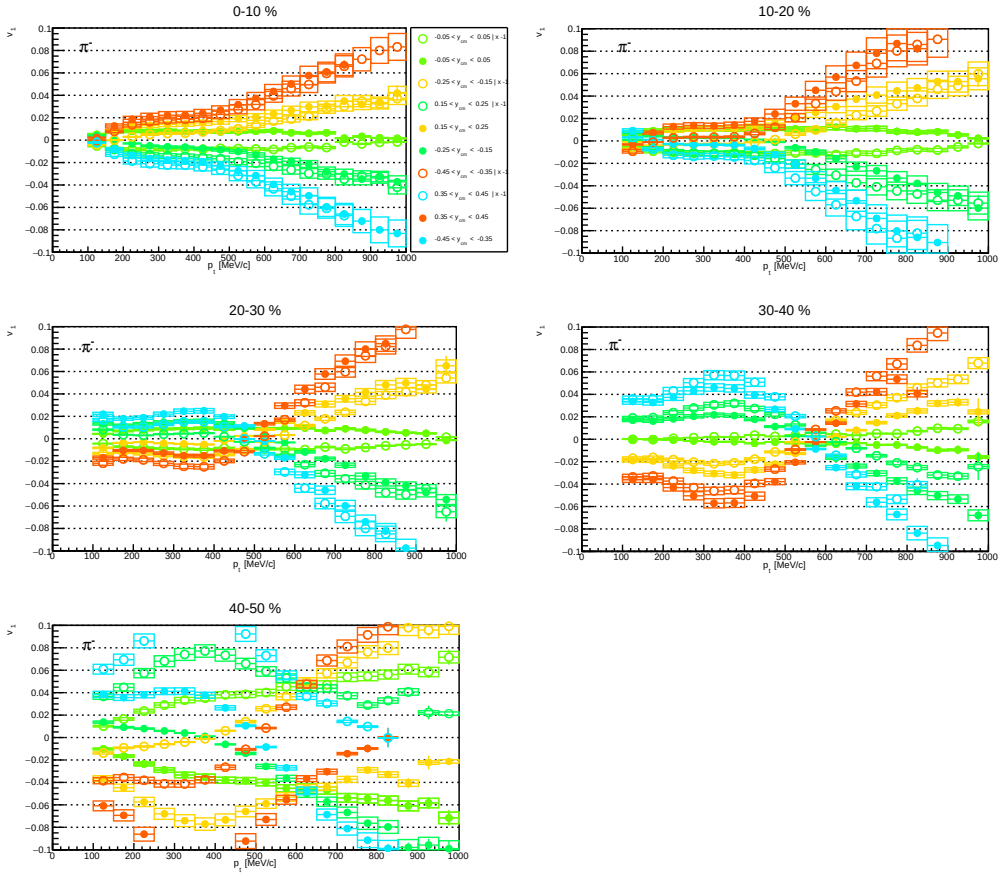

Figure 3.47: v_1 (π^-) as a function of transverse momentum for the rapidity bins: $y_{cm} = 0 \pm 0.05$, $y_{cm} = |0.2| \pm 0.05$ and $y_{cm} = |0.4| \pm 0.05$. Unfilled points correspond to reflected data points, multiplied by -1.

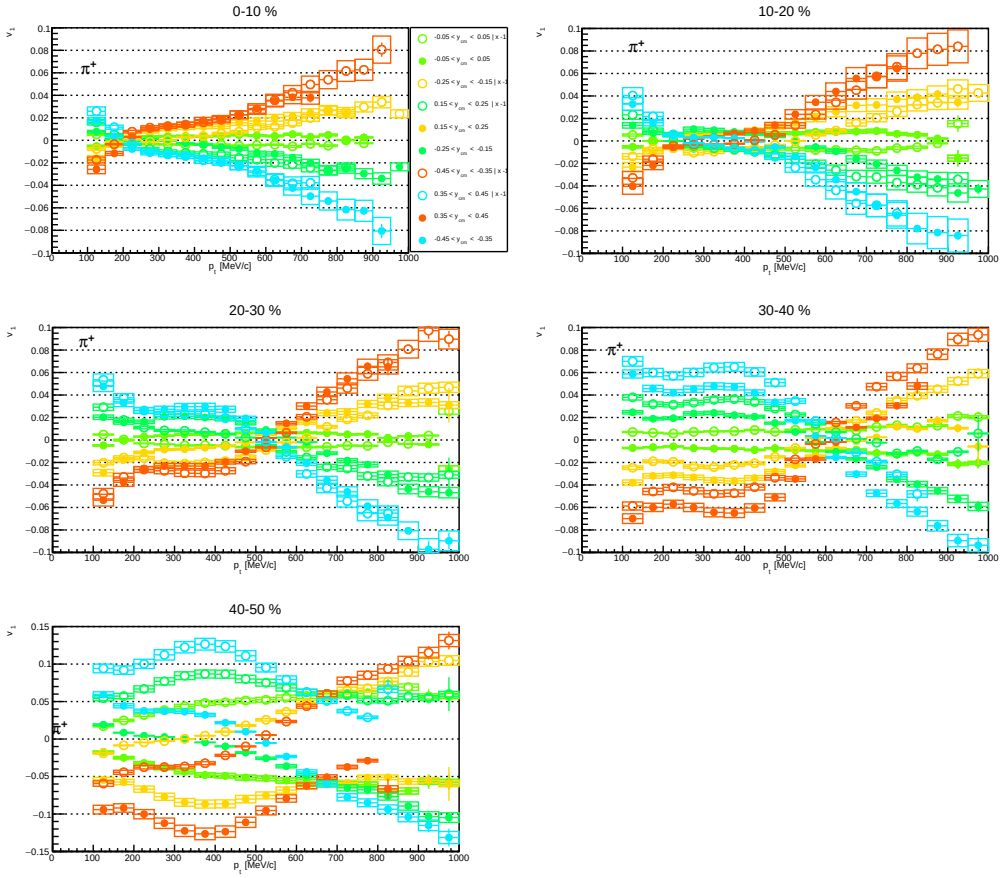

Figure 3.48: v_1 (π^+) as a function of transverse momentum for the different rapidity bins: $y_{cm} = 0 \pm 0.05$, $y_{cm} = |0.2| \pm 0.05$ and $y_{cm} = |0.4| \pm 0.05$. Unfilled points correspond to reflected data points, multiplied by -1.

For v_1 of the π^- candidates, it is visible that the harmonics do not lie at zero at mid-rapidity. Instead, a shift by around 0.01 units upwards is observed, affecting also the symmetry behaviour. It is clearly seen that some of the reflected points do not coincide well with the corresponding data points. A too high value for v_1 at mid-rapidity is observed for the centrality range of 0-30 %. For 30-40 % centrality, v_1 is already close to zero at mid-rapidity, yet symmetry issues are visible. The worst behaviour regarding v_1 is observed for the 40-50 % most central collisions. In this region, the deviations from being zero at mid-rapidity are more likely predominantly caused by events originating in non-pure Ag+Ag collisions.
The p_t-dependence of v_1 at mid-rapidity and point-symmetry for the π^+ is depicted in figure (3.48). As opposed to the π^-, v_1 is slightly closer to zero at mid-rapidity for the π^+ mesons. The observed shift is around 0.007 units upwards for the 0-30 % centrality classes. For both charges, approximate constancy in terms of p_t at the mid-rapidity bin is observed for the centrality range up to 30 % only. For peripheral events, especially within the centrality class $40 - 50$ %, a deviation from a flat shape as well as strong asymmetry is exhibited. As mentioned, this might indicate contamination with Ag+C events, which implies that the introduced ERAT-selection is not sufficient concerning the flow analysis in the most peripheral events. Hence the centrality class 40-50 % is

omitted in the flow analysis. In summary, considering the described behaviour of v_1, it is concluded that occupancy effects are exhibited for both charges. However, for positive pions, such effects are less dominant than found for the π^-. A possible explanation is that occupancy might be dependent on the bending direction of the magnetic field [60]. This is also reflected in the sector-wise rapidity distributions, where the yields' fluctuations between the different sectors are found to be more crucial for the π^- than for the π^+ mesons. (1.6.3).

3.6.1. Correction Procedure

The correction of the observed effects requires an experimentally accessible measure for occupancy. Since occupancy correlates with the multiplicity in a particular active detector volume, the number of tracks per event as a function of the polar angle, and because we want to investigate the impact to the azimuthal anisotropy, also as a function of the emission angle relative to the event plane, is a proper observable to consider. Based on this information, thereafter, efficiency matrices are derived, which are used for weighting the analysed tracks accordingly. All the steps required to estimate the efficiencies related to occupancy are explained in the following two subsections.

3.6.2. Local Track Density

The extent of occupancy is evaluated by analysing the local track density ρ_{track}. It is defined as the number of tracks N_{tracks} per event N_{events}. Local refers to the fact that this quantity is looked at for different bins of the polar angle θ as well as a function of the azimuthal emission angle relative to the event plane $d\phi = \phi - \Psi_{EP}$. It is considered for all selected particle tracks, not only for charged pions, in order to have a probe that significantly depends on occupancy. The track selection criteria are $\chi^2_{RK} < 400$ and $\chi^2_{META} < 3$ as well as the discussed MDC edge cut. As a multiplicity dependency is exhibited, the local track density is investigated as a function of the collision centrality. In order to be as precise as possible, the track density is analysed in a granular binning of 5 % per centrality class.

$$\rho(d\phi, \theta, centr)_{track} = \frac{N_{tracks}(d\phi, \theta, centr)}{N_{events}}. \tag{3.63}$$

Figure (3.49) displays the obtained local track density $\rho(d\phi, \theta, centr)_{track}$ as a function of the polar angle θ and the emission angle relative to the event plane for the centrality classes 0-5 % and 30-35 % as examples. The bin size is 1x1 degrees. It is observed that the highest track densities are reached for small angles ($20° < \theta < 30°$) in the polar direction. The track density decreases towards higher polar angles, which the arrangement of the experimental set-up can explain. In terms of the collision centrality, the track density decreases towards peripheral events as there are fewer production sources available.

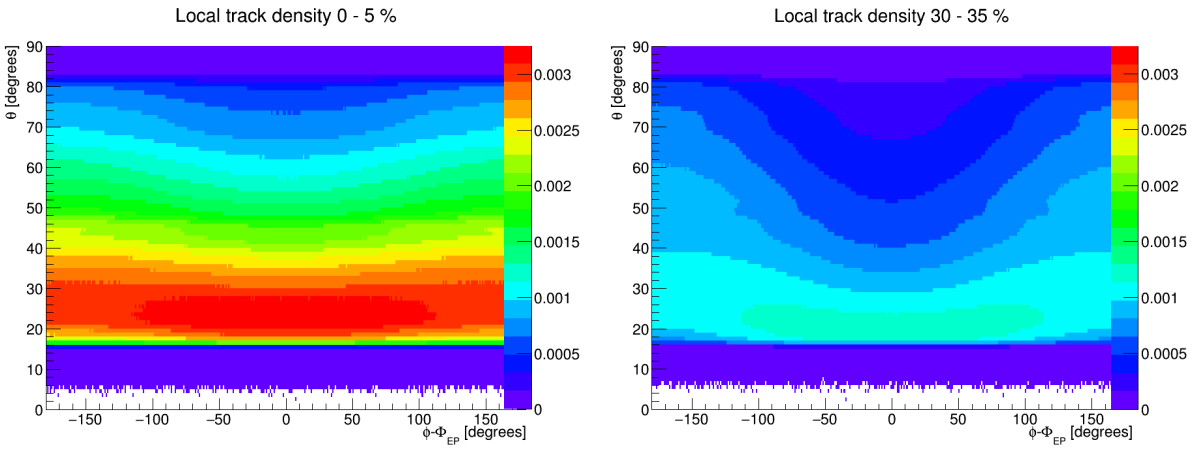

Figure 3.49: Obtained track density matrices as a function of $\phi - \Psi_{EP}$ and the polar angle θ for most central (right) and more peripherals events (left).

The θ angle is reconstructed in terms of the measured hit in the inner MDC track segment, approximately corresponding to the angle under which the particles were emitted from the target reaction before being distorted by the magnetic field.

3.6.3. Efficiency

For the next step, the efficiency for each $d\phi$ vs $d\theta$ cell is derived. By using the GEANT package it has been shown that the efficiency can be related to the local track density [22]:

$$\epsilon(\rho_{track}) = \epsilon(d\phi, \theta, centr) = \epsilon_{single} - c_\epsilon \rho(d\phi, \theta, centr)^n_{track}. \tag{3.64}$$

Where ϵ_{single} corresponds to the maximal efficiency. In previous investigations this value has been estimated via simulations to be at $\epsilon_{single} = 0.98$ [22]. c_ϵ is a slope parameter, describing the strength of the scaling in terms of $\rho(d\phi, \theta, centr)_{track}$. It is defined as

$$c_{epsilon} = \frac{\epsilon_{single} - \epsilon_1}{(\rho_{track,max} - \rho_{track,min})^n} \tag{3.65}$$

and depends on the smallest $\rho_{track,min}$ and highest $\rho_{track,max}$ local track density in regard of all centrality classes. ϵ_1 corresponds to lowest efficiency which is expected in environments with highest track densities. $\rho_{track,max}$, $\rho_{track,min}$ are obtained by searching over all differential angle bins as well as all centrality classes. For charged pions, a linear scaling with $n = 1$ as a function of track density is chosen. The parameter ϵ_1 is adjusted in such way that the directed flow harmonic v_1 comes close to being zero at mid-rapidity as well as approximately point-symmetric to mid-rapidity. The analysed pion tracks are then weighted with the inverse of the efficiency $w = \frac{1}{\epsilon(d\phi,\theta,centr)}$:

$$v_n = \frac{\int_{-\pi}^{+\pi} \frac{1}{\epsilon(d\phi,\theta,centr)} \frac{dN}{d(\phi-\Psi_{RP})} cos(n(\phi - \Psi_{EP}))d(\phi - \Psi_{RP})}{\int_{-\pi}^{+\pi} \frac{dN}{d(\phi-\Psi_{RP})}}. \tag{3.66}$$

For the purpose of finding an optimal value for ϵ_1, a set of efficiency matrices for parameters in the range of 0.5 and 0.95 has been prepared and systematically tested. For the π^- it is found that the requirements are best fulfilled for $0.81 < \epsilon_1 < 0.85$, in the

centrality range of $0-30$ %. For more peripheral centralities, only an overcorrection can be realised. Thus, occupancy correction is performed only for the centrality range of $0-30$ %. The optimal efficiency parameters for the π^+ are slightly higher; they are found to be in the range of $0.89 < \epsilon_1 < 0.91$. Figure (3.50) depicts the chosen efficiency functions in terms of the local track density.

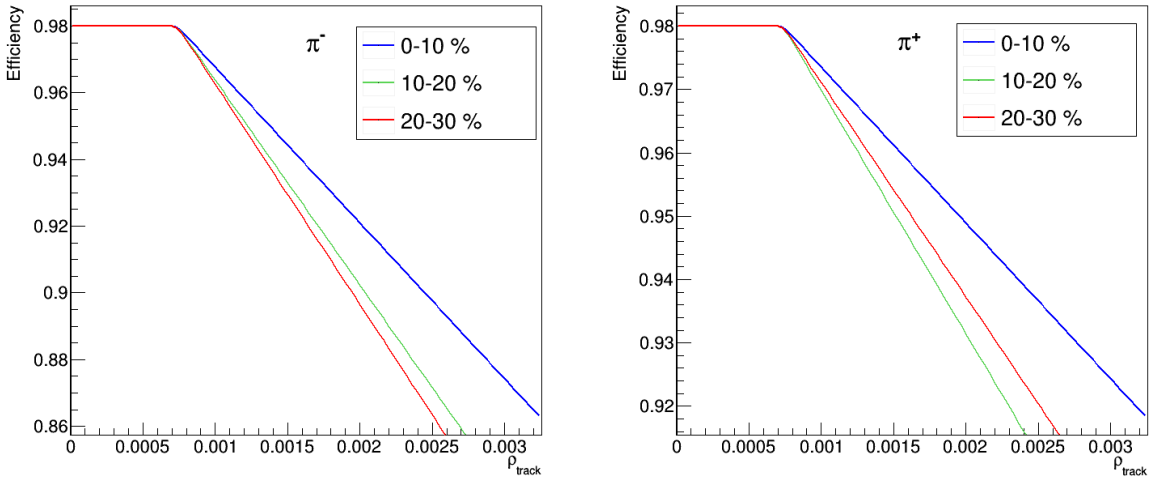

Figure 3.50: Generated efficiency functions, depending on the track density. Right: π^-, left: π^+.

As occupancy effects are relevant for regions with high hit multiplicity, the correction is applied for bins with a track density higher than 0.00024 units only. Below that boundary, the efficiency is set to the highest estimated efficiency ϵ_1=0.98, determined by simulations [22]. Considering the π^-, for all higher track densities three different ϵ_1 are chosen: $\epsilon_1 = 0.828$ for 0-10 % centrality, $\epsilon_1 = 0.78$ for 10-20 % and $\epsilon_1 = 0.765$ for 20-30 %. The employed efficiency functions, with the used parameters, are denoted in equation (3.67).

$$\epsilon(d\phi, \theta, centr) = \begin{cases} = \epsilon_{single} & \rho < 0.00024 \\ = \epsilon_{single} - 46.717 \cdot (\rho_{track} - 0.0024) & \rho > 0.00024 \text{ for } 0-10\% \\ = \epsilon_{single} - 61.470 \cdot (\rho_{track} - 0.0024) & \rho > 0.00024 \text{ for } 10-20\% \\ = \epsilon_{single} - 66.081 \cdot (\rho_{track} - 0.0024) & \rho > 0.00024 \text{ for } 20-30\% \end{cases} . \tag{3.67}$$

(3.68) the denotes the efficiency function for the π^+. In this case, for $\rho_{track} > 0.00024$ the optimal value ranges between $\epsilon_1 = 0.855$ and $\epsilon_1 = 0.9$ and is dependent on the centrality class. As for the negatively charged pions, occupancy correction is not applied for the most analysed peripheral events in the centrality class $30-50$ %.

$$\epsilon(d\phi, \theta, centr) = \begin{cases} = \epsilon_{single} & \rho < 0.00024 \\ = \epsilon_{single} - 24.588 \cdot (\rho_{track} - 0.0024) & \rho > 0.00024 \text{ for } 0 \text{ - } 10 \text{ \%} \\ = \epsilon_{single} - 38.419 \cdot (\rho_{track} - 0.0024) & \rho > 0.00024 \text{ for } 10-20\% \\ = \epsilon_{single} - 33.809 \cdot (\rho_{track} - 0.0024) & \rho > 0.00024 \text{ for } 20-30\% \end{cases} \tag{3.68}$$

The presented efficiency functions are subsequently used to calculate for each differential angle bin with a given track density a value for the efficiency. This results in centrality-dependent efficiency matrices as depicted in figure (3.51). The matrices are then linked to the analysis of the pion tracks. When computing the harmonics, the tracks are weighted according to equation (3.66).

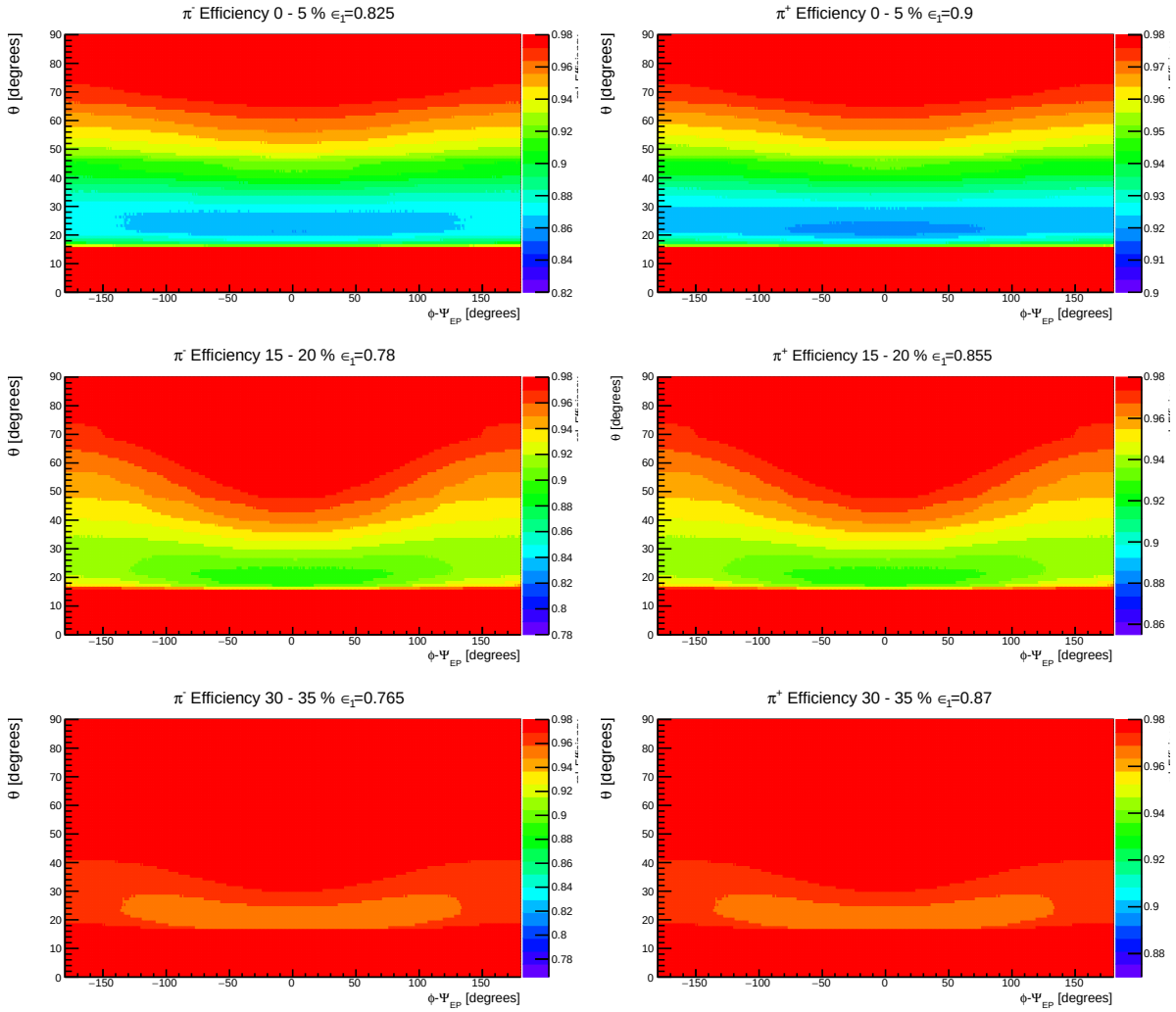

Figure 3.51: Instances for the used efficiency matrices, generated based on the efficiency function denoted in (3.50), (3.67).

The behaviour of directed flow after applied occupancy correction is displayed in figure (3.52) and (3.53).

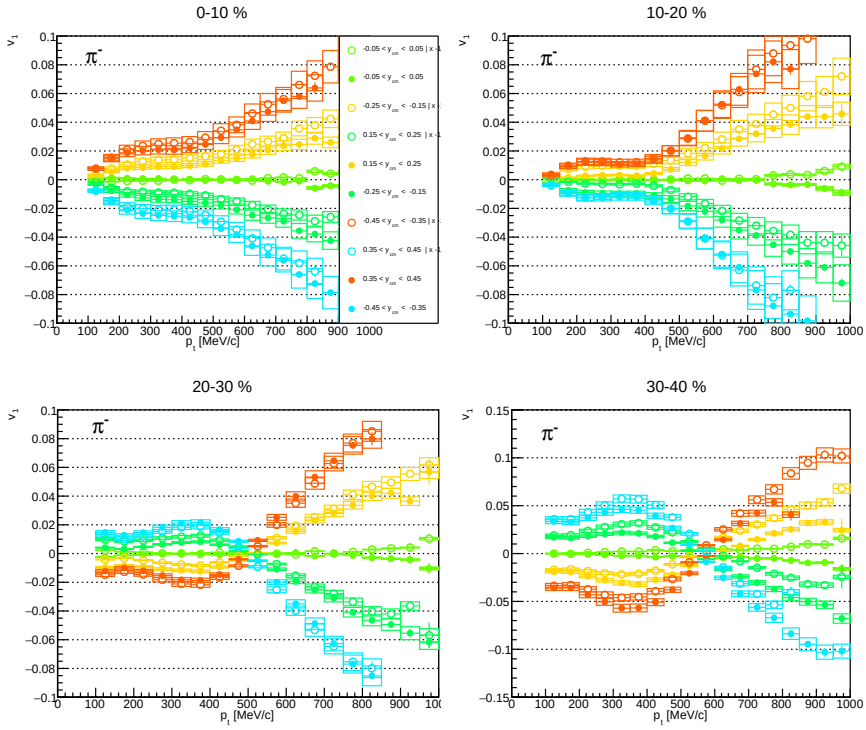

Figure 3.52: v_1 (π^-) with occupancy correction as a function of transverse momentum for the rapidity bins: $y_{cm} = 0 \pm 0.05$, $y_{cm} = |0.2| \pm 0.05$ and $y_{cm} = |0.4| \pm 0.05$. Unfilled points represent reflected data points, multiplied by -1.

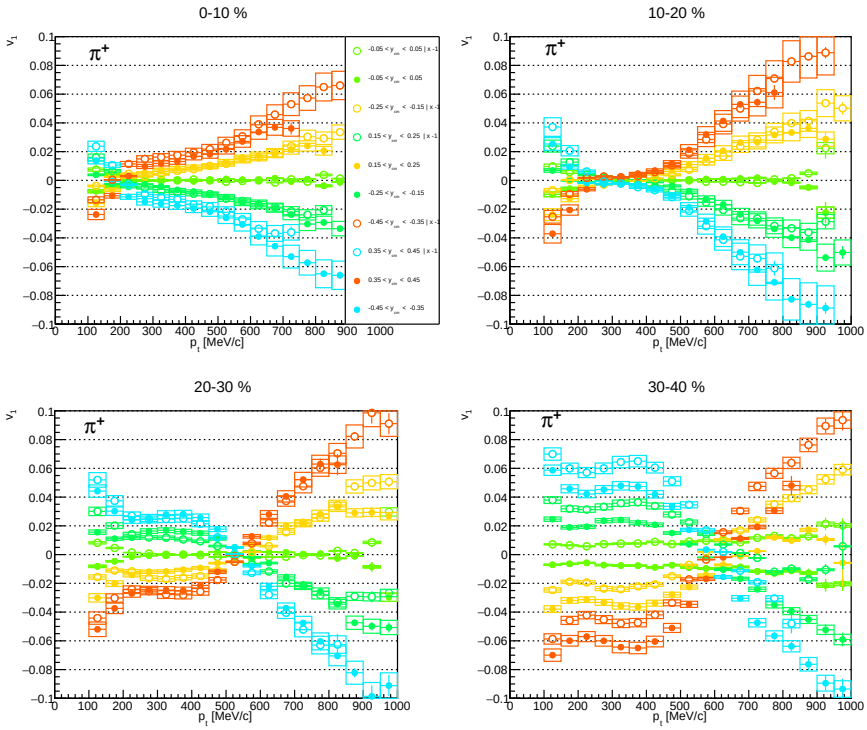

Figure 3.53: v_1 (π^+) with occupancy correction as a function of transverse momentum for the different rapidity bins: $y_{cm} = 0 \pm 0.05$, $y_{cm} = |0.2| \pm 0.05$ and $y_{cm} = |0.4| \pm 0.05$. Unfilled point represent reflected data points, multiplied by -1.

Looking at the functional behaviour of directed flow as a function of transverse momentum after the applied correction, one observes that v_1 is closer to zero at mid-rapidity as expected from a physical point of view. In addition, till 700 MeV/c, the functional shape is relatively flat. The point-symmetry between forward and backward bins is for most of the cases in agreement with the statistical or systematic error, see section (3.7). This holds for the π^- for the centrality classes up to 30 %. As discussed, for more peripheral collisions, occupancy correction does not lead to better behaviour of v_1 and is not applied. The impact of contaminated events plays a major role in this case. It seems that the ERAT selection does not reject sufficient Ag+C events in order to allow for better data quality in flow analysis.
For the π^+ mesons, the situation at mid-rapidity is close to zero for the centrality range $0 - 30$ %, within the momentum interval $200 - 800$ MeV/c. As Opposed to the π^-, a divergence is seen for lower transverse momenta. An explanation might be the Coulomb effect since it leaves its traces especially for low transverse momenta, as discussed in section (2.2). As for the π^-, for more peripheral track multiplicities (30-50 % centrality), the occupancy correction is not applied.

3.7. Systematics

In order to investigate systematic effects, on the one hand, the two introduced methods of extracting the Fourier harmonics are compared: The standard method for the harmonic extraction is the direct calculation of the harmonics. This assumes orthogonality of the

coefficients v_n. Another approach is adjusting a finite number of Fourier terms to the angular distribution with the v_n coefficients as parameters supposed to be adjusted. The systematic is investigated without applying the occupancy correction.
The kinematic analysis of the harmonics is redone by following the fitting method. Thus, for each phase space bin on the same grid as defined in (3.9, the distribution of the azimuthal angle relative to event plane $\phi - \Psi_{EP}$ is obtained and fitted by the first three terms of the Fourier series:

$$\frac{dN}{d(\phi - \Psi_{RP})} = A \cdot (1 + 2 \cdot v_1 cos(n(\phi - \Psi_{EP})) + 2 \cdot v_2 cos(n(\phi - \Psi_{EP}) + 2 \cdot v_3 cos(n(\phi - \Psi_{EP}))). \tag{3.69}$$

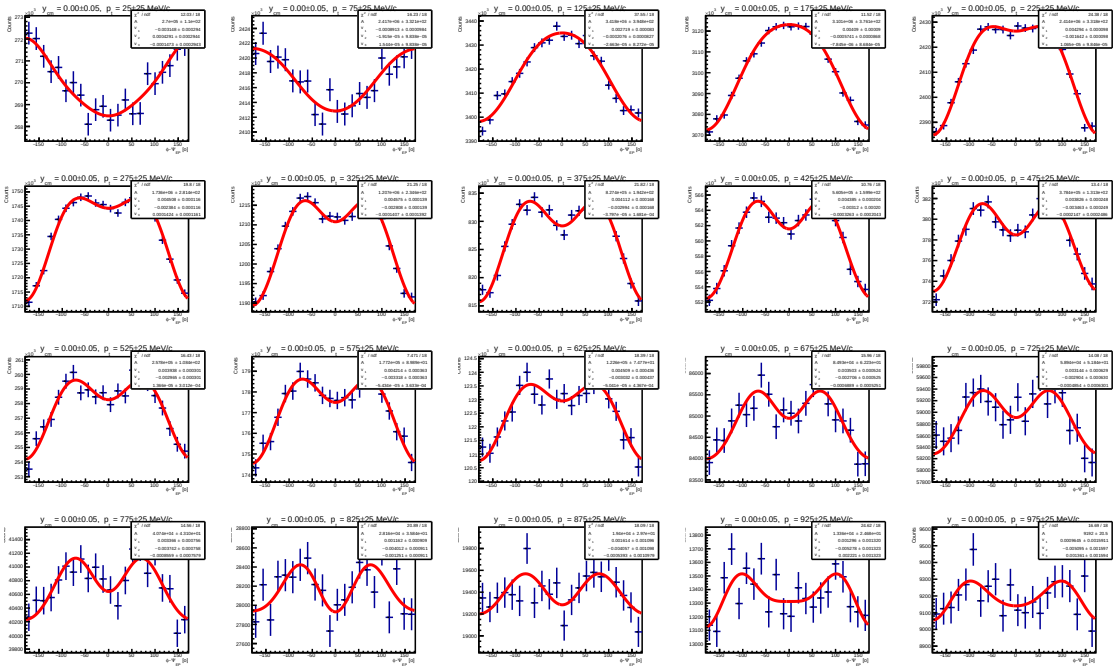

Figure 3.54: Distributions of the emission angle relative to the event plane $\phi - \Psi_{EP}$ for different transverse momentum bins at mid-rapidity, $y_{cm} = 0.0 \pm 0.05$. In order to extract the flow coefficients the first 3 terms of the Fourier series according to equation (3.69) are fitted with the v_n as free parameter.

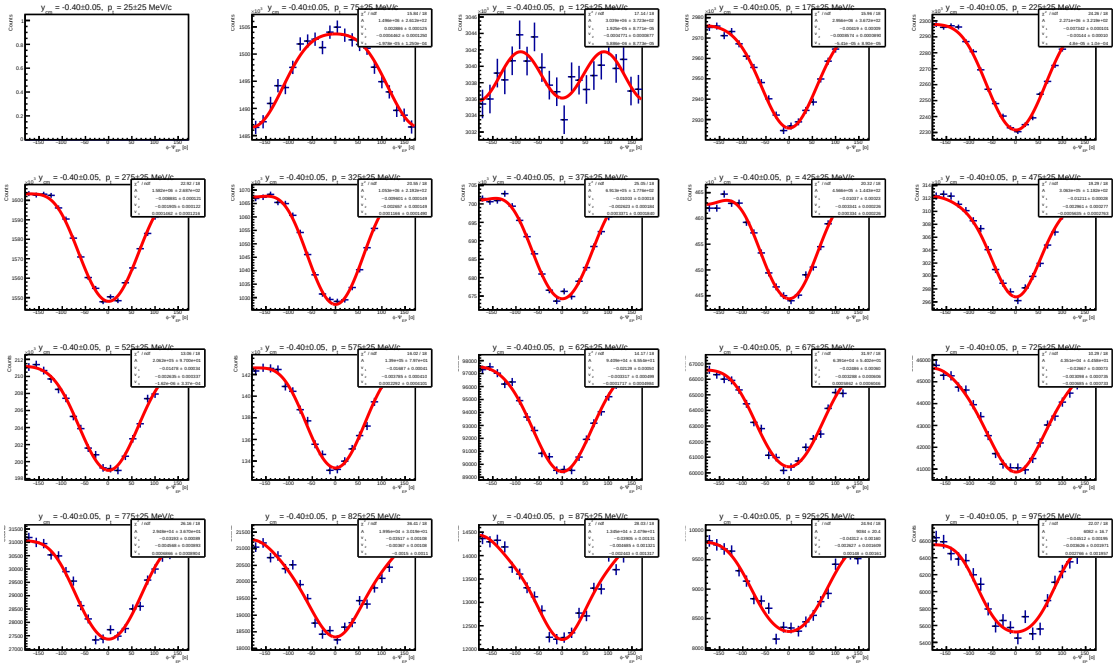

Figure 3.55: Distributions of the emission angle relative to the event plane $\phi - \Psi_{EP}$ for $y_{cm} = -0.4 \pm 0.05$

The angle bin width is 4 degrees. The adjusted parameters are afterwards extracted and filled into a 2D histogram of the phase space observables to have the same situation as for direct calculation, making the two methods comparable to another. To conduct a quantitative comparison, the magnitude of the harmonics' differences between the two methods relative to the standard method (direct calculation) is computed for each bin for which neither one of the two methods delivered a relative statistical error more significant than 100 %. Finally, an averaged systematic error is calculated, corresponding to the average overall bins that fulfil the requirement on the statistical error. The systematic error evaluation is, besides the kinematic observables, considered as a function of collision centrality and the order n of the harmonic. The yielded average relative systematic deviations between the two methods are depicted in figure (3.56).

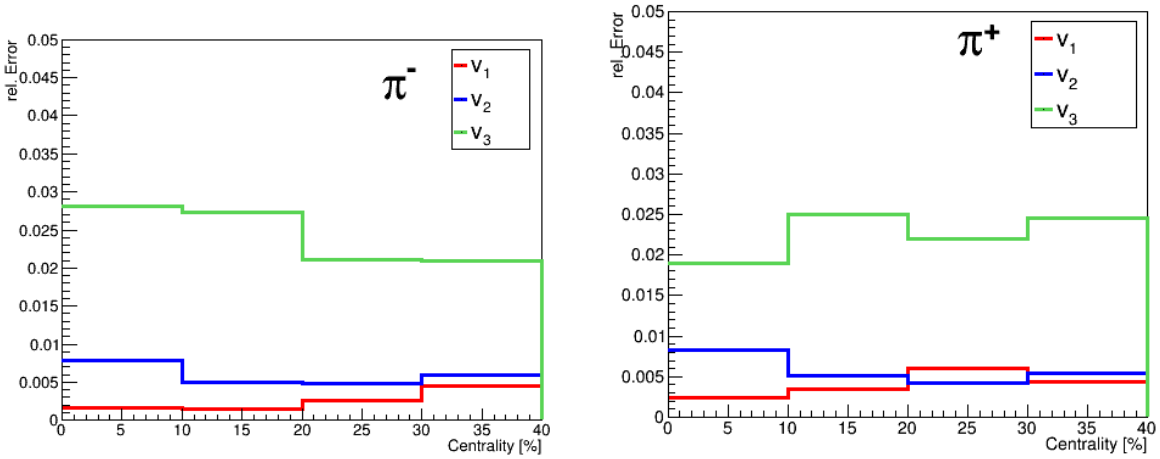

Figure 3.56: Average relative differences between the two employed methods of flow extraction: Direct calculation assuming orthogonality, and fitting of the first 3 terms of the Fourier series to the angular distribution. The relative difference is with respect to the method of direct calculation. The differences are plotted up to the third-order as function of centrality.

The relative differences of the first order flow harmonic v_1 lie between 0.25 and 0.5 %, for both the π^- and the π^+ mesons. The maximal deviations for elliptic flow are around 1 % for both charges. For the v_3 harmonic, the relative differences are slightly higher in the range between 2 % and 3 % for the negatively charged pions. For the positive pions, the relative difference for v_3 are between 2 and 2.5 %.
Another systematic effect that is checked is the impact of the variation of the bandwidth of the graphical PID selection cuts on the β vs p spectra. As discussed in (3), for the standard analysis, a cut of 2σ is applied. The value of σ is now reduced to 1σ. Both variants are compared as proceeded for evaluating the method-systematic. Hence, a common systemic error is calculated by averaging all phase space bins with statistical errors smaller than 100 %. Again, the error is considered as a function of the flow order and centrality of the collisions, see figure (3.57).

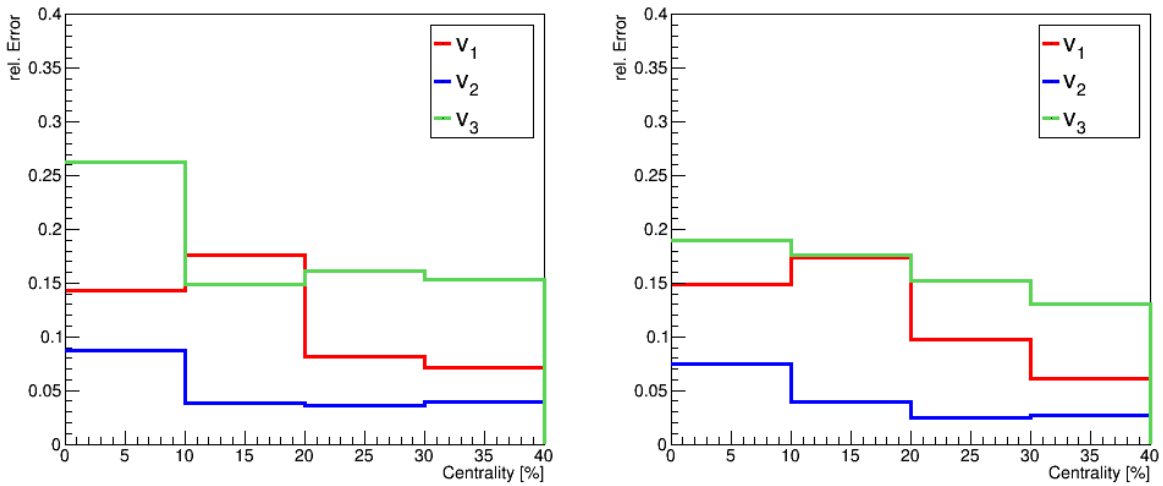

Figure 3.57: Average relative differences of the flow harmonics between the analysis with 1σ and 2σ PID cuts. The difference of the flow harmonics are plotted up to the third order as a function of centrality. The differences are relative to the variant with the standard PID with 2σ.

The relative differences exhibit the highest values for the v_3 harmonic, namely up to 25 % in the most central centrality class for the π^-. In the case of the π^+ rel. differences are in between 15 % and 20 %. For directed flow, the errors are slightly smaller, in range of 5 % and 15 % for both polarities. The smallest systematic differences are observed for elliptic flow. The v_2 differences are in the range between 3 to 8 % for both charges.
Finally, the two evaluated systematic errors are combined. It is plausible that they are uncorrelated and can therefore be summed up quadratically. The square-root leads to the total relative systemic error, subsequently applied on the flow spectra presented in the coming sections.

$$\triangle v_n = \sqrt{\triangle^2_{PID} + \triangle^2_{Methods}} \tag{3.70}$$

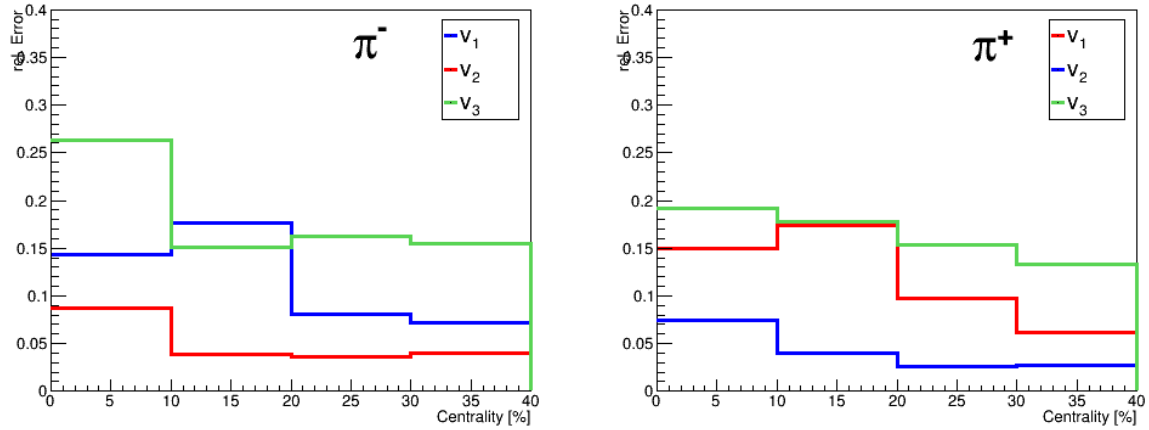

Figure 3.58: Combined average relative systematic errors resulting from PID cut variation (3.57) and the two compared methods of harmonics extraction (3.56).

3.8. Results

This section presents the obtained anisotropic flow harmonics of charged pions as a function of transverse momentum and rapidity. Plotted are the statistical errors (lines) as well as the discussed systematic errors (boxes) (3.7). The centrality dependence is investigated in the centrality range of 0-40 % with a 10-% binning. Within the scope of this section, the observed functional behaviour is described, a physical interpretation is conducted in the discussion section (3).

3.8.1. Directed Flow v_1

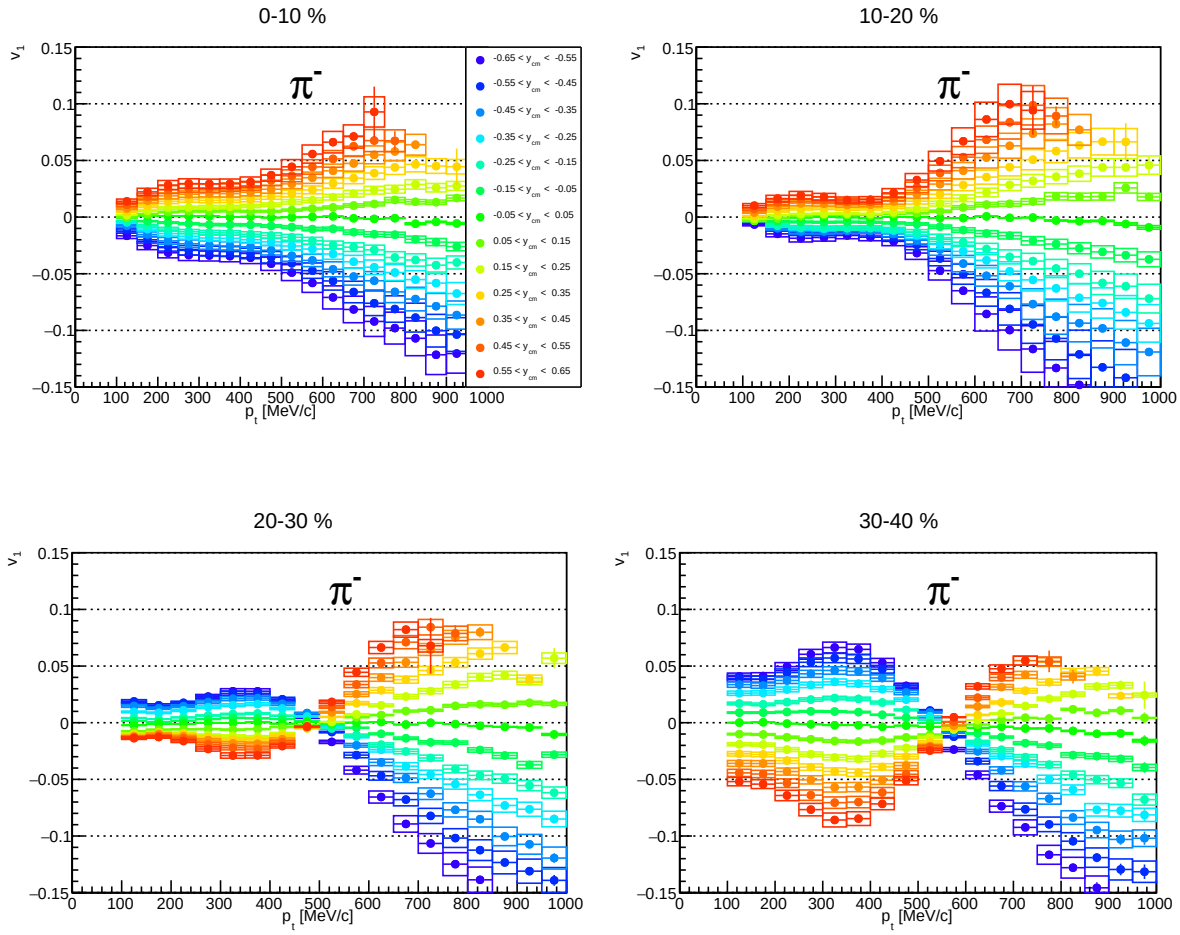

Figure 3.59: π^-: v_1 flow as a function of p_t, for the centrality classes 0-10 %, 10-20 %, 20-30 % and 30-40 %. The plotted spectra are for different rapidity bins within the interval of $-0.65 < y_{cm} < 0.65$. The boxes correspond to the systematic errors. Lines represent statistical errors.

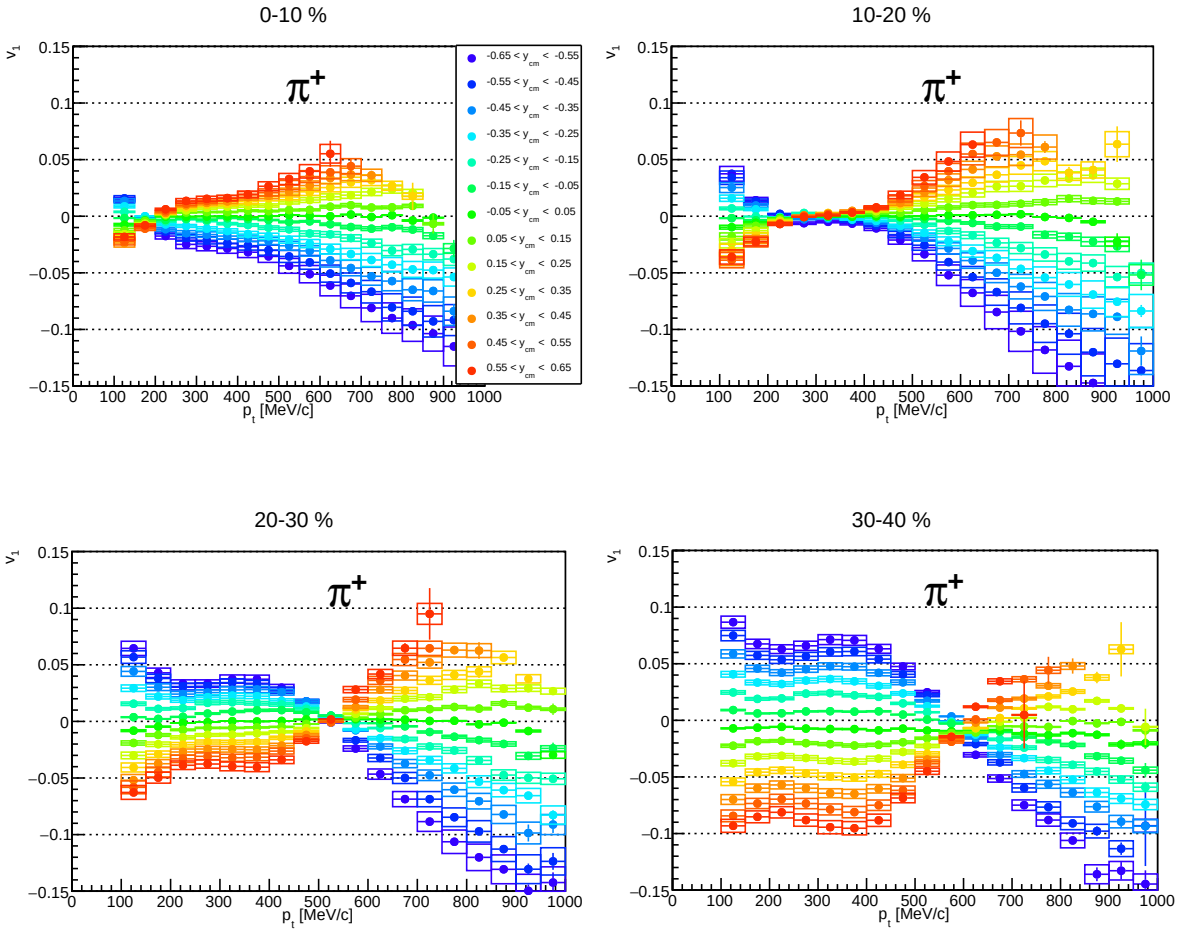

Figure 3.60: π^+: v_1 flow as a function p_t for the centrality classes 0-10 %, 10-20 %, 20-30 % and 30-40 %. The plotted spectra are for different rapidity bins within the interval of $-0.65 < y_{cm} < 0.65$. The boxes represent to the systematic errors. Lines correspond to the statistical errors.

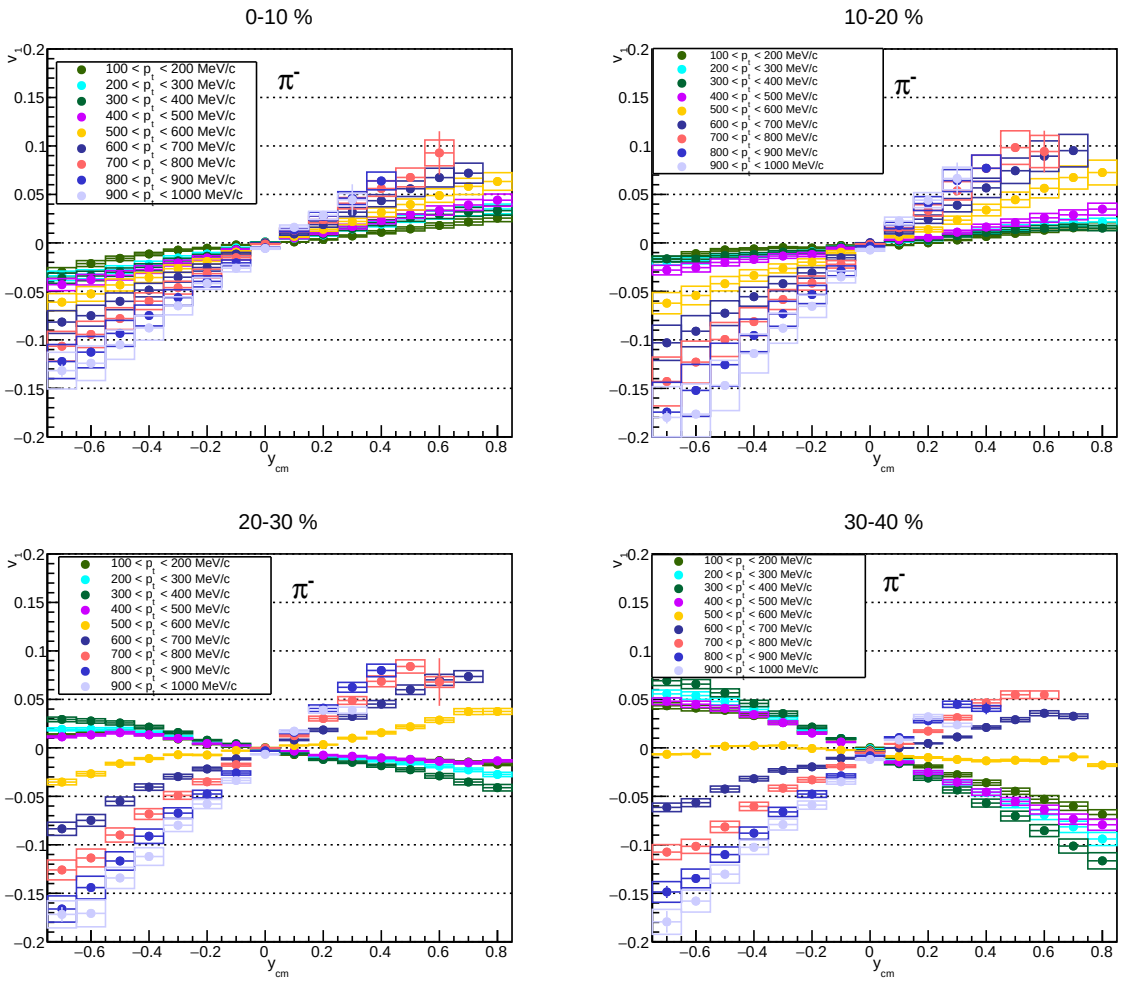

Figure 3.61: π^-: v_1 flow for the centrality classes 0-10 %, 10-20 %, 20-30 % and 30-40 %. The functional dependence is displayed for the centre of mass rapidity y_{cm}. The spectra are for different transverse momentum bins for the range of 100 to 1000 MeV/c. The bin width is 100 MeV/c. The boxes correspond to the total systematic errors. Lines represent statistical errors.

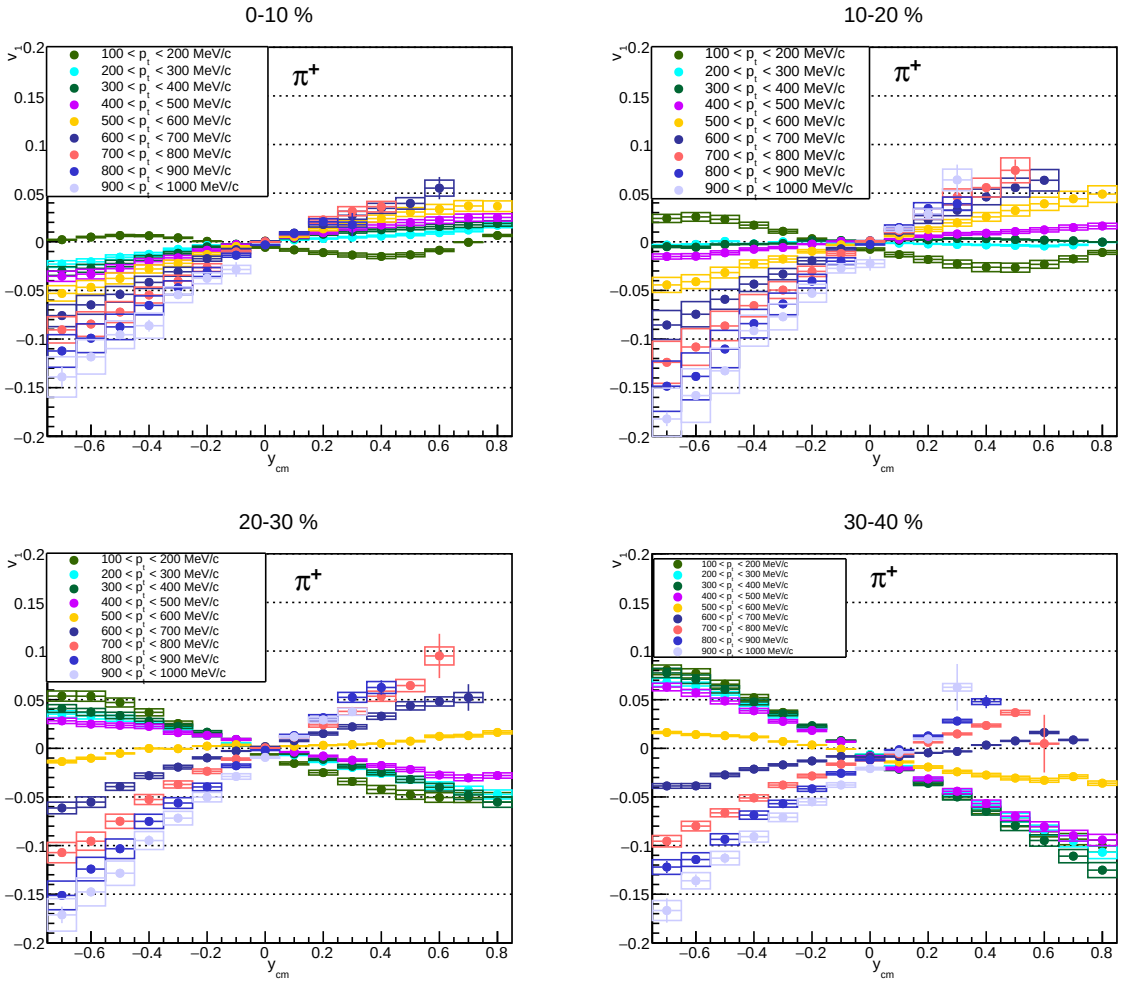

Figure 3.62: π^+: v_1 flow for the centrality classes 0-10 %, 10-20 %, 20-30 % and 30-40 %. The functional dependence is displayed for the centre of mass rapidity y_{cm}. The spectra are for different transverse momentum bins in the range of 100 to 1000 MeV/c. The bin width is 100 MeV/c. The boxes correspond to the total systematic errors. Lines represent statistical errors.

Looking at the transverse momentum dependence of directed flow (3.59) (3.60), for all centrality classes and both polarities, an increase of v_1 towards higher transverse momenta as well as a divergence between the different rapidity bins is observed. Thereby the maximum reached for the most outer rapidity bin ($y_{cm} = 0.65$), increases with decreasing collision centrality, reaching a maximum for 20-30 % centrality. For 30-40 % it slightly decreases.
For the π^-, in the low momenta region, a wave-like pattern is visible: v_1 is smallest towards zero p_t. For rising p_t, a local maximum is reached, after which v_1 slightly decreases, reaching a local minimum before the mentioned increase towards 1000 MeV/c starts. The position of both the maximum and minimum at the transverse momentum axis within the wave-pattern region rises towards peripheral collisions. Yet, for 0-10 % centrality, the maximum and minimum are not that enhanced; instead, a plateau-like behaviour is observed. For 10-20 % centrality, the local maximum is reached at

around 200 MeV/c, the minimum is located at 350 MeV/c. For 20-30 % centrality the maximum is at 300 MeV/c, the minimum is reached at around 450 MeV/c. Though, for 500 MeV/c, junction points are visible, meaning that for nearly all rapidity bins, v_1 crosses the zero line. The same pattern is found for the most peripheral collisions in the 30-40 % centrality class. The local maximum are located at around 350 MeV/c. The local minimum is reached at 500 MeV/c.
For the positively charged pions, as observed for the negative ones, an increase of directed flow towards high transverse momenta ($p_t > 600\ MeV/c$) is observed over all centrality classes. Also, a wave-like structure is observed. Opposed to the π^- an increase of v_1 as well as a divergence between the different rapidity bins is observed for the low p_t-range ($p_t < 200\ MeV/c$). Whereby, the maximum of the most outer rapidity bin, reached for $p_t < 50\ MeV/c$, increases with decreasing centrality. For $0-10$ % centrality, a minimum is exhibited at around 200 MeV/c. For 10-20 %, the minimum is exhibited between 250 and 400 MeV/c in the form of a vale-like shape with v_1 close to zero. Instead, for 20-40 % also a maximum with two local minima in the range of $200-400\ MeV/c$ is visible.
Comparing the different rapidity bins, it is found that v_1 is the smaller the more the rapidity bin is close to mid-rapidity ($y_{cm} = 0 \pm 0.05$). This is expected from collision symmetry and holds for both charges. The explicit rapidity dependence of directed flow is displayed in the figures (3.61) and (3.62).
One observes an approximate point-symmetric behaviour with respect to mid-rapidity. For $0-20$ %, for the π^- mesons it is observed that for all transverse momentum bins the slope is positive, meaning that for $y_{cm} < 0$, v_1 is always negative and for $y_{cm} > 0$ always positive. However, this is not true for the 20-40 % centrality range. Here, for the momentum bins in the interval $100-300\ MeV/c$ a negative slope is exhibited. For positively charged pions, for $0-20$ % centrality, only for transverse momenta with $p_t < 200$ MeV/c directed flow is positive for $y_{cm} < 0$, changing sign for $y_{cm} > 0$. For even more peripheral events (20-40 %), this also holds for the next tree higher transverse momentum intervals.

3.8.2. Elliptic Flow v_2

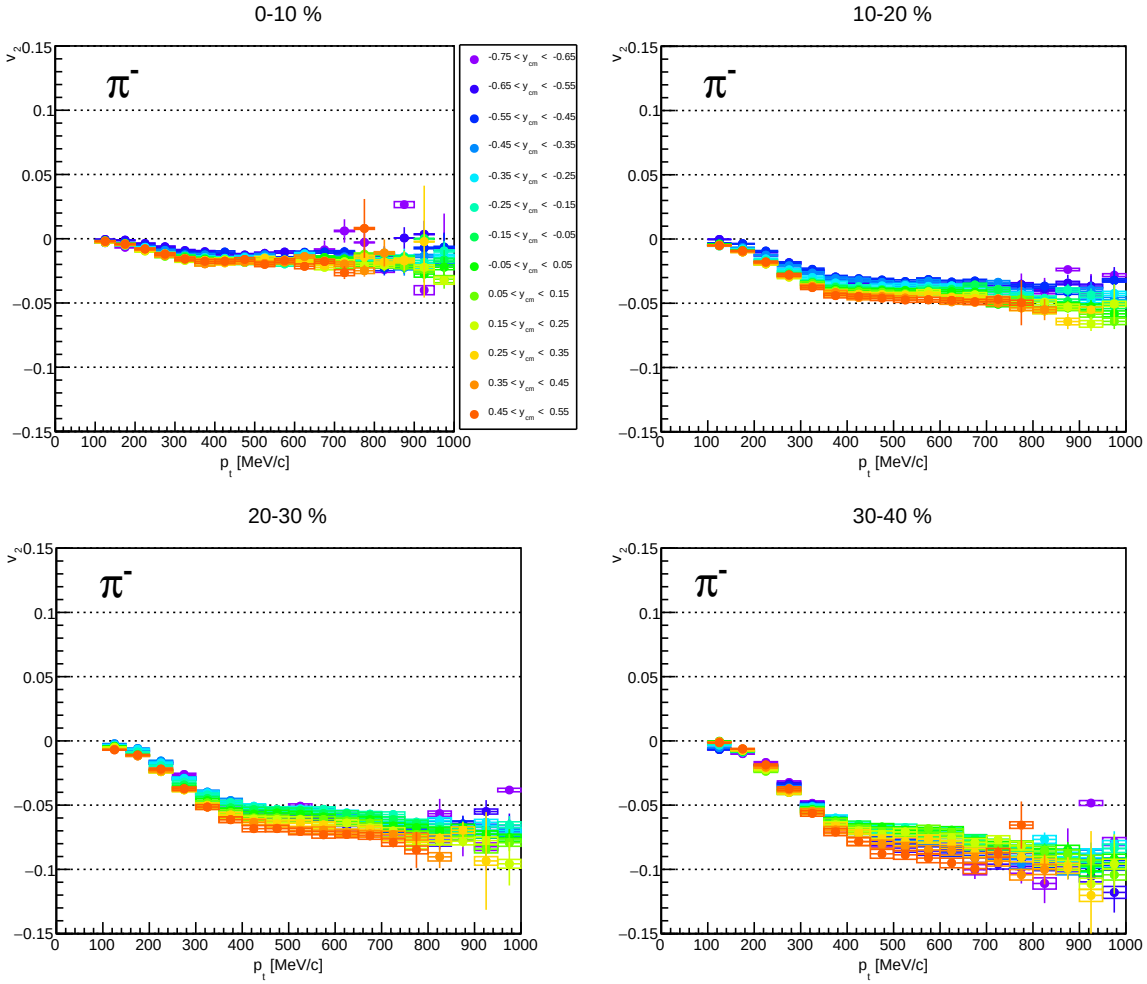

Figure 3.63: π^-: v_2 for the centrality classes 0-10 %, 10-20 %, 20-30 % and 30-40 %. Displayed is the functional dependence from transverse momentum p_t. The plotted spectra are for different rapidity bins in the range of $-0.65 < y_{cm} < 0.65$. The boxes correspond to the total systematic errors. Lines represent statistical errors.

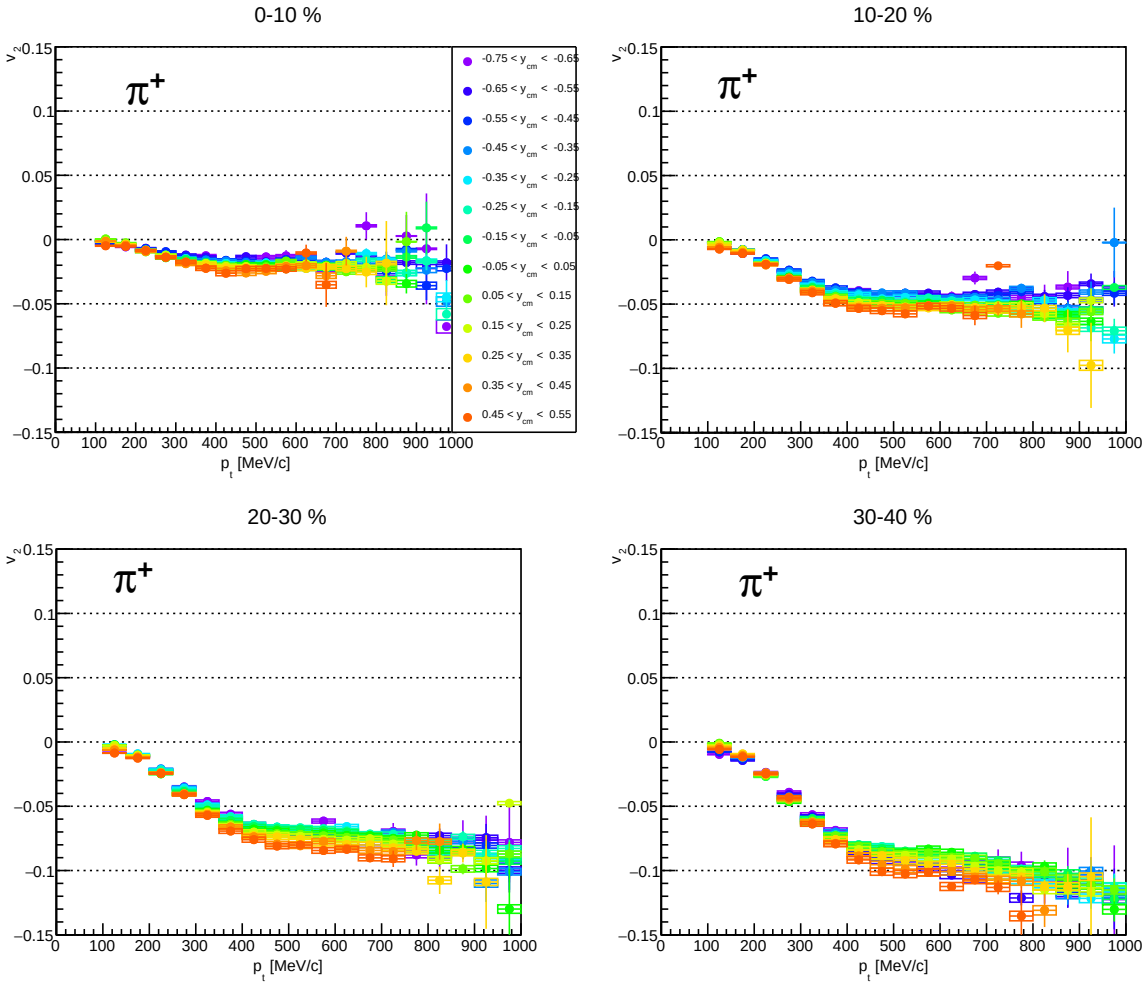

Figure 3.64: π^+: v_2 flow for a 10 % centrality binning up to 40 % most central collision. Displayed is the functional dependence from transverse momentum p_t. The plotted spectra are shown for different rapidity bins within the range of $-0.65 < y_{cm} < 0.55$ The boxes correspond to the total systematic errors. Lines represent statistical errors.

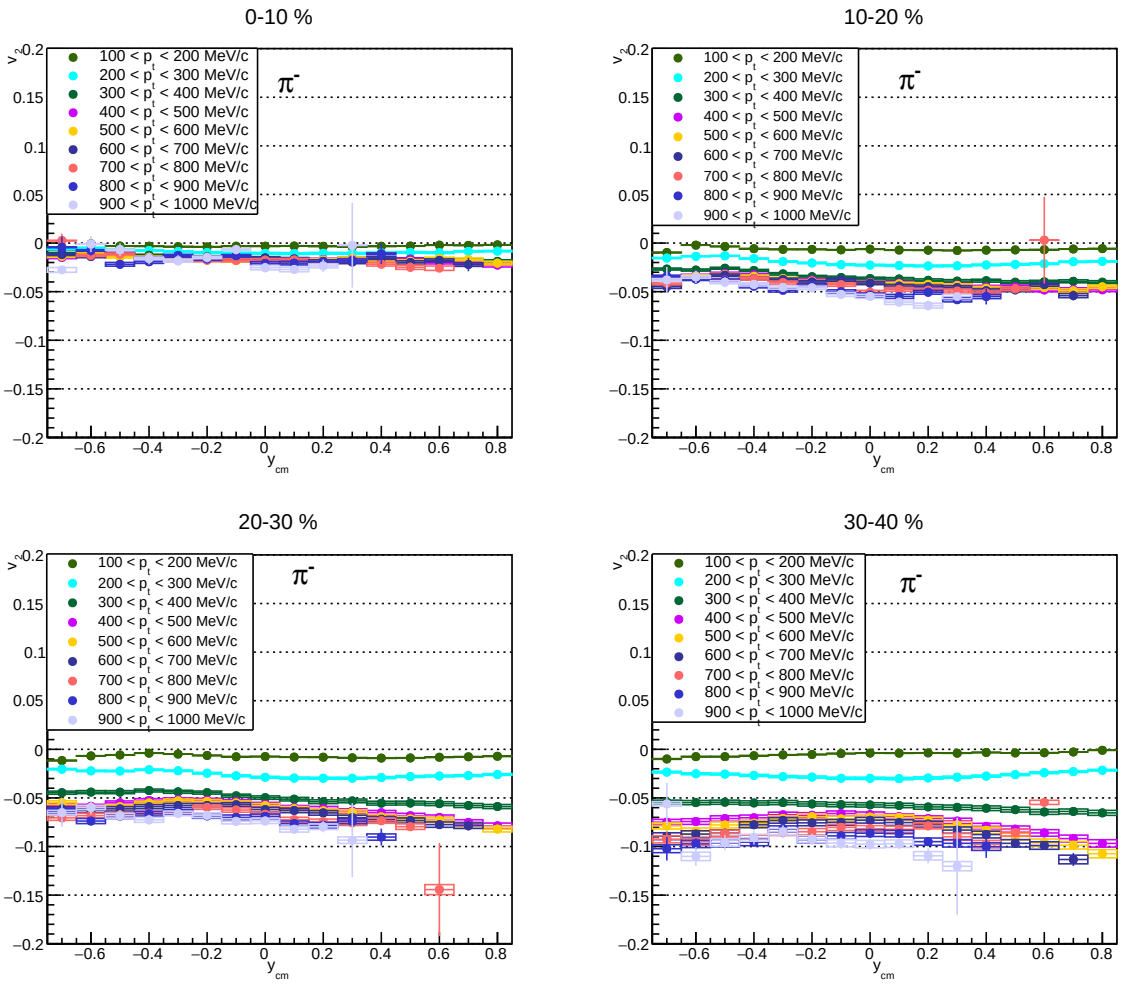

Figure 3.65: π^- v_2 for the centrality classes 0-10 %, 10-20 %, 20-30 % and 30-40 %. Displayed is the functional dependence in terms of the centre of mass rapidity y_{cm}. The spectra are shown for different transverse momentum bins in the range of 100 to 1000 MeV/c. The bin width is 100 MeV/c. The boxes correspond to the total systematic errors. Lines represent statistical errors.

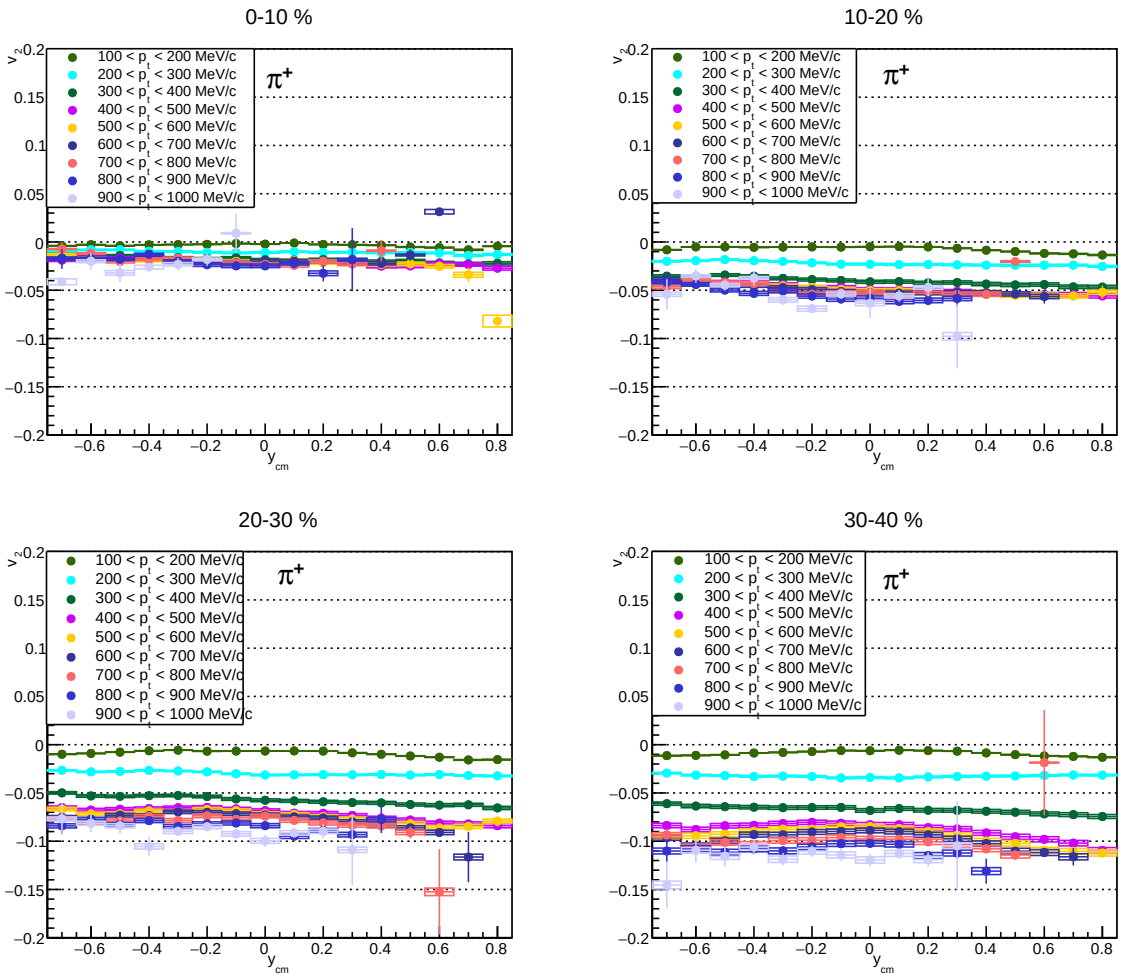

Figure 3.66: π^+: v_2 for the centrality classes 0-10 %, 10-20 %, 20-30 % and 30-40 %. Depicted is the functional dependence in terms of the centre of mass rapidity y_{cm}. The spectra are for different transverse momentum bins in the range of 100 to 1000 MeV/c. The bin width is 100 MeV/c. The boxes correspond to the total systematic errors. Lines represent statistical errors.

Figure (3.65) and (3.66) reveal that elliptic flow is found to be rather low ($|v_2| < 0.04$) for 0 to 200 MeV/c. For $p_t > 200$ MeV/c, the magnitude of v_2 increases. This holds till $p_t \approx 400$ MeV/c. For higher transverse momenta v_2 exhibits a saturation plateau, which maximum value increases towards peripheral collisions. Comparing the π^- with the π^+ mesons, it is observed that the reached plateau value of $|v_2|$ is in general slightly higher for positively charged pions. Comparing the different rapidity ranges reveals that they approximately exhibit the same qualitative shape. Also, quantitatively, they are similar as they lie on top of each other. This holds in particular for $p_t < 500$ MeV/c. For higher momenta, the difference between rapidity bins slightly increases. This is visible explicitly, when looking at the rapidity dependence in figure (3.65) and (3.66) for the bins with higher transverse momenta: In the range of $p_t < 500\ MeV/c$, a rather flat shape is observed. For higher transverse momenta $p_t > 500\ MeV/c$, the constant behaviour declines and fluctuations between the different rapidity bins occur. Yet, also

the statistical uncertainties increase in this region.
Overall, it is observed that the elliptic flow coefficient is negative for both charges and all centrality classes, leading to the conclusion that charged pions are generally emitted out off the reaction plane, particularly those with transverse momenta larger than 200 MeV/c.

3.8.3. Triangular Flow v_3

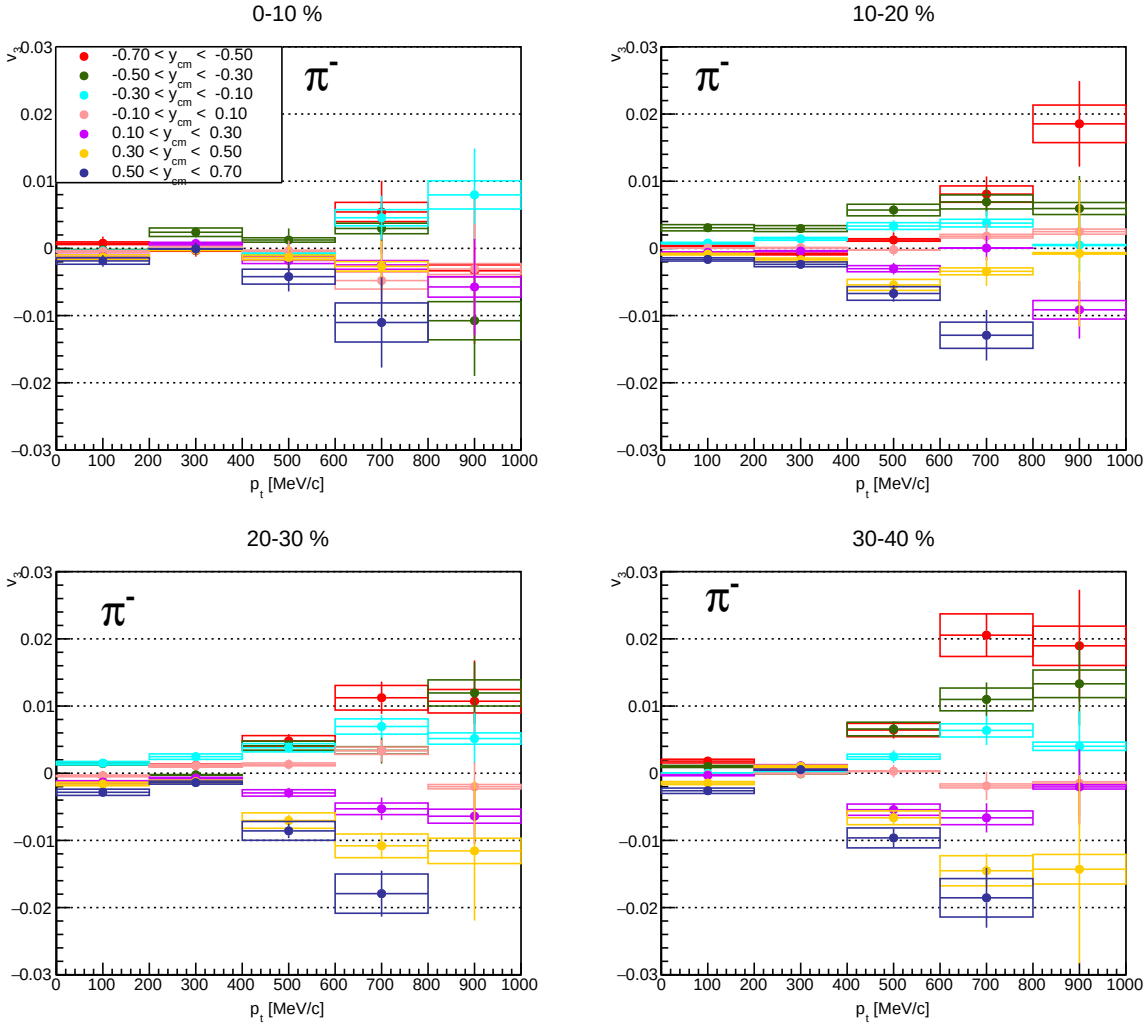

Figure 3.67: π^-: v_3 for the centrality classes 0-10 %, 10-20 %, 20-30 % and 30-40 %. Displayed is the functional dependence in terms of transverse momentum p_t. The spectra of different rapidity bins are shown with in the range of $y_{cm} = -0.7$ and $y_{cm} = 0.7$. The bin size is 0.2. The boxes correspond to the total systematic error. Lines represent statistical errors.

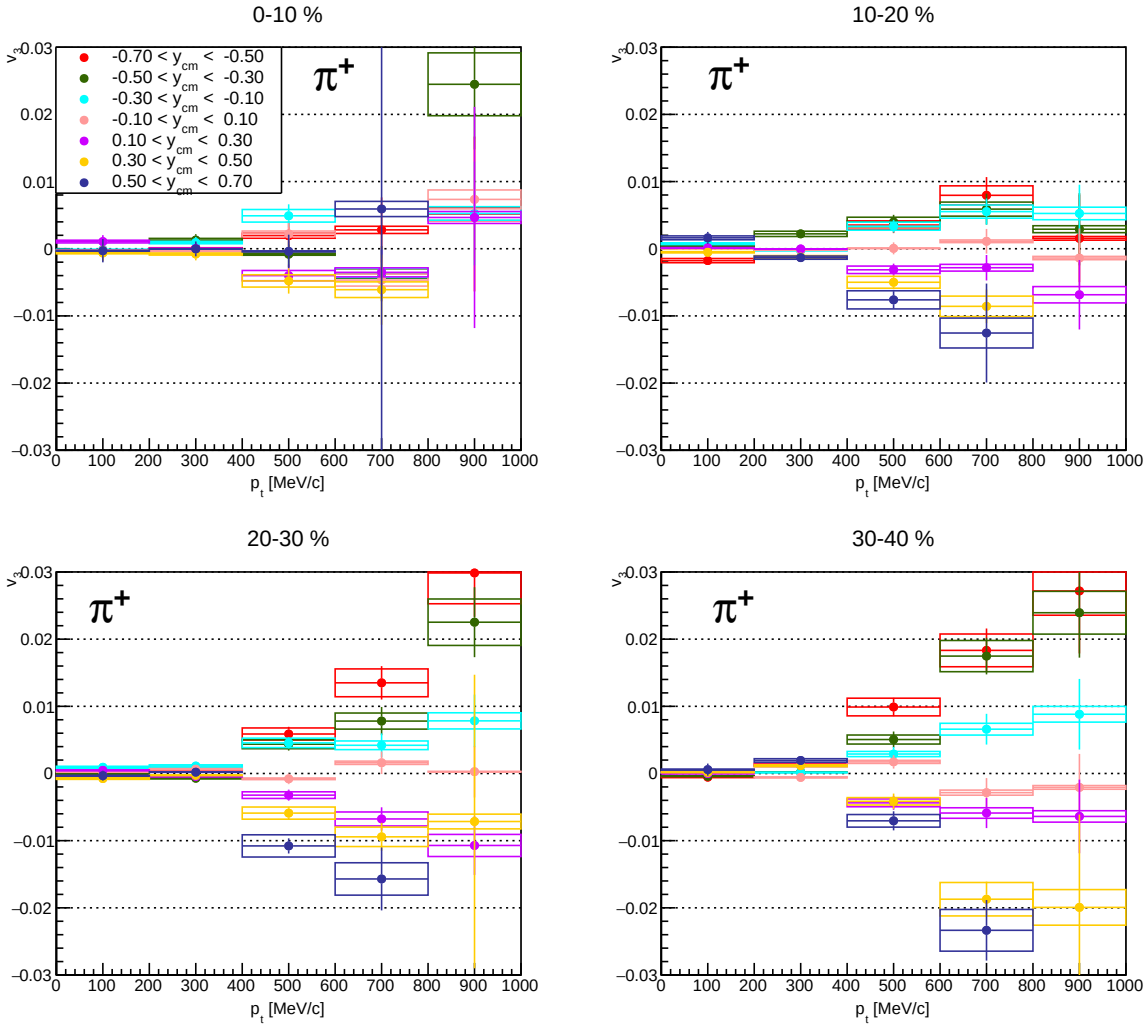

Figure 3.68: π^+ v_3 flow for the centrality classes 0-10 %, 10-20 %, 20-30 % and 30-40 %. Displayed is the functional dependence in terms of transverse momentum p_t. The spectra of different rapidity bins are shown with in the range of $y_{cm} = -0.7$ and $y_{cm} = 0.7$. The bin size is 0.2. The boxes correspond to the total systematic error. Lines represent statistical errors.

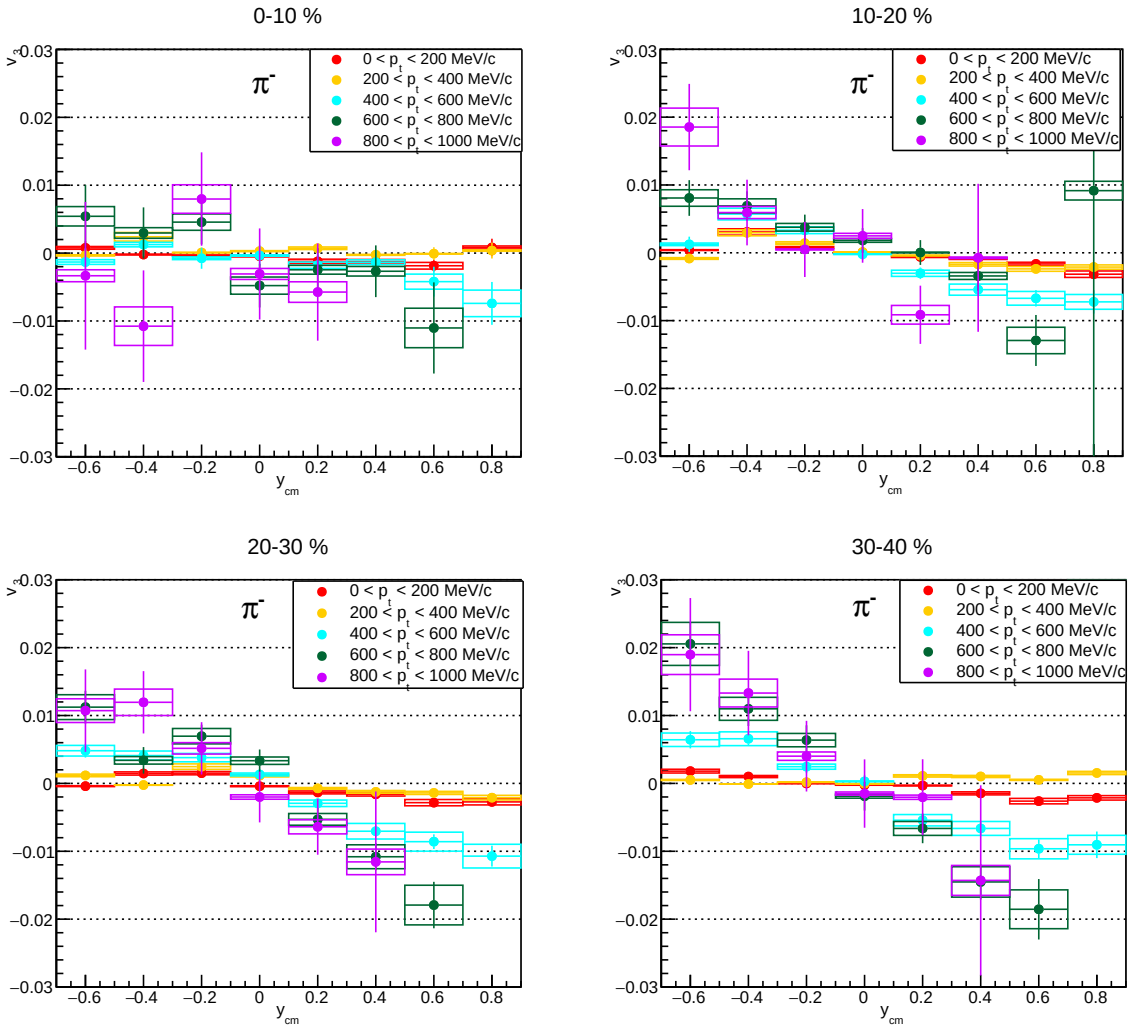

Figure 3.69: π^-: v_3 flow for the centrality classes 0-10 %, 10-20 %, 20-30 % and 30-40 %. Displayed is the functional dependence in terms of centre of mass rapidity y_{cm}. The spectra of different transverse momentum bins are shown in range the of 0 and 1000 MeV/c. The bin size is $\Delta p_t = 200\ MeV/c$. The boxes correspond to the total systematic error. Lines represent statistical errors.

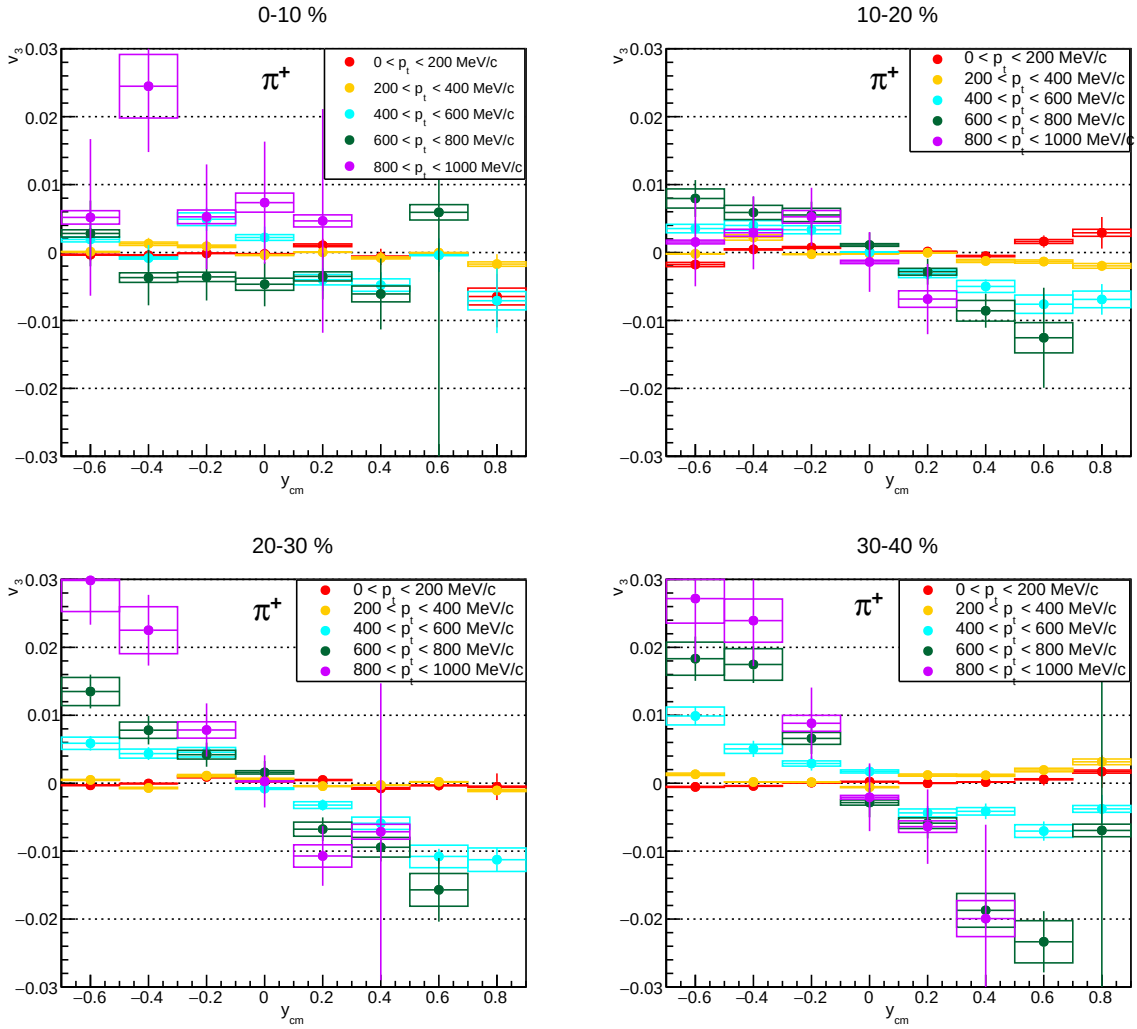

Figure 3.70: π^+: v_3 flow for the centrality classes 0-10 %, 10-20 %, 20-30 % and 30-40 %. Displayed is the functional dependence in terms of centre of mass rapidity y_{cm}. The spectra of different transverse momentum bins are shown in the range of 0 and 1000 MeV/c. The bin size is $\Delta p_t = 200\ MeV/c$. The boxes correspond to the total systematic error. Lines represent statistical errors.

Compared to the lower order harmonics, the contribution of triangular emission is found to be much smaller, in the order of $v_3 < 0.03$. Triangular flow as a function of p_t (3.67) (π^-) and (3.68) (π^+) exhibits a pattern similar to directed flow (3.8.1): Triangular flow is getting closer to zero and somewhat flat towards mid-rapidity. For increasing magnitude in rapidity, a rising v_3-flow is observed for transverse momenta higher than 400 MeV/c. In the most outer rapidity bin, a maximum of v_3 flow of 0.02 and 0.03 for the π^- and π^+ is measured. In general, the divergence between the forward and backwards bin seems to be roughly point-symmetric relative to mid-rapidity. This symmetry can also be explicitly inspected when looking at the direct rapidity dependence, shown in figure (3.69) and (3.70). As observed for directed flow, approximate point-symmetry is exhibited. As for the lower harmonics in general, an increase of the maximal reached flow is observed for the most outer rapidity bins with high transverse momenta ($p_t > 800\ MeV/c$).

4. Discussion and Summary

In this chapter, the obtained results are discussed regarding potential physical interpretations. The structure is as follows: At first, the findings of the extracted Coulomb potential and the derived baryon density as well as an estimation of the baryon-chemical potential in terms of their scaling as a function of the number of participants is examined. Furthermore, the extracted Coulomb potential out of mid-rapidity and the π^-/π^+-ratio are explored and interpreted.
In the second part of this chapter, the determined 4π-production rates are considered as a function of the system size and contrasted to the world data on charged pion production from the same energy regime. Furthermore, the differences of the dN/dy distributions between low and high transverse energy pions are interpreted.
The last part of this chapter covers the findings of the anisotropic flow analysis: Discussed are the observed functional dependencies of the harmonics v_1, v_2 and v_3 from the considered kinematic variables: transverse momentum and rapidity. To provide a condensed picture, v_1 is considered p_t integrated and its slope is determined at mid-rapidity. Finally, to initiate the understanding of underlying physical processes leading to the emergence of azimuthal anisotropies, a comparison with the transport models UrQMD Cascade, GiBUU and UrQMD EOS is conducted.

1. Coulomb Effect

1.1. A_{part}-Scaling of the Coulomb Potential and Baryon Density

In section 2 the $Acc \cdot Eff$-corrected transverse spectra of charged pions, emitted in Ag+Ag collisions at $1.58A\ GeV$, are fitted by a modified version of the Boltzmann functions, aiming to provide a description of the Coulomb interaction. Within the implemented Coulomb model proposed in [14], it is assumed that the protons generate the net charge in the fireball. The spectator charges are ignored with the argument that they move rapidly out of the collision zone. This is justifiable, particularly for the most central collisions, as the number of spectators is small compared to the number of protons in the reaction zone. However, with increasing impact parameter as well as beyond mid-rapidity, the impact of the spectator charges might play a non-negligible as indicated in [59]. Their effect will be discussed further in the subsequent section (1.3). The expansion of the fireball is considered by assuming an effective potential that depends on the pion energy and the proton's velocity distribution. The scaling of the extracted Coulomb potential in terms of the number of participants A_{part} is investigated at mid-rapidity, see figure (4.1). For the centrality class 0-10 %, exhibiting an average number of participants of $< A_{part} >= 160.9 \pm 6.9$, the Coulomb potential is largest with a value

of $V_c = 8.1 \pm 0.5\ MeV$. V_c decreases towards peripheral collisions, reaching the lowest measured value at $< A_{part} >= 38.1 \pm 4.7$ (40-50 %) with $V_c = 2.3 \pm 0.5$. The observed scaling can be qualitatively explained by the decreasing number of protons within the reaction zone towards peripheral collisions. It is found that the A_{part}-dependence, quantified by $\alpha = 0.77 \pm 0.1$, see figure (4.1), is weaker than linear. This observation can be interpreted by assuming that the radius of the assumed charged sphere is a function of the number of participating nucleons: If the radius of the fireball scales like a nucleus, it would hold: $R \approx A_{part}^{1/3}$, see, e.g. [13]. According to equation (3.40) for the mean potential of a charged sphere follows: $V_c \approx A^{2/3}$. However, for the experimental data, α is larger than this prediction by 17 %, which might be due to the neglected spectators' charges.
The observed A_{part}-scaling is qualitatively in accordance with the results from charged pions in Au+Au reactions at $1.23A\ GeV$ [21]. A direct comparison for the centrality class 0-10 % is difficult as the beam energy differs and the Coulomb potential has not been extracted for the same average number of participants. When extrapolating to $< A_{part} >= 303$ using the fitted scaling function one yields a potential of 13.2 ± 0.7 MeV, compared to the Coulomb potential of $V_c = 13.6 \pm 0.7\ MeV$ which has been extracted for Au+Au [21] at 0-10 % centrality. A lower value might be the result of the higher beam energy of the Ag+Ag experiment: As figure (1.6) from [21] visualizes, the Coulomb Potential in general decreases rapidly with increasing beam energy.

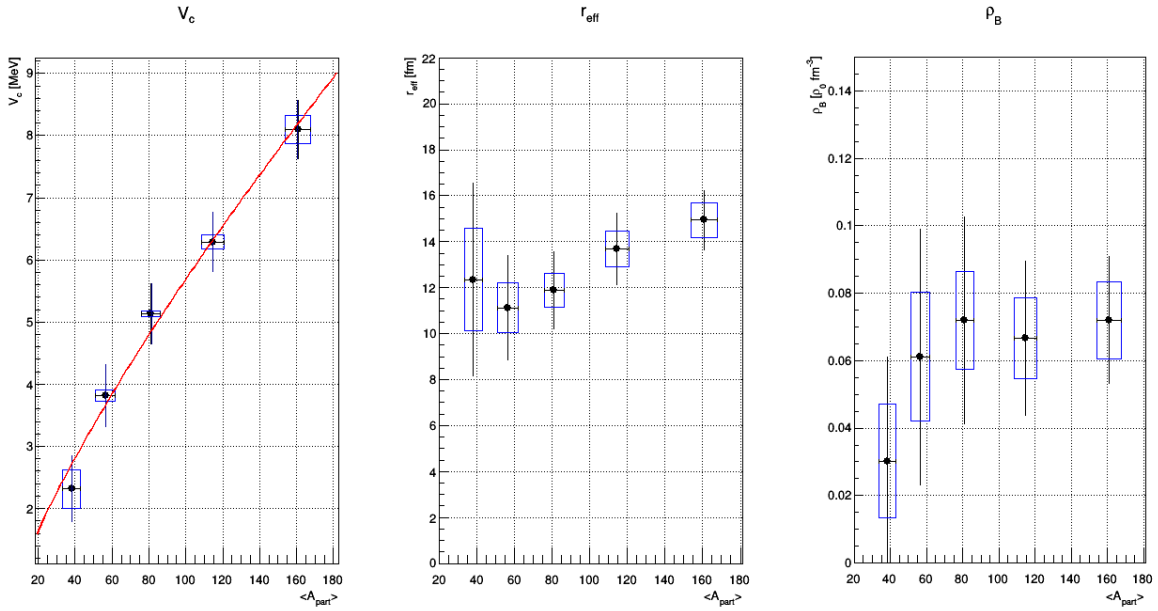

Figure 4.1: Left: Extracted Coulomb potential at mid-rapidity as a function of $< A_{part} >$. The values shown correspond to the average between the p_t and m_t based spectra analysis, see section (3.25) for details. Plotted are both the statistical (lines) and systematic errors (Boxes, difference between p_t and m_t). Middle: Derived effective radius of the assumed spherical fireball. Right: Calculated baryon density. The error of r_{eff} and ρ_B result from Gaussian error propagation of the errors of V_c.

Based on the assumption that the Coulomb field is generated by an uniform charge

distribution exhibiting spherical geometry, an effective radius r_{eff} of the fireball is calculated for each centrality class, see section (3.42). The observed scaling in regard of the number of participants A_{part} results in $\alpha = 0.23 \pm 0.2$ for the radius-A_{part}-scaling after propagating the A_{part}-dependence of V_c in equation (3.40). The calculated effective radius is in the range from $15.0 \pm 1.1\ fm$ (0-10 % most central event) to $12.8 \pm 2.7\ fm$ (40-50 % most central events). Based on the volume of the assumed effective charge distribution, the baryon density ρ_B is estimated, see figure (4.1) (right). The calculated baryon densities are in the range of $0.07 \pm 0.02\ \rho_0 \cdot fm^{-3}$ (0-10 %) to $0.03 \pm 0.03\ \rho_0 \cdot fm^{-3}$ (40-50 %) [1]. The errors are enhanced through the propagation in equation (3.35) leading to uncertainties of up to 30 % in the most peripheral collisions. This prevents serious statements about the functional dependence. From a theoretical point of view, assuming a $A^{2/3}$-scaling of the Coulomb potential, constancy of ρ_B as function of A_{part} is expected. Considering the error range this can be confirmed. However, it has to be kept in mind that the fireball is described by an idealized charge distribution, which probably does not exactly correspond to the situation in nature. Moreover, in order to enable more advanced descriptions, models that also consider the reaction dynamics and interaction processes on a microscopic level as well as properly incorporate the spectator charges are required.

The inverse-slope-parameters extracted at mid-rapidity are displayed in figure (4.2) as a function of the number of participants. Plotted are both the results from the Coulomb fits assuming common parameters for the two polarities as well as the ones obtained with the standard Double Boltzmann functions with distinct slope parameters for the charges. For all variants a linear increase with increasing $< A_{part} >$ is observed. This might be explained by the number of scattering processes which increases with a rising number of particles in the system, resulting in an average higher kinetic energy, manifesting in a higher freeze-out temperature. A deviation between the parameters from the two different transverse functions is found. According to the Coulomb inclusive version an effective temperature of $T_2 = 99.15 \pm 2$ and $T_1 = 54.7 \pm 0.8$ is extracted at mid-rapidity for the most 0-10 % central events. For the standard fitting procedure, using different inverse slope parameter for the two polarities, values of $T_2 = 97.8 \pm 0.6$ (π^-) and $T_1 = 50.6 \pm 0.7$ (π^-) and $T_2 = 104 \pm 2$ (π^+) and $T_1 = 61 \pm 1$ (π^+) are extracted.

[1] $\rho_0 = 0.16\ fm^{-3}$ corresponds to the nuclear saturation density [13].

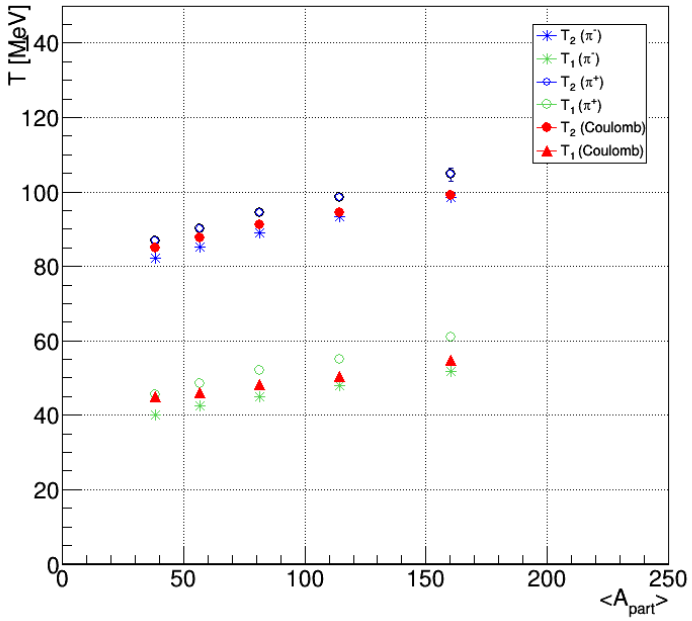

Figure 4.2: Extracted inverse-slope parameters at mid-rapidity for the 0-10 % most central events. For the Coulomb fits common T_1 and T_2 for the two charges are assumed (red symbols). Furthermore, T_1 and T_2 from the Standard-Boltzmann fits with different values for π^- and π^+ are displayed.

1.2. Baryon-Chemical Potential

The estimated baryon density enables to draw a conclusion to the baryon-chemical potential μ_B, allowing to approximately determine the location in the QCD-Phase space diagram of the fireball created in Ag+Ag collisions at $1.58A\ GeV$. In order to connect the baryon density with a chemical-potential, an appropriate relation between the two macroscopic quantities μ_B and ρ_B has to be assumed. For an ideal hadron gas, the relation is given as, e.g. in [39]:

$$\mu = m_N + T \cdot ln(\frac{\rho_B}{g}(\frac{m_N \cdot T}{2\pi})^{-3/2}(\hbar c)^{-3}). \tag{4.1}$$

Where $m_N = 938\ MeV$ corresponds to the mass of a nucleon. g describes the degeneracy of the hadron gas, for nucleons g is set to 4. T corresponds to the temperature of the hadron gas. Thereby, the underlying assumption is, on the one hand, that after the kinematic freeze-out, the reaction products behave according to an ideal hadron gas. Though, this is not necessarily the case, e.g. due to weak decays. On the other hand, an appropriate value for the temperature T has to be assumed. An adequate description requires a determination of a realistic temperature that is representative of the whole fireball at the point of freeze-out. Based on the charged pion analysis, the temperature range can be constrained using the inverse slope parameters T_1 and T_2 from the Boltzmann fits.

In figure (4.3) the computed baryon-chemical potential at mid-rapidity is displayed as a function of the average number of participating nucleons $< A_{part} >$ for both T_1

(left) and T_2 (right). The errors shown originate from Gaussian error propagation of the statistical parameter errors in equation (4.1).

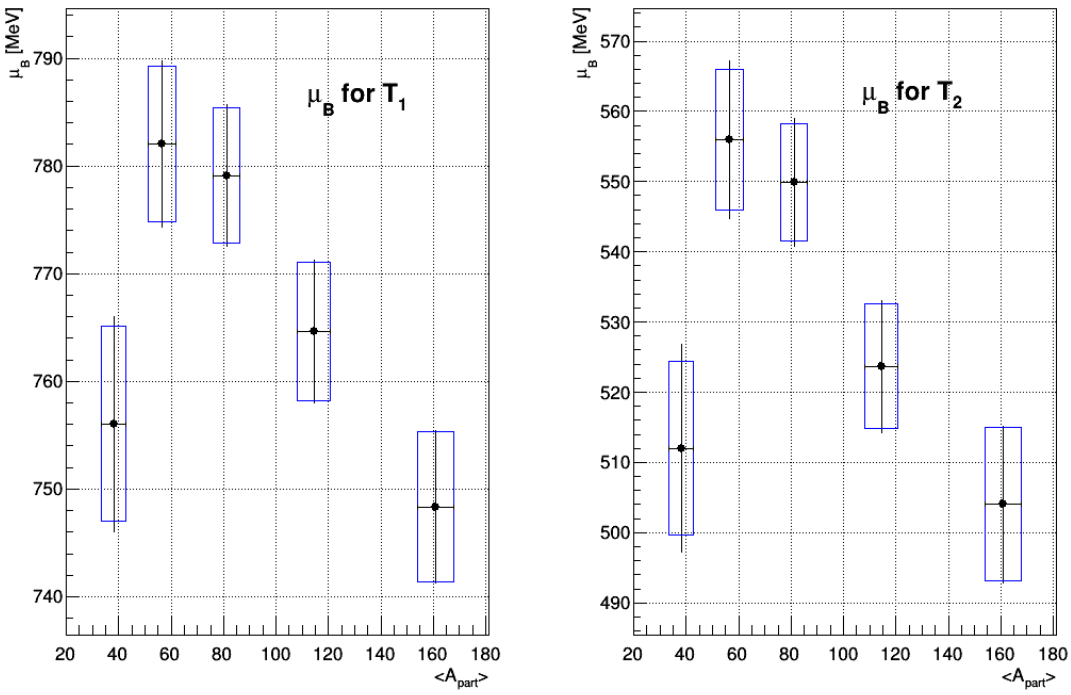

Figure 4.3: Estimated baryon-chemical potential μ_B at mid-rapidity as a function of $< A_{part} >$. The calculation is based on the baryon density, which is calculated assuming a spherical and uniform charge distribution, see section (4.6). μ_B is obtained by equation (4.1), describing an ideal hadron gas. In addition μ_B is determined by the temperature of the hadron gas. From the charged pion spectra fits two inverse-slope parameter are available. As it is not unambiguous which parameter provide the most representative description of the fireball, μ_B is calculated for both variants. The left plot displays μ_B for T_1, describing the low energy regions of the transverse spectra. The right plot displays μ_B for T_2. The plotted errors follow from Gaussian error propagation.

It is observed that the higher values of T_2 lead to a baryon-chemical potential of $503 \pm 11\ MeV$, in the most 0-10 % central events. This is by 32 % lower compared to the calculation based on the inverse-slope parameter T_1: In this case the chemical potential is $747 \pm 6\ MeV$ in the most 0-10 % central events. For the dependence in terms of $< A_{part} >$, a small increase towards peripheral events, exhibiting a local maximum within the centrality class $20 - 30$ %, is observed. As the Delta-Resonances dominate, they represent the bulk of the fireball matter. Hence the calculation based on T_1 might provide a more realistic one.

1.3. Coulomb Potential away from Mid-Rapidity

The Coulomb modified Boltzmann function is used to fit the transverse charged pion spectra out of mid-rapidity, see section (2.3.3). In figure (4.4), the symmetrised [2] value of V_c as a function rapidity is displayed. The potential rises with increasing rapidity throughout all analysed centrality classes, with an approximate parabolic pattern. However, a precise quantitative statement about the functional behaviour in regard to rapidity is not reliable as the parameter errors increase, and the underlying Coulomb model dose does not include the spectator charges. Besides that, out of mid-rapidity, the assumption is incorporated that the parametrisation of the inverse slope parameters for both the pions and protons follow the prediction of the statistical model, exhibiting a $1/cosh(y_{cm})$-scaling. Yet, this is not precisely the case, especially for the pions originated in lower transverse energy regions, mainly attributed to Delta-Resonances (see discussion section (2.2)). Furthermore, the expansion model of the fireball assumes isotropy, which is also not exactly realised as the analysis of anisotropic collective flow proves.
From a qualitative perspective, the observed behaviour, that V_c rises with increasing forward/backward rapidity can be attributed to the spectators: Charged pions with high longitudinal velocities (high magnitude of centre of mass rapidity) are more likely to enclose spectator charges, which causes them to fell a higher Coulomb force. This dependence has been already predicted indirectly by the CBUU transport model by examining the π^-/π^+-ratio as a function of the polar emission angle (as an alternative measure for the longitudinal kinematics) in the centre of mass system [59].

[2] Symmetrized: The resulting value corresponds to the average between the forward and backward value.

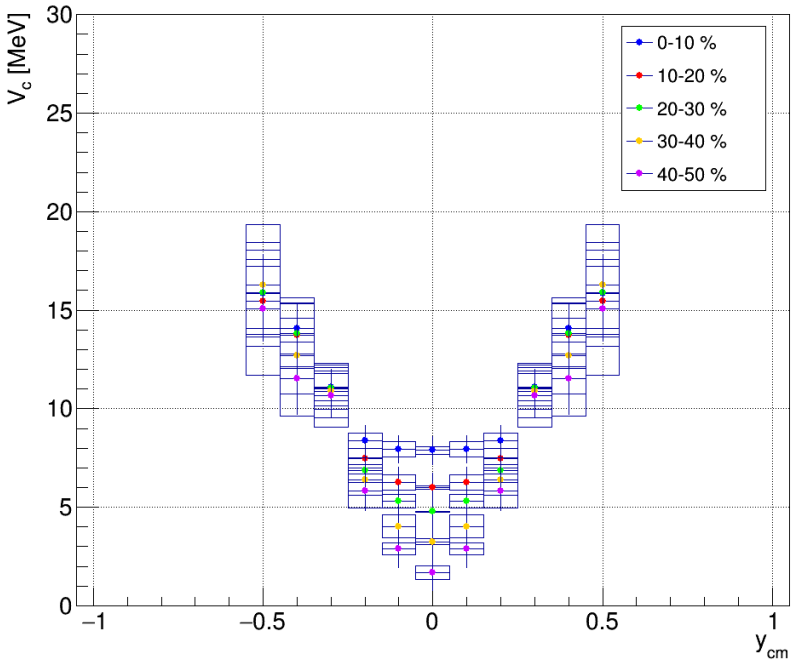

Figure 4.4: Symmetrized Coulomb potential as a function of rapidity in the centre of mass system for the five analysed centrality classes. V_c exhibits a minimum at around mid-rapidity. With increasing forward and backward rapidity the potential increases as well. Lines correspond to the statistical errors and boxes to the differences between m_t and p_t based analysis.

1.4. Coulomb Modified Extrapolation and π^-/π^+-Ratio

It is found that the Coulomb function provides a slightly better agreement with the measured data in low transverse momenta (mass) bins, for the π^+, see section (3.36). The resulting differential yields on the rapidity density distribution dN/dy are compared to the variant of standard Boltzmann extrapolation, see figure (3.7). The differences are found to be small for the π^-, for the transverse spectra around mid-rapidity, the relative difference is less than 1 %, only for the outer rapidity bins the relative differences increase. For the positively charged pions, the observed differences around mid-rapidity are more considerable. The yield for the π^+, using the Coulomb modified function, is by 3 % smaller compared to the standard Boltzmann transverse extrapolation. This difference between the polarities is due to the sightly better coverage for the π^-, making the yield less dependent on the extrapolation. For the total yield with respect to the entire solid angle of 4π, the Coulomb transverse extrapolation results in $9.6 \pm 0.7 \pm 0.2$ π^+-mesons per event for the centrality class 0-10 %. Instead, for the standard Boltzmann extrapolation, the total yield is $9.9 \pm 0.7 \pm 0.2$ π^+-mesons per event. This, of course, also impacts the ratio between the π^- and π^+ multiplicities. In the case of the standard Boltzmann extrapolation, the ratio is 1.38 ± 0.12 in the centrality class 0-10 %. For the most central events, the transverse extrapolation considering the Coulomb effect increases the ratio to a value of 1.45 ± 0.12. The ratio is also looked at as a function of rapidity, see figure (4.5).

It is revealed that the ratio varies between 1.33 ± 0.2 and 1.55 ± 0.2. At mid-rapidity, a ratio of 1.39 ± 0.2 is found. For the rapidity bins $y_{cm} = 0.6 \pm 0.05$ and $y_{cm} = -0.5 \pm 0.05$ local maxima are exhibited with a ratio of 1.52 ± 0.18 and 1.57 ± 0.18. This structure might indicate a correlation with spectator effects for charged pion emitted with higher rapidities.
The observed polarity asymmetry, expressing in the higher abundance of negatively charged pions, has also been reported by various other heavy-ion experiments with a neutron excess in the investigated systems. The isobar model [61], which is based on iso-spin conservation, predicts a theoretical ratio of: $\frac{5N^2+N*Z}{5Z^2+N*Z} = 1.54$. Hereby A=108 and Z=47 are the mass and proton number of a sliver nuclei.

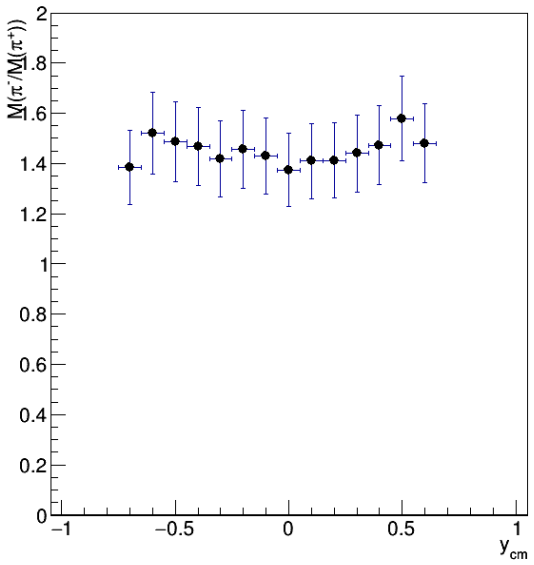

Figure 4.5: π^-/π^+ ratio as a function of the centre of mass rapidity. The prediction of the iso-bar model is 1.54. As a function of rapidity, the found ratios vary between 1.33 ± 0.18 and 1.55 ± 0.18.

In summary, the Coulomb inclusive Boltzmann model allows for a better description of the data in the low transverse momentum region, leading to a more sophisticated extrapolation to zero p_t and extraction of the effective temperature, in particular for the positively charged pions. For mid-rapidity, the exacted Coulomb potential as a function of the number of participant nucleons is connected to an effective system size of the fireball at the point of kinematic freeze-out. Moreover, this allows to roughly estimate the baryon density as well as, if an ideal hadron gas is presumed, the baryon-chemical potential. For a more accurate analysis of the Coulomb effect, especially out of mid-rapidity, more sophisticated Coulomb models, like transport based approaches, needed to be employed, which also tread the influences of the spectators.

2. Charged Pion Production

2.1. Yield A_{part}-Scaling

The pion production analysis is performed in terms of the centrality of the collision with 5 different classes, for the range 0-50 % with a 10 % binning, aiming to investigate the system size dependence. In order to check the scaling of the 4π yields, the obtained

multiplicities are plotted as a function of the average number of participating nucleon $< A_{part} >$. In order to quantify the scaling, the multiplicities as function of $< A_{part} >$ are fitted by a simple polynomial function with a free exponent:

$$M(\pi^{\pm}) = C < A_{part} >^{\alpha} . \tag{4.2}$$

C describes the slope, and α indicates whether the scaling deviates from a linear form. The scaling is checked for both the yields resulting from the Standard-Boltzmann and the Coulomb modified approach.

The fitted functions reveal a scaling that can be regarded as approximately linear for both variants. For negatively charged pions, it is found: $\alpha = 1.02 \pm 0.10$ (Standard-Boltzmann-Transverse-Extrapol.) and $\alpha = 1.04 \pm 0.12$ (Coulomb-Boltzmann-Transverse-Extrapol.). For positively charged pions, alpha is found to be $\alpha = 0.98 \pm 0.07$ (Standard-Boltzmann-Transverse-Extrapol.) and $\alpha = 0.98 \pm 0.12$ (Coulomb-Boltzmann-Transverse-Extrapol.).

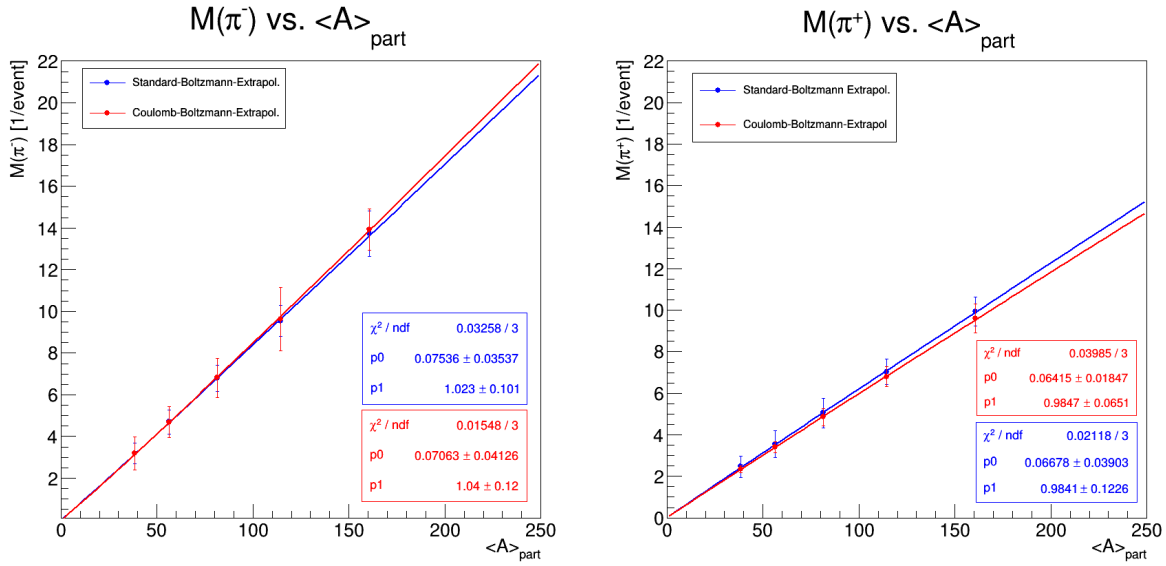

Figure 4.6: Charged pion multiplicities as a function of the number of participating nucleons (Left: π^-, Right: π^+). The A_{part} scaling is quantified by the parameter α, corresponding to the exponent of a simple polynomial function (4.2).

2.2. Rapidity Pattern - Differences between Charged Pions in the Low and High Transverse Momentum Region

The rapidity pattern in dependence on the transverse energy region, is investigated by integrating the adjusted Double-Boltzmann terms separately, see section (1.8.2). As opposed to the extrapolation of the superposed yield, the adjusted analytic functions are integrated only. As figure (4.7) displays, the rapidity distribution dN/dy_1 for the low energy region are broader compared to the dN/dy_2 distribution, for the high transverse energy region. The width of the fitted Gaussians of dN/dy_1 increases towards peripheral collisions. In the most considered central events (0-10 %), the σ of dN/dy_1 is 2 times higher compared to the pions in the higher transverse energy region. In the considered most peripheral events, for the centrality class 40-50 %, the σ of dN/dy_1 is even 10 times

higher than for dN/dy_2 and not any more describable by a simple Gaussian. Throughout all centrality classes, the yield of dN/dy_1 is higher than for dN/dy_2, suggesting that the charged pion emission is dominated by Δ-resonances. A difference in the width of the distributions has also been reported for charged pions from Au+Au reactions in the energy regime around 1A GeV in [37].
Another remarkable characteristic observed is the formation of a plateau for dN/dy_1 towards peripheral collisions. In the centrality class 30-40 % local maxima start to appear, for $y_{cm} = -0.4$ and $y_{cm} = +0.4$. Such a structure is similar to the rapidity pattern observed for protons in semi-central events [55]. To investigate this further, the dN/dy distributions of the protons extracted from the same experiment are plotted on the right hand side of figure (4.7) on top of dN/dy_1 of the π^+ mesons. Whereby the proton spectra are scaled to be at the same value as the pions at mid-rapidity. For the protons it also observed that the width of the distributions increase towards peripheral collisions and in the 10-20 % most central collisions also a vale like structure is exhibited. For 20-30 % centrality, maxima are found at the edges. The distribution width is similar to what is found for dN/dy_1 of the charged pions. Yet, the shape around the maxima does not exactly coincide with the value of dN/dy_1. The kinematic similarities on the rapidity pattern between low transverse energy pions and protons support the assumption that these pions mainly originated via production channels that involve Δ-resonances. Δ are only sightly heavier (by 20 %), so it is plausible that they exhibit similar kinematic properties as the ground state. The observed plateau pattern, manifesting in local maxima, might be explained by the target projectile fragmentation, as this structure is enhanced towards peripheral collisions. This indicates that with increasing impact parameters, low transverse energy pions are produced in Δ-Resonance of excited nucleons not fully stopped in the collision zone. Whereas, the pattern of dN/dy_2 points towards a more thermal-like production scenario for the high energy pions.

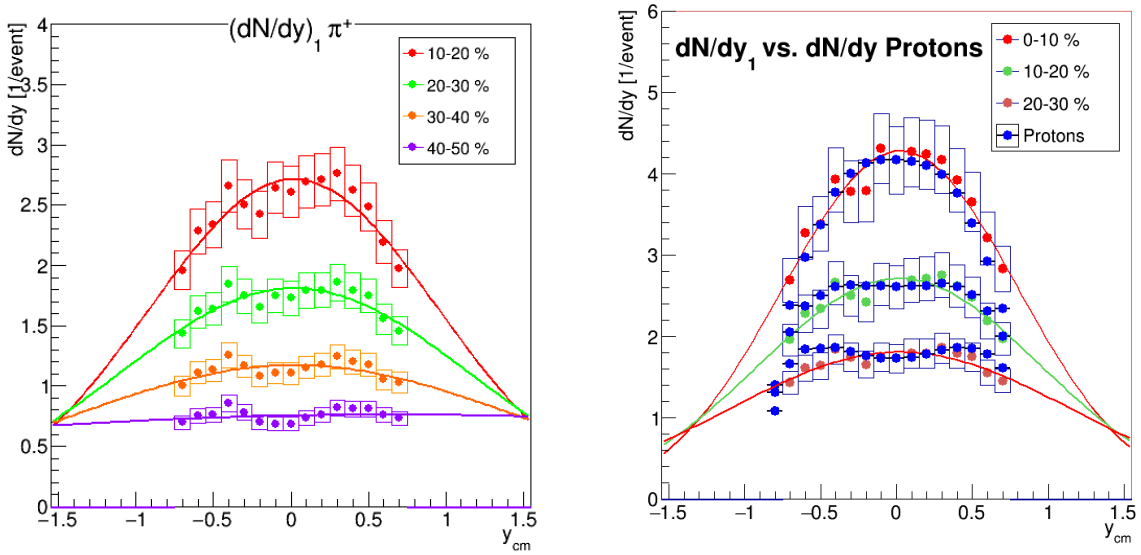

Figure 4.7: Left: Rapidity density distribution dN/dy_1 of positively charged pions, obtained when integrating the two Boltzmann terms with the lower inverse-slope-parameter T_1. dN/dy_1 shows the formation of a plateau structure with maxima towards peripheral events. Right: Comparison between dN/dy_1 of the π^+ mesons with the protons. The proton distributions are scaled to the pion distribution by considering the value at mid-rapidity. The distribution width of dN/dy_1 is found to be similar to the protons. This observation supports the assumption, that low transverse energy pions are mainly produced via Δ-resonances, as they are considered as excited nuclei.

2.3. Comparison with World Data

In this subsection, the obtained yields are contrasted to the world data on pion production for low energy collisions in the regime from 1 to 2.5A GeV. The total number of pions is calculated to compare with the world data. For charged pion one yields for the 0-10 % centrality class: $M(\pi^{\pm}) = M(\pi^-) + M(\pi^-) = 23.4 \pm 1.5$. The multiplicity of the electrical neutral pion is estimated from the charged pion yield. For this purpose, it is assumed that approximate Isospin symmetry holds [2]. It then follows: $M(\pi) = M(\pi^{\pm}) + \frac{1}{2} \cdot (M(\pi^-) + M(\pi^-) = 35.3 \pm 1.5$. The centrality classes are not suited for comparisons between experiments with different energies and systems. Therefore, the multiplicities are normalised to the average number of participant nucleons $< A_{part} >$. The left hand side of figure (4.8) displays the energy dependence of the total pion yield reconstructed from various experiments: Shown are the results from C+C reactions measured by TAPS [70] and HADES [5], from Ca+Ca, Ar+Ca, Ar+KCl-collision measured by TAPS [70], HADES [4], FOBI [52], as well as Au+Au data measured by HADES [2], FOPI [52] and E895 [38]. The orange points correspond to the obtained total pion yield obtained in this analysis for 0-10 % centrality. The depicted curves describe the excitation function; they exhibit the shape of a second-order polynomial and are the same as published in [2]. It is found that the value of $M(\pi)/ < A_{part} >= 0.22 \pm 0.01$ for Ag+Ag collisions is by 18 % lower compared to the prediction of the curve describing the scaling for Ca+Ca, Ar+Ca and Ar+KCl, but by 22 % higher than the value of the curve for Au+Au

collisions. This fits in the general observed systemic trend that the yield is increasing with decreasing system size. In order to determine an excitation function for the Ag+Ag system, measurements for other beam energies are needed in the future.
The right hand side of figure (4.8) displays a comparison of the A_{part} dependence to previous results from HADES. Considered is again the normalised yield as a function of A_{part}. Plotted in red are the results from Au+Au reactions [2], blue points correspond to measurements on the system Ar+KCl [4] and the black points to the yield from C+C collisions [5]. For the pions from Ag+Ag collision, both the results based on transverse extrapolation using the standard Boltzmann function as well as the Coulomb-Boltzmann functions are depicted. In order to allow for a valid comparison, the yields of the other HADES experiments are scaled to the analysed beam energy of $1.58A\ GeV$ using the excitation functions, shown in world data plot [2]. The used scaling factor is 1.43. For the range of 50 to 160 participants, we observe a rather flat functional dependence, with no major difference between the two extrapolation variants. As seen for the world data comparison, the yield of Ag+Ag lies in between the Ar+KCl and Au+Au reaction results, which supports the discussed system size trend. Nevertheless, this is not significant as the error bars overlap. Besides that, the applied energy scaling introduces additional uncertainty. Especially for the Au+Au data, the used excitation function has tensions as there are discrepancies between FOPI and TAPS in the energy range from 0 to 1 GeV.

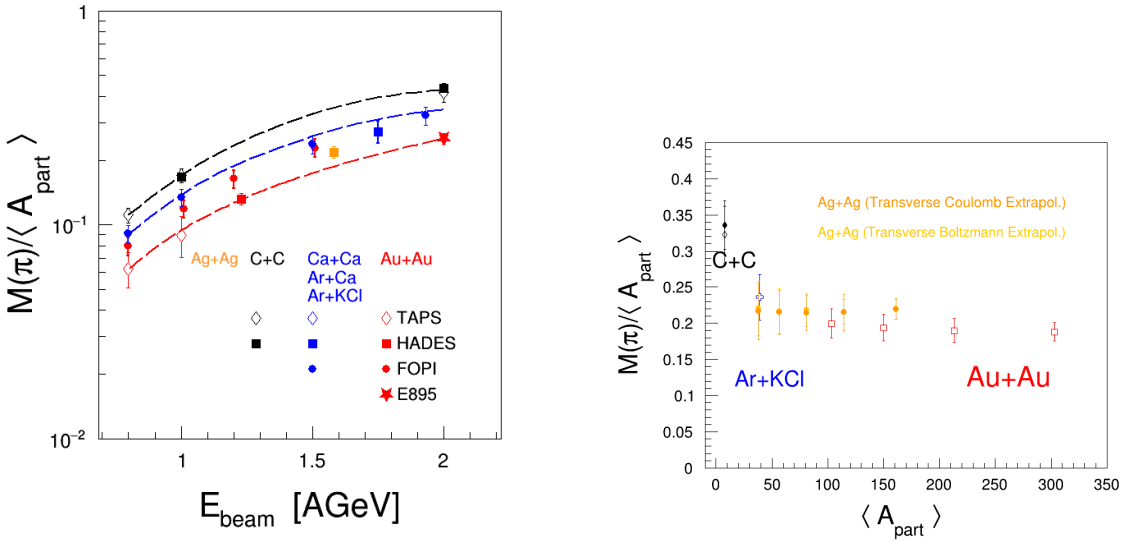

Figure 4.8: Left: Obtained total pion yield normalized to the number of $< A_{part} >$ as a function of the beam energy per nucleon in comparison with other low energy data for Ca+Ca, Ar+Ca, Ar+KCL and Au+Au collisions. Right: HADES data of $M(\pi)/ < A_{part} >$ as a function of $< A_{part} >$. Plotted in red are the results from Au+Au collisions [2], blue correspond to measurements on the system Ar+KCl [4], and the black points correspond to the yield from C+C [5] reactions. The obtained results for Ag+Ag collisions is plotted for both variants of traverse extrapolation methods based on standard Boltzmann function and Coulomb modified one. Plot taken from [2].

3. Azimuthal Anisotropies in Charged Pion Emissions

This thesis conducts a multi-differential analysis of directed, elliptic and triangular flow harmonics of charged pions from Ag+Ag collisions at $1.58A\ GeV$. The harmonics are investigated in terms of rapidity in the centre of mass system and the transverse momentum as well as a function of the collision centrality in the range from 0-40 %. The raw flow harmonics are subjected to two correction procedures. The first one accounts for fluctuations that occur in the reconstruction of the event plane due to finite hit multiplicities in the Forward wall (see section (3.4)). In order to account for the fact that the track reconstruction behaviour is multiplicity dependent, the occupancy correction is implemented to correct for non-zero directed flow at mid-rapidity (3.6). The occupancy correction is feasible for both charges for the 0-30 % centrality range. For the peripherals events, particularly for the centrality class 40-50 %, the correction does not help. However, in these events, the impact of occupancy is expected to be relatively small due to lower hit multiplicities. Here, the observed deviation of v_1 from being zero at mid-rapidity is probably due to another cause, like, e.g. influences of particles emitted from Ag+C events, which survive the applied ERAT-cut.
For all collision centralities, the magnitude of the harmonics increases with the decreasing degree of centrality of the collisions. This observation results from the increase of the spatial anisotropy of the colliding nuclei with rising impact parameter b. As discussed in section (2.1), the spatial anisotropy is translated into the momentum space, causing rising anisotropic flow with peripheral collisions. Moreover, the extracted magnitude of the flow harmonics of charged pions is found to be smaller than the harmonics determined for the protons in the same experiment [48]. E.g. in the centrality class $20-30$ % the highest reached magnitude in v_1 flow for the protons is found to be at $v_1 \approx 0.4$ [48] within the interval $0-1000\ Me/c$ at the $y_{cm} = 0.6$-bin. In the case of the charged pions the highest observed magnitude in v_1 is below ≈ 0.17 in this regions. This observation is in line with the findings from other experiments in the same beam energy regime.

3.1. Directed Flow

The results of directed flow as function of y and p_t are displayed in section (3.8.1). It is observed that directed flow increases for both polarities with increasing forward and backward rapidity. The magnitude rises with increasing transverse momentum, whereby the sign of v_1 changes at mid-rapidity. Within the statistical and systematic errors, v_1 is point-symmetric with respect to mid-rapidity. This behaviour can be understood when imaging the spatial situation right before a semi-central collision in the x-z plane (z corresponds to the beam axis): In the centre of mass system, the two nuclei move in the opposite direction relative to another. When the collision takes place, momentum conversation and the symmetry of the systems imply that the bounce off into the reaction plane has to happen in the opposite direction for the two hemispheres. Looking at v_1, as a function of rapidity, it is observed that the sign is positive for $y_{cm} > 0$ and negative for $y_{cm} < 0$ within the centrality scope of 0-20 % for the transverse momentum range $0-300$ MeV/c. Yet, the opposite is observed for more peripheral centrality ranges in the 20-40 % most central events. In order to make a condensed statement about the functional dependence of directed flow as a function of rapidity, v_1 is considered integrated over all transverse momentum bins. This condensed picture is also contemporary for comparisons

with results from other experiments and models.

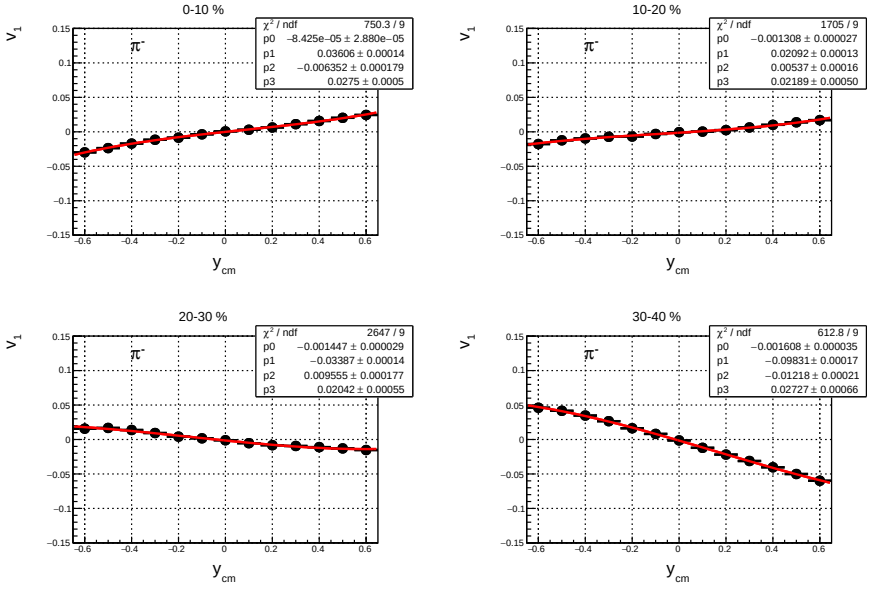

Figure 4.9: Pt-integrated directed π^- flow as a function of rapidity in the centre of mass system. The functional dependence is displayed in terms of the four analysed centrality classes in the range of 0-40 %. For quantification a third-order polynomial is fitted to extract the differential change of v_1 at mid-rapidity.

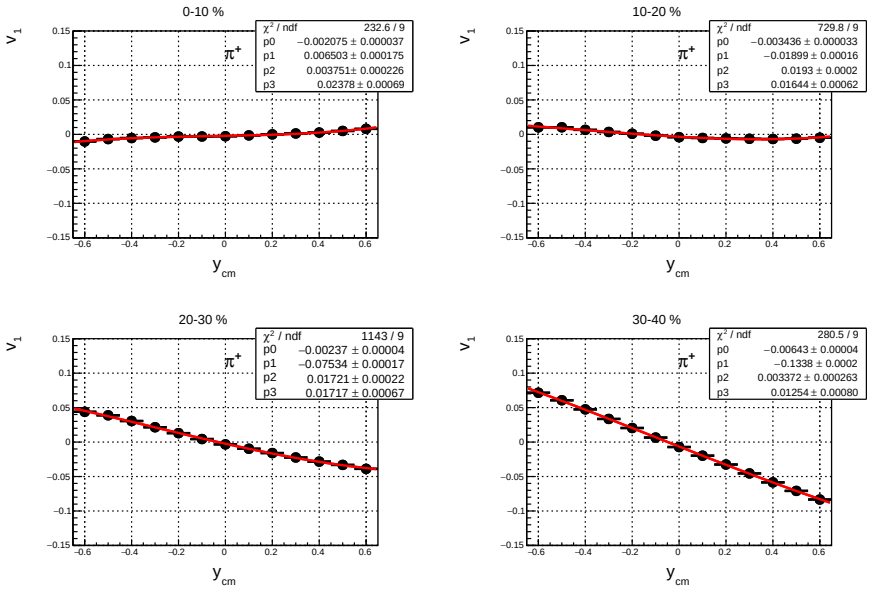

Figure 4.10: Pt-integrated directed π^+ flow as a function of rapidity in the centre of mass system. The functional dependence is displayed in terms of the four analysed centrality classes in the range of 0-40 %.

In figure (4.9) p_t-integrated directed flow as a function of rapidity is displayed. It

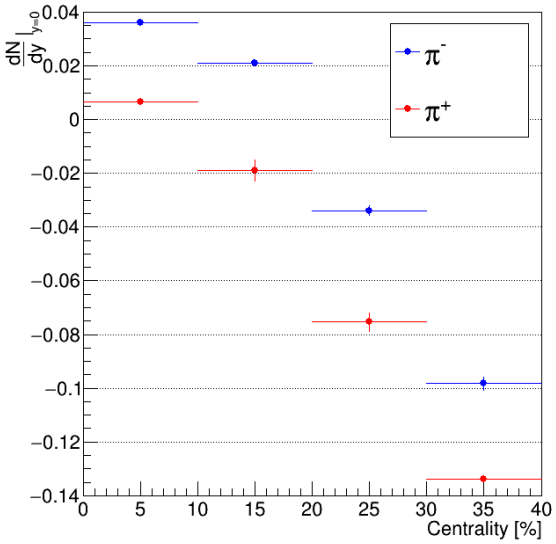

Figure 4.11: Extracted slope of v_1 at-mid-rapidity as a function of centrality. The slope is obtained by calculating the derivative $\frac{dv_1}{dy}$ of the adjusted third order polynomial. $\frac{dv_1}{dy}$ is evaluated at $y_{cm} = 0$. Red points correspond to the π^+, blue points to π^- mesons.

is observed that the slope of the course of v_1 depends on the centrality of the collision. In order to quantify the slope, a polynomial is fitted to the data points. The chosen polynomial-order is 3 as the functional dependence is point-symmetric but not of linear nature; instead, a "S" shaped structure is exhibited. The fit function used is:

$$v_1(y_{cm}) = Ay_{cm}^3 + By_{cm}^2 + Cy_{cm} + D. \tag{4.3}$$

A, B, C, D are free coefficients adjusted by χ^2 minimization. To extract the slope of v_1, the derivative of equation (4.3) of the third order polynomial is considered:

$$\frac{dv_1}{dy}(y_{cm}) = 3Ay_{cm}^2 + 2By_{cm} + C. \tag{4.4}$$

The slope is measured at mid-rapidity $y_{cm} = 0$ for all centrality classes, see figure (4.11). For the π^- mesons, the slope is positive for the centrality range 0-20 %. For 0-10 %, the exacted slope is 0.036 ± 0.002, it decrease to 0.021 ± 0.002 for the 10-20 % most central collisions. For 20-30 %, a change in sign occurs to a value of -0.034 ± 0.002. The magnitude of negative slope increase further to -0.098 ± 0.002 at 30-40 % centrality. For the π^+ mesons, the slope is close to zero for the 0-10 % most central collisions, at 0.006 ± 0.001 and decreases to -0.019 ± 0.004 within the centrality range of 10-20 %. For 20-30 %, the slope assumes the value of -0.075 ± 0.004. The highest magnitude of the slope is extracted for the considered most peripheral collisions with a value of -0.133 ± 0.001. The observed deviation between the charges is in qualitative agreement with the findings of charged pion flow in Au+Au collision [42].

For a more detailed investigation of the physical reasons, a comparison with appropriate models is necessary. Therefore, the rapidity dependence is contrasted to three different transport-based models: UrQMD (Ultra-relativistic-Quantum-Molecular-Dynamic) Cascade (Version 3.4) [47], UrQMD EOS [32], GiBUU (Giessen Boltzmann-Uehling-Uhlenbeck Project) (Release 2021) [69]. UrQMD [16] cascade corresponds to the Ag+Ag simulation also employed for the acceptance and efficiency correction within the differential yield analysis. Like the GiBUU model, UrQMD cascade is a pure transport based

model, meaning that the collision dynamics is modelled on a microscopic level for each particle. In contrast, the modified version UrQMD EOS (Equation-of-State) receives as input an equation of state additionally. The EoS is implemented by a hard Skyrme potential [32]. The model predictions are plotted together with the experimentally measured spectra, depicted by black points in figure (4.12). UrQMD Cascade is displayed in red, UrQMD EOS in green and GiBUU in blue. We observe that all models exhibit a general point symmetric behaviour as found in the experimental data. Yet, the slopes differ significantly compared to the data. For the π^- mesons, for the centrality class 0-20 %, the sign of the slope deviates from data for all of the models. For positively charged pions, the sign difference is only found for the 0-10 % most central events and only for the UrQMD Cascade model. For centralities of 20-40 %, the signs of the slopes are the same compared to the experimental data. In general, it is visible that the magnitude of highest directed flow, measured for $y_{cm} = 0.6$ and $y_{cm} = -0.6$, is, in general, slightly higher compared to the experimental data. The best quantitative agreement with the data for the $0 - 10$ % most central collisions is exhibited by UrQMD EOS. This might hint that aspects related to the equation of state influence the emergence of directed flow for charged pions.

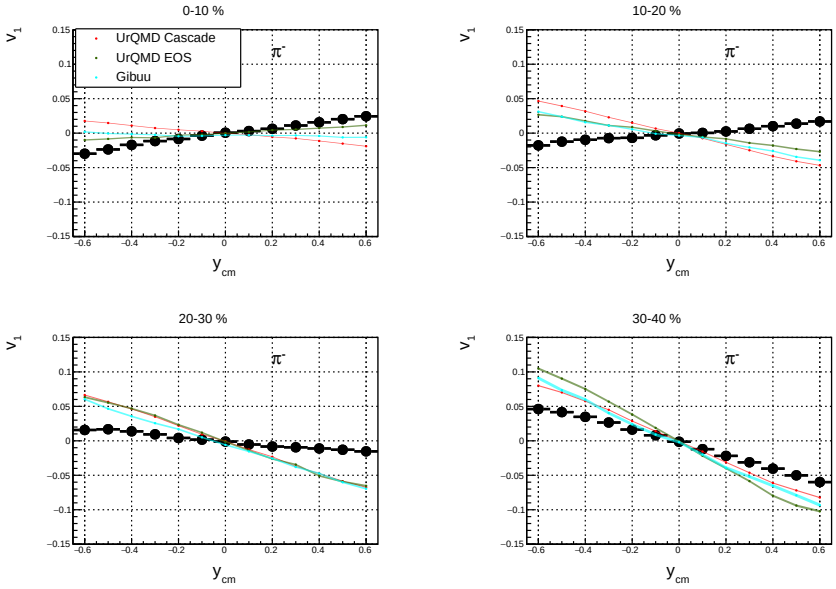

Figure 4.12: π^- v_1 flow, p_t integrated as a function of the rapidity in the centre of mass system. The experimental data (black) is compared to the predictions of 3 different models: UrQMD cascade [16] (red), the UrQMD EOS [32] (dark green) and the GiBUU [69] model (turquoise).

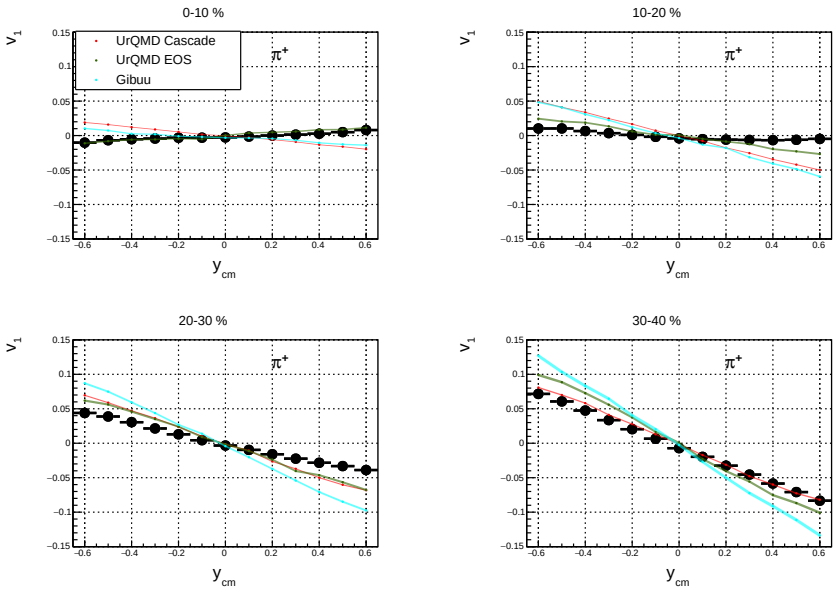

Figure 4.13: π^+ v_1 flow, p_t integrated as a function of the rapidity in the centre of mass system. The plots are for the 4 analysed centrality classes for the range 0-40 %. The experimental data (black points) is compared to the predictions of 3 different models: UrQMD cascade [16] (red), the UrQMD EOS [32] model (dark green) and the GiBUU [69] model (turquoise).

Furthermore, directed flow is investigated out of mid-rapidity as a function of transverse momentum. As described in (3.8.1), a wave-like structure exhibiting local maxima and minima or a plateau in the range from 200 to 400 MeV/c is found. Towards higher p_t a rise and divergence between the different rapidity bins are observed. Comparisons between the two polarities reveal, next to quantitative differences, a qualitative deviation in the low momentum range: For the positively charged pions, a divergence between the different rapidity bins is observed. For the negative pions, such behaviour is not found. The fact that this difference is present for low transverse momenta might indicate a correlation to the Coulomb interaction.
A comparison of the data with the models GiBUU and UrQMD EOS is displayed in figure (4.14) as a function of transverse momentum for the same rapidity intervals as analysed in the experiment. The models are plotted in a transparent style.

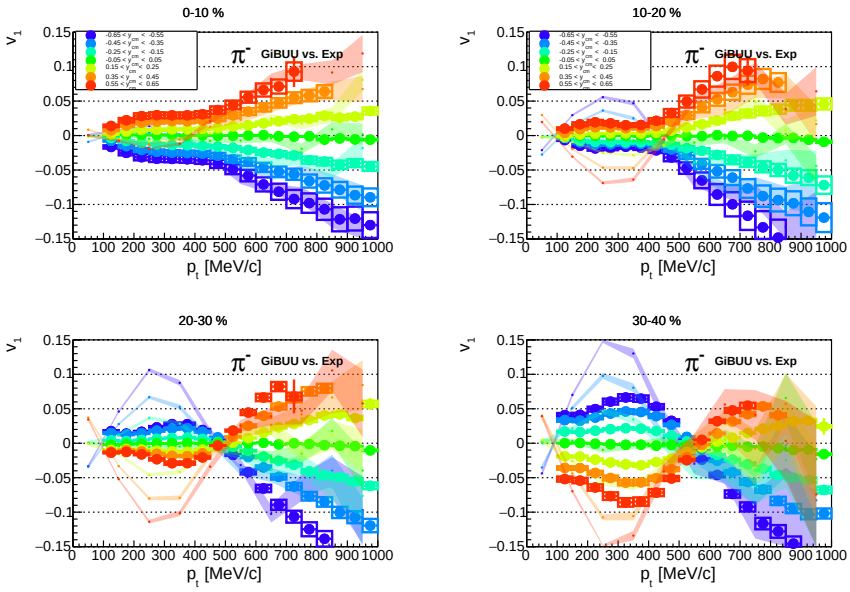

Figure 4.14: Directed flow harmonic v_1 of the π^- mesons as a function of transverse momentum for different rapidity bins in the interval $-0.65 < y_{cm} < 0.65$ with a bin size of 0.1 units of rapidity. For the same rapidity bins the prediction of v_1 from the model GiBUU is displayed. The data points and error bars are plotted in solid lines. The simulation are depicted in the same color as the data, but in a transparent style.

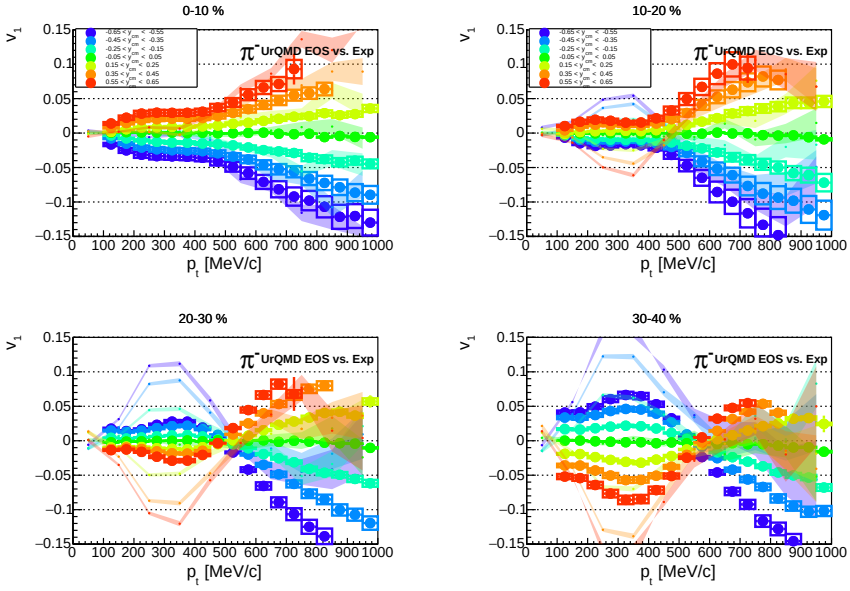

Figure 4.15: Directed flow harmonic v_1 of the π^- mesons as a function of transverse momentum for different rapidity bins in the interval $-0.65 < y_{cm} < 0.65$ with a bin size of 0.1 units of rapidity. For the same rapidity bins the prediction of v_1 from the model UrQMD EOS is displayed. The data points and error bars are plotted in solid lines. The simulation are depicted in the same color as the data, but in a transparent style.

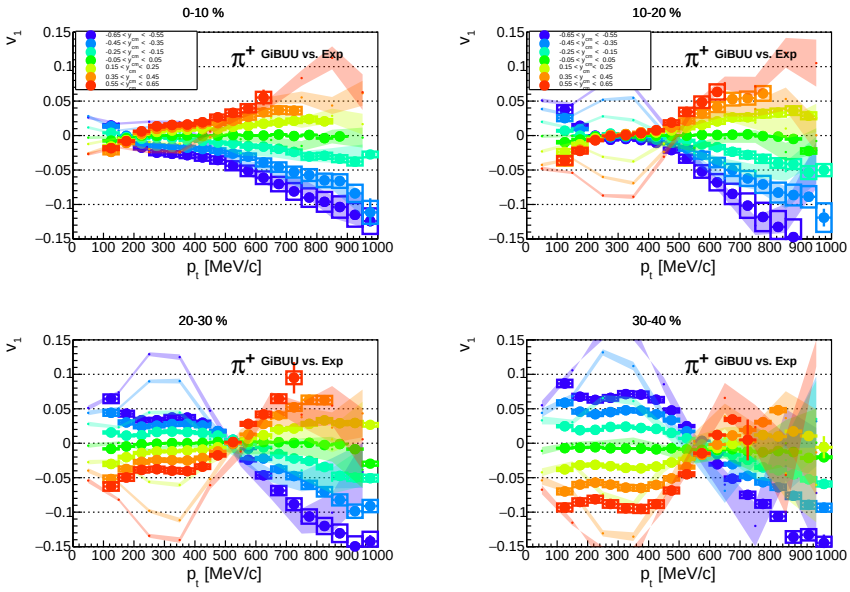

Figure 4.16: Directed flow harmonic v_1 of the π^+ mesons as a function of transverse momentum for different rapidity bins in the interval $-0.65 < y_{cm} < 0.65$ with a bin size of 0.1 units of rapidity. For the same rapidity bins the prediction of v_1 from the model GiBUU is displayed. The data points and error bars are plotted in solid lines. The simulation are depicted in the same color as for the data, but in a transparent style.

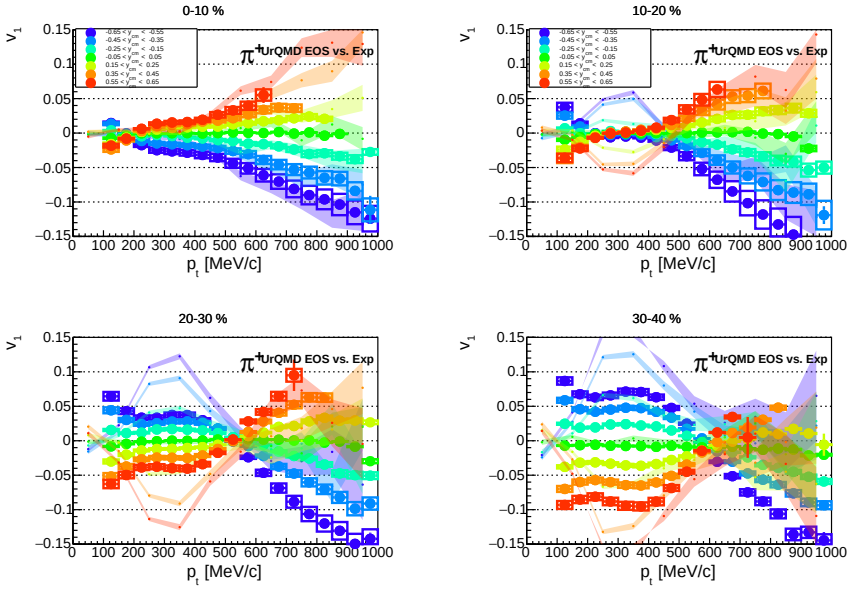

Figure 4.17: Directed flow harmonic v_1 of the π^+ mesons as a function of transverse momentum for different rapidity bins in the interval $-0.65 < y_{cm} < 0.65$ with a bin size of 0.1 units of rapidity. For the same rapidity bins the prediction of v_1 from the model UrQMD EOS is displayed. The data points and error bars are plotted in solid lines. The simulation are depicted in the same color as for the data, but in a transparent style.

The model comparisons, first of all, reveal that the local maxima or plateau, exhibited in the region from 200 to 400 MeV/c, is in general significantly higher compared to the experimental data. This is observed for both the UrQMD EOS and the GiBUU model, as well as for both polarities. As in the experimental data, a divergence between the different y-bins for $p_t > 800$ MeV/c is observed for the models. Yet, they quantitatively differ, especially for the centrality classes 20-40 %. Concerning the difference between the two models, it is observed that v_1, according to UrQMD EOS reaches slightly higher values towards higher transverse momenta.

3.2. Elliptic Flow

The elliptic flow harmonic is found to be rather small in the region of low momenta $p_t < 200$ MeV/c. For $p_t > 200$ MeV/c, the magnitude of v_2 starts to rise until a saturation plateau is reached, which value increases with increasing impact parameter. An explanation for this is again the discussed increase of the eccentricity of the collision, see theory section (2.1). The functional dependence as a function of transverse momentum is similar for all rapidity bins. For higher transverse momenta ($p_t > 800$ MeV/c), fluctuations and increasing statistical errors occur. Overall, throughout all centrality classes, elliptic flow is negative, indicating that the emission of charged pions happens slightly dominantly out of the reaction plane. The presence of the spectators can explain this observation: Charged pions that are emitted within the reaction plane have higher portability to the encounter spectator nucleons and thus are more likely to interact. The interaction might lead to absorptions or Δ-Resonances, which sightly shields the pion emission in this region, leading overall to a smaller number of pions emitted within the direction of the event plane. The enhanced out-off plane emission for charged pions is in accordance with other experiments probing the same beam energies [13]. For Au+Au collisions at $1.23A$ GeV, the same functional transverse momentum behaviour has been found from a qualitative perspective [42].
The π^+ mesons exhibit a higher magnitude of elliptic flow at the saturation plateau than the π^- mesons; see the comparison in figure (4.18). The charge difference thereby increases with rising impact parameter. Possible explanations, which are in discussion, next to the Coulomb effect, are chiral magnetic waves [63] or iso-spin effects [52].

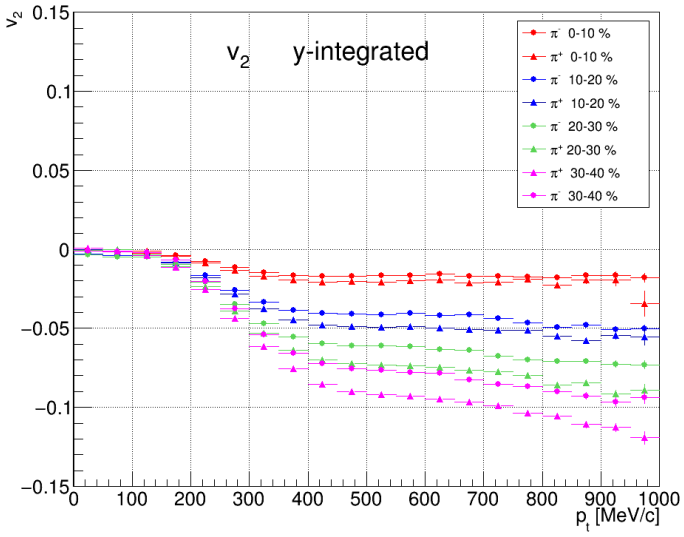

Figure 4.18: Comparison of v_2 between the positively and negatively charged pions for the different centrality classes. The π^+ mesons (triangular markers) exhibit in general a higher magnitude of v_2 flow than the π^- mesons (circled markers).

As conducted for directed flow, in order to provide a more condensed picture, the rapidity integrated elliptic flow is compared to the models UrQMD Cascade, UrQMD EOS [32] and GiBUU [69]. The comparison of the transverse momentum behaviour is displayed in figure (4.19). Qualitatively, we obverse the same behaviour as found in the experimental spectra for all models. Yet, for the pure transport-based models GiBUU and UrQMD cascade, a smaller degree of elliptic flow is predicted. Only UrQMD EOS is on a quantitative perspective closer to the measured data.

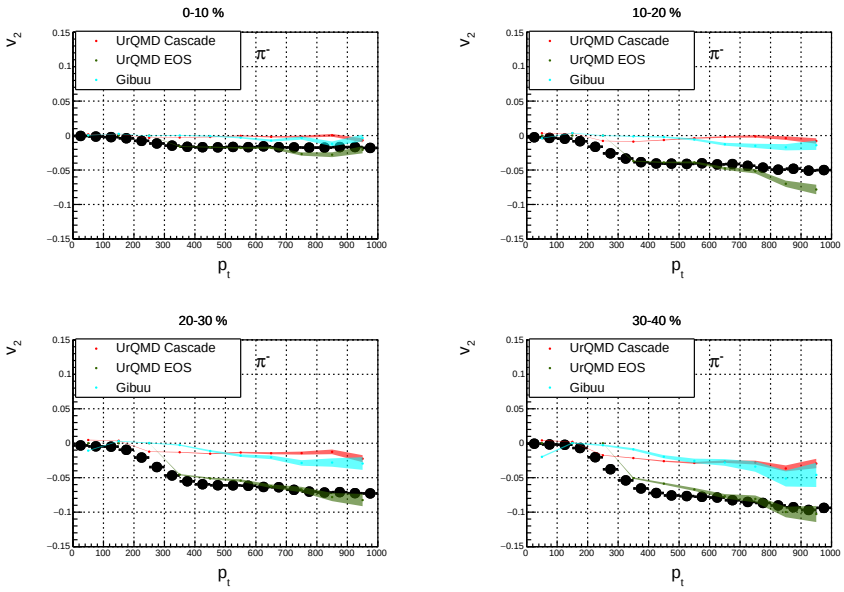

Figure 4.19: π^- v_2 elliptic flow, p_t integrated as a function of transverse momentum and the 4 analysed centrality classes for the range 0-40 %. The experimental data (black points) is compared with the predictions of 3 different models: UrQMD cascade [16] (red), UrQMD EOS [32] (dark green) and GiBUU [69] (turquoise).

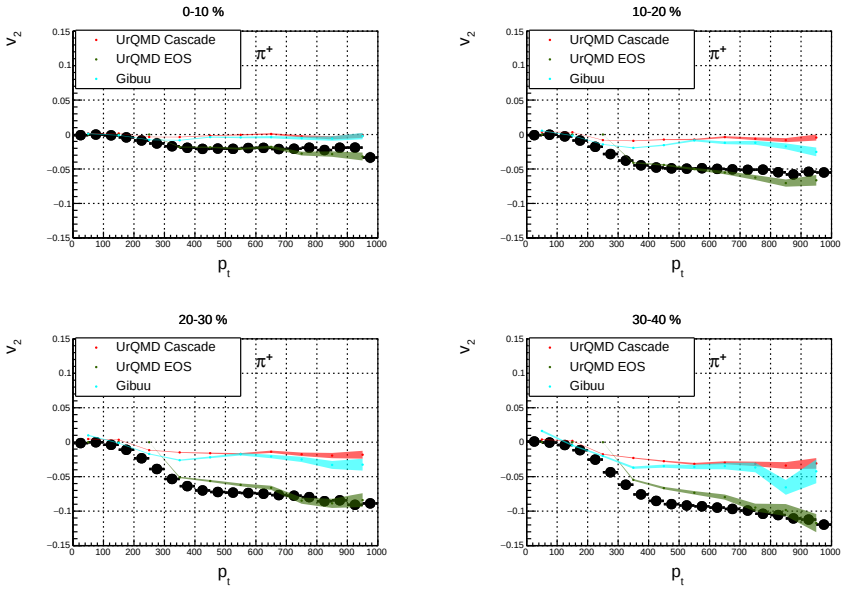

Figure 4.20: π^+ v_2 elliptic flow, p_t integrated as a function of transverse momentum and the 4 analysed centrality classes for the range 0-40 %. The experimental data (black points) is compared with the predictions of 3 different models: UrQMD cascade [16] (red), UrQMD EOS [32] (dark green) and GiBUU [69] (turquoise).

3.3. Triangular Flow

Finally, the third-order flow harmonic is investigated as a function of rapidity and transverse momentum, see figure (3.68) and (3.67). The v_3 harmonic exhibits a much smaller magnitude than the lower order flow coefficients. This observation is in accordance with the expectancies that high order harmonics contribute less to the azimuthal anisotropy [13]. Triangular flow is close to zero for low p_t up to 400 MeV/c. Towards higher momenta, an increase is observed. The explicit dependence in rapidity reveals an approximate point symmetric pattern as observed for v_1. This confirms the prediction that odd-order harmonics show qualitatively the same features regarding the rapidity symmetry [13]. A rough point-symmetry is also observed after pt-integration, see figure (4.21) and (4.22). Yet, the statistical errors are in order of 20 %. To set a basis for conclusions to physical processes that are responsible for the emergence of triangular flow, again, a comparison with the introduced models GiBUU [69] and UrQMD EOS [32] is conducted. A rough point-symmetry is visible for the models as well, yet the available statistics is very low. The error intervals for the UrQMD models is too high in order to make a statement. For the GiBUU model, it is significant that the slope of the trend exhibits the opposite sign compared to the data in the centrality class 20-30 % and 30-40 %. A comparison as a function of p_t for different rapidity bins is not carried out. A higher statistic for the models is necessary to allow for such detailed quantitative comparison.

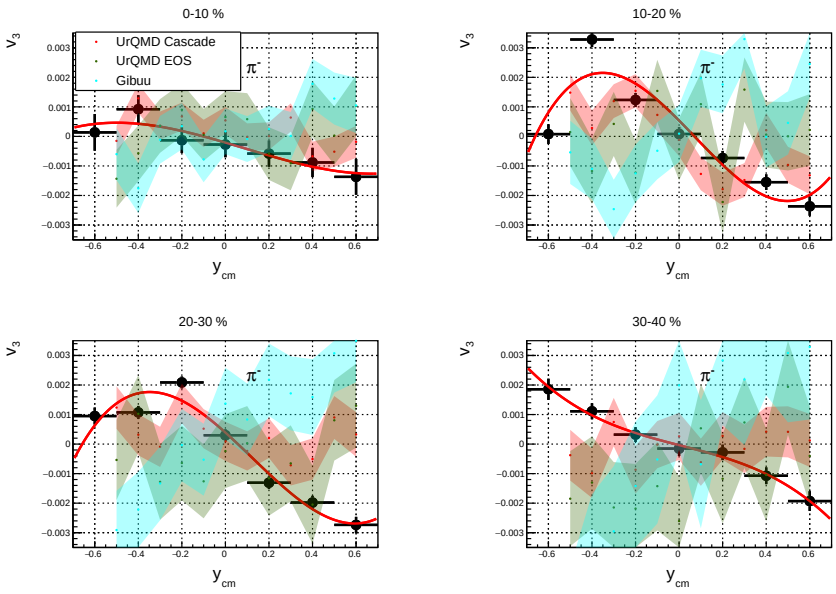

Figure 4.21: π^- v_3 flow p_t integrated as a function of the rapidity in the centre of mass system (black). The experimental data (black) is compared to the predictions of 3 different models: UrQMD cascade [16] (red), UrQMD EOS [32] (dark green) and GiBUU [69] (turquoise).

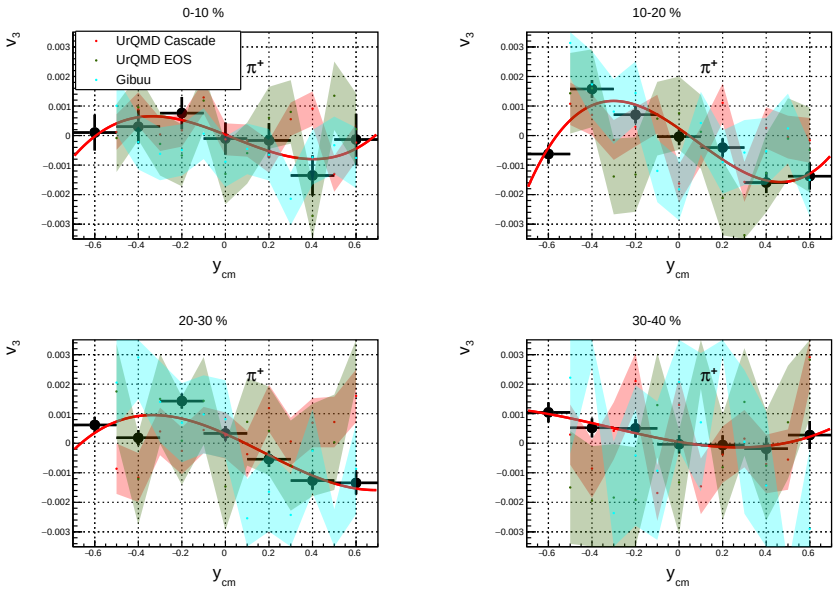

Figure 4.22: π^+ v_3 flow p_t integrated as a function of the rapidity in the centre of mass system (black). The experimental data (black) is compared to the predictions of 3 different models: UrQMD cascade [16] (red), UrQMD EOS [32] (dark green) and GiBUU [69] (turquoise).

5. Outlook

Within the aim of quantifying the impact of the Coulomb field in more detail, the next step is the implementation of an intensity interferometry analysis. This allows investigating potential systematic differences to another model with different assumptions. Moreover, the extraction of the Coulomb potential for the fitting approach can be improved assuming a more realistic charge distribution, e.g. a Wood-Saxon distribution. For a more precise extraction of the Coulomb spectra out of mid-rapidity as well as at mid-rapidity for peripheral collisions, more sophisticated model are required, that also describe the influences of the spectator charges adequately. When it comes to estimating the baryon-chemical potential, it has to be investigated whether the assumptions of an ideal hadron gas are valid for the fireball state, especially what temperature to choose.
Concerning the anisotropic flow analysis, further systematic error sources need to be evaluated. E.g. with respect to the methods used to extract the event plane and its correction for fluctuations. Next to the classical approach, employed in this analysis as well as in previous flow analyses in HADEs, the flow harmonics can be determined by the Scalar product method [41]. The most peripheral centrality class 40-50 % has been discarded from the analysis as the influences of Ag+C is still too large for precise flow measurement. Hence, more advanced methods than the ERAT-cut, like machine learning methods, need to be tested to reduce Ag+C contaminations further.
Regarding the physical interpretation of the investigated flow harmonics' found behaviour, detailed explorations of the model specifics are necessary. Furthermore, there are various other transport or hybrid models that can be compared to the experimental data, aiming to understand the underlying physics that is related to the emergence of azimuthal flow, like the SMASH [68] or the IQMD model [7].
In this analysis, only the azimuthal anisotropies have been investigated. Yet, anisotropies are also excepted as function of the polar emission angel, as the results of Au+Au collisions suggest [2].

6. Attachment

1. Centrality Dependence

1.1. Transverse Mass Spectra

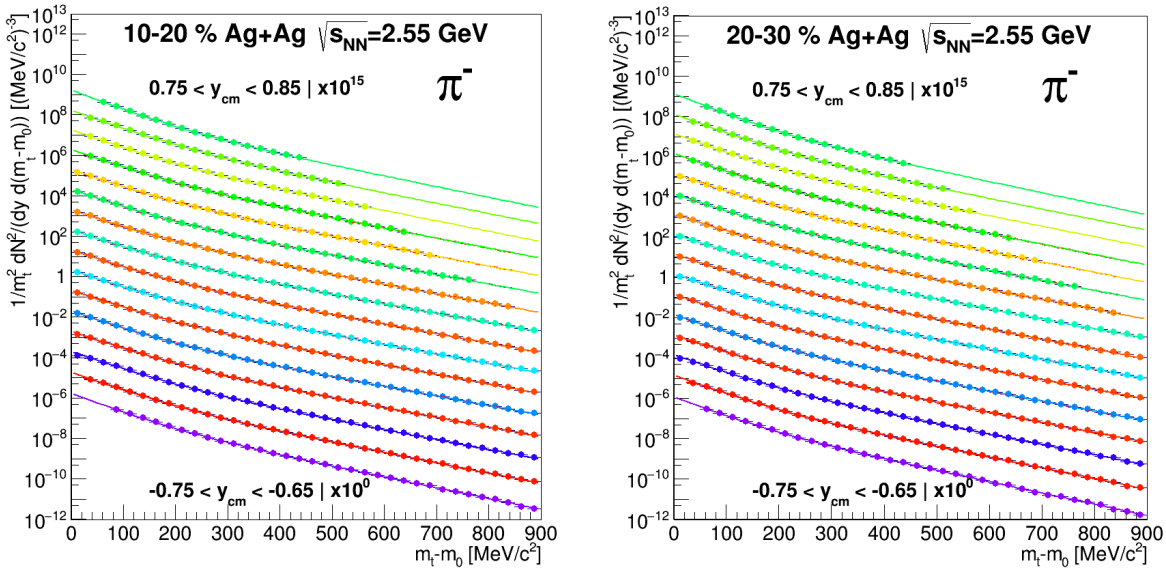

Figure 6.1: π^- Transverse reduced mass spectra for the 10-20 % and 20-30 % most central events.

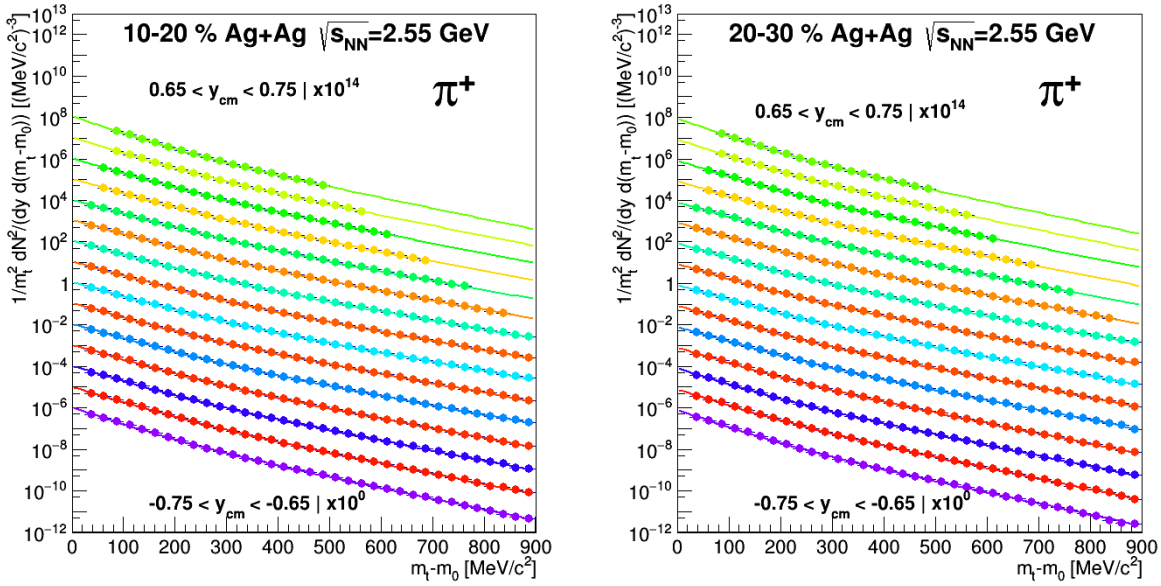

Figure 6.2: π^+ Transverse reduced mass spectra for the 10-20 % and 20-30 % most central events.

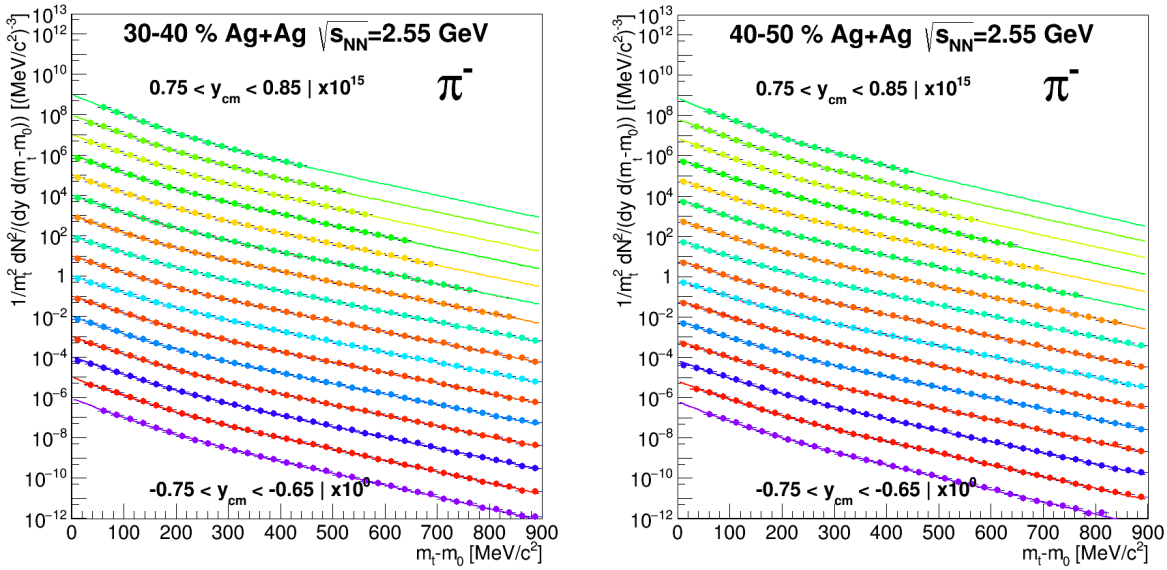

Figure 6.3: π^- Transverse reduced mass spectra for the 30-40 % and 40-50 % most central events.

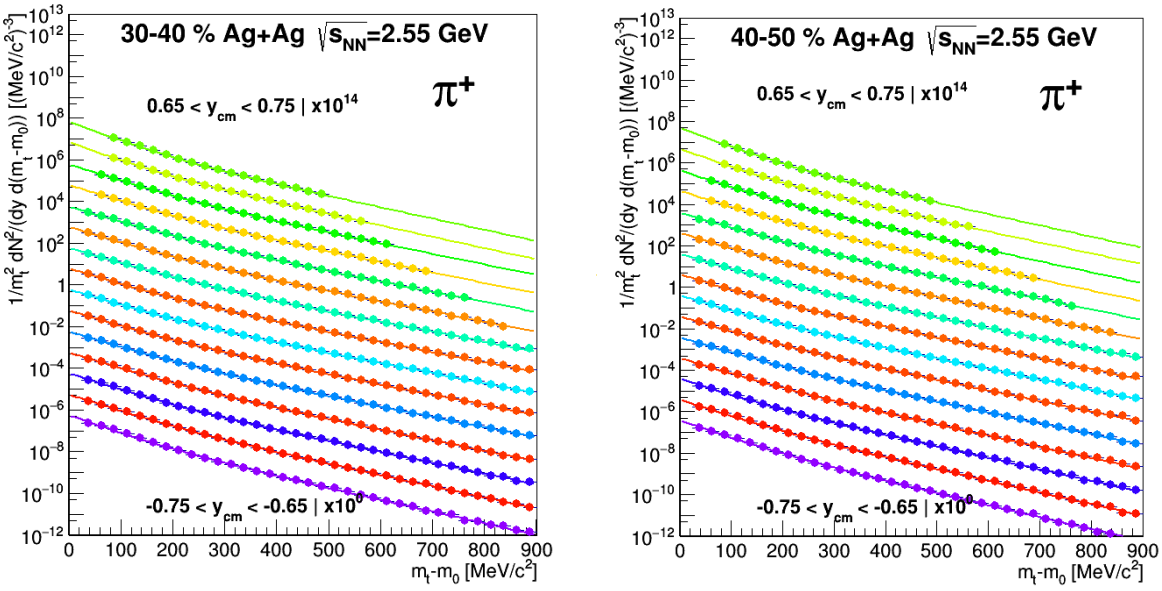

Figure 6.4: π^+ Transverse reduced mass spectra for the 30-40 % and 40-50 % most central events.

1.2. 2D Coulomb Fits out of Mid-Rapidity

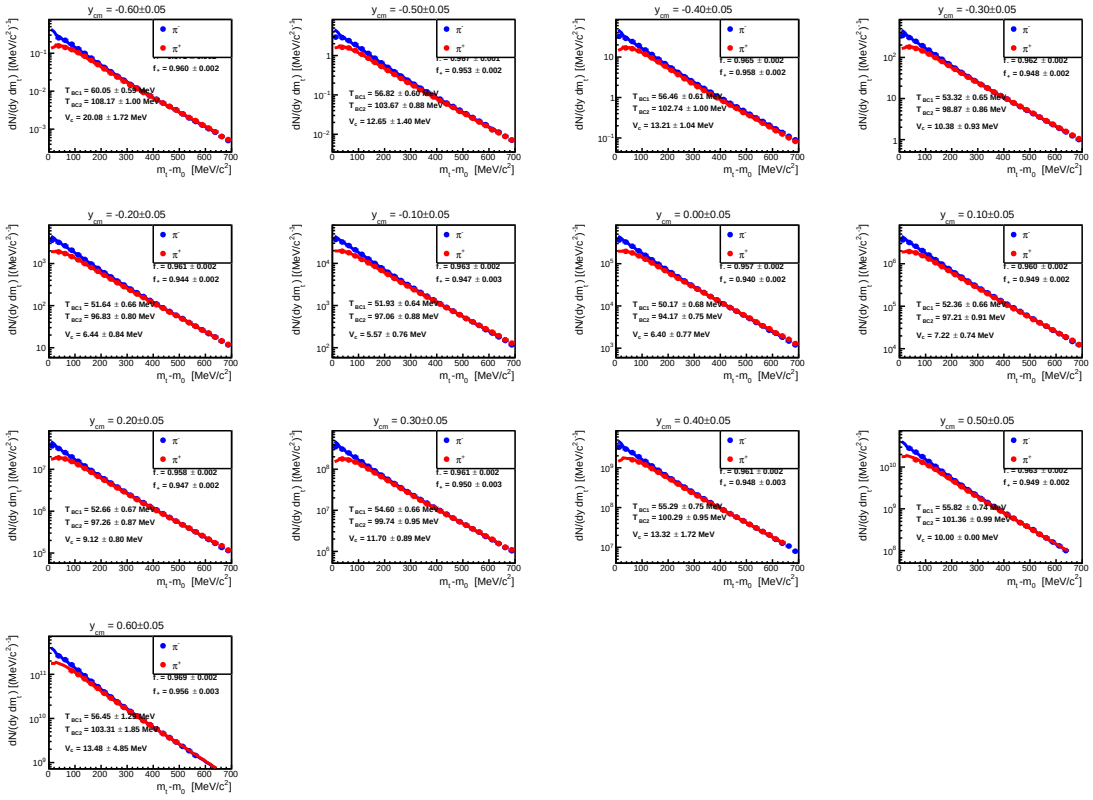

Figure 6.5: 2D Coulomb fits for the 10-20 % most central events.

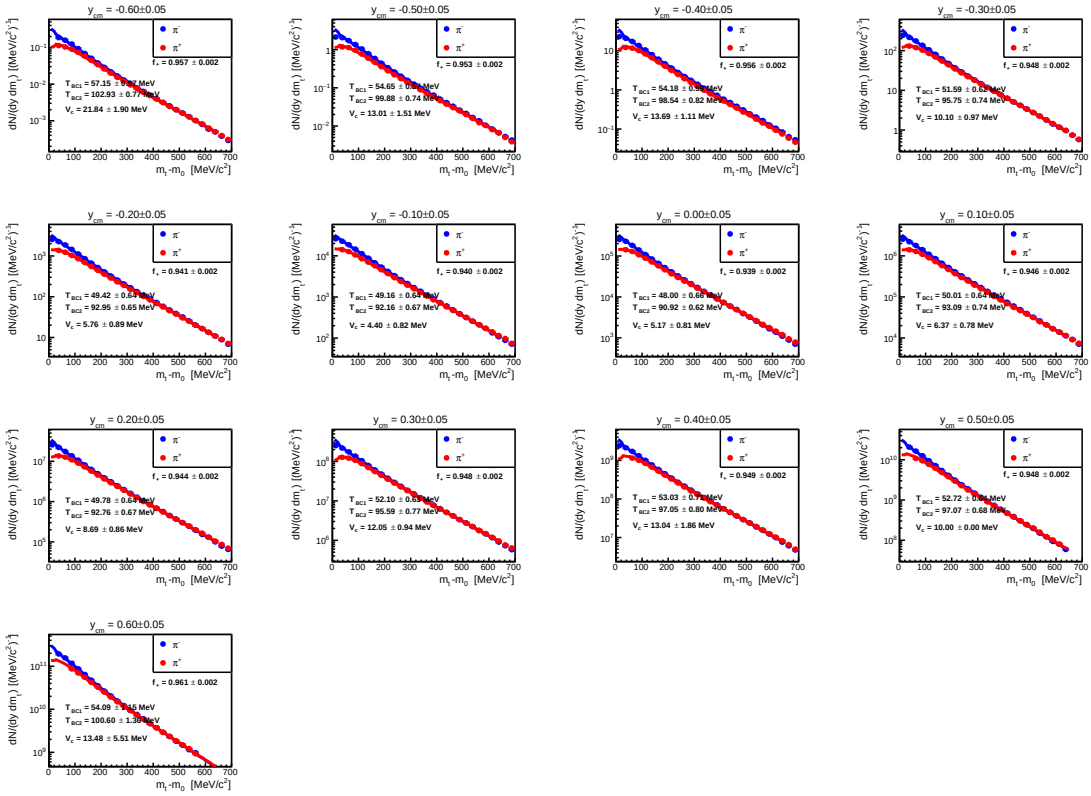

Figure 6.6: 2D Coulomb fits for the 20-30 % most central events.

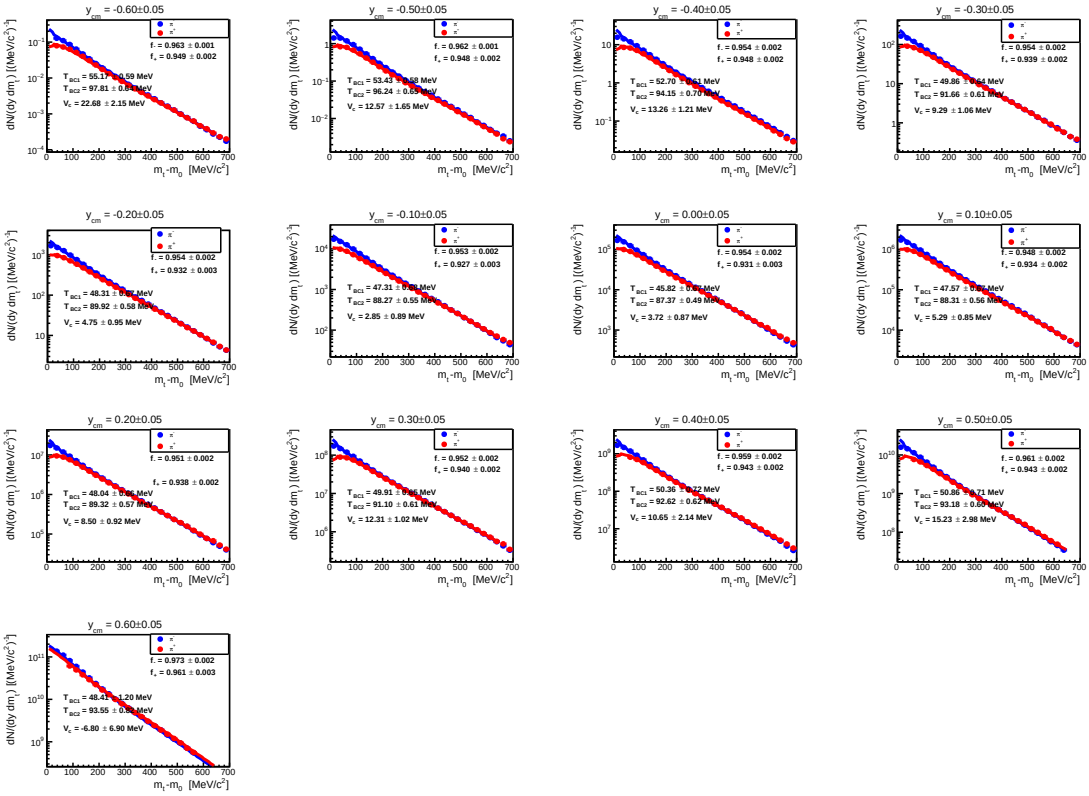

Figure 6.7: 2D Coulomb fits for the 30-40 % most central events.

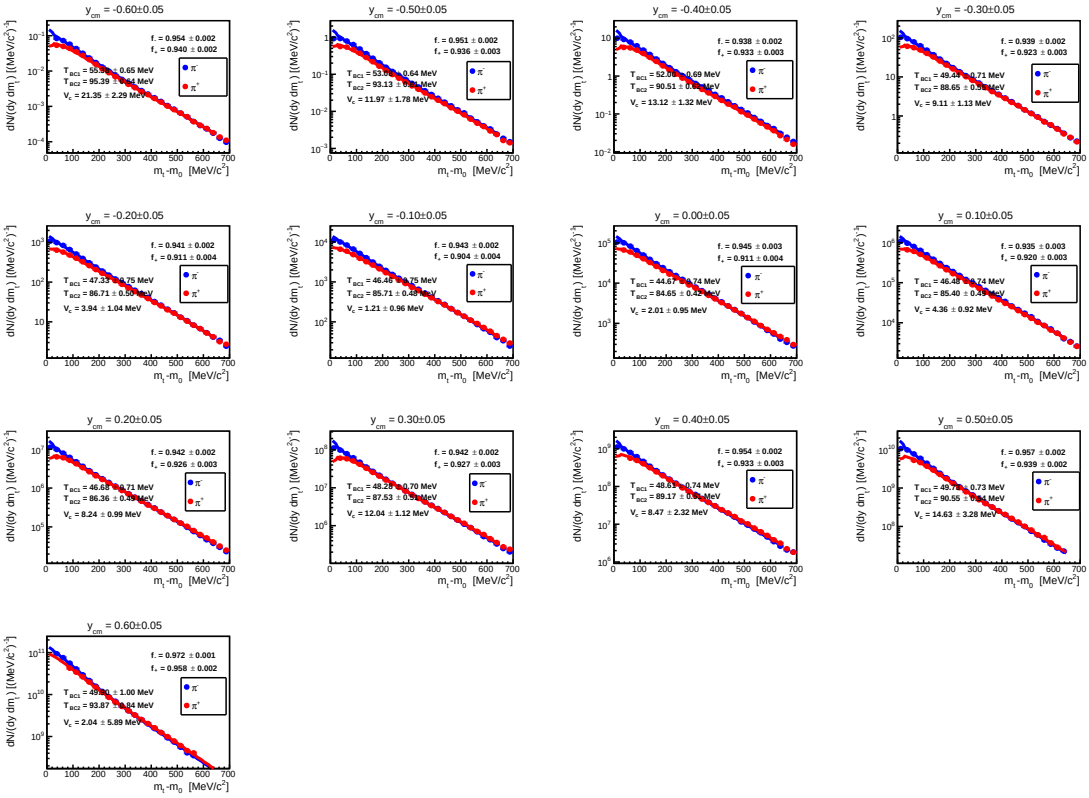

Figure 6.8: 2D Coulomb fits for the 40-50 % most central events.

7. References

Bibliography

[1] W. Reisdorf et al. (FOPI Collaboration). *Nucl. Phys. A781.* 459(2007).

[2] J. Adamczewski-Musch et al. "Charged-pion production in $\mathbf{Au + Au}$ collisions at $\sqrt{\mathbf{s_{NN}}} = 2.4$ **GeV**: HADES Collaboration". In: (Jan. 2020).

[3] G. Agakichiev et al. "The high-acceptance dielectron spectrometer HADES". In: *The European Physical Journal A* 41.2 (July 2009), pp. 243–277. ISSN: 1434-601X. DOI: 10.1140/epja/i2009-10807-5. URL: http://dx.doi.org/10.1140/epja/i2009-10807-5.

[4] G. Agakishiev et al. "Dielectron production in Ar + KCl collisions at 1.76AGeV". In: *Physical Review C* 84.1 (July 2011). ISSN: 1089-490X. DOI: 10.1103/physrevc.84.014902. URL: http://dx.doi.org/10.1103/PhysRevC.84.014902.

[5] G. Agakishiev et al. "Measurement of charged pions in 12C + 12C collisions at 1 A GeV and 2 A GeV with HADES". In: *The European Physical Journal A* 40.1 (Apr. 2009), pp. 45–59. ISSN: 1434-601X. DOI: 10.1140/epja/i2008-10746-7. URL: http://dx.doi.org/10.1140/epja/i2008-10746-7.

[6] Adamczewski-Musch et al. "Probing dense baryon-rich matter with virtual photons". In: *Nature Phys.* 15.10 (2019), pp. 1040–1045. DOI: 10.1038/s41567-019-0583-8. URL: https://hal.archives-ouvertes.fr/hal-02383397.

[7] C. Hartnack et al. *Modelling the many-body dynamics of heavy ion collisions: Present status and future perspective.* Eur. Phys. J. A 1, 151 (1998), 1998.

[8] C. Müntz et al. *The HADES tracking system.* Nucl. Instrum. Meth., vol. A535, pp. 242–246, 2004.

[9] G. Agakishiev et al. *Statistical model analysis of hadron yields in proton-nucleus and heavy-ion collisions at SIS 18 energies.* 2015. arXiv: 1512.07070 [nucl-ex].

[10] J. Adamczewski-Muschet al. *Proposal for experiments at SIS18 duringFAIR Phase-0.* Internal report, GSI Helmholtzzentrum für Schwerionenforschung GmbH, 2015.

[11] Yasumichi Aoki et al. "The QCD transition temperature: results with physical masses in the continuum limit II". In: *Journal of High Energy Physics* 2009.06 (June 2009), pp. 088–088. ISSN: 1029-8479. DOI: 10.1088/1126-6708/2009/06/088. URL: http://dx.doi.org/10.1088/1126-6708/2009/06/088.

[12] J. Barrette et al. "Proton and pion production in Au+Au collisions at10.8AGeV/c". In: *Physical Review C* 62.2 (July 2000). ISSN: 1089-490X. DOI: 10.1103/physrevc.62.024901. URL: http://dx.doi.org/10.1103/PhysRevC.62.024901.

[13] J. Bartke. *Introduction to Relativistic Heavy Ion Physics*. 2009.

[14] H. W. Barz et al. "Coulomb effects on particle spectra in relativistic nuclear collisions". In: *Phys. Rev. C* 57 (5 May 1998), pp. 2536–2546. DOI: 10.1103/PhysRevC.57.2536. URL: https://link.aps.org/doi/10.1103/PhysRevC.57.2536.

[15] W. Benenson et al. "Low-Energy Pion Production at 0° with Heavy Ions from 125 to 400 MeV/Nucleon". In: *Phys. Rev. Lett.* 43 (10 Sept. 1979), pp. 683–686. DOI: 10.1103/PhysRevLett.43.683. URL: https://link.aps.org/doi/10.1103/PhysRevLett.43.683.

[16] M Bleicher et al. "Relativistic hadron-hadron collisions in the ultra-relativistic quantum molecular dynamics model". In: *Journal of Physics G: Nuclear and Particle Physics* 25.9 (Sept. 1999), pp. 1859–1896. ISSN: 1361-6471. DOI: 10.1088/0954-3899/25/9/308. URL: http://dx.doi.org/10.1088/0954-3899/25/9/308.

[17] John C. Buther. *The Numerical Analysis of Ordinary Differential Equations. Runge-Kutta and General Linear Methods*. A Wiley-Interscience publication, 1987.

[18] C. F. Powell C. M. G. Lattes G. P. S. Occhialini. *A determination of the ratio of the masses of pi-meson and mu-meson by the method of grain-counting*. Proceedings of the Physical Society, 1948.

[19] N. Cabibbo and G. Parisi. "Exponential hadronic spectrum and quark liberation". In: *Physics Letters B* 59.1 (1975), pp. 67–69. ISSN: 0370-2693. DOI: https://doi.org/10.1016/0370-2693(75)90158-6. URL: https://www.sciencedirect.com/science/article/pii/0370269375901586.

[20] D. Cebra et al. *Coulomb effect in Au+Au and Pb+Pb collisions as a function of collision energy*. 2014. arXiv: 1408.1369 [nucl-ex].

[21] HADES Collaboration. *Charged pion emission and the central Couloumb potential in heavy-ion collisions at energies of a few GeV*. Goethe-Universitaet, Frankfurt am Main, 2021.

[22] HADES Collaborationa. *Proton, deuteron and triton flow measurments with HADES*. 22 May 2018.

[23] F. Wilczek D. J. Gross. "Ultraviolet Behavior of Non-Abelian Gauge Theories". In: *Phys. Rev. Lett.* **30**.1343 ((1973)).

[24] Yu.L. Dokshitzer and B.R. Webber. "Power corrections to event shape distributions". In: *Physics Letters B* 404.3 (1997), pp. 321–327. ISSN: 0370-2693. DOI: https://doi.org/10.1016/S0370-2693(97)00573-X. URL: https://www.sciencedirect.com/science/article/pii/S037026939700573X.

[25] Carlos García Canal. "HERA has Been Closed, LHC is Being Opened: Near Past and Near Future of Particle Physics". In: *Brazilian Journal of Physics - BRAZ J PHYS* 38 (Sept. 2008). DOI: 10.1590/S0103-97332008000400004.

[26] Walter Greiner. *Klassische Elektrodynamik*. Verlag Harri Deutsch, 2008.

[27] David J. Gross and Frank Wilczek. "Ultraviolet Behavior of Non-Abelian Gauge Theories". In: *Phys. Rev. Lett.* 30 (26 June 1973), pp. 1343–1346. DOI: 10.1103/PhysRevLett.30.1343. URL: https://link.aps.org/doi/10.1103/PhysRevLett.30.1343.

[28] Particle Data Group. *Pion data sheet*. URL: https://pdg.lbl.gov/2020/listings/rpp2020-list-pi-plus-minus.pdf.

[29] *GSI Helmholtzzentrum für Schwerionenforschung - Beschleuniger- anlage - Website*. URL: https://www.gsi.de/forschungbeschleuniger/%20beschleunigeranlage.htm.

[30] T. Galatyuk et al HADES collaboration. *HADES overview*. Nucl.Phys. A931 (2014) 41-51, 2014.

[31] M. Q. Haseeb. *Flow in Quark Gluon Plasma*. 2021. URL: http://ncp.edu.pk/docs/%20snwm/Mahnaz_Haseeb_Flow_in_QGP.pdf..

[32] Paula Hillmann et al. "First, second, third and fourth flow harmonics of deuterons and protons in Au+Au reactions at 1.23A GeV". In: *Journal of Physics G: Nuclear and Particle Physics* 47.5 (Mar. 2020), p. 055101. DOI: 10.1088/1361-6471/ab6fcf. URL: https://doi.org/10.1088/1361-6471/ab6fcf.

[33] B. Hong et al. "Charged pion production in 4496Ru+4496Ru collisions at 400A and 1528A MeV". In: *Physical Review C* 71.3 (Mar. 2005). ISSN: 1089-490X. DOI: 10.1103/physrevc.71.034902. URL: http://dx.doi.org/10.1103/PhysRevC.71.034902.

[34] K. G. Wilson. "Confinement of Quarks". In: *Phys. Rev. D* **10**.2445 (Oct. (1974)).

[35] Behruz Kardan. *Centrality determination at 1.23 agev gold-gold collision and readout-electronics for the hades electromagnetic calorimeter*. Goethe-Universitaet, Frankfurt am Main, 2015.

[36] Behruz Kardan. "Collective flow and correlations measurements with HADES in Au+Au collisions at 1.23 AGeV". In: *Nuclear Physics A* 982 (2019). The 27th International Conference on Ultrarelativistic Nucleus-Nucleus Collisions: Quark Matter 2018, pp. 431–434. ISSN: 0375-9474. DOI: https://doi.org/10.1016/j.nuclphysa.2018.09.061. URL: https://www.sciencedirect.com/science/article/pii/S0375947418302495.

[37] J. L. Klay et al. "Charged pion production in 2A to 8A GeV central Au+Au Collisions". In: *Physical Review C* 68.5 (Nov. 2003). ISSN: 1089-490X. DOI: 10.1103/physrevc.68.054905. URL: http://dx.doi.org/10.1103/PhysRevC.68.054905.

[38] J. L. Klay et al. "Charged pion production in 2A to 8A GeV central Au+AuCollisions". In: *Physical Review C* 68.5 (Nov. 2003). ISSN: 1089-490X. DOI: 10.1103/physrevc.68.054905. URL: http://dx.doi.org/10.1103/PhysRevC.68.054905.

[39] L.D. Landau and E.M Liftshitz. *Statistical Physics 2nd ed. Course of Theoretical Physic*. Pergamon Press Ltd., 1969.

[40] *LHC - Der Große Hadronen Speicherring, CERN – Europäische Organisation für Kernforschung*. URL: https://cds.cern.ch/record/971033/files/brochure-2006-002-ger.pdf.

[41] Matthew Luzum and Jean-Yves Ollitrault. "Eliminating experimental bias in anisotropic-flow measurements of high-energy nuclear collisions". In: *Phys. Rev. C* 87 (4 Apr. 2013), p. 044907. DOI: 10.1103/PhysRevC.87.044907. URL: https://link.aps.org/doi/10.1103/PhysRevC.87.044907.

[42] P.Tusty M.Gumberdize and L.Chald. *Talk: Paper proposal: Pion and Kaon Flow in Au+Au collisions at 1.23A GeV*. XL HADES Collaboration Meeting, 2021.

[43] Christian Müntz. *E-Mail communcitaction*. Goethe-Universitaet, Frankfurt am Main, 2021.

[44] Marvin Nabroth. *Bachelor thesis: Produktion geladener Pionen bei Ag+Ag 1.58A GeV*. Goethe Universitaet Frankfurt, 2020.

[45] S. Nagamiya et al. "Production of pions and light fragments at large angles in high-energy nuclear collisions". In: *Phys. Rev. C* 24 (3 Sept. 1981), pp. 971–1009. DOI: 10.1103/PhysRevC.24.971. URL: https://link.aps.org/doi/10.1103/PhysRevC.24.971.

[46] Y. Nambu and G. Jona-Lasinio. "Dynamical Model of Elementary Particles Based on an Analogy with Superconductivity. I". In: *Phys. Rev.* 122 (1 Apr. 1961), pp. 345–358. DOI: 10.1103/PhysRev.122.345. URL: https://link.aps.org/doi/10.1103/PhysRev.122.345.

[47] Thendo Emmanuel Nemakhavhani, Mohammed Younus and Azwinndini Muronga. "The Equation of State (EoS) of hadronic matter from the microscopic Ultra-relativistic Quantum Molecular Dynamics (UrQMD) model". In: Feb. 2020.

[48] Naomi Oei. *Bachelor thesis: Messung des Kollektiven Flusses von Protonen mit HADES in Ag+Ag Kollisionen bei 1.58A GeV*. Goethe Universitaet Frankfurt, 2020.

[49] Jean-Yves Ollitrault. *Reconstructing azimuthal distributions in nucleus–nucleus collisions*. 1997.

[50] Owe Philipsen. *Qunatenfeldtheorie und das Standardmodell der Teilchenphysik*. Springer Spektrum, 2018.

[51] H. David Politzer. "Reliable Perturbative Results for Strong Interactions?" In: *Phys. Rev. Lett.* 30 (26 June 1973), pp. 1346–1349. DOI: 10.1103/PhysRevLett.30.1346. URL: https://link.aps.org/doi/10.1103/PhysRevLett.30.1346.

[52] W. Reisdorf et al. "Systematics of pion emission in heavy ion collisions in the regime". In: *Nuclear Physics A* 781.3-4 (Jan. 2007), pp. 459–508. ISSN: 0375-9474. DOI: 10.1016/j.nuclphysa.2006.10.085. URL: http://dx.doi.org/10.1016/j.nuclphysa.2006.10.085.

[53] Adrian Rost. *Design, installation and commissioning of new read-outelectronics for HADES ECAL and diamond detectors forT0-reconstruction and beam diagnostics*. TU Darmstadt, 2020.

[54] Timo Scheib. *Lambda and K0S Productionin Au+Au Collisions at 1.23A GeV*. Goethe-Universitaet, Frankfurt am Main, 2017.

[55] Simon Spies. *Strange Hadron Production in Ag+Ag Collisions at 1.58A GeV*. Goethe Universitaet Frankfurt, 2021.

[56] Peter Spiller et al. "Status of the FAIR Synchrotron Projects SIS18 Upgrade and SIS100". In: July 2014.

[57] I. Selyuzhenkov et al. STAR collaboration. *Azimuthal charge particle correlations as a probe for local strong parity violation in heavy-ion collisions*. arXiv:0910.0464 [nucl-ex], 2014.

[58] J. P. Sullivan et al. "Strong Coulomb effects on pions produced in heavy ion collisions". In: *Phys. Rev. C* 25 (3 Mar. 1982), pp. 1499–1517. DOI: 10.1103/PhysRevC.25.1499. URL: https://link.aps.org/doi/10.1103/PhysRevC.25.1499.

[59] Stefan Teis et al. "Probing nuclear expansion dynamics with π^-/π^+-spectra". In: *Zeitschrift fuer Physik A Hadrons and Nuclei* 359 (1997), pp. 297–304.

[60] Pavel Tulsty. *E-Mail communcitaction*. GSI, 2021.

[61] B. J. VerWest and R. A. Arndt. "single pion production cross sections below 1500 MeV". In: *Phys. Rev. C* 25 (4 Apr. 1982), pp. 1979–1985. DOI: 10.1103/PhysRevC.25.1979. URL: https://link.aps.org/doi/10.1103/PhysRevC.25.1979.

[62] A. Wagner et al. "Evidence for different freeze-out radii of high- and low-energy pions emitted in Au+Au collisions at 1 AGeV". In: *Physics Letters B* 420.1-2 (Feb. 1998), pp. 20–24. ISSN: 0370-2693. DOI: 10.1016/s0370-2693(97)01549-9. URL: http://dx.doi.org/10.1016/S0370-2693(97)01549-9.

[63] Gang Wang. "Search for Chiral Magnetic Effects in High-Energy Nuclear Collisions". In: *Nuclear Physics A* 904-905 (2013). The Quark Matter 2012, pp. 248c–255c. ISSN: 0375-9474. DOI: https://doi.org/10.1016/j.nuclphysa.2013.01.069. URL: https://www.sciencedirect.com/science/article/pii/S0375947413000882.

[64] *Webseite der HADES Kollaboration*. 2020. URL: https://hades.gsi.de/.

[65] *Websieite des GEANT4-Tooklkits*. 2020. URL: http://geant4.web.cern.ch/.

[66] *Website ALICE*. URL: https://alice-collaboration.web.cern.ch/.

[67] *Website The STAR experiment at the Relativitsic Heavy Ion Collider*. URL: https://www.star.bnl.gov/.

[68] J. Weil et al. "Particle production and equilibrium properties within a new hadron transport approach for heavy-ion collisions". In: *Phys. Rev. C* 94.5 (2016), p. 054905. DOI: 10.1103/PhysRevC.94.054905. arXiv: 1606.06642 [nucl-th].

[69] Janus Weil and Ulrich Mosel. "The GiBUU transport model". In: *EPJ Web of Conferences* 52 (June 2013), pp. 06007–. DOI: 10.1051/epjconf/20125206007.

[70] A. R. Wolf and Appenheimer et. al. "Multistep Production of eta and Hard pizero Mesons in Subthreshold Au-Au Collisions". In: *Phys. Rev. Lett.* 80 (24 June 1998), pp. 5281–5284. DOI: 10.1103/PhysRevLett.80.5281. URL: https://link.aps.org/doi/10.1103/PhysRevLett.80.5281.

[71] P.A. Zyla et al. "Review of Particle Physics". In: *PTEP* 2020.8 (2020), p. 083C01. DOI: 10.1093/ptep/ptaa104.

Danksagung

Mein Dank gilt Prof. Dr. Joachim Stroth, der mir nach der Bachelorarbeit die Möglichkeit gab auch meine Masterarbeit in seiner Arbeitsgruppe und innerhalb der HADES Kollaboration zu schreiben. Auch danke ich ihm für wertvolle Anregungen und Kommentare zu meiner Analyse.
Besonders danken möchte ich Dr. Manuel Lorenz, der trotz Elternzeit meine Masterarbeit stets mit vielen Anregungen, verständlichen Erklärungen zu physikalischen Hintergründen hervorragend betreut hat. Auch danke ich ihm für seine Geduld die er mir gegenüber während meines langwierigen Schreibprozesses aufbrachte.
Ein großes Dankeschön geht an Dr. Malgorzata Gumberdize für die kontinuierliche Begleitung meiner Pionenanalyse und der Beantwortung meiner Fragen sowie der vielen Hilfsstellungen, wie z.B. die Einführung in die Flowanalyse. Besonderer Dank gilt ihr auch für die Bereitstellung der Transportmodellrechnungen. Dr. Romain Holzmann danke ich für seine Paperstudien zum Coulombeffekt und der Beantwortung meiner Fragen zur Herleitung der Coulomb-Funktionen.
Behruz Kardan danke ich für die Entwicklung der Softwareklassen zur Zentralitätsselektion und Event Plane Extraktion und sowie seiner ausführlichen Beschreibung des Verfahrens der Occupancy Korrektur. In diesem Zusammenhang danke ich auch Dr. Pavel Tlusty und Lucas Chald. Lucas Chald danke ich zudem für die Mitwirkung bei der Bereitstellung der Transportmodelle.
Simon Spies danke ich für wertvolle Tipps und Hilfestellungen sowie für die Bereitstellung der Protonendaten. Danken möchte ich auch Marvin Kohls, Holger Huck, Leon Skorpil und Mirco Parschau sowie allen anderen Teilnehmern unserer morgendlichen Meetings für die Aufmerksamkeit, Diskussionen zu Analyseergebnissen und Tipps zur besseren Darstellung von Plots.
Des Weiteren danke ich allen Mitgliedern der HADES Kollaboration, insbesondere denen die an der Umsetzung der Silberstrahlzeit beteiligt waren und an der Aufbereitung der Daten arbeiten. Ohne sie wäre diese Arbeit nicht möglich gewesen. Zuletzt möchte ich meinen Eltern danken, die mich während meines Studiums immer unterstüzt haben.

Selbständigkeitserklärung

Erklärung nach § 30 (12) Ordnung für den Bachelor- und dem Masterstudiengang

Hiermit erkläre ich, dass ich die Arbeit selbstständig und ohne Benutzung anderer als der angegebenen Quellen und Hilfsmittel verfasst habe. Alle Stellen der Arbeit, die wörtlich oder sinngemäß aus Veröffentlichungen oder aus anderen fremden Texten entnommen wurden, sind von mir als solche kenntlich gemacht worden. Ferner erkläre ich, dass die Arbeit nicht - auch nicht auszugsweise - für eine andere Prüfung verwendet wurde.

Frankfurt, den